The clinical application of multispectral fluorescence lifetime imaging of human skin using multiphoton microscopy.

Dr Rakesh Patalay

B.Sc. MBBS MRCP (UK)

October 2013

Division of Experimental Medicine/Department of Medicine

Imperial College of Science, Technology and Medicine

Thesis submitted in partial fulfilment of the requirements for the degree of Doctor of Philosophy (Ph.D.)

Abstract

The work presented in this thesis employed multiphoton microscopy of tissue autofluorescence to investigate spectrally and fluorescence lifetime resolved images obtained from normal skin and cutaneous malignancies. This was achieved by adapting a commercially available CE-marked multiphoton tomograph (DermaInspect®) to allow fluorescence lifetime imaging (FLIM) simultaneously in four spectral channels and corresponding steady-state hyperspectral images using a prism-based spectrometer to be acquired.

The images generated were analysed through the manual identification of morphological criteria and through manual and automatic segmentation of individual cells within FLIM images followed by automated morphological and spectroscopic analysis.

The analysis of FLIM images acquired from normal skin *ex vivo* and *in vivo* identified subpopulations of cells based on their autofluorescence characteristics and allowed intra- and interpatient variations to be assessed. The mean cellular lifetime was found to decrease between 691-1286 picoseconds (ps) with depth, increase between 199-550 ps with age and a statistically significant decrease between 286-1436 ps with skin phototype (I-IV) was found, depending on spectral channel.

The manual identification of morphological features from BCC images acquired *ex vivo* allowed the correct diagnosis to be made with a sensitivity/specificity of 79%/93%. Cellular fluorescence lifetimes were statistically significantly longer by between 19.9-39.8% compared to normal skin. A linear discriminant analysis combining both spectroscopic and morphological cellular parameters allowed BCCs to be discriminated from normal skin with an AUC of 0.83.

Manually identified morphological features were able to distinguish dysplastic naevi from melanomas with a sensitivity and specificity of 75% and 81% respectively from *ex vivo* FLIM images. However, no contrast in cellular fluorescence lifetime was observed.

A motorised stage has also allowed multispectral FLIM image mosaics of depth resolved images from unsectioned skin to be presented for the first time.

In conclusion tissue autofluorescence and FLIM detect clinically useful differences in the skin.

Contents

Author Declaration

All the work presented in this thesis is my own with the following exceptions:

- The design, construction, installation and testing of the 4-channel TCSPC and spectrometer detector modules for the DermaInspect® instrument was performed by Dr Clifford Talbot.
- Software for controlling data acquisition and processing for the spectrometer detector module was written by Dr Talbot.
- A software interface to integrate the multiple DermaInspect® and TCSPC software applications was also written by Dr Talbot.
- The analytical software for ROI analysis of FLIM data was written by Dr Yuriy Alexandrov. Dr Alexandrov also performed all of the data processing for the ROI morphology and fluorescence decay analysis, including the statistical tests, discriminant analysis and MATLAB histogram generation.
- Software for analysis of FLIM and spectral data acquired using the modified DermaInspect® system was written by Dr Clifford Talbot and Dr Sean Warren with input from Dr Yuriy Alexandrov and Dr Ian Munro. Batch analysis of FLIM images was performed by Dr Martin Lenz.
- The semi-automated merged mosaic of a naevus was carried out by Dr Sunil Kumar.

Copyright Declaration

Acknowledgements

This work presented in this thesis represents the collaborative efforts of many people. Nothing would have been possible without the efforts of the 'core team', consisting of Dr Clifford Talbot, Dr Yuriy Alexandrov and myself. Cliff's expertise and technical skills in both optics and programming allowed the modified detector modules to be created and continue to function throughout the project, despite a number of technical challenges. The speed and efficiency of the data analysis was only made possible when Yuriy joined the team, with his expertise in data/image analysis, programming and bright ideas. Dr Christopher Dunsby's work also requires specific mention. He kept the cogs turning over the duration of the project and who's keen attention to detail and encyclopedic knowledge in this field kept us all focused.

Executive and strategic guidance came from the thought provoking discussions with Professor Anthony Chu, Professor Gordon Stamp and Professor Paul French and who's input has been invaluable in shaping my understanding of what research questions I should be asking and answering.

I am also grateful for the work that Dr Sunil Kumar and Dr Martin Lenz have done to process the mountain of FLIM images that have been generated over the course of this project. Within the Photonics group I would also like to extend my thanks to all the other PhD students and post-docs that have both taught me and entertained me over coffee in equal measure. In addition to those named above, this includes (but is not necessarily limited to) Dom, Romain, Sean, Doug, Hugh, both Lionels, James, Joao, Sergio, Tom and Stephane.

I would also like to thank the patience of Dr Fernanda Teixeira, Dr Sangeeta Punjabi and all the nurses and administration staff in the outpatient's department at the Hammersmith Hospital whom have supported me in collecting the clinical data, despite its disruptive effect on tremendously busy clinics.

All of the work presented was funded by the EC SKINSPECTION project. The original DermaInspect® instrument was provided by JenLab (GmbH, Germany) as part of this project and so I would like to extend my thanks to Karsten König, Hans Georg Breunig, Rainer Bückle and Marcel Kellner-Höfer.

List of Abbreviations

AF	Autofluorescence
ALA	Aminolevulinic acid
ATP	Adenosine triphosphate
AUC	Area under the curve
BCC	Basal Cell Carcinoma
CCD	Charge-coupled device
CFD	Constant fraction discriminator
CI	Confidence Interval
CV	Coefficient of Variation
DCSP	Dichroic short pass filter
DMSO	Dimethyl sulphoxide (solvent)
EEM	Excitation emission matix
ELCOR	Elastin to collagen ratio index
EMCCD	Electron-multiplying charge-coupled device
F	Female
FAD	Flavin adenine dinucleotide
FIFO	first-in first-out
FLIM	Fluorescence lifetime imaging microscopy
FMN	Flavin mononucleotide
FOV	Field of view
GOI	Gated optical intensifier
H&E	Hematoxylin and eosin stain
HFUS	High frequency ultrasound
LDA	Linear discriminant analysis
LED	Light emitting diode
LREC	Local Research Ethics Committee
M	Male
MDMS	Multiphoton dermis morphology score
MFSI	Multiphoton to SHG index (inverse of the SAAID score)
MHz	megahertz
µm	Microns
mm	Millimeters
mW	Milliwatts

MW	Molecular weight
MPE	Multiphoton excitation
MPM	Multiphoton microscopy
MPT	Multiphoton tomography
NADH	Nicotinamide adenine dinucleotide (reduced form)
NAD(P)H	Nicotinamide adenine dinucleotide phosphate (reduced form)
NHS	National Health Service
NIR	Near infrared
nm	Nanometers
ns	Nanosecond
NMSC	Non-melanoma skin cancer
NREC	National Research Ethics Committee
OA	Optoacoustics
OCT	Optical coherence tomography
PC	Personal computer
PCA	Principal Component Analysis
PMT	Photomultiplier tube
ps	picosecond
RCLM	Reflectance confocal light microscope
RF	Relative Fluorescence
ROI	Region of interest
s	second
SAAID	SHG to autofluorescence aging index of dermis
SCC	Squamous cell carcinoma
SHG	Second Harmonic Generation
SD	Standard deviation
τ	Tau (the symbol for fluorescence lifetime)
TAC	Time to amplitude converter
TCSPC	Time correlated single photon counting
TPE	Two photon excitation
UV	Ultraviolet

List of Figures

List of Tables

Chapter 1. Introduction to the skin

1.1 Introduction

The research presented in the thesis investigates the use of multiphoton microscopy to image the skin non-invasively. Both normal skin and skin cancer have been investigated. This chapter therefore provides a brief introduction to three topics – the structure and function of normal human skin; the most common malignancies that occur in the skin i.e. basal cell carcinoma, squamous cell carcinoma and melanoma; and finally a brief synopsis of the major non-invasive imaging modalities that have been applied to the skin.

1.2 Normal Skin

The skin is the largest organ system in the human body and has many functions. Its primary function is to act as a physical, chemical and biological barrier to exogenous substances and organisms. It is also involved in thermoregulation, sensation and calcium/vitamin D homeostasis. It is composed of three main layers – the epidermis, dermis and subcutis.

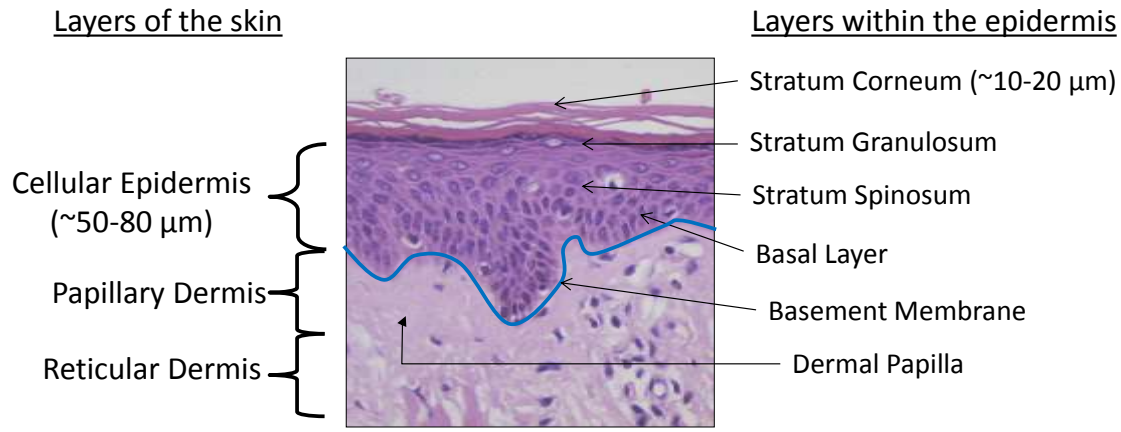

Figure 1.1 An annotated H&E stained section of the epidermis and dermis of normal skin

The epidermis is the most superficial layer of the skin and is structured into a number of distinct layers defined by their histological appearance, see figure 1.1. Keratinocytes account for 95% of the cells within this layer. The epidermis is separated from the dermis by the basement membrane and varies in thickness depending on age and body site (typically 60-100 µm (Sandby-Moller, Poulsen et al. 2003)). This multilayered membrane acts as a mechanical and functional barrier between the two layers. It serves many functions including orientating the proliferative basal keratinocytes' direction of growth and anchoring the basal layer of the epidermis to the papillary dermis. Both congenital and acquired defects in this layer give rise to many blistering skin disorders (Fassihi, Wong et al. 2006).

After dividing in the basal layer, keratinocytes migrate towards the skin surface with an accompanying change in cellular morphology and function. The cells lose the ability to divide, undergo programmed cell death and change their expression of intracellular keratins in a process called terminal differentiation and apoptosis (Fuchs 2008) as they mature. The keratinocytes in the basal layer are cuboidal in shape, small in size and have a large nuclear to cytoplasm ratio. As cells progress to the *Stratum Spinosum* and *Stratum Granulosum* they become flatter in shape, progressively lose their nuclei and intracellular organelles and accumulate dense keratohyalin granules within them. The most superficial epidermal layer, the *Stratum Corneum* consists of compacted, water resistant, richly keratinised layers of dead keratinocytes termed corneocytes.

Melanocytes are usually found alongside keratinocytes in the basal layer of the epidermis and in the papillary dermis. Their primary role is to synthesize and distribute melanin to the surrounding keratinocytes, thus protecting their nuclei from UV photodamage by absorbing light in the UV spectral range. Most melanocytes are found individually at regular intervals in the basal layer and provide melanin for on average 36 keratinocytes, collectively termed a epidermal melanin unit.

The term melanocytic naevus or mole is used for benign proliferations of melanocytes. The location of these within the skin allow them to be classified as junctional naevi (along the basal layer), dermal naevi (in the papillary dermis), or compound naevi (containing both junctional and dermal components).

Langerhans cells are present within the *Stratum Spinosum* of the epidermis but are poorly visible by Hematoxylin and Eosin (H&E) staining of fixed, sectioned tissue, (the most common stain used to evaluate skin samples). They are dendritic in morphology with numerous protrusions extending between keratinocytes. They are specialised cells that can ingest particulate matter around them and have an immune- surveillance role within the skin.

Finally Merkel cells are involved in sensory perception and are situated in the basal layer near associated sensory nerve endings. They can't be visualised using the H&E stain and require specific immunostaining to be seen histologically.

Regional variation can be found in normal skin depending on body site e.g. thicker *S.Corneum* is found on the palms and soles. Changes also accompany malignancy, such as migration of malignant cells across the basement membrane and the destruction of normal epidermal/dermal architecture.

The dermis lies beneath the basement membrane and provides physical support and nutrients for the epidermis above. The superficial dermis is called the papillary dermis and is defined by protrusions of the dermis, called dermal papillae, interdigitating with the epidermis. The reticular

dermis lies below this layer and can be distinguished by a change in the orientation of the collagen fibres within it.

Structures found within the dermis include the pilosebaceous unit (hair and sebaceous gland), nerves, sweat glands, sensory receptors and the vasculature. The vasculature is arranged into a superficial plexus that lies in the papillary dermis and a communicating deep plexus, found deeper in the dermis. The structural support of the dermis is provided by a matrix of proteoglycan macromolecules, type I and III collagen and elastin. The collagen provides strength and accounts for on average 56% of the dry weight of the dermis (Lovell, Smolenski et al. 1987) whilst elastin provides the elastic recoil of the skin and accounts for 2-4% of the dry weight (Kielty, Sherratt et al. 2002; Burns, Breathnach et al. 2010).

The lower reticular dermis has more densely packed collagen and provides more mechanical strength and elasticity to the skin than the papillary dermis.

The subcutis lies beneath the dermis. It consists of loose connective tissue and attaches the skin to the underlying musculoskeletal system. Adipocytes account for the majority of the cells in this layer and contain approximately 80% of the body's fat (Burns, Breathnach et al. 2010). Although the adipocytes main function is for insulation and mechanical cushioning, they also have an endocrine function.

1.3 Skin Cancer

The incidence of all types of skin cancer in the western world is rising (Diepgen and Mahler 2002). The most prevalent skin cancers are basal cell carcinoma and squamous cell carcinoma, which are often referred to as non-melanoma skin cancer (NMSC), and malignant melanoma. In the UK malignant melanoma has risen most in incidence over the last decade compared to NMSC (CancerResearchUK 2010).

1.3.1 Basal Cell Carcinoma

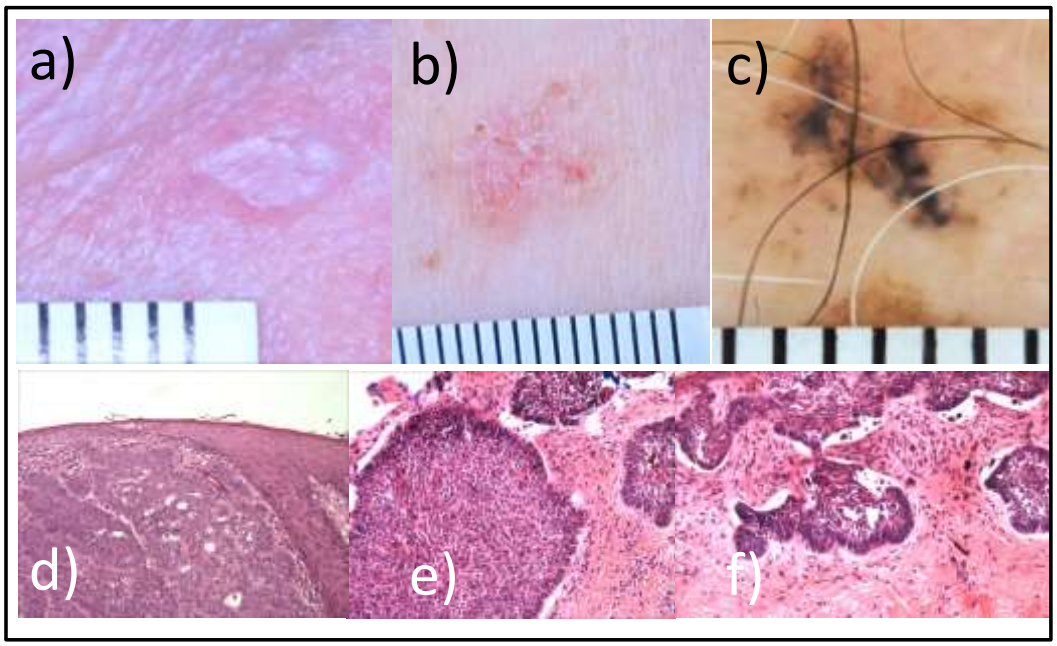

Figure 1.2 a-c) Different clinical presentations of BCCs a) nodular b) superficial c) pigmented. d-f) Histological images of BCCs stained with H&E showing clusters of BCC cells within the epidermis and dermis.

Basal cell carcinoma (BCC) has high prevalence in the western world (Diepgen and Mahler 2002; Demers, Nugent et al. 2005). It is the most common skin malignancy in Caucasian populations with a rising incidence in all age groups (Christenson, Borrowman et al. 2005; Staples, Elwood et al. 2006). The incidence is estimated at between 105-128 per 100,00 in the UK (Holme, Malinovszky et al. 2000). They arise through cumulative exposure to the sun (Kricker, Armstrong et al. 1995) and therefore typically occur in sun exposed sites, such as the face and mainly occur in fair skinned individuals.

Its name derives from the histological resemblance of the malignant cells to those found in the basal cell layer of the epidermis. These tumours have a low metastatic potential and thus their mortality is very low. They can, however cause significant morbidity from local tissue destruction if lesions are not diagnosed and treated. The incidence of recurrent primary tumours in patients with a BCC is also high, with an estimated risk of developing a second tumour within 3 years of 44% (Marcil and Stern 2000).

A number of clinical/histological subtypes exist, see figure 1.2. Nodular BCCs are most prevalent and have a distinctive pearlescent texture, telangectasia (small blood vessels) with rolled edges developing in larger lesions. Histologically malignant cells are grouped into well-defined clusters with characteristic stroma between. The treatment of choice for cure in most patients is surgical

excision. However excellent results are still gained by radiotherapy for patients not suitable for surgery (Telfer, Colver et al. 2008).

Morphoeic and infiltrative BCCs are poorly defined clinically and histologically. They therefore require wider surgical margins to ensure complete excision (Wolf and Zitelli 1987) and have a higher recurrence rate than nodular BCCs. Mohs micrographic surgery is a tissue sparing technique that can be used in this context. It entails removing the tumour progressively. Frozen sections of the fresh tissue can be prepared quickly (in comparison to fixed sections) and are reviewed during the surgical procedure. Small amounts of tissue are removed progressively until surgical clearance of the tumour margin is gained. In this way, the amount of normal tissue removed and the incidence of incompletely excised tumour is minimised. Unfortunately the technique is time consuming, labour intensive and expensive and therefore tends to be reserved for recurrent tumours or those in cosmetically sensitive sites.

1.3.2 Squamous Cell Carcinoma

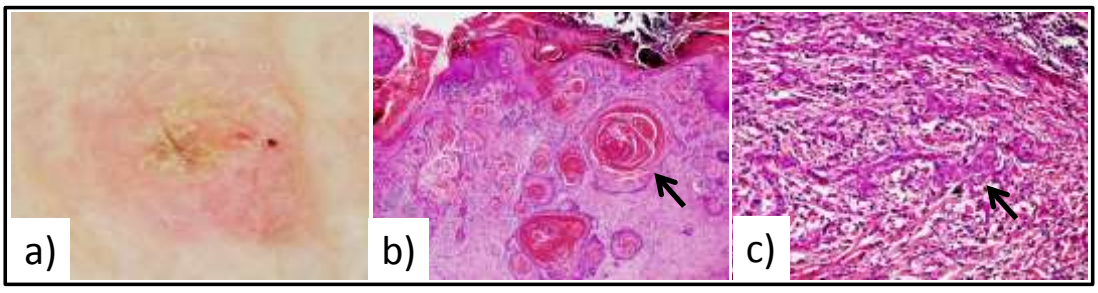

Figure 1.3 (a) Clinical image of SCC (b) histological image of moderately differentiated SCC stained with H&E illustrating keratin deposits within the dermis (black arrow) within the tumour (c) histological image of poorly differentiated SCC stained with H&E illustrating strands of epithelial cells invading the dermis(black arrow) (Images courtesy of Dr A Robson, St Johns Institute of Dermatology, London).

The incidence of squamous cell carcinoma (SCC) in the UK has been estimated at 25.5 per 100,000 (Holme, Malinovszky et al. 2000) with an increase in incidence with age greater than BCCs. (Diepgen and Mahler 2002).

This malignancy arises from keratinocytes and most often occurs in cells that have undergone photodamage induced by chronic, cumulative sun exposure (Armstrong and Kricker 2001). SCCs can also arise from sites of chronic infection, inflammation or previous radiotherapy.

The premalignant lesion, actinic keratosis is a UV induced intraepidermal neoplasia and can lead to SCCs. The prevalence is as high as 25% in Caucasian populations above the age of 60, with up to 10%

transforming into an invasive SCC (De Berker, McGregor et al. 2007). Once invasive, SCCs have the potential to metastasize, with mortality dependent on tumour characteristics.

There is great variation in the clinical appearance of lesions that typically appear as raised areas of red skin with surface scale, see figure 1.3. This can make the distinction between actinic keratosis from early SCCs difficult.

Histologically, key indicators for the risk of local recurrence or metastatic spread are depth of invasion of the tumour and cellular differentiation (well, moderate or poor). Poorly differentiated tumours greater than 6mm in depth carry the greatest risk of recurrence. The standard treatment is surgery for these tumours. However, radiotherapy can be used in selected situations. (Motley, Kersey et al. 2002).

1.3.3 Melanoma

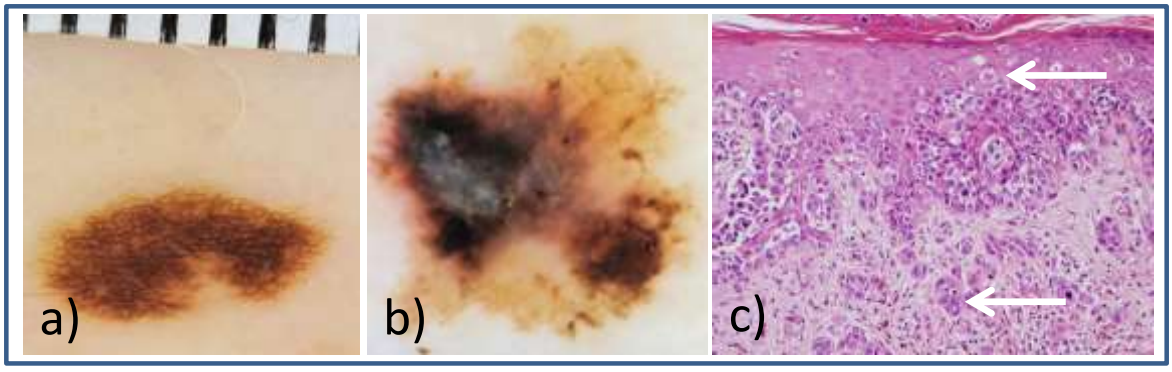

Figure 1.4 a) Clinical image of a benign Junctional Naevus b) Clinical image of a Melanoma c) Histological image of the melanoma seen in (b) stained with H&E. Arrows indicate melanoma cells spreading to the epidermis and invading the dermis.

Melanoma is a malignancy arising from melanocytes. Since melanocytes are not exclusively found in the skin, primary melanomas can arise within other organs. Cutaneous melanoma accounts for 4% of cancers in the UK with approximately 10,400 new cases diagnosed annually (CancerResearchUK 2010). It is however responsible for 80% of skin cancer related deaths (Miller and Mihm 2006). Its incidence increases with age and has quadrupled over the last thirty years. It is currently the 3rd most common cancer in the 15-39 age group in the UK (CancerResearchUK 2010). An individual's risk is influenced by family history, skin phototype (a measure of the skin's ability to tan and easy of burning), sun exposure (Elwood and Jopson 1997) and having atypical naevi syndromes.

Melanoma is suspected by a change in size, shape or colour of a mole accompanied by a supporting history, see figure 1.4. However these changes are not specific for malignant change and it can only be confirmed histologically by the presence of cytologically malignant melanocytes invading the

dermis i.e. crossing the epidermal basement membrane. As most clinically suspicious moles for melanoma are not histologically confirmed as malignant, a large number of non-malignant naevi are excised, even with the aid of dermatoscopy (Argenziano, Cerroni et al. 2012). This is potentially unnecessary, invasive, scarring to the patient and has a financial cost.

A number of histological variants of melanoma are recognised. The most common is superficial spreading malignant melanoma. Nodular, lentigo maligna (found on chronically sun exposed skin) and acral lentiginous melanomas (occuring on palms and soles) are less common. Despite the use of histological criteria, it can remain difficult to classify some melanocytic proliferations as benign or malignant e.g. Spitz naevi are lesions that appear in childhood and are often histologically indistinguishable from malignant melanoma. However, they behave in a clinically benign manner.

The primary treatment for melanoma remains surgery. The prognosis of patients correlates well with the Breslow thickness of the lesion at excision, defined as the maximum depth of tumour invasion from the *stratum granulosum* layer of the epidermis. Increased Breslow thickness increases the incidence of metastatic disease which is poorly responsive to chemotherapy or radiotherapy. Early diagnosis is therefore critical. Melanoma patients with a Breslow thickness of less than 1mm have a 5 year survival of 95-100%. In contrast, a thickness of 2.1-4mm has a 60-75% survival rate at 5 years (Roberts, Anstey et al. 2002).

1.4 Non-invasive imaging

Financial and clinical pressures have led to the development of a number of non-invasive imaging modalities. Improvements to non-invasive diagnostic techniques have the potential to diagnose skin cancers earlier and more accurately, allow direct monitoring of the effects of treatment and avoid unnecessary over-treatment. These improvements in patient care could be matched by significant financial savings.

Also, accurate non-invasive assessment of the depth of tumour invasion would be useful in planning surgical excision margins. For example the standard practice for the treatment of melanoma is to excise the tumour, determine the depth of invasion of the tumour histologically, then resect a further margin of tissue based on that depth. An accurate initial assessment would remove the need for a second surgical procedure. Similarly, the wide surgical margins currently used for surgical excision of infiltrative BCCs could be reduced in many cases.

Finally, non-invasive imaging could play a role in monitoring response to topical chemotherapy agents. For example 5-fluorouracil can be used to treat superficial BCCs and actinic keratosis.

Current practice relies on clinical assessment alone to determine adequate response to therapy. This is commonly impaired in the short term by the degree of inflammation induced by the treatment.

1.4.1 Dermatoscopy

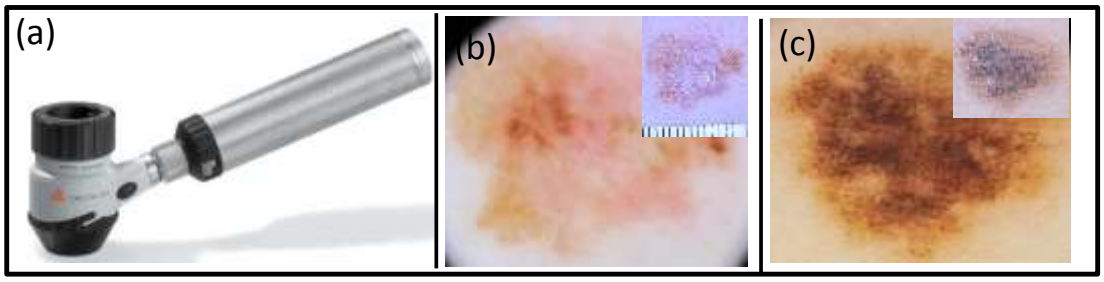

Figure 1.5 a) Dermatoscope (www.heine.com). b,c) Typical dermatoscopic images of melanomas with corresponding macroscopic image inset .

Dermatoscopy is a technique that magnifies the skin and allows visualisation of structures to the depth of the papillary dermis. Dermatoscopes illuminate the skin around a central lens and are held either over the surface or in direct contact with the skin, see figure 1.5. Classical dermatoscopy uses a fluid interface (usually alcohol gel or oil) to interface between the instrument and the skin. The fluid eliminates reflected light and renders the *stratum corneum* transparent, allowing the structures beneath to be more clearly visible. Although dermatoscopy can be applied to all dermatoses, its primary role is in the assessment of solid lesions, particularly melanocytic lesions. It provides greater morphological information and increases clinical diagnostic sensitivity compared with clinical examination alone (Kittler, Pehamberger et al. 2002).

A number of diagnostic algorithms using dermatoscopy have been validated for the diagnosis of melanoma. These include the ABCD system (asymmetry, boarder irregularity, colour, diameter) (Nachbar, Stolz et al. 1994), pattern analysis (Argenziano, Soyer et al. 2003), 7 point score (Dal Pozzo, Benelli et al. 1999) and the Menzies method (Menzies, Ingvar et al. 1996). All have been shown to have a high sensitivity (range 83-86%) and specificity (range 70-83%) for identifying melanomas from other pigmented lesions (7 point score, Menzies method) or from pigmented melanocytic lesions (ABCD system, pattern analysis). Although these algorithms have allowed more melanomas to be diagnosed at the bedside, they are most valuable for their negative predictive power i.e. to exclude melanoma and thus have reduced the rate of unnecessary biopsies. Computer algorithms have also been written to stratify dermatoscopic images by likelihood of malignancy, with varying success (Rubegni, Burroni et al. 2002; Rajpara, Botello et al. 2009).

Despite the widespread use of dermatoscopy in clinical practice, the number of naevi excised for every melanoma still range from 8.7 to 29.4 between dermatology centres (Argenziano, Cerroni et

al. 2012). This creates potentially unnecessary procedures, cost and disfiguring scars for patients and creates a clinical and financial need for better non-invasive modalities to be developed.

1.4.2 High Frequency Ultrasound

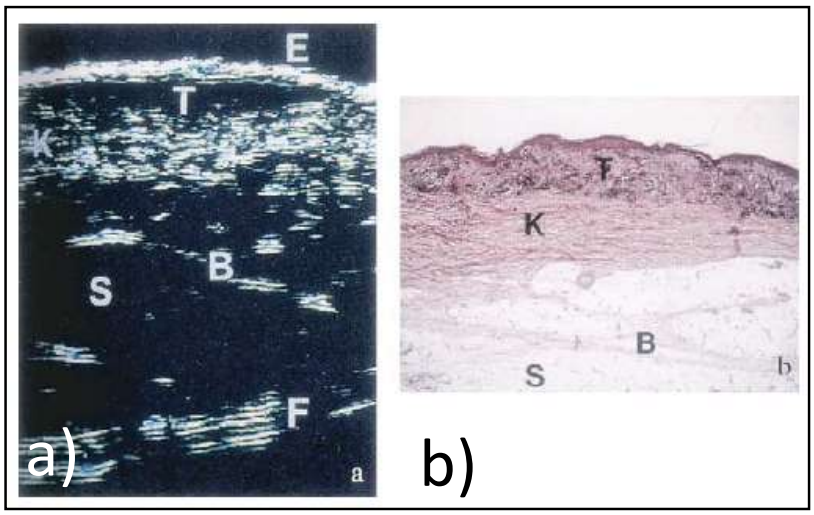

Figure 1.6 a) HFUS image of a melanoma taken at 20MHz and b) corresponding histology stained with H&E. Key-E entry echo, T tumour, K *stratum corneum*/derims B blood, S subcutis, F fascia. Reproduced from (Marghoob, Swindle et al. 2003)

Ultrasound imaging uses the echoes from reflected sound waves from interfaces between tissue types to reconstruct a 2 dimensional vertically sectioned image, see figure 1.6. The optimal ultrasound frequency balances the depth of penetration (deepest at low frequencies) with the resolution (highest at high frequencies). Traditional ultrasound equipment for medical imaging operates at 7.5 MHz which has inadequate resolution for skin imaging. High frequency ultrasound (HFUS) between 20 MHz to 1 GHz has been more successful when imaging skin, allowing axial image resolutions between 200µm and 16µm to be achieved respectively. They have been used to assess various aspects of normal skin and pathology e.g skin thickness (Alexander et al. 1979), vascular disorders (Betti et al. 1990), dermatological diseases (Gupta et al. 196; Machet et al. 2006) and skin tumours (Gupta et al. 1996).

Desai et al. showed good correlation between tumour margins of superficial and nodular BCCs between HFUS at 20 MHz and histology. However, they were unable to detect margins from infiltrative or morphoeic BCCs (Desai, Desai et al. 2007).

Their use for reliably differentiating between benign melanocytic nevi and melanomas diagnostically has not been possible to date using 20MHz (Harland et al. 2000). Hayashi et al. however showed that the depth of tumour invasion of melanomas assessed using HFUS at 30 MHz correlated sufficiently well with histology to allow accurate classification of lesions into the correct AJCC/UICC staging category i.e. ≤1mm or >1.01mm depth (T1, T2). (Hayashi, Koga et al. 2009). Gambichler et al. too

showed that the measured tumour depth was shown to correlate well to the histologically measured depth to within 33.9 µm for 20 MHz, increasing to 16 µm for 100MHz frequencies for melanomas under 1mm in depth (Gambichler, Moussa et al. 2007). For melanomas between 0.4-7.6 mm, moderate agreement was found in thickness between HFUS and histology with a mean thickness (±SD) of 1.96±2.15 mm and 1.95±2.62 mm respectively. This degree of accuracy was sufficient to predict the correct re-excision margins in 26/31 subjects investigated (84%, 95% CI 66-95)(Machet, Belot et al. 2009) .

In summary the contrast and resolution of this modality is lower than reflectance confocal light microscopy and optical coherence tomography and it has been found to be best suited for providing dimensional rather than diagnostic information. Most recently, HFUS has been combined/directly compared with optical imaging modalities to combine the strengths of each modality e.g. optical coherence tomography (Mogensen et al. 2009) and multiphoton microscopy (König & Speicher 2010).

1.4.3 Optical Coherence Tomography

Optical Coherence Tomography (OCT) is the optical analogue to ultrasound. It uses a high bandwidth light source (typically infrared) and collects the back scattered light that arises between tissue interfaces with differing refractive indexes. It uses interferometry to compare the scattered light to light reflected from a second, known path length to calculate the tissue depth of these interfaces between tissue layers. It has a poorer resolution than reflectance confocal light microscopy (3-20µm laterally and axially) but has a greater depth of penetration of 1-2mm (Mogensen, Thrane et al. 2009), see figure 1.7.

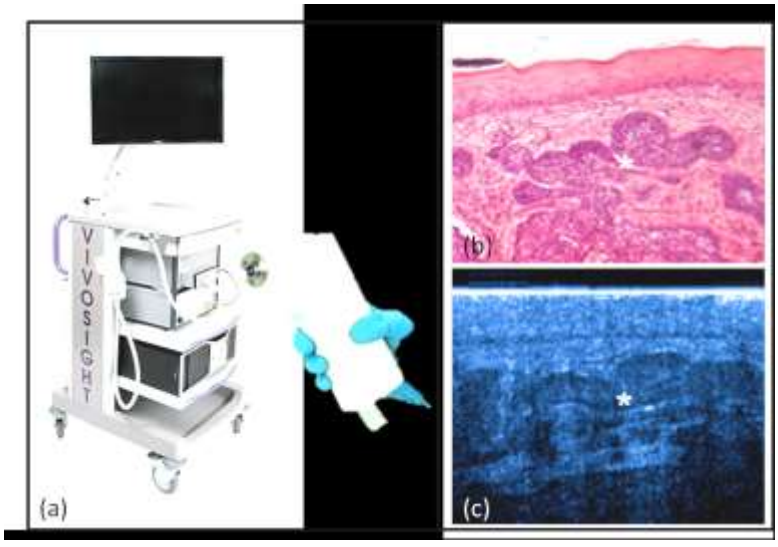

Figure 1.7 (a) OCT device for skin imaging - Vivosight, Michelson Diagnostics Ltd. (b)H&E stained histological section of a nodular BCC and (c) corresponding OCT image taken *in vivo*. Reprinted from J. Dermatological Science 45(3),p170

Gamichler, Orlikov et al. In vivo optical coherence tomography of basal cell carcinoma. Copyright (2007), with permission from Elsevier. (Gambichler, Orlikov et al. 2007).

An early study using OCT to diagnose NMSC was by Mogensen et al. (Mogensen, Joergensen et al. 2009). They used a self-built system with illumination centred at 1,318 nm, a bandwidth of 66 nm, an axial resolution of 8 µm and lateral resolution 24 µm. 115 images of lesions clinically diagnosed as NMSC and imaged *in vivo* were compared with 105 images from peri-lesional normal skin. Histologically these lesions included 64 BCCs, 1 baso-squamous carcinoma, 39 actinic keratosis, 2 malignant melanomas and 9 benign lesions. Blinded observers were able to distinguish these lesions correctly with a sensitivity ranging from 58-94 % and specificity between 43-96 %. A drawback of OCT found in the study was that only 59% of the OCT images taken were of sufficient quality/completeness for analysis and their inability to distinguish actinic keratosis from BCCs.

Mogensen et al. also compared the accuracy of tumour thickness assessment of NMSC using both OCT and 20 MHz HFUS compared to histology (Mogensen, Nurnberg et al. 2009). They examined 34 lesions that were <2 mm in depth (actinic keratosis and BCCs). Both methods overestimated lesion thickness compared with histology but OCT was more precise than HFUS (difference of 0.392 mm vs.0.713 mm). These results were reproduced by Hinz et al. (Hinz, Ehler et al. 2012) who also found OCT could determine the tumour depth more accurately than 20 MHz HFUS compared to histology (median difference 0.13 vs 0.3 mm). Both groups commented that peri-tumour inflammation made tumour depth assessment more difficult and led to an overestimate of tumour depth (Mogensen, Nürnberg et al. 2011).

Coleman et al. also used OCT to measure tumour margins in NMSC (Coleman, Richardson et al. 2012). They analysed OCT images taken *in vivo* from a 5 mm central area from 18 BCCs (4 superficial, 12 nodular and 2 infiltrative) and 5 SCCs (4 in situ, 1 invasive). They used the VivoSight® (MDL Ltd, Orpington, UK) with light centred at 1305 nm wavelength, resolution of <7.5 µm laterally and <10 µm axially, and a maximum imaging depth of 1.5 mm. They found that tumours <1 mm in depth, such as superficial BCCs, correlated better with histology (0.17±0.3 mm) than tumours >1 mm in depth (-0.54±1.14 mm), which were underestimated in depth by OCT. This was in contrast to the findings by Mogensen et al. (outlined above). They also noted that hyperkeratosis in SCCs caused increased shadowing and made OCT images more difficult to interpret. In this study the difficulty acquiring usable OCT images *in vivo* was also highlighted. Although 78 patients were recruited, only 23 (29.5%) image stacks were suitable for analysis.

This same group also assessed the VivoSight® OCT system's ability to diagnose remaining tumour within freshly excised tissue sections, taken during Mohs micrographic surgery compared with

frozen section histological (Cunha, Richardson et al. 2011). 75 sections from BCCs were assessed from 38 patients. They found that images were of insufficient quality or sections were incomplete in 48/75 (64%) sections. In the remaining sections, concordance was poor with only 4/26 and 23/49 OCT images able to confidently diagnose a histological section as positive or negative for tumour respectively. This gave a sensitivity of 19%, and specificity of 56%.

Most recently Boone et al. found that a high definition OCT device (Skintell®; Agfa Healthcare, , Belgium) was able to identify features defining each histological sub-type of BCCs *in vivo* from images taken from 21 patients (Boone, Norrenberg et al. 2012). The device also imaged in the infra-red spectrum but had a lateral and axial resolution of 3 μm, an maximum imaging depth of 570 μm and a field of view of 1.8x 1.5 mm.

Although OCT has been used widely for the investigation of retinal and choroidal pathology, including naevi and melanomas (Say, Shah et al. 2011), its application in cutaneous melanoma has been limited. Two groups have tried to detect morphological changes associated with melanoma (Giorgi, Stante et al. 2005; Gambichler, Regeniter et al. 2007). However the assessment of tumour depth and diagnostic accuracy has not been validated for pigmented lesions yet. Hinz et al. compared the depth of 26 melanocytic lesions measured by OCT and 20 MHz HFUS to histology (Hinz, Ehler et al. 2011). They found a median lesion thickness of 0.31 mm (range 0.10–0.77 mm) with OCT compared to of 0.25 mm (range 0.06–1.5 mm) measured by histopathology, with a correlation coefficient of r=0.734. This was superior to HFUS, which had a correlation coefficient of 0.390.

In summary OCT has been shown to distinguish morphological features of NMSC non-invasively *in vivo* by several groups. It should be noted that many studies compared *in vivo* depth with measures taken from fixed, sectioned histopathological samples. This comparison inherently lead to artefactual errors such as shrinkage of the tissue after fixation with formalin and the sampling error for depth, as only a fraction of the tissue is sectioned. Despite this, OCT was shown to be accurate for assessing tumours <2 mm in depth but was less precise assessing thicker tumours. It has also been shown in several studies to be more accurate for tumour margin assessment than 20 MHz HFUS. As studies using OCT for melanocytic lesion are limited, its use for their assessment still remains unclear.

1.4.4 Reflectance Confocal Light Microscopy

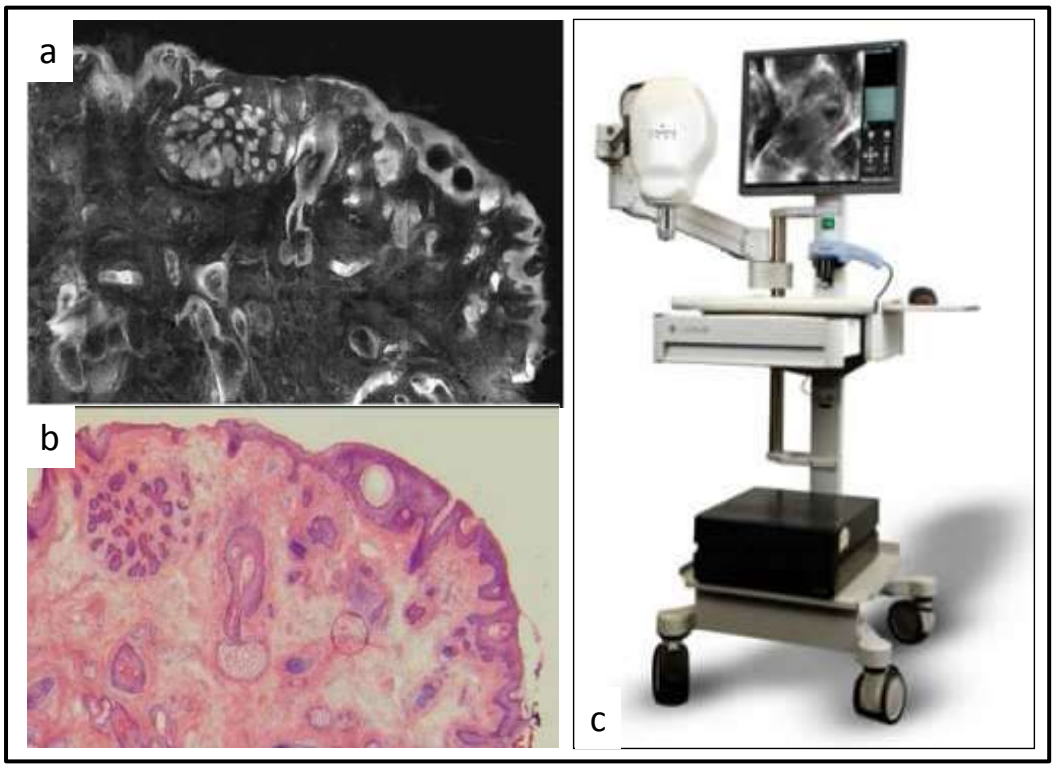

Figure 1.8 (a)BCC mosaic taken using RCLM (b) corresponding histology stained with H&E. Reproduced from(Karen, Gareau et al. 2009). (d) Commercially available RCLM - Vivoscope® 1500 (www.lucid-tech.com)

The first report of reflectance confocal laser microscopy (RCLM) used to image skin *in vivo* was 1995 (Rajadhyaksha, Grossman et al. 1995). It uses variation in the refractive index within tissue to provide contrast. RCLM focuses light to a point in the sample. The scattered and reflected light is then collected by a photomultiplier tube detector. To generate a horizontally sectioned image the point of focus must be scanned in two dimensions. Scattered/reflected light must pass through a point aperture before it reaches the detector which spatially rejects light from outside the focal plane. RCLM can provide high resolution, depth resolved images of the epidermis and papillary dermis to a cellular resolution, see figure 1.8. The range of RCLM instruments for use in skin, manufactured by Lucid® Inc (Rochester,NY) emit light at 830 nm with a maximum power of 35 mW. They have a resolution of 0.5-1 µm laterally, 4- 5 µm axially and a depth of penetration of 350 µm, with fields of view of 500 x 500 µm usually taken.

Study	Sensitivity %	Specificity %	Nos. of Diagnostic Features in Assessment
Pellacani (2005)	97.3	72.3	6
Pellacani (2007)	92	69	6

Langley (2007)	97.3	83	7
Gerger (2008)	97.5	99	not specified

Table 1.1 Sensitivity and Specificity of RCLM for the diagnosis of melanoma (Pellacani, Cesinaro et al. 2005; Langley, Walsh et al. 2007; Pellacani, Guitera et al. 2007; Gerger, Hofmann-Wellenhof et al. 2008). Adapted from (Psaty and Halpern 2009).

As melanin has a high refractive index, it appears bright in images taken by RCLM (Rajadhyaksha, Grossman et al. 1995). This high contrast has allowed a number of morphological features to be defined that distinguish benign from malignant pigmented lesions (Busam, Charles et al. 2001; Langley, Rajadhyaksha et al. 2001; Scope, Benvenuto-Andrade et al. 2007). Several studies found that these criteria have a high sensitivity and specificity, see Table 1.1. A direct comparison between dermatoscopy and RCLM also published by Langley et al. found dermatoscopy to be more sensitive than RCLM for the diagnosis of melanoma (97.3% vs 89.2%). However, both modalities were found to have a similar specificity (84.1% vs 83%) (Langley, Walsh et al. 2007).

A group from Modena, Italy found an 87.6% sensitivity and 70.8% specificity for the 7 criteria they defined for the diagnosis of melanomas from RCLM images taken *in vivo* (Guitera, Menzies et al. 2012). Gerger et al. also examined 162 lesions that included images taken *in vivo* from (27) melanomas and (15) BCCs (Gerger, Koller et al. 2006). They found RCLM could distinguish these malignancies with a positive predictive value of 94.22%.

RCLM has also been used to evaluate BCCs both *ex vivo* (Gerger, Horn et al. 2005) and *in vivo* (González and Tannous 2002) with promising results. When the 5 *in vivo* criteria defined by Gonzalez et al. were applied retrospectively to confocal images taken *in vivo* from 152 skin lesion (benign and malignant), containing images from 83 BCCs, a sensitivity of 82.9% and specificity of 95.7% was obtained when ≥4 criteria were met (Nori, Rius-Diaz et al. 2004). Another set of 8 criteria were tested by Guitera et al. by the group in Modena (Guitera, Menzies et al. 2012). They found that their criteria gave a 100% sensitivity and 88.5% specificity for the diagnosis of 52 BCCs.

Work has also been performed to evaluate the accuracy of tumour margin assessment by RCLM. Pan et al. have shown that the surgical margins of BCC measured *in vivo* by RCLM correlated well to the margins assessed by frozen section in 12/13 cases (Pan, Lin et al. 2012).

In summary RCLM has been shown to have a high degree of accuracy and reproducibility for imaging both pigmented and non-pigmented skin cancers *in vivo*.

1.4.5 Multiphoton Microscopy

Multiphoton microscopy (MPM) is an emerging optical imaging technique (Denk, Strickler et al. 1990) that excites fluorescence from the sample through the simultaneous absorption of two or more photons of infrared light. This process requires a high intensity of excitation light and so is confined to the tightly focused excitation spot. Images are generated by raster-scanning the excitation spot across the specimen in two dimensions. MPM offers a spatial resolution similar to histopathology at high power magnification (<1 µm lateral, <2 µm axial resolution, (König and Riemann 2003)) and is licenced for clinical use *in vivo*.

The skin contains naturally occurring fluorophores that can be imaged using MPM without the need for exogenous contrast agents. These include collagen, elastin, melanin, keratins, porphyrins, NAD(P)H and flavins. Fluorescence intensity imaging using MPM has been used to study skin morphology with subcellular resolution (Masters, So et al. 1997; König, Raphael et al. 2011; Levitt, McLaughlin-Drubin et al. 2011). Further discrimination can be gained measuring the fluorescence emission spectrum (Palero, de Bruijn et al. 2007; Dimitrow, Riemann et al. 2009) and fluorescence lifetime (Cicchi, Sestini et al. 2008; Sanchez, Prow et al. 2010; Benati, Bellini et al. 2011; Seidenari, Arginelli et al. 2012), which measures the rate of decay of the fluorescence signal following a short pulse of excitation light. Manfredini et al. have found MPM images from BCCs to have a good concordance with reflectance confocal light microscopy (Manfredini, Arginelli et al. 2013). A more detailed account of MPM, tissue autofluorescence, fluorescence lifetime and fluorescence lifetime imaging can be found in chapter 2 (pp43).

1.4.6 Optoacoutstics

Optoacoustics (OA) also known as photoacoustics is a relatively new method for biological imaging. It combines the contrast and resolution benefits of optical imaging with the depth of penetration of ultrasound. During imaging, the tissue is first irradiated by a short pulsed laser beam (optical). The energy from the light is absorbed by the tissue and converted to heat. A rapid thermoelastic expansion then occurs within the tissue followed by a resulting pressure wave (acoustic) which propagates as an ultrasound wave and is detected by a standard ultrasound probe.

Optoacoustics has been shown to be a promising modality for imaging of the skin. However, to date, the published literature remains limited. Early studies have demonstrated that cutaneous microvasculature can be imaged with a high resolution by this modality (Favazza, Jassim et al. 2011) and glucose could be monitored non-invasively through the skin (Pleitez, Lieblein et al. 2012). Grootendorst et al. used optoacoustics in a preliminary study to image freshly excised lymph nodes to look for metastatic melanoma (Grootendorst, Jose et al. 2012). The device had a Q-switched

Nd:YAG as its laser light source operating at 10 Hz which allowed imaging in the 720-800 nm spectral range. It had a lateral resolution of 150 µm and an axial resolution of 1 mm. They were able to detect the foci of metastatic disease in 3/6 positive nodes by the increased signal strength. They further stated that optical density of melanin would restrict the functional depth of imaging to 5 mm into the lymph node.

A number of OCT devices have been designed that combine OCT with other imaging modalities such as OA & OCT (Zhang, Povazay et al. 2011) and OA & fluorescence confocal microscopy (Wang, Maslov et al. 2010).

1.5 Conclusions

I have described the structure and function of normal skin; the common skin cancers, namely BCCs, SCCs and melanoma. Finally, I have outlined the main non-invasive imaging modalities available to date, with a focus on their application to skin cancer assessment. The evidence behind the modalities described varies greatly between the more mature modalities, such as RCLM and those newer modalities, such as optoacoustics.

Although all imaging modalities are promising, no modality alone has been able to match to resolution, depth of penetration and contrast that formalin fixed, sectioned, stained histological slides currently offer. As a result devices using multiple imaging modalities are being trialled e.g. Zhang et al. have combined OA, that gives better contrast for vasculature, with OCT, that gives optical contrast and has a good depth of penetration into the skin (Zhang, Povazay et al. 2011). Similarly König et al. have combined HFUS, that has good depth of penetration for skin imaging but gives poor resolution, with MPM, which gives cellular resolution images but has a poorer depth of penetration (König, Speicher et al. 2010).

MPM currently provides the highest resolution images of all the modalities described above. This modality provides the greatest endogenous contrast (as multiple autofluorophores exist) and the only modality that can provide both structural and functional information about the skin. MPM would be excellent for the assessment of epidermal and upper dermal disease *in vivo*. Its depth of penetration would restrict the investigation of deeper dermal diseases to using *ex vivo* samples. MPM therefore offers the greatest information and therefore most likely to be useful diagnostically. In contrast, other imaging modalities, such as HFUS and OCT have a greater depth of penetration but offer lower resolution images. They would therefore be best suited to assess the size of lesions, once the diagnosis had already been made.

Chapter 2. Fluorescence in the skin

2.1 Introduction

This chapter provides an introduction to the principles, techniques and prior knowledge that directly relate to the work described in this thesis. The principles of fluorescence and fluorescence lifetime and the methods used for their measurement, including multiphoton excitation will be discussed. The endogenous fluorophores of the skin are then described in detail followed by an overview of the dynamic changes in fluorescence and fluorescence lifetime associated with malignancy. Finally a comprehensive literature review of the published literature on skin autofluorescence is given, focusing on research using multiphoton microscopy to study skin cancer.

2.2 Fluorescence

Fluorescence can arise in tissue autofluorophores, naturally present within the tissue or from artificially inserted fluorophores (physically or genetically). It is caused by the absorption of energy that promotes electrons from the S_0 ground state to higher more energetic electronic states (S_n). Between these discrete, relatively stable electronic states, can exist less stable vibrational energy states (V_n) (Redmond 2003; Lakowicz 2006). This is illustrated by the Jablonski diagram, shown in figure 2.1

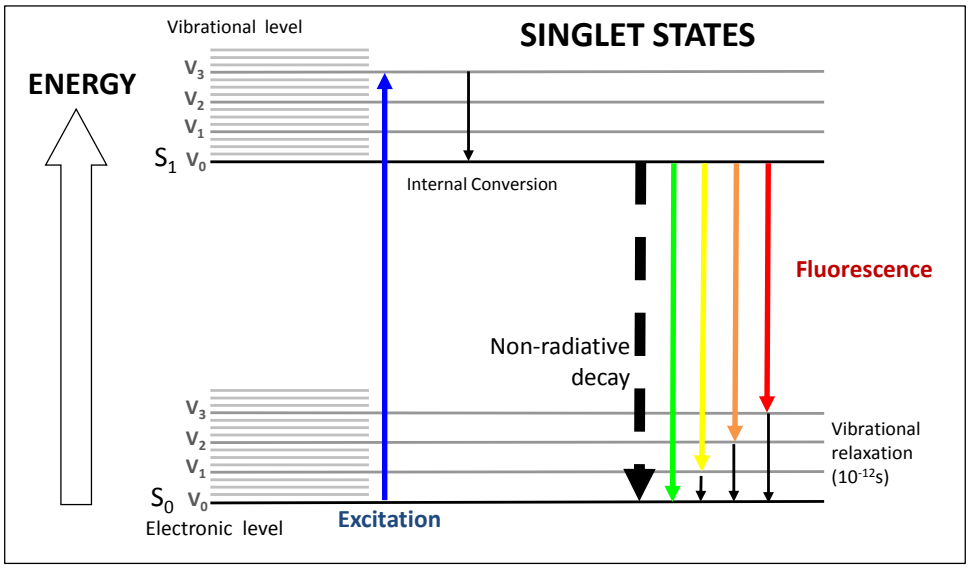

Figure 2.1 Jablonski Diagram illustrating the change in singlet energy states of an electron excited by a photon of light and the loss of energy as fluorescence.

When paired electrons in a molecule have balanced opposing spins, they are said to be in the singlet state. A drop of energy between singlet electronic energy states, in the form of emitted light, is

generally referred to as fluorescence. Following excitation of a molecule to an excited vibrational state through absorption of a photon, energy is typically lost by internal conversion to the lowest vibrational state (V_0) of the excited singlet electronic energy state (S_n). This is typically S_1 for most compounds. The molecule can then return to the ground singlet state (S_0) by radiative (fluorescence) or non-radiative relaxation. A drop of energy to different vibrational levels in the ground state leads to fluorescence emission of varying wavelength. An excited molecule can undergo inter-system crossing, which results in it being in a triplet state. Radiative decay directly from a triplet state in the above way is forbidden and must occur via a slower process (lifetimes ~1 μs) known as phosphorescence.

2.3 Multiphoton excitation

Multiphoton excitation (MPE) typically refers to the simultaneous absorption of two photons instead of one, to increase the energy state of the molecule from the ground to a higher electronic state. The probability of this event is low and so excitation is usually focused in order to achieve a sufficiently high peak power using femtosecond duration pulses in a subfemtolitre volume. The fluorescence intensity induced varies quadratically with the excitation power in two photon excitation, and to the third power for three photon microscopy. The principle was first described in 1931 by Göppert-Mayer in her PhD thesis (Göppert-Mayer 1931) but was not applied to microscopy until 1990 by Denk et al. (Denk, Strickler et al. 1990). It has a number of advantages over confocal microscopy for obtaining optically sectioned images from biological tissue. These include the following:-

1. It is an intrinsically optically sectioning technique because fluorescence is restricted to the focal volume. Optically sectioned MPE images can be obtained if the focal spot is scanned across the focal plane without the need to reject light from out of focus planes using a pinhole, as is required by confocal microscopy.

2. MPE is therefore a more optically sensitive technique than confocal microscopy when imaging in scattering media, as all emitted fluorescence is collected.

3. NIR excitation light is absorbed and scattered less than UV or visible light and therefore tissue penetration is deeper.

4. NIR photons have lower energy than the UV /visible light used for one photon excitation and is therefore less photo-damaging to cells away from the focal plane.

In addition to the emission of fluorescence, high intensity NIR illumination of non-centrosymmetric molecules (such as collagen) can cause energy to be converted via second harmonic generation (SHG) to visible light. This signal occurs near instantaneously and at exactly 1/2 of the excitation light wavelength, and is a dominant signal when imaging in the collagen rich dermis.

2.4 Quantification of fluorescence

The emitted fluorescence from a fluorophore can be described and quantified using a number of parameters – absorption and emission spectra, emission intensity, lifetime and polarisation. Each parameter contributes to the fluorescence signature for that fluorophore.

2.4.1 Fluorescence intensity

This measures the number of emitted fluorescence photons from a substance. It is proportional to the quantum yield of the substance but will also vary with the excitation power used to illuminate the sample and the absorption and scattering properties of the sample measured. Although simple to measure, reproducible quantitative measurements can be difficult to achieve.

2.4.2 Fluorescence spectra

The distribution of electronic and vibrational energy states varies between molecules. Their distribution determines the shapes of the absorption and emission spectra. As the vibrational energy states remain similar between electronic energy states in some molecules, the absorption and emission spectra of a molecule are often mirror images except for the Stokes Shift (shift towards longer wavelength of the emitted spectrum).

The absorption and emission spectra of some molecules are affected by their local environment and this dependence can therefore be used to monitor pH, temperature, etc. As absolute measurements of fluorescence intensity are challenging due to variation in excitation efficiency, detection efficiency, scattering, etc... , ratiometric measures of the intensity taken at two discrete wavelengths are often used to cancel out these unknowns.

2.4.3 Fluorescence polarisation

Fluorophores with their absorption transition dipole moment parallel to the electric field vector of the illuminating light are preferentially excited. Therefore illumination using polarised light coupled with polarised detection can be used to monitor changes in the orientation of molecules, their binding state, their rotational mobility and the viscosity of their solvent.

2.4.4 Fluorescence lifetime

The fluorescence lifetime is the average length of time an electron remains in its excited state before returning to the ground state (Lakowicz 2006). It can be defined as the inverse of the total decay rate, which is the sum of the radiative (k_r) and non-radiative (k_{nr}) decay rates, see equation 2.1.

$$\tau = \frac{1}{k_r + k_{nr}} \qquad \text{Equation 2.1}$$

Following excitation with a short pulse of light (such as with MPE), the fluorescence intensity decays exponentially with time, as described by the equation in figure 2.2 below.

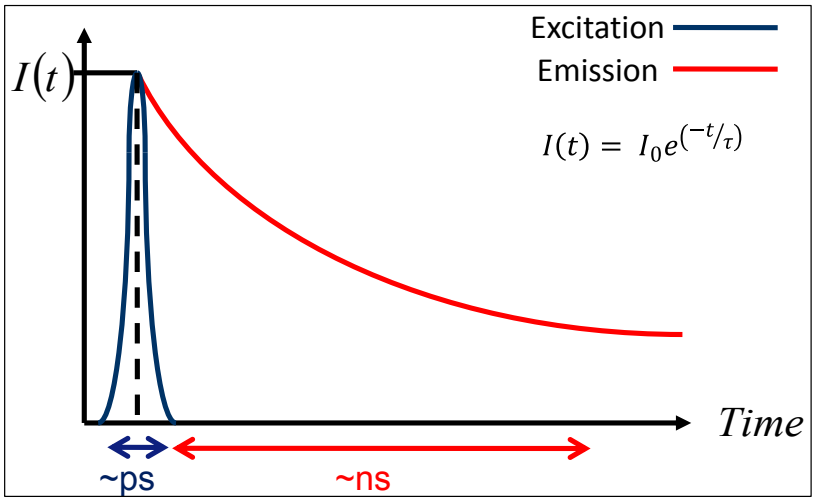

Figure 2.2 Schematic illustrating the fluorescence intensity decay over time following excitation from a short pulse of light. Key: t - time, $I(t)$- Intensity at time t, I_0- Intensity at time 0, τ – fluorescence lifetime.

Biological fluorophores have different lifetimes in different states e.g. oxidised and reduced state, protein bound and unbound state, and for different species in tissue where multiple decay components are expected within each pixel. It is therefore useful to fit more complex fluorescence decay models, such as described by equation 2.2, where each decay constant, τ_i has an initial contribution a_i to the total fluorescence intensity.

$$I(t) = \sum_{i=1}^{n} a_i \, e^{(-t/\tau_i)} \qquad \text{Equation 2.2}$$

As the number of lifetime decay components to be fitted increases, so must the number of photons to be collected in order for the model fit parameters to be determined accurately. Tissue fluorophores typically have more species present than the number of lifetime components fitted that can reasonably be fitted to real data and so a compromise must be made.

A bi-exponential decay model is therefore commonly adopted and the mean fluorescent lifetime (τ_{mean}) can then be expressed as either a species (amplitude) weighted or a photon (intensity) weighted mean of the two lifetime components, see equation 2.3.

$$a)\ \tau_{mean\ species} = \frac{(a_1\tau_1 + a_2\tau_2)}{(a_1 + a_2)}$$

$$b)\ \tau_{mean\ photon} = \frac{a_1\tau_1^2 + a_2\tau_2^2}{a_1\tau_1 + a_2\tau_2}$$ Equation 2.3

The lifetime is a ratiometric measure and is not dependent on the absolute fluorescence intensity making it suitable for comparative assessment between fluorophores and between instruments. A fluorophore's lifetime can be sensitive to its binding state or local environment and therefore can be used to monitor intracellular changes non-invasively in biological tissues.

2.5 Fluorescence lifetime imaging microscopy (FLIM)

FLIM refers to the acquisition of time resolved, fluorescence images acquired on the time scale of a fluorescence decay. Lifetimes are then typically displayed using a false colour map to provide spatially resolved lifetime information. The lifetime colour map is often merged with the fluorescence intensity image so as to provide both lifetime and intensity information.

Experimental methods for FLIM can be divided into two categories– frequency domain or time domain. Both methods can provide equivalent information but require different equipment and analytical methods.

2.5.1 Frequency Domain

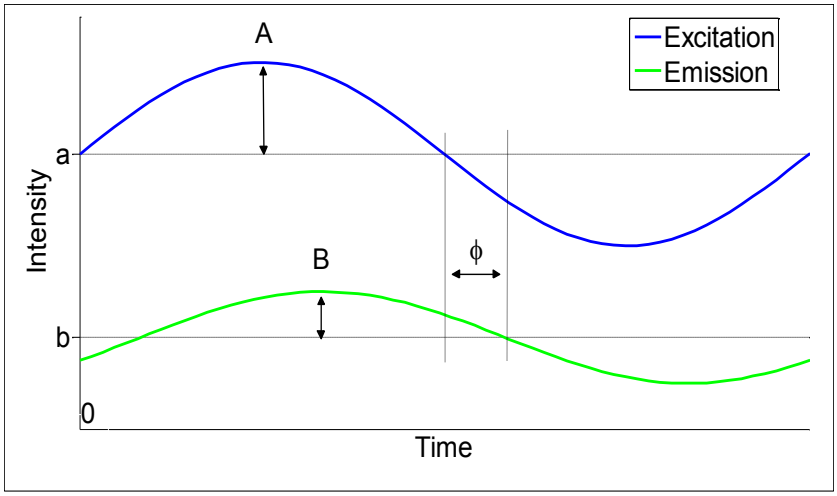

Figure 2.3 A diagram illustrating the changes measured in the excitation light with frequency domain FLIM. Key: A – amplitude of excitation light, B – amplitude of emitted light, ϕ - Phase shift angle

Frequency domain FLIM uses sinusoidally modulated excitation and requires the lifetime to be comparable to the reciprocal of the modulation frequency (ω) of the excitation wave. The phase shift angle (ϕ) in the frequency OR the reduction in intensity modulation (m=(B/b)/(A/a)) between the excitation and emission light (see figure 2.3) can then be used to calculate the lifetime using the following equations (2.4) in the case of a single exponential decay.

$$\tan \phi_\omega = \omega t$$

$$m_\omega = (1 + \omega^2 \tau^2)^{-1/2} \qquad \text{Equation 2.4.}$$

For samples with multiple lifetimes it is necessary to measure the phase shift angle and intensity modulation over a range of modulation frequencies (Lakowicz 2006).

2.5.2 Time Domain

Time domain FLIM uses a femtosecond, pulsed laser light source and measures the change in fluorescence intensity as a function of time following the excitation pulse. The fluorescence lifetime is then calculated by performing a fit to the measured decay data. Two techniques are used.

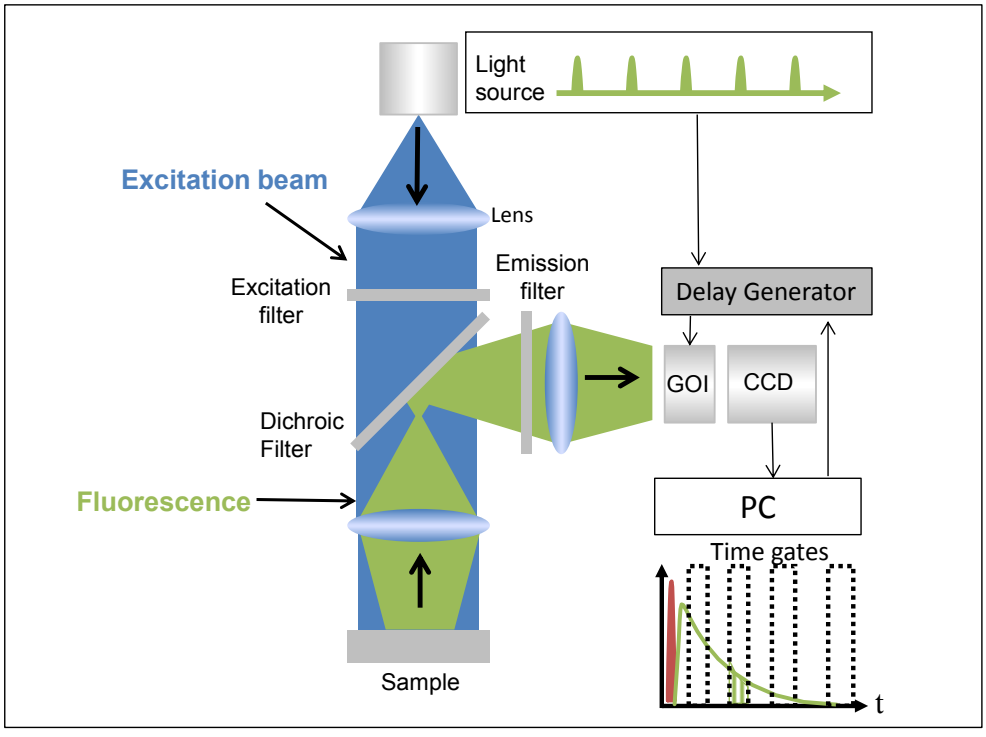

Figure 2.4 A schematic illustrating widefield time domain FLIM. Key: GOI – Gated optical intensifier.

Widefield time domain FLIM gives a high lifetime accuracy in a given acquisition time by acquiring the fluorescence intensity from whole field of view as a single image using a gated optical intensifier

(GOI) to act as a fast shutter and a CCD camera, see figure 2.4. Sequential images taken with varying time delays from the excitation pulse, using a time delay generator attached to the GOI, create time gated images. These can then be used to track the decay of the fluorescence in every pixel of the image simultaneously and allow a lifetime to be fitted to each pixel. Typical gate widths vary from 100-1000 ps while the gate separation is chosen to cover the range of the fluorescence decay.

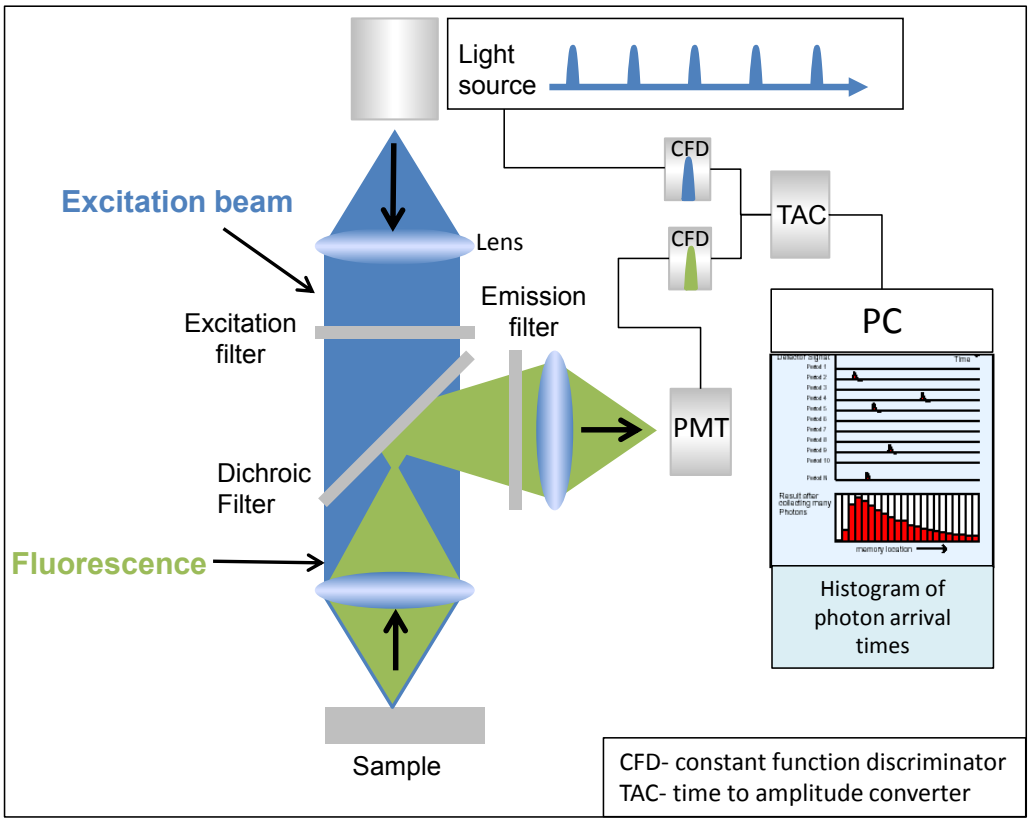

Figure 2.5 A schematic illustrating time correlated single photon counting FLIM.

Time Correlated Single Photon Counting (TCSPC) is the most common method of time domain FLIM and gives the highest lifetime accuracy per detected photon. It is usually implemented on confocal or multiphoton scanning microscopes and therefore collects the fluorescence from single pixels at a time. As illustrated in figure 2.5, the electrical signals from the pulsed light source and single photons detected by the PMT are passed through CFDs. The time difference between them is then converted into a voltage by the time to amplitude converter (TAC) and recorded. This technique can only detect a single photon per excitation pulse. Therefore, unless the excitation power is sufficiently low, further emitted photons are not detected which biases the measured lifetimes towards shorter lifetimes. The excitation power is therefore set below this power threshold and so the maximum count rate for the equipment is not exceeded over the imaging time period. This is typically set to produce a maximum of one single detected photon for every 100 excitation pulses (Lakowicz 2006).

As the focal point is scanned across the field of view, a histogram of photon arrival times is constructed. The lifetime is then calculated for each pixel by fitting an appropriate decay model to the decay histograms.

2.6 Tissue Autofluorescence

A number of endogenous molecules in living cells fluorescence. Although their fluorescence tends to be weaker in intensity than exogenous fluorophores, their advantage is that information can be recorded in biological systems and organisms without the need to administer exogenous labels and without the need to consider associated safety issues and pharmokinetics perturbing their homeostatic state. The addition of exogenous fluorophores into live cells can alter cell physiology and protein expression, sometimes creating uncertainty whether findings truly represent biological phenomena or are artefactual.

Below is an introduction to the main tissue fluorophores found in skin that can be imaged using MPT without the need for exogenous contrast agents. These include collagen, elastin, melanin, keratins, porphyrins, NAD(P)H and flavins. Figure 2.6 illustrates the absorption spectra of these proteins, which is adapted from Wagnieres et al. (Wagnieres, Star et al. 1998). Emission spectra from these fluorophores and the spectral channels into which their fluorescence would be collected using the modified DermaInspect® used in this project (see chapter 4.4, pp89) can be seen in figure 2.7

These spectra of complex proteins such as collagen, elastin, melanin and keratin vary between published sources because the fluorescence emission spectra and lifetimes will vary on how the proteins were prepared and their local environment. Also, NADH and flavins are known to shift their emission spectra and change lifetime when bound to enzymes. Therefore, a purified solution may have a slightly different fluorescent signature compared to when it has been fixed for histological tissue sections or measured in a live biological system. In addition, measurements made directly from tissue (*in vivo* or *ex vivo*) often contains fluorescence from other fluorophores as pure fluorophores rarely exist in isolation.

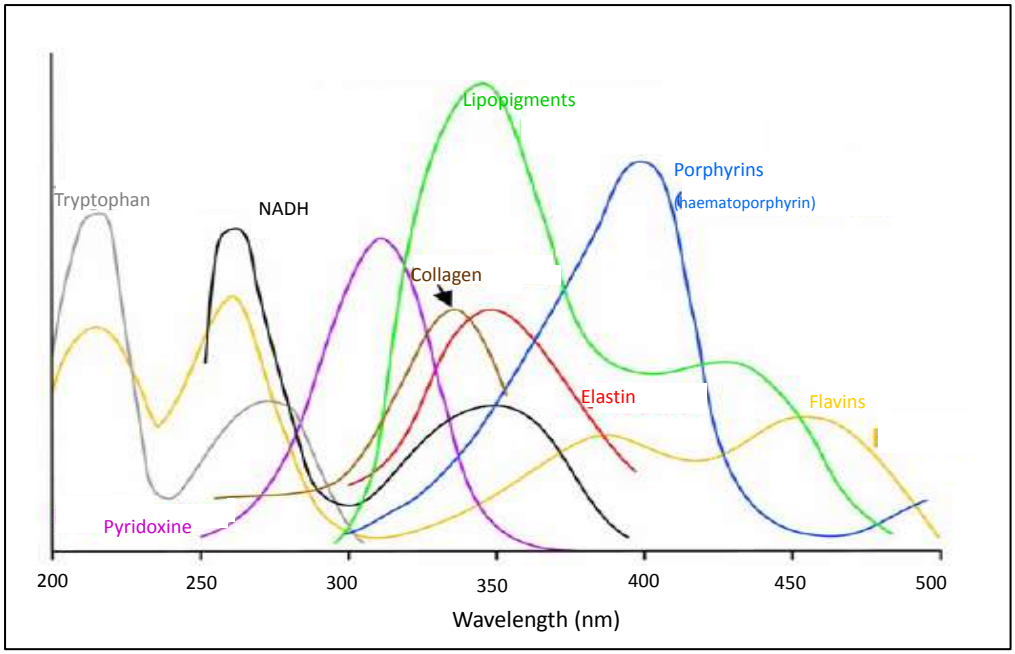

Figure 2.6 Excitation spectra adapted from (Wagnieres, Star et al. 1998)

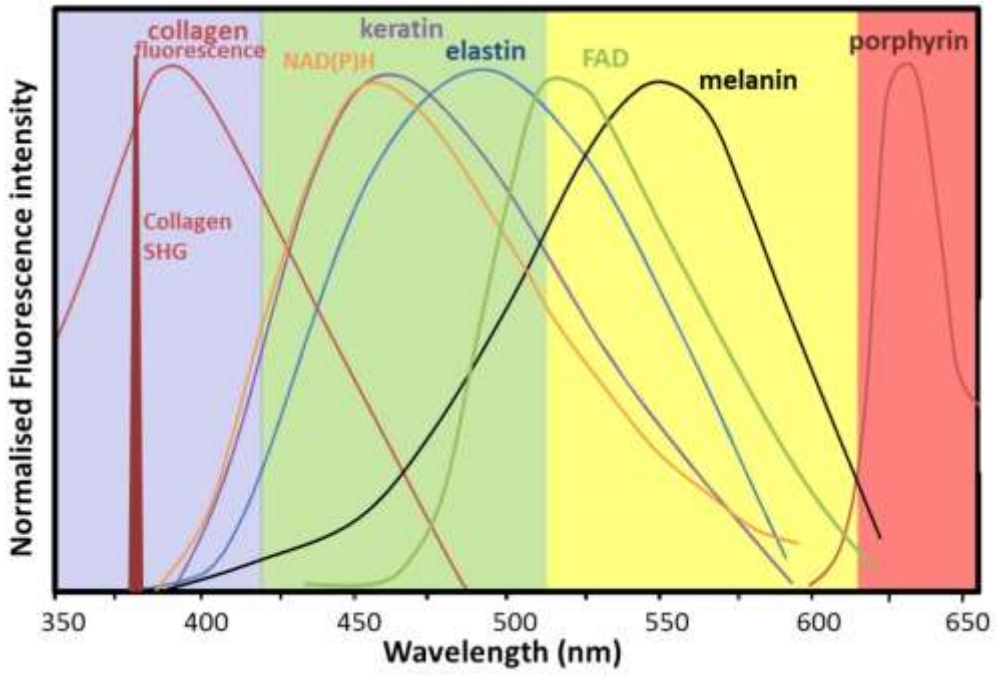

Figure 2.7- Emission spectra from fluorophores found in the skin. Adapted from (Wagnieres, Star et al. 1998; Palero, de Bruijn et al. 2007). Reprinted from Biophysical Journal **93**(3): 992-1007.Palero, J. A., H. S. de Bruijn, et al. (2007). Spectrally resolved multiphoton imaging of in vivo and excised mouse skin tissues. Pages No. 1002, Copyright (2007), with permission from Elsevier.

Two studies have measured complete excitation-emission matricies (EEMs) for purified fluorophores. DaCosta et al. performed this using single photon excitation (DaCosta, Andersson et al. 2003), and Yu et al. (Yu, Lee et al. 2012) performed a similar study using multiphoton excitation. It has been shown that the single photon and two photon excited emission spectra are similar for NAD(P)H and flavins by Kierdaszuk et al. (Kierdaszuk, Malak et al. 1996) and Huang et al. (Huang, Heikal et al. 2002) respectively. However Teuchner et al. demonstrated a red shift in the emission spectrum of melanin in solution using two photon excitation compared to single photon excitation (Teuchner, Freyer et al. 1999), see figure 2.8 below.

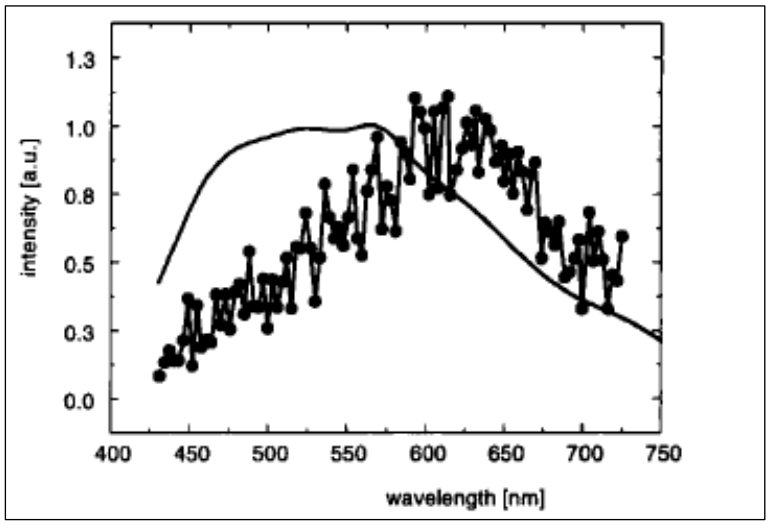

Figure 2.8 Fluorescence spectrum of melanin dissolved in DMSO. Solid curve – single photon excitation at 400 nm. Line with dots- two photon excitation at 800 nm. Reproduced from Teuchner et al. (Teuchner, Freyer et al. 1999).

2.6.1 Keratin

Keratins are structural proteins in the Intermediate Filament (IF) family and found mostly in the epidermis in the skin, hair and nails. The basic structural unit consists of dimers between acidic (Type I) and basic (Type II) keratin Intermediate Filaments. These polymerise into fibrils of increasing size. The structural and chemical properties depend on which acidic and basic subunits are paired. The expression of the intracellular keratins by the keratinocytes alters with migration from the basal layer towards the *s.corneum* in normal skin and in pathological states. For instance Type 14 and 5 keratin IF are expressed in the basal layer, type 10 and 1 in the *s.spinosum* and Type 11 and 2 are expressed in the *s.granulosum*. Following terminal differentiation and apoptosis of the keratinocytes, the *s.corneum* has a high concentration of keratin (Fuchs and Cleveland 1998; Fuchs 2008). It therefore fluoresces brightly in comparison to other intracellular fluorophores in the *s.corneum*.

Keratin autofluorescence varies with its local environment. Pena et al. (Pena, Strupler et al. 2005) studied the excitation and emission spectra from purified human epidermal keratin (intracellular keratins) dissolved in urea and sections of formalin fixed skin using both single and multiphoton excitation. The keratin solution demonstrated a main absorption peak at 277 nm and another at 210 nm in its absorption spectrum with single photon excitation. The absorption spectrum measured in solution using two photon excitation was significantly broader, with a peak at ~700 nm and reducing with wavelength to ~950 nm.

A fluorescence emission peak at 382 nm was found with single photon excitation when excited at 277 nm and was consistent with that of Kollias et al. who illuminating intact *s.corneum* with a xenon lamp at 295 nm and measured fluorescence in the range of 340-400 nm (Kollias, Zonios et al. 2002). Sterenborg et al. also excited healthy skin *in vivo* using volunteers but at 375 nm excitation wavelength from a filtered xenon arc lamp via a fibre optic cable (Sterenborg, Motamedi et al. 1994). They found a spectral peak at a longer wavelength than above of 435 nm and concluded that this was from keratin from the s.corneum because the fluorescence intensity significantly reduced following tape stripping of the skin.

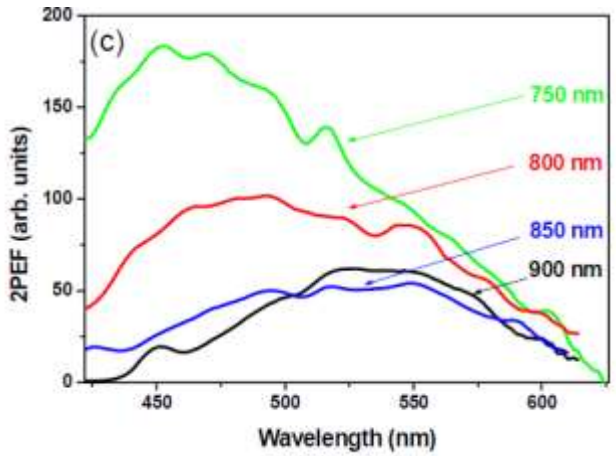

Figure 2.9 Fluorescence emission spectra from keratin solution when excited by TPE at varying wavelengths between 750-900 nm. Reproduced from Pena et al. (Pena, Strupler et al. 2005)

Pena et al. used TPE with various excitation wavelengths to study fluorescence from keratin solution and measured the emitted fluorescence spectrum, shown in Figure 2.9 (Pena, Strupler et al. 2005). It shows that the peak emission shifts towards longer wavelengths as the excitation wavelength is increased. At 760 nm excitation wavelength (used with our system) a peak around 475 nm was seen. This correlated well with an emission peak at 477 nm measured using the same excitation wavelength from the extracellular keratin in the *s.corneum* from fixed sections of normal skin also by

Pena et al. Palero et al. also used human epidermal keratin in solution to record a spectral peak at ~465 nm using 764 nm excitation (Palero, de Bruijn et al. 2007).

The lifetime for pure keratin can be fitted using a monoexponential decay model with a lifetime of 1.4 ns (Ehlers, Riemann et al. 2007). Ehlers et al. also found that hair keratins had more complex decays which varied with hair colour. Breunig et al. recorded the lifetime from the *s.corneum in vivo* from human skin using an excitation wavelength of 720 nm. Fluorescence was filtered through a BG39 filter (~345–605 nm 50% transmittance) and the lifetime was fitted to a double exponential decay model with resulting lifetime components of τ_1=200 ps and τ_2=2600 ps.

2.6.2 Collagen

Collagen is a structural protein that is produced by fibroblasts and found mainly extracellularly in the dermis of the skin but can also be found in other connective tissues such as tendons, ligaments and cartilage. Currently 28 types of collagens exist which vary in their helical composition and post translational modification. Type I and III fibrillary collagen are found in the dermis, type IV and VII and XVII collagen can be found around the basement membrane between the epidermis and dermis and around blood vessels. Type I fibrillar collagen accounts for ~80% of the dermal collagen and is formed from a triple helix of two α_1 (I) chains and a single α_2 (I) chain in which every third amino acid is a glycine. Type III collagen accounts for ~15% and consists of three α_1 (III) chains and can increase to account for ~25% of dermal collagen with photoaging (Lovell, Smolenski et al. 1987; Brinckmann, Açil et al. 1995).

Lutz et al. have characterised the differences in fluorescence with the collagen subtype using MPT (Lutz, Sattler et al. 2012). They excited rat tail derived type I and placental derived type III collagen *in vitro* using a DermaInspect® at 750 nm and collected fluorescence between 400-700 nm. SHG signals were collected using 820 nm excitation wavelength and a 410 nm long pass filter. They found that both collagen types had similar emission spectra with a peak ~460 nm, see figure 2.10 a. In contrast, previous studies of collagen have found an emission peak around 420 nm for type I collagen derived from calf skin and 385 nm for placentally derived type III when excited at 337 nm i.e. using single photon excitation (Marcu, Cohen et al. 2000).

The difference in the emission spectra found between the groups may be caused by the source and experimental conditions of the samples being measured. For example the placental collagen varied in purification method between sources.

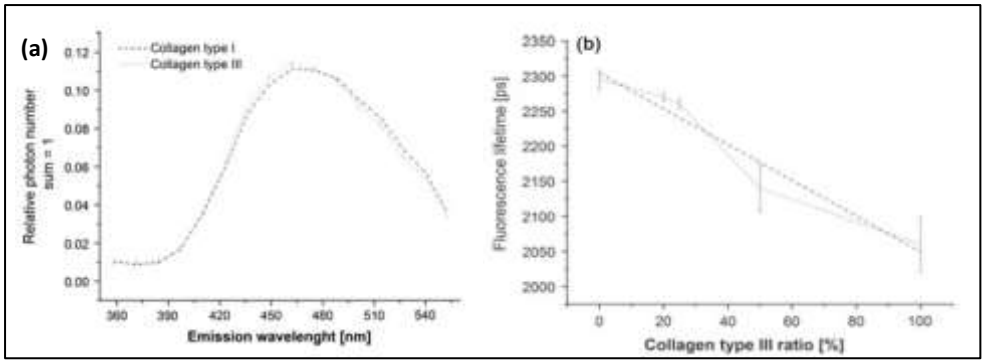

Figure 2.10 a) Fluorescence Intensity of purified collagen type I and III. b) Fluorescence lifetime mixtures of collagen type I and III. Reproduced from Lutz et al. (Lutz, Sattler et al. 2012)

Lifetimes were fitted by Lutz et al. using a double exponential decay model (Lutz, Sattler et al. 2012). A τ_{mean} of 2466 ps was found for type I collagen, and ~2400 ps for types II and and IV using collagen manufactured by Abcam® (UK) when excited at 750 nm. When collagen type I & III manufactured by Sigma-Aldrich® (USA) was tested, a lifetime between 2060-2295 ps was obtained. When varing proportions of type I and type III collagen (from Sigma-Aldrich®) were mixed, a linear reduction from 2295 – 2060 ps in lifetime was found as the proportion of type III collagen was increased, see figure 2.10b.

When using MPE collagen can both emit fluorescence and a much stronger signal by second harmonic generation (SHG) as it is a non-centrosymmetric molecule. Lutz et al. also found that the intensity of the SHG signal reduced with an increasing ratio of collagen Type III:Type I and increased collagen crosslinking (Lutz, Sattler et al. 2012).

The lifetimes calculated for collagen type I and III by Lutz et al. are in broad agreement with those found by Marcu et al. Marcu et al. measured a lifetime of τ_1=0.9 ps, τ_2=5 ns with a_1 of 0.65 when excited at 390 nm (τ_{mean}=2335 ps) for collagen I and τ_1=~1.3 ns, τ_2=~6.75 ns with a_1 of 0.525 when excited at 390 nm (τ_{mean}=3880 ps) for type III collagen (Marcu, Cohen et al. 2000).

The clinical significance of the change in lifetime with ratio of collagen subtypes is uncertain. From the data presented by Lutz et al. the 10% change in ratio between collagen subtypes (that could be expected with photoaging) would result in a 25 ps change in lifetime and no detectable change in the emission spectra.

2.6.3 Elastin

Elastic fibres can be found in the extracellular space in the dermis. They consist of about 2-4% of the dermis and consist of elastin and elastin associated microfibrils. Together they provide elastic recoil and tensile strength to the skin (Kielty, Sherratt et al. 2002; Burns, Breathnach et al. 2010).

The fluorescence properties of elastin have been studied by a number of groups using a number of sources. The emission spectra of Bovine neck ligament elastin was found to have a peak at ~500 nm when excited at 764 nm (Palero, de Bruijn et al. 2007). The same group also found the fluorescence from dermal elastin from mouse skin *in vivo* to be similar. Pena et al. measured the fluorescence from elastin powder derived from human aorta at 760 nm and recorded an emission spectrum peak at ~ 445 nm. (Pena, Strupler et al. 2005). The same group also imaged the dermis of a sample of formalin fixed normal skin. When excited at 760 nm, a broad emission spectral peak at 471 nm was recorded and attributed to elastin fluorescence with weaker contributions from the fibroblasts and collagen.

Maarek et al. measured the lifetime from elastin derived from bovine neck ligament (Maarek, Marcu et al. 2000). They found little difference in its lifetime between its dry and hydrated form when excited over a range of wavelengths using single photon excitation. They used a double exponential decay model and calculated at τ_1 1.3 ns, τ_2 5.7 ns with f_1 of 0.63 when exciting at 390 nm for dry elastin. This did not change significantly with hydration. From the values in the paper a τ_{mean} between 2.93 and 3.08 ns can be calculated for dry and hydrated elastin respectively for this excitation wavelength.

Several years later, Fang et al. (affiliated with Marcu et al.) calculated a τ_{mean} of 2.05 ns for elastin derived from human aorta when excited at 380 nm. They measured a similar τ_1 1.5 ns, τ_2 5.84 ns and τ_{mean} of 2.11 ns averaged over emission wavelengths 380-520 nm (Fang, Papaioannou et al. 2004).

2.6.4 Melanin

Melanin is synthesized by melanocytes in a number of organs including the inner ear, iris of the eye and the skin. Within the epidermis, melanocytes can be found evenly spaced along the basement membrane. They can also be aligned adjacent to each other along the basement membrane to form junctional naevi or in nests in the dermis to form intradermal naevi. The malignant transformation of naevi gives rise to melanoma and has been discussed in Chapter 1.3.3 (pp32).

The 2 melanin pigments found in the skin are eumelanin which is brown/black in colour and pheomelanin which is yellow/red. Both are derived through the oxidation of tyrosine by tyrosinase and packaged into intracellular organelles called melanosomes. These are then distributed by the melanocytes to their surrounding keratinocytes in the epidermis to confer the nucleus of the cells protection against UV light. Both types can be found in benign naevi and melanomas but the ratio of eumelanin to pheomelanin can increase in malignancy (Marchesini, Bono et al. 2009). It has been difficult to characterise the 2 types of melanin using conventional light or fluorescence microscopy because neither are found in their pure form biologically, their absorption spectra are similar and

their *in vivo* structure, which affects their fluorescence characteristics, have not been possible to reproduce. Recently however Matthews et al. have used a non-linear optical pump-probe method to distinguish the pigments from fixed, sections from pigmented skin lesions (Matthews, Piletic et al. 2011).

The absorption spectrum of synthetic melanin (most similar to eumelanin) reduces with wavelength between ~250nm to 800nm. The emission spectrum of synthetic melanin is broad with a spectral peak at 550 nm (Teuchner, Freyer et al. 1999; Palero, de Bruijn et al. 2007). Recently, Krasieva et al. attempted to distinguish the emission spectra between eumelanin and pheomelanin in their *in vivo* state by imaging black, red and grey hair using MPM spectroscopy (Krasieva, Stringari et al. 2013). They assumed that the emission spectrum from grey hair arises from keratin only with the addition of eumelanin from black hair and pheomelanin from red hair. They subtracted the keratin spectrum and were able to distinguish the emission spectra between the melanin types when excited at 1000 nm, see figure 2.11. This figure demonstrates a longer emission peak than that found with synthetic melanin and with a peak between 615-625 nm for pheomelanin and 640-680 nm for eumelanin.

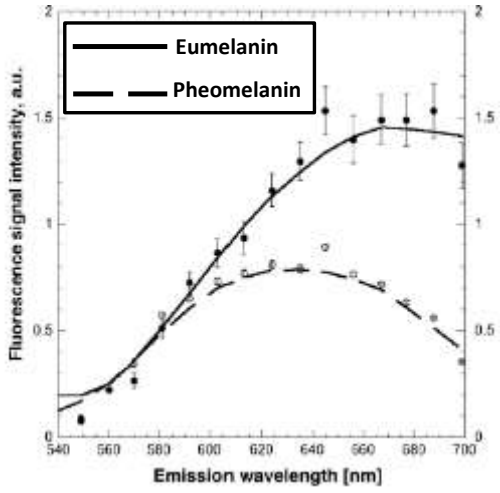

Figure 2.11 Emission spectra from eumelanin and pheomelanin from hair using MPM spectroscopy. Reproduced from (Krasieva, Stringari et al. 2013).

Dancik et al. further showed that the fluorescence intensity of melanin increased linearly with melanin concentration in solution (Dancik, Favre et al. 2013).

The fluorescence lifetime from melanin has been measured by a number of groups and been summarised in the paper by Dancik et al. (Dancik, Favre et al. 2013). A tri-exponential fluorescence decay lifetime model was found to provide the best fit with lifetimes components (and contributions) of 0.2 (0.56), 1.5 (0.32) , 5.8ns (0.11) (Teuchner, Freyer et al. 1999). This gives a calculated τ_{mean} of 1.23 ns.

In vivo eumelanin forms complex granules intracellularly with aggregates of varying molecular weight. Nofsinger et al. confirmed that the absorption spectrum of eumelanin from *Sepia officinalis* was broad, ranging from the UV through the visible wavelength range (see figure 2.12 a) and was affected by the molecular weight of the granule aggregates. The emission spectrum was less affected by the molecular weight when excited at 375 nm (Nofsinger and Simon 2001). This study found an emission peak closer to 450 nm rather than the peak near 550 nm previously reported. They suggested that the difference could be explained by the polymerisation and oxidization status of the melanin being examined.

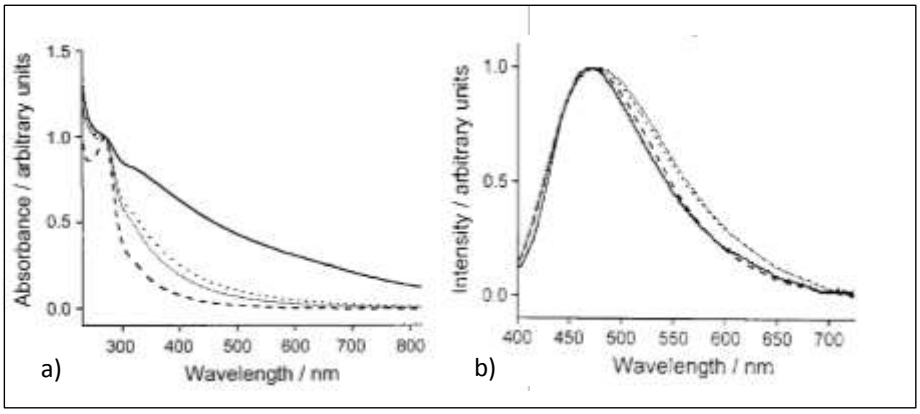

Figure 2.12. a) Changes in absorption spectra of eumelanin from *S. officinalis* with molecular size. b) Changes in emission spectra of eumelanin with molecular size when excited at 375 nm. Key: Molecular Weight (MW) >10 000 (solid), 10 000>MW>3000 (dot), 3000> MW>1000 (short dot) and MW< 1000 (dash). Reproduced from (Nofsinger and Simon 2001).

This group also fitted the lifetime of eumelanin using a multi-exponential decay lifetime model but used four exponential components which they considered related to the molecular size of the aggregate (<1000, >10,000 molecular weight). Their calculated lifetime components (and contributions) were τ_1= 121-144 (0.03-0.05) ps, τ_2= 800-960 (0.14-0.15) ps, τ_3= 5.03-5.37 ns (0.29-0.3) and τ_4= 11.8-12.8 ns (0.51-0.53). This gives a calculated τ_{mean} of 8.06 ns.

As discussed above, Krasieva et al. separated the emission spectra between the types of melanins using hair. They demonstrated a difference in the fluorescence lifetime between eumelanin and pheomelanin on phasor plots using phasor FLIM analysis (Krasieva, Stringari et al. 2013) and their lifetimes were distinct from those of free and protein bound NADH.

2.6.5 NAD(P)H

NADH and NADPH are the reduced forms of two nucleotide molecules involved in redox reactions in cellular metabolism.

NADH is derived from nicotinic acid, is a key co-enzyme in the oxidation of glucose to pyruvate in glycolysis and is involved in the Citric acid cycle/electron transport chain (part of cellular oxidative respiration) in the mitochondrion during the synthesis of ATP. Within the cell NADH acts primarily as a reducing agent and therefore the oxidised state (NAD^+) predominates.

NADPH binds to several enzyme complexes that are diverse in function. For example, it is involved in the anabolic synthesis of lipids and cholesterol, conversion of pyruvate to lactate and the generation of free radicals in cells of the immune system. In contrast to NADH, it acts primarily as an electron donor in the cell and therefore the reduced state (NADPH) predominates.

Although NADH and NAD(P)H serve different functions within the cell, their fluorescence profiles (i.e. absorption, emission and lifetimes) are similar. Both NADH and NADPH only fluoresce at ~ 450 nm in their reduced state and spectroscopically are typically considered together as NAD(P)H. However, the fluorescence of NADH dominates. It is found in greater concentrations within the cell (x5) and has higher quantum efficiency than NADPH (Avi-Dor, Olson et al. 1962; Wang, Wei et al. 2009).

At an excitation wavelength of 760 nm, NAD(P)H has an emission spectral peak between 450-470 nm (König and Schneckenburger 1994; Palero, de Bruijn et al. 2007).

In aqueous solution, a double exponential decay can be fitted with a τ_1=0.35 and τ_2= 0.76 ns, with a τ_{mean} of 444 ps (Vishwasrao, Heikal et al. 2005). Skala et al. fitted a double exponential decay to NAD(P)H fluorescence measured from cheek epithelium and attributed the short component to free NAD(P)H (τ_1=0.29) and the long component to protein bound NAD(P)H (τ_2= 2.03 ns (f_2=0.37)), with a τ_{mean} of 934 ps (Skala, Riching et al. 2007).

Lakowicz et al. was the first group to perform lifetime imaging of NADH. They determined that enzyme bound NADH had a longer lifetime than its free form (Lakowicz, Szmacinski et al. 1992). When Vishwasrao et al. measured the fluorescence lifetime in hippocampal tissue and fitted it using a quadruple exponential decay model, decay components ranging from 155ps to 6.04ns (τ_{mean}948ps) were calculated. In conjunction with fluorescence anisotropy measurements, the shortest and 3 longer components were attributed to free and protein bound NADH respectively (Vishwasrao, Heikal et al. 2005).

2.6.6 Flavins

Flavins are co-enzymes derived from riboflavin and are involved in oxidation/reduction reactions in the cell. They act as electron carriers for redox reactions in the Citric Acid Cycle and the electron transport chain within the mitochondrion. The most studied fluorescent flavins are the co-enzymes

flavin mononucleotide (FMN) and flavin adenine dinucleotide (FAD). In their oxidised form the fluorescence arise from their isoallozazine ring. However their reduced forms are not fluorescent. This distinction can be used to monitor changes in intracellular metabolism.

The flavins have a broad absorption spectrum between 200 and 500 nm with an emission peak at 525nm (König and Schneckenburger 1994; Palero, de Bruijn et al. 2007).

Free FMN has been found to have a monoexponential decay lifetime between 4.6 -5.2 ns (König and Schneckenburger 1994; Yang, Luo et al. 2003) with protein bound FMN having a faster, multiexponential lifetime decay. For example, Yang et al. used four lifetime components to best fit the decay for protein (enzyme) bound FMN, which were 8 ps (19%), 50 ps (39%), 250 ps (39%) and 4.5 ns (3.6%), with a τ_{mean} of 281 ps (Yang, Luo et al. 2003). They also fitted protein bound FAD using four similar lifetime components, which were 28 ps (25%), 200 ps (52.1%), 460 ps (21.5%) and 3.3 ns (1.2%), with a τ_{mean} of 250 ps. This lifetime is longer than that determined in 1980 by Nakashima et al. They found monomeric and dimers of protein (enzyme) bound FAD to have a mean lifetime of 130 ps and 40 ps, whilst free FAD had a lifetime of 2.3 ns (Nakashima, Yoshihara et al. 1980).

2.6.7 Porphyrins

The porphyrins consist of a family of proteins derived from the tetrapyrrole molecule- porphyrin. They are found as intermediate metabolic products during the synthesis of haem. The most important ones are protoporphyrin IX, coproporphyrin III, uroporphyrin III and haematoporphyrin IX. Once haem is bound to iron in haemoglobin, its fluorescence is quenched and therefore cannot be detected. Normally the concentration of these molecules is low and the only detectable fluorescence from porphyrins in mammals arise from chlorophyll when a diet rich in plants has been ingested and from phototrophic bacteria, such as *Propionibacterium acnes,* that colonise sebaceous glands of the skin. The presence of porphyrins in these bacteria, that aggravate acne vulgaris, can be targeted by photodynamic therapy to improve acne.

In pathology affecting this metabolic pathway, such as congenital enzyme defects (porphyrias) or acquired defects or malignancy, porphyrins can be detected in the skin, blood or internal organs. Red fluorescence from porphyrins arising from malignancies was first detected by Policard et al. in 1924 (Policard 1924). Protoporphyrin IX was later isolated as the main fluorophore found in squamous cell carcinomas (Ghadially and Neish 1960).

Exogenously applied topical precursors to porphyrins, such as 5-aminolevulinic acid are used for photodynamic therapy in skin cancers. This photosensitising drug is preferentially taken up by rapidly proliferating cells such as malignant cells. This artificially increases their intracellular

concentration of protoporphyrin IX and means that phototherapy can act preferentially on malignant tissue. This technique has used been for photodetection of tumour margins but still remains an area for research as current studies have had mixed results for the assessment of BCC margins (Wetzig, Kendler et al. 2010; Sandberg, Paoli et al. 2011; van der Beek, de Leeuw et al. 2012).

The absorption spectrum of porphyrins consists of 4 peaks, the Soret band at 400 nm and four smaller Q-bands ranging from 500-630 nm. Its fluorescence emission spectrum peaks between 624-633 nm, depending on the porphyrin. For example, when excited at 407 nm protoporphyrin IX was found to have a fluorescence peak at 633 nm whilst coproporphyrin had its peak at 632 nm (König, Flemming et al. 1998).

The fluorescence lifetime of protoporphyrin IX following incubation with the photosensitiser aminolaevulinic acid, measured *in vivo* from a chick embryo model, was found to have 2 lifetime components when excited at 390 nm. A dominant long lifetime component of ~19 ns (a_2=0.9) was thought to be from the Protophorphyrin IX, whilst the short lifetime component of 5.2 ns (a_1=0.1) was thought to arise from photoproducts (Schneckenburger, König et al. 1993). This has been used by Cubeddu et al. to enhance the lifetime of BCCs compared to normal skin in FLIM images acquired *in vivo* (Cubeddu, Comelli et al. 2002)

2.6.8 Lipofuscin

Lipofuscin is an intracellular pigment that has been found in a number of organs of the body, including the brain, heart, liver and retina. It consists of an aggregate of granules that can arise from the phagocytosis of degraded lipid from organelles. In the skin, it is most visible in solar lentigenies (Berezin 2010) but can also arise as a result of amiodarone drug therapy for cardiac arrhythmias (Weedon 2002).

Lipofuscin has an excitation spectrum between 440-470 nm, with an emission spectrum between 510-700 nm (Schweitzer, Schenke et al. 2007). This falls within the excitation wavelength range of the DermaInspect®, with the emission spectrum expected to fall within the yellow and red spectral channels.

Schweiter et al. have measured the emission spectra and lifetimes from fluorophores found within the retina of a healthy volunteer (Schweitzer, Schenke et al. 2007). They used an excitation wavelength of 468 nm and fluorescence was collected between 510-700nm and fitted using a tri-exponential decay model. τ_1= 190ps was attributed to the pigmented retinal epithelium (dominated by lipofuscin), τ_2=750 ps to the neural retinal and τ_3 = 3550 ps to connective tissue and the lens.

2.6.9 Amino Acids

Only tryptophan, tyrosine and phenylalanine autofluoresce with emission wavelengths above the ultraviolet range (>300 nm). Tryptophan emits its fluorescence in the range 340-380 nm. It has 2 lifetime components of ~0.5 ns and ~3 ns, although the longer lifetime component becomes 8.7 ns in alkaline environments (Ross and Jameson 2008).

Both phenylalanine and tyrosine have poor quantum yields and therefore are often swamped by the signal from tryptophan.

2.7 Dynamic Changes of Cellular Autofluorescence

2.7.1 Changes with Metabolism

As outlined above, the intracellular fluorophores NAD(P)H and flavins are co-enzymes involved in oxidation/reduction reactions in the citric acid cycle and electron transport chain, part of cellular oxidative respiration. The proportion of each co-enzyme in the oxidised or reduced state therefore can be used as an indirect measure of the redox state i.e. the metabolic state of a cell. As the fluorescence of NAD(P)H and flavins are confined to their reduced or oxidised state respectively, measuring their fluorescence emission allows the opportunity to gain an insight into the metabolic state of cells non-invasively and *in vivo*. In 1979, Chance et al. defined the Redox Ratio as FAD / (NAD(P)H +FAD). He suggested that this ratio was a more reliable indicator of cellular metabolism than measuring the absolute amounts individually (Chance, Schoener et al. 1979). A reduced ratio indicated an increased metabolic state and vice versa. Since this time NADH fluorescence individually and the redox ratio have been studied extensively and are reviewed elsewhere (Mayevsky and Rogatsky 2007; Wang, Wei et al. 2009).

It has also be found that changes in the fluorescence lifetimes of NAD(P)H, arising from changes in the ratio of free to bound protein, could also be used to assess intracellular hypoxia, cell necrosis and malignancy. For example, Vishwasrao et al. measured the lifetime of NADH from slices of brain tissue and fitted its decay using four components. When using chemically induced hypoxia, they found a decrease in proportion of the longer lifetime components of NADH (reflecting decrease protein binding) and a shortening of all lifetime components (resulting in a reduced τ_{mean} from 948 to 780 ps)(Vishwasrao, Heikal et al. 2005). Wang et al. used HeLa and 143B osteosarcoma cell lines *in vitro* to determine differences in lifetime between induced cell apoptosis (using staurosporine) and induced cell necrosis (using hydrogen peroxide). They found an increase in lifetime from 1.3 to 3.5 ns at the start of apoptosis but no increase when cell necrosis was induced (Wang, Gukassyan et al. 2008).

2.7.2 Changes with Malignancy

Changes in intracellular autofluorescence are also associated with the metabolic changes that occur with malignant transformation of cells. Under normal conditions non-dividing, differentiated cells use aerobic glycolysis and oxidative phosphorylation to synthesis ATP in the presence of oxygen for their energy requirements. In the absence of sufficient extracellular oxygen anaerobic glycolysis is used instead to generate ATP. However this process is less efficient for the production of ATP, generating 2 vs 36 molecules of ATP per glucose molecule.

Warburg et al. noticed that proliferative tissues, including tumour cells, favour anaerobic glycolysis to generate ATP, despite the presence of sufficient oxygen (Warburg, Wind et al. 1927; Warburg 1956). The exact reasons for this "Warburg Effect" are still speculative but may arise from cancer cells favouring the accumulation of nutrients into the cell in anticipation of cell division over efficient energy production (Vander Heiden, Cantley et al. 2009). This switch to anaerobic glycolysis is thought to occur in malignant cells before characteristic morphological/histological changes are seen and therefore presents the opportunity to detect malignant transformation early.

An important paper linking the change in metabolism associated with malignancy to changes in cellular autofluorescence was published by Skala et al. in the Journal of Biomedical Optics. They measured the fluorescence lifetimes from epithelial cells in a hamster cheek pouch *in vivo*. The lifetimes were fitted using a double exponential decay model and τ_1 and τ_2 were calculated as 0.29 and 2.03 ns in normal epithelium and attributed to the free and protein bound states of NADH respectively (Skala, Riching et al. 2007). Chemically induced dysplasia/ *in situ* carcinoma was associated with a decrease in τ_2 (from 2.03 to 1.83 ns) caused by a decrease in protein bound NADH:free NADH ratio, and hence a reduced contribution (α_2). This therefore reduced the mean lifetime. They then inhibited aerobic glycolysis *in vitro* using a breast cancer cell line (MCF-10A) and replicated the shortening of τ_2. From this they suggested that the decrease in protein bound NADH was associated with the switch from oxidative glycolysis/phosphorylation to anaerobic glycolysis for ATP production in dysplastic cells.

Skala et al. published a 2nd paper in PNAS in 2007. In this they reported an increase in the variability in the redox ratio with dysplasia. In high grade dysplasia, they also found an increase in τ_1 for protein bound FAD but a decrease in its contribution (Skala, Riching et al. 2007).

Lin et al. examined the changes in extracellular fluorescence associated with BCCs using formalin fixed sections of tissue (Lin, Jee et al. 2006). They correlated the remodelling of the extracellular matrix surrounding the tumour with a reduced SHG signal from collagen, in comparison to normal skin.

2.8 Conclusions

In conclusion, this chapter has introduced the principles of fluorescence and the main methods for fluorescence lifetimes imaging are then briefly outlined. The following section describes the main fluorophores to be found in the skin and details their fluorescence characteristics. Finally the changes in fluorescence and fluorescence lifetime described with alterations in cellular in metabolism and malignancy are outlined.

Chapter 3. Literature Review of tissue autofluorescence lifetime spectroscopy and imaging.

3.1 Introduction

As described in Chapter 2.6 (pp50), the skin contains a number of endogenous fluorophores including extracellular structural proteins such as keratin, collagen and elastin and intracellular functional molecules, such as NAD(P)H, flavins and melanin. These provide opportunities to use autofluorescence lifetime to investigate contrast in both normal skin and changes caused by disease. Fluorescence lifetime measurements of human skin have been carried out using a wide range of instruments, from non-imaging fibre-optic probe-based point measurements using single photon excitation through to multiphoton microscopy and tomography providing sub-cellular resolution images.

This chapter aims to review the current literature concerning fluorescence and fluorescence lifetime measurements of skin, with a focus towards investigations of skin cancer and the use of multiphoton microscopy (MPM). It is important to consider this field in the context of the extensive work on steady-state and spectrally resolved measurements of autofluorescence of human skin. A number of studies have shown that the autofluorescence characteristics of neoplastic skin differ from those of normal tissue. Detailed reviews of this existing work are discussed in several reviews, e.g. (Richards-Kortum and SevickMuraca 1996; Wagnieres, Star et al. 1998; Ramanujam 2000; Zeng and MacAulay 2003).

The chapter is organised by the type of instrumentation used and the type of disease studied. The initial sections cover results employing single photon excitation, while sections 3.4 (pp69) onwards consider multiphoton imaging.

3.2 Fibre optic point-based probes

3.2.1 Spectroscopy

Most of the studies cited in this section have discriminated between normal and neoplastic tissue by detecting differences in the measured steady-state fluorescence intensities or spectra using a point-based spectrometer.

Using point-based measurements *in vivo*, Lohmann et al. (Lohmann and Paul 1988) reported an increase in 366 nm excited autofluorescence intensity from the edges of melanomas with a strong peak at 475 nm not present in benign naevi in a study of 82 patients. Later work using the same

instrument was still able to contrast benign naevi from dysplastic naevi/melanomas using fresh frozen samples (n=147), but could not contrast dysplastic naevi from melanomas (Lohmann, Nilles et al. 1991). Chwirot et al. used a digital imaging approach with the same excitation wavelength and collecting autofluorescence at 475 nm. They used the perilesional and lesional fluorescence intensity to distinguish melanomas from common/dysplastic naevi (Chwirot, Chwirot et al. 1998). When this technique was used to screen melanomas in a multicentre trial, they found a sensitivity of 82.7% in detecting the 56 melanomas from 7228 pigmented lesions, and specificity of 24% for discriminating common/dysplastic naevi in the 568 cases in which histology was taken (Chwirot, Chwirot et al. 2001).

A number of groups have applied point spectroscopy of autofluorescence in basal cell carcinomas (BCCs) with broadband near-ultraviolet excitation (350-375nm). Both Na et al. and Brancaleon et al. have reported that the autofluorescence intensity from BCCs at these excitation wavelengths is significantly lower than that from normal skin (Brancaleon, Durkin et al. 2001; Na, Stender et al. 2001). It has been suggested that this may be due to the degradation of dermal collagen by BCC tumour matrix metalloproteinases, resulting in reduced collagen fluorescence from the upper dermis (Brancaleon, Durkin et al. 2001). Conversely, Sterenborg et al. demonstrated no significant differences between the autofluorescence from BCCs and normal skin (Sterenborg, Motamedi et al. 1994). Other groups have successfully used longer (410-440nm) (Panjehpour, Julius et al. 2002; Zeng and MacAulay 2003) or shorter (295nm) (Brancaleon, Durkin et al. 2001) wavelengths of excitation light to differentiate BCCs from normal skin.

The group of Tunnel et al. (Rajaram, Aramil et al. 2010) have applied an instrument combining diffuse reflectance spectroscopy and fluorescence spectroscopy to the study of non-melanoma skin cancers. The diffuse reflectance spectroscopy provided information on blood volume fraction, oxygen saturation, blood vessel size, tissue micro-architecture and melanin content and the fluorescence spectroscopy used excitation at 337 nm and 445 nm to provide native fluorophore contributions of NADH, collagen and FAD. This instrument was used to study non-melanoma skin cancer in 48 lesions from 40 patients and demonstrated differentiation of basal cell carcinomas from normal skin with a sensitivity and specificity of 94% and 89% respectively (Rajaram, Reichenberg et al. 2010).

Although fluorescence intensity measures were used to distinguish normal from neoplastic skin in the studies described above, fluorescence intensity measurements are sensitive to fluctuations in excitation intensity, tissue scattering and absorption and are difficult to quantify and compare between samples. The spectrally-resolved measurements provided additional information in these

studies, but fluorescence emission spectra of many tissue fluorophores are broad and overlap significantly (Cubeddu, Pifferi et al. 1999).

3.2.2 Fluorescence lifetime

Autofluorescence lifetime measurements provide a further opportunity to contrast different tissue fluorophores for different disease states, beyond those provided by fluorescence intensity and spectral measures. The following studies have primarily measured fluorescence lifetimes from normal skin, skin from diabetics and from BCCs.

Pitts and Mycek developed a fibre-optic point-probe device able to collect spectrally and temporally resolved fluorescence decays and this instrument was applied to measurements of human skin autofluorescence in 2001 (Pitts and Mycek 2001). The forearm from a healthy volunteer was excited using light from a pulsed nitrogen laser at 337 nm with a repetition rate of 10 Hz and fluorescence was collected above 460 nm. Fluorescence decays were fitted using a double exponential decay model, which yielded decay components $\tau_{,\tau}$ and τ_2 of 0.938 ns and 5.3 ns respectively from the skin surface, which were thought to be compatible with the expected fluorescence decay of collagen.

In 2006 Katika et al. (Katika, Pilon et al. 2006) used a pulsed LED excitation source at 375 nm and collected the fluorescence decays using time correlated single photon counting (TCSPC) in 4 emission bands between 442-496 nm. Their aim was to compare differences in the fluorescence lifetime with age, sex and skin type. The skin from both palms was recorded from 35 volunteers and various body sites were examined in one patient. A tri-exponential decay model was used to analyse the data and decay components at 0.4, 2.7 and 9.7 ns were observed with the 442 nm emission filter. Whilst the two shorter fluorescence decay components were thought to be due to NAD(P)H, the longest component was postulated to arise from advanced glycation end-products, which are described in the following paragraph. The authors found no correlation of the fluorescence lifetime with skin type, gender or age.

Advanced glycation end products (AGEs) are the final product of chemical reactions between sugars, proteins, lipids and nucleic acids. Although these accumulate naturally with age, the rate increases in diabetics. Some AGEs, such as pentosidine, fluoresce and therefore there is the potential that fluorescence spectroscopy can be used for non-invasive monitoring of diabetics.

Blackwell et al. (Blackwell, Katika et al. 2008) used the same fibre-optic probe instrument described by Katika et al. above to collect time-resolved fluorescence decays *in vivo* from the skin with the aim to screen for type 2 diabetes. Data was collected from the palms of 38 type 2 diabetic and 37 non diabetic patients *in vivo* and a triple exponential decay model was employed for the fluorescence

decay analysis. In normal skin, the decay component lifetimes of 0.5, 2.6 and 9.2 ns were calculated. The shorter two decay components were thought consistent with that of protein bound and free NADH respectively. No statistical differences in lifetime with age, gender, skin type or between the two patient populations were observed. They also made a comparison of the fluorescence decay from 18 diabetic patients with foot ulcers (a marker for microvascular disease) versus age-matched healthy controls. They showed a change in τ_1 (477 ps to 510 ps, p = 0.038) and both fractional components f_1 (0.769 to 0.761, p = 0.012) and f_2 (0.196 to 0.217, p = 0.002). The authors speculated that the change was related to differences in the metabolic rate of the tissues, rather than the presence of AGEs.

In 2007 De Beule et al. (De Beule, Dunsby et al. 2007) presented another point-based probe for measuring time (4096 time bins) and spectrally resolved (16 spectral channels) fluorescence decays in skin. This instrument was used to measure the fluorescence from freshly excised lesions. Lesions were excited at both 355 nm and 435 nm using pulsed laser diodes and fluorescence decays were collected using TCSPC and were fitted using a double exponential decay model. The fluorescence lifetimes collected using 355 nm excitation showed little contrast between benign and malignant skin. However, excitation at 435 nm of basal cell carcinomas (BCCs) yielded a mean fluorescence lifetime (τ_{mean}) of 2.44 ns vs. 2.96 ns measured for surrounding uninvolved skin. Six samples allowed paired lesional and peri-lesional measurements, which showed a decrease in τ_{mean} of 620 ps for BCCs ($p<0.03$) using 435 nm excitation. Further spectrally resolved lifetime histograms for SCCs, naevi, melanomas and seborrhoeic keratosis were presented but there were insufficient patient numbers to support further statistical analysis.

Thompson et al. (Thompson, Coda et al. 2012) applied similar equipment as De Beule et al. (except for the second laser wavelength being changed from 435 nm to 445nm) to measure the fluorescence from a number of lesions on the skin *in vivo*, including 10 BCCs. Consistent with the data collected by De Beule et al. from *ex vivo* samples, excitation at 355 nm did not show a consistent change in lifetime between normal skin and BCC. However, once again, when excited at 445 nm, they found that the spectrally averaged, intensity weighted τ_{mean} were consistently shorter for BCCs than paired peri-lesional normal skin (2240 ± 480 ps BCC vs 3130 ± 413 ps normal). This shift of 886 ps was statistically significant (p = 0.002) and greater than the average variability found in the surrounding normal skin of 175 ps.

3.3 Wide-field FLIM of skin

The studies described below have used wide-field FLIM to measure fluorescence images from the surface of the skin i.e. spatially resolved fluorescence lifetimes but not depth resolved. This allowed

variation in fluorescence lifetimes to be correlated with the clinical appearance of the skin and margins of a tumour.

Galletly et al. (Galletly, McGinty et al. 2008) published work evaluating 25 freshly excised BCCs and their margins by collecting FLIM images from the tissue surface. Tissue was excited at 355 nm using a frequency tripled mode locked Nd:YVO_4 laser with a repetition rate of 80 MHz and fluorescence was collected at wavelengths >375 nm and >445 nm using a wide-field time-gated FLIM system. Each pixel was defined manually as lesional or peri-lesional normal skin using the reflectance white light image and a single exponential decay was fitted to the data. Unlike many previous studies, e.g. (Brancaleon, Durkin et al. 2001), no consistent changes were seen in fluorescence intensity between normal and lesional skin. A significant difference was found in the fluorescence lifetime between BCCs and normal perilesional skin (means of 1.4 ns vs. 1.6 ns respectively, $p<0.001$). This contrasts to the studies discussed above by De Beule et al. (De Beule, Dunsby et al. 2007) and Thompson et al. (Thompson, Coda et al. 2012) who found no significant change in autofluorescence lifetime at this excitation wavelength. This may be explained by the differences in excitation/collection geometry between fibre-optic point-probe and wide-field imaging systems and the differences in detection of the wavelength bands employed.

Wide-field FLIM has also been applied to skin following treatment with photosensitisers. In 1999, Cubeddu et al. (Cubeddu, Pifferi et al. 1999) and in 2000 Anderson-Engles et al. (Andersson-Engels, Canti et al. 2000) published studies investigating the potential to increase the contrast of fluorescence from BCC/SCCs by applying aminolevulinic acid (ALA) topically, which is a precursor to the fluorescent protoporphyrin IX and preferentially accumulates in cancerous tissue compared to normal tissue. FLIM of the skin surface was implemented with excitation from a pulsed dye laser operating at 405 nm that provided sub-1 ns pulses. Subsequently an *in vivo* study of 48 lesions in 34 patients (benign and malignant, mainly BCC) reported that, following application of ALA, tumours were found to have a longer lifetime of 18 ns compared to normal skin of 10 ns (Cubeddu, Comelli et al. 2002).

3.4 Multiphoton imaging of normal skin

The first publication of multiphoton imaging of human skin *in vivo* was published in 1997 by Masters et al. (Masters, So et al. 1997). This work contrasted autofluorescence spectra and lifetimes from images taken from two depths in the skin (0-50 μm and 100-150 μm), exciting fluorescence at 730 nm and 960 nm using a tunable femtosecond pulsed Ti:Sapphire laser. An emission peak at 445-460 nm consistent with that of NAD(P)H was found to dominate images at both depths when excited at 730 nm. When exciting at 960 nm, a spectral peak centred at 520 nm consistent with the emission

spectrum of flavins was found. Another peak at 450 nm was also found but its origin was not identified. Mean fluorescence lifetimes were calculated for each pixel using frequency domain FLIM and values ranging from 0.5 to 3 ns were observed.

König et al. (Konig 2000; Konig, Wollina et al. 2002; König and Riemann 2003) developed a multiphoton tomograph (DermaInspect®, JenLab GmbH) capable of measuring both fluorescence intensity and lifetimes in optically sectioned images of skin both *ex vivo* and *in vivo*. A tunable modelocked Ti:Sapphire laser was used to excite the tissue and imaging with submicron lateral spatial resolution and TCSPC FLIM with 250 ps temporal resolution was implemented. In this initial work, *ex vivo* samples from a variety of dermatoses including psoriasis, naevi, a melanoma and fungal infection were studied and the forearms of two volunteers were also examined *in vivo*. The fluorescence decays acquired at each pixel were fitted to a double exponential decay model and the τ_{mean} of cellular autofluorescence was found to be in the range of 1.8-2.4 ns. The DermaInspect® instrument was subsequently CE marked for clinical use *in vivo* and currently remains the only commercially available multiphoton imaging device licenced for *in vivo* imaging of the skin.

Koehler et al. (Koehler, Vogel et al. 2010) used the DermaInspect® to study epidermal thickness. Image depth stacks were acquired from the dorsal forearm and the dorsum of the hand in 30 volunteers. Skin was excited at 800 nm and 2 spectral channels with filters were used to collect the SHG using a 400 nm band pass filter and the second channel collecting autofluorescence between 410-490 nm. They described an objective method of distinguishing the levels in the skin using the number of photon counts per image of the autofluorescence and SHG signals. Using the peak in SHG signal to signify the papillary dermis, they used ~9000 images to calculate the epidermal thickness from the acquired image depth stacks. The dorsum of the hand was found to have thicker total epidermis, cellular epidermis and *stratum corneum* and higher depths of the papillary dermis than the forearm. No thickness differences were found with age. No significant variation was observed in the undulations of the dermo-epidermo junction with age.

The same authors (Koehler, Zimmermann et al. 2011) also present a study of 30 patients with normal skin, discussing tissue morphology and quantifying three parameters for two different body sites (dorsal forearm and dorsum of the hand) in three age groups (young, mid-aged and old). The parameters investigated were the number of papillae per square millimetre, (in the stratum granulosum) the mean number of keratinocytes per unit area and the mean nuclear area. The total number of papillae was found to be significantly decreased in the old group compared with the young and keratinocytes were found to be smaller from the dorsum of the hand compared with the dorsal forearm. They also defined MPT features for distinguishing the layers in the epidermis (see

figure 3.1). They defined the *s.granulosum* as consisting of relatively large cells with a dark nucleus and a granular cytoplasm with a strong fluorescence signal. The dark inter-cellular spaces in this layer appeared wider compared with the *s.spinosum*. The *s.spinosum* has small cells and the cytoplasm is more homogenous than the *s.granulosum*. The basal layer appears as a lattice of densely packed small, round, homogenously fluorescing cells, resulting in a 'cobblestone' pattern. The bright cytoplasmic fluorescence is from melanin and the lack of a visible nucleus in some cells is caused by the vertical orientation of the basal cells because of the basal position of the nucleus within the cell. In some sections, the cobblestone pattern is interrupted by round structures which correspond to the apices of the dermal papillae.

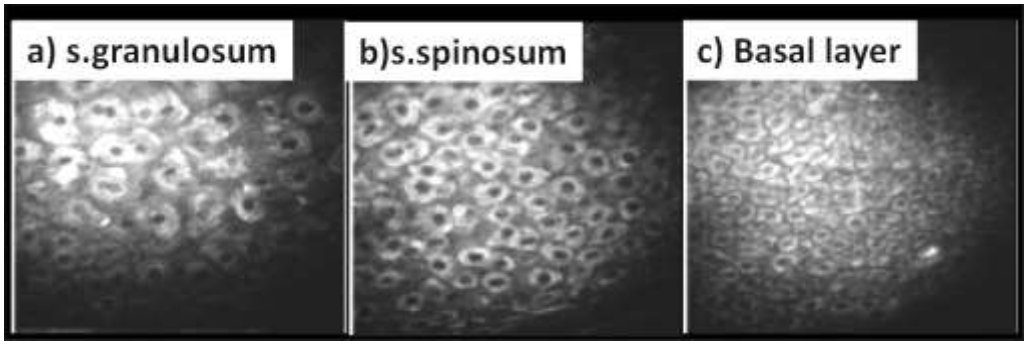

Figure 3.1. MPT images taken from different layers in the epidermis of normal skin. Reproduced from Koehler et al.(Koehler, Zimmermann et al. 2011)

3.4.1 Spectrally resolved MPM

This section includes studies that use MPM to acquire depth resolved images from the skin that are spectrally resolved.

Early spectrally resolved multiphoton imaging of the dermal layer of *ex vivo* human skin was carried out by Buehler et al. (Buehler, Kim et al. 2005) using a 16 channel multi-anode photomultiplier tube. It allowed the emission spectra from collagen-rich and elastin-rich regions of the image to be compared.

Laiho et al. (Laiho, Pelet et al. 2005) imaged 5 samples of normal skin that had been stored at -3°C before use. Each sample was excited at 730, 780 and 830 nm using a tunable modelocked Ti:Sapphire laser and the fluorescence was detected in 10 spectral channels between 375 nm and 600 nm using a filter wheel. The spatially and spectrally resolved images were collected at 5 μm intervals in depth throughout the sample. The spatially integrated emission spectrum from the whole sample correlated well with those taken from 4 specific depths. Within the emission spectra obtained from exciting the skin at 3 wavelengths they identified consistent peaks at 475 nm and 550 nm which were thought to be consistent with NAD(P)H and melanin respectively. Fluorescence

lifetime measurements were also undertaken using TCSPC (64 time bins) for which the decay profile from each pixel was fitted to a double exponential decay model. This allowed second harmonic generation (SHG) in collagen to be distinguished from elastin autofluorescence in images taken from the dermis.

Pena et al. (Pena, Strupler et al. 2005) investigated autofluorescence from keratin using single- and two-photon microscopy and spectroscopy. They presented multiphoton imaging of autofluorescence and SHG from fixed sectioned normal human skin excited at 860 nm and their spectral analysis of autofluorescence indicated that keratin and elastin spectra are similar (with spectral peaks at 477 nm and 471 nm respectively when excited at 760 nm).

Chen et al. (Chen, Zhuo et al. 2006) performed multiphoton imaging with a modelocked Ti:Sapphire laser excitation source and a 32 channel hyperspectral detector. Emission spectra of both epidermis and dermis were recorded using two-photon excitation wavelengths in the range 790-830 nm. They observed that the spectral peak for the epidermis shifted towards longer wavelengths and the fluorescence intensity decreased with excitation wavelength. They also found the maximum SHG signal from dermis was obtained using 800 nm excitation. Zhuo et al. (Zhuo, Chen et al. 2006) used the same instrument to study spectrally resolved images of dermis of fresh frozen human skin and were able to identify dermal components such as collagen and elastin with high spatial and spectral contrast.

The group of Gerritsen presented spectrally resolved multiphoton imaging of mouse skin *in vivo* using a prism-based spectrometer readout by a high speed EMCCD camera providing 100 spectral channels over the range 350-600 nm (Palero, de Bruijn et al. 2006; Palero, Latouche et al. 2008). Images were acquired using an excitation wavelength of 760 nm and images were converted into a RGB scale for real-colour visualisation. The authors performed a detailed analysis of the spectral signatures of mouse skin (Palero, de Bruijn et al. 2007) and determined the relative contributions and emission spectra of keratin, melanin, NAD(P)H, flavins, collagen and elastin. Subsequent work included a study of the effect of ischemia on the emission spectrum of NAD(P)H (Palero, Bader et al. 2011) and of the two-photon excited emission spectra of human skin *in vivo* (Bader, Pena et al. 2011). The images of normal skin from 2 people with different skin types clearly demonstrated the high spatial resolution of the system and its ability to distinguish collagen, elastin, NAD(P)H/FAD and melanin based on spectra alone.

Subsequently, a prism-based spectrometer incorporating a fibre-bundle spot-to-line converter was incorporated into a DermaInspect®-based instrument and used to acquire spectrally resolved images

of human skin *ex vivo* from a suspected nodular BCC with excitation at 760 nm and 840 nm (Talbot, Patalay et al. 2011).

Breunig et al. (Breunig, Studier et al. 2010) used the DermaInspect® to characterise the influence of the excitation wavelength on the fluorescence emission intensity from various depths within normal skin *in vivo*. As found by Chen et al. above, intracellular autofluorescence reduces whilst collagen SHG signal increases in intensity as the excitation wavelength was increased from 720 – 880 nm and the authors discussed the optimum excitation wavelength for each of the fluorescent species investigated. They concluded that the spectral contribution of each fluorophore changed with excitation wavelength, which contributed to the differences in fluorescence intensity seen. They also found a corresponding change in the calculated fluorescence lifetimes for a field of view in the papillary dermis with excitation wavelength resulting from this change in contribution.

3.4.2 Lifetime resolved MPM

The studies outlined below focus on lifetime resolved images from normal skin. In addition, the study discussed immediately above by Breunig et al. investigated both spectrally and lifetime resolved images.

Sugata et al. (Sugata, Sakai et al. 2010) applied the DermaInspect® to evaluate the fluorescence lifetime of melanin within normal skin *in vivo* and compared it to melanin found in the hair bulb and from melanocytic 3D cell cultures. Ultrafast excitation pulses at 760 and 800 nm were employed and fluorescence decays collected using TCSPC were fitted to a double exponential decay model. Fluorescence lifetimes in the basal epidermal layer of τ_1 = 132 ps and τ_2 = 1762 ps were obtained using 760 nm excitation. The authors concluded that, for all samples, the short τ_1 component was dominated by melanin fluorescence and while the longer τ_2 component mainly represented other fluorophores. The authors then fixed the lifetimes of the two decay components (to 120 and 1100 ps) in the fitting software and used the resulting ratio maps of the amplitude of the short and long fluorescence decay components (a_1/a_2) to produce maps of melanin concentration.

Benati et al. (Benati, Bellini et al. 2011) have published a comprehensive *in vivo* study of the fluorescence lifetimes from normal skin using multiphoton imaging. 49 patients in total from 2 age groups had images taken from different body sites and depths. A DermaInspect® was used with 760 nm excitation and fluorescence decays were collected using TCSPC and fitted using a single exponential decay model to estimate the mean fluorescence lifetime. The fluorescence lifetimes in the skin were found to vary with body site, to increase with age and shorten with tissue depth. The shorter lifetimes lower in the skin were partially attributable to the higher melanin content in the

basal layers of the skin. A more detailed summary of this paper can be found in discussion sections of Chapter 6.5 (pp146) & 6.6 (pp155)

In 2011, Sanchez et al. (Sanchez, Prow et al. 2010) outlined the effect of excision, temperature and the use of culture media on the autofluorescence from NAD(P)H in freshly excised human skin. A detailed discussion of this paper and that of Palero et al. whom also examined the effects of ischaemia on mouse skin using spectrally resolved images (Palero, Bader et al. 2011), can be found in the Chapter 5.2.1 (pp115).

A number of further studies of diseased tissue have studied normal tissue as part of the investigation. Therefore, to avoid repetition, these papers are discussed in sections below covering diseased tissue.

3.4.3 MPM of skin to study the effects of aging

The SHG signal to autofluorescence (AF) aging index of dermis (SAAID) has been defined as SAAID = (SHG-AF)/(SHG+AF), which provides a useful numerical index to assess the age of skin using multiphoton imaging (Lin, Wu et al. 2005). Lin et al. (Lin, Wu et al. 2005) investigated 3 samples of vertically sectioned, formalin fixed sections of facial skin from patient of differing ages. Multiphoton images were obtained exciting the tissue at 760 nm and collecting the fluorescence from areas in the superficial dermis at 380 nm for SHG and >435 nm for autofluorescence. The SAAID was found to decrease with age to -0.93 in a 70 year old patient and correlated with an increase in elastin in the dermis in the form of solar elastosis and decrease in SHG signal from collagen causing an increase in the collagen:elastin ratio.

Koehler et al. (Koehler, König et al. 2006) looked at the skin from the inside forearm from 18 volunteers *in vivo*. The skin was excited at 820 nm with the SHG collected at 410 nm and autofluorescence collected above 470 nm. Five fields of view were acquired from each patient from the upper dermis and the SAAID was calculated for each pixel. The results showed that SAAID generally reduced with age (linear regression R^2=0.57) but there was large inter-patient variability. This drop was greater for women (R^2=0.89) compared with men (R^2=0.68). In subsequent work, the same group (Koehler, Hahn et al. 2008) assessed quantitatively the dermal matrix composition and showed characteristic changes with aging. In methodology identical to their 2006 study, 18 volunteers had the inside of their forearm imaged using the DermaInspect® and 5 images were acquired from the upper dermis. The dermis was evaluated using a multiphoton imaging-based dermis morphology score (MDMS). Images were evaluated for 8 parameters in the following categories – fibre spread and fibre aspect, network pattern and image homogeneity (SHG images only), clot formation (autofluorescence images only). A single MDMS score was calculated, which

correlated strongly (linear regression R^2=-0.9) with age, less strongly with SAAID (R^2=0.66) and did not show gender specific differences.

In 2009 Koehler et al. looked at the skin of 60 healthy volunteers including the young, old and women using tanning salons (Koehler, Preller et al. 2009). The skin elasticity was measured using both mechanical methods and SAAID. The skin was excited at 800 nm from the volar and dorsal aspect of the forearm and SHG was collected at 400 nm and fluorescence collected from 410-490 nm. 16 regions at approximately 180 µm below the *stratum granulosum* were measured and averaged for each patient. The authors found that older patients had lower SAAID scores. Sun exposed areas had a lower SAAID (significant in old men, old women and young women using tanning but not in young men and young women). Mechanical measurements of skin elasticity (cutometry) indicated loss of elasticity with age and a higher elasticity on the outside forearm than the inside was found in all groups. The procedures used in this study reduced the intra- and inter-patient variability compared to the 2006 and 2008 studies and this study confirmed that SAAID decreased with age in a larger sample size. The authors found a lower SAAID in sun exposed dorsal forearm compared to the sun-protected volar forearm in the old and in young women using tanning salons, but were not able to detect any damage done by tanning beds.

Kaatz et al. examined the influence of depth and epidermal thickness on the SAAID index (Kaatz, Sturm et al. 2010). The forearms of 30 healthy volunteers divided into 3 age groups were examined *in vivo*. Skin was excited at 800 nm using a DermaInspect® and SHG was collected at 400 nm and autofluorescence at 410-490 nm. The fluorescence intensities from the images were then analysed based on changes in the autofluorescence and SHG intensity with depth. The maximum penetration depth was found to be 130-180 µm based on the plateau in the autofluorescence and SHG intensities below this depth and the authors determined the papillary dermis was reached at 91±16 µm. The position of the basal layer and the presence of solar elastosis in older patients could be seen through small peaks in the plots of tissue autofluorescence intensities as a function of depth. A sharper decline in the SHG signal after the dermis was reached was found in the elderly compared to the young. The SHG peak in the upper dermis was due to the high content of fibrillar collagen (types I and III). The most significant differences between ages were found in the SAAID index when a constant depth below the surface was assessed (below the SHG peak and above the penetration depth) e.g. 150 µm.

Koehler et al. looked at the variation of tissue autofluorescence lifetimes using TCSPC from the dermis with age, sex and body site (Koehler, Preller et al. 2011). They used the DermaInspect® to excite both the medial and lateral forearms of 47 volunteers at 800 nm wavelength.

Autofluorescence was collected from 16 fields of view using a 450±40 band pass filter. Due to the low photon counts per pixel, fluorescence was summed for each image at each time point and bi-exponential decays were fitted to the data to find τ_1 and τ_2. They found the mean of τ_1 to be between 700-1000 ps and τ_2 to be between 3475 – 3600 ps. They found no variation between the sexes and no consistent variation with body site. They did however find that the fluorescence lifetimes in the dermis increased with age, which is consistent with the findings by Benati et al. of the changes in fluorescence lifetime of the epidermis with age (Benati, Bellini et al. 2011). They attributed this change to the replacement of collagen and elastin in the dermis with the accumulation of solar elastosis.

Puschmann et al. attempted to refine the SAAID index to quantify aging of the skin and described the elastin to collagen ratio (ELCOR) (Puschmann, Rahn et al. 2012). They used the DermaInspect® to acquire images from normal skin *in vivo* from 45 women to assess aging and 12 to assess photodamage. The skin was excited at 820 nm and collected at 410 nm for collagen SHG, and excited at 750 nm and collected between 548±150 nm for elastin autofluorescence. Although both methods measure SHG to determine dermal collagen, the ELCOR uses a manually defined mask to remove autofluorescence from other dermal structures before calculating the ratio. This index showed a progressive statistically significant increase with age and a statistically significant increase for sun-exposed (temple) body sites compared to photo-protected sites (upper arm). In contrast the sensitivity of the SAAID index was only sufficient to detect a statistically significant difference between the young/middle aged groups and the elderly age groups' skin.

3.5 MPM in non-melanoma skin cancer

In one of the first studies of skin cancer using multiphoton imaging (Lin, Jee et al. 2006) autofluorescence intensity images were collected from 9 fixed, sectioned slices from BCCs. Serially acquired images were montaged together to generate an autofluorescence image covering a large area crossing tumour margins and this was presented with an exact correlative histopathological image. The SHG from dermal collagen was spectrally filtered from the emitted fluorescence and the authors used an index of multiphoton-excited autofluorescence to SHG (MFSI, equivalent to the negative of the SAAID index, see section 3.4.3) to distinguish cancer cells/stroma from normal dermis in BCCs. The authors found that the MFSI ratio was greatest within the tumour, lower in cancer stroma and lowest in normal dermal stroma and could be used to identify the tumour.

Paoli et al (2008) published a study of the morphological features observed in multiphoton-excited autofluorescence intensity images. 14 freshly excised specimens of non-melanoma skin cancer – including squamous cell carcinoma *in situ*, superficial BCCs and nodular BCCs – were imaged using

780 nm excitation. They looked for the presence of 8 features in squamous cell carcinoma *in situ* (bowenoid dysplasia, multinucleated cells, widened intercellular spaces, hyperkeratosis, keratin pearls, dyskeratosis, loss of cell polarity and speckled perinuclear fluorescence) and 5 features in superficial BCCs (hyperkeratosis, thickened subcorneal epidermis, elongated cells and nuclei polarisation, peripheral palisading and speckled perinuclear fluorescence). Their study confirmed that many of the established histopathological features could be seen using the *en face* multiphoton imaging although image features characteristic of disease were only found in one of three nodular BCCs due to the limited penetration depth.

The group of Pavone has applied *en face* multiphoton imaging and FLIM to assess freshly excised BCCs (Cicchi, Massi et al. 2007; Cicchi, Sestini et al. 2008; De Giorgi, Massi et al. 2009). Using autofluorescence excitation at 740 nm and SHG imaging at 840 nm, they presented examples of the morphological features seen in multiphoton imaging images of BCCs and compared them directly to correlative histology. The SAAID index (see section 3.4.3) was used to distinguish BCC tumours (negative index), stromal interface (marginally positive index) and the dermis (negative index). The autofluorescence emission spectrum of 4 BCCs was studied and found to be shifted towards the blue for BCC compared to normal skin (shift in fluorescence to <525 nm) with this shift being greatest for depths in the range 30-50 μm. They also studied fluorescence lifetime histograms obtained from FLIM images acquired at different depths and found the fluorescence lifetime to be longer for BCC compared to normal skin tissue for most depths with a peak difference of +91 ps at 30 μm depth.

Our group, Patalay et al. (Patalay, Talbot et al. 2011) evaluated BCCs *ex vivo* using a DermaInspect® to acquired FLIM data in two emission spectral channels (300-500 nm & 500-640 nm) prior to the investigation described in this thesis. Whole excised, fresh tissue samples were imaged using excitation at 760 nm. Each cell in every image was identified manually and all pixels within each region of interest (ROI) summed to provide a single fluorescence decay per cell. This approach increased the number of photons available in order to fit a double exponential decay model to the data. In total, fluorescence decays from 615 cells from 3 nodular BCCs and 566 cells from 4 naevi were defined and fitted. The mean fluorescence lifetimes for naevi vs nBCC were calculated as 2516 vs 2786 ps (<500 nm channel) and 1334 vs 2085 ps (>500 nm channel). Shorter fluorescence lifetimes were observed in both spectral channels for naevi and this was attributed to the increased melanin content in the naevi. Fitting fluorescence decays on a cell-by-cell basis allowed populations of naevi cells to be contrasted with nBCC via their lifetime and it was suggested that the variation in the melanin content in cells could be responsible for the lifetime histograms obtained. This study also indicated a large inter-patient variability in fluorescence lifetimes of skin lesions.

Seidenari et al. (Seidenari, Arginelli et al. 2013) investigated a range of morphological image descriptors – building on those identified by Paoli et al. (Paoli, Smedh et al. 2008) – with the aim to optimise the differentiation of BCC from normal skin using multiphoton imaging . Initially, training image stacks acquired at 10 depths from one field of view per sample were acquired *ex vivo*, imaging 24 BCCs and 24 samples of normal skin. These multiphoton imaging stacks were used to identify 9 morphological criteria/descriptors. Figure 3.2(a,b) illustrate the 3 epidermal descriptors and (c)-(h) illustrate the remaining dermal descriptors.

In the main study, image stacks from a further 66 BCCs, 66 other lesions (23 nevi, 8 melanomas, 17 skin tumours and 18 other skin lesions) and 66 normal regions of skin were acquired. The resulting images were then assessed by three independent observers who assessed each sample for the presence or absence of each descriptor. The mean number of descriptors per lesion was 2.64 for BCCs, 0.17 in other lesions and 0 for normal skin. The presence of 'Aligned elongated cells' was found in 73% of BCCs but in only 5% of other lesions. An overall sensitivity/specificity of 95/89% was achieved when using the presence of one or more BCC descriptor(s) as the diagnostic criterion, whereas 83/95% was obtained when using the presence of two or more descriptors. These results indicate the potential utility of multiphoton imaging as a diagnostic tool.

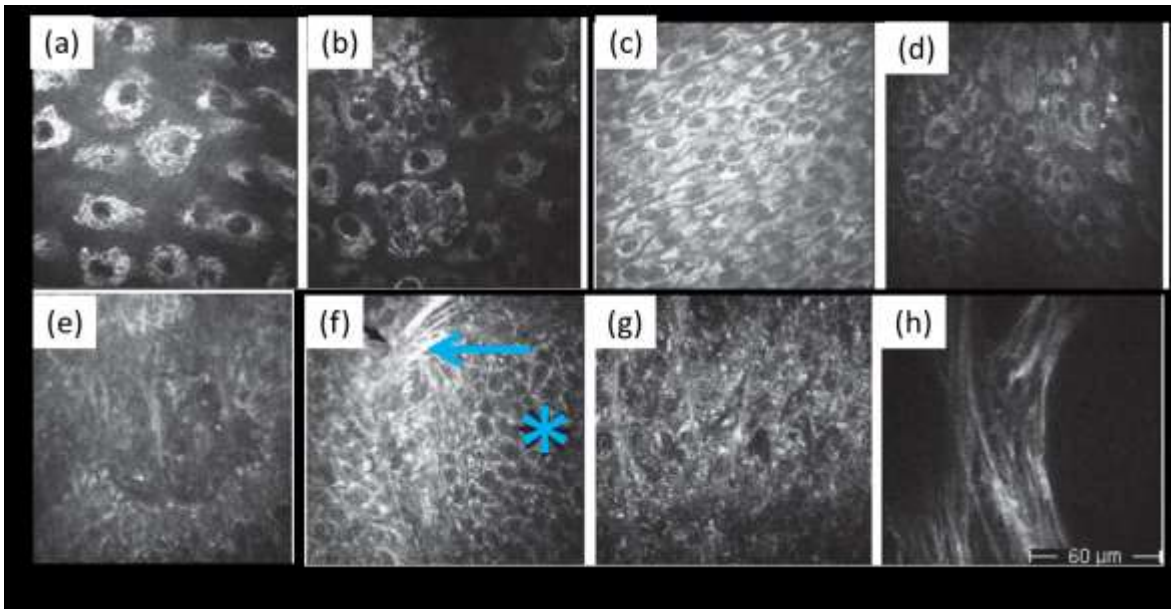

Figure 3.2.Morphological criteria/descriptors for defining BCCs from MPT images defined by Seidenari et al. (a) detached cells with increased intercellular spaces (b) cells with irregular contours & random arrangement of cells (c) Elongated cells aligned along a single axis (d) cells aligned in two directions.(e) Palisading i.e. cells at the periphery of a BCC nest aligning perpendicularly to the surrounding dermis. (f) BCC nodule (asterix) surrounded by fibres (arrow) (g) sheets of cells intermingled with fibres. (h)BCCs cells are not seen when excited at 800 nm causing the appearance of 'phantom cells'. Images (a)-(g) Excited at 760 nm, (h) excited at 800 nm. Reproduced from Seidenari et al. (Seidenari, Arginelli et al. 2013).

Seidenari et al. extended this approach to the combination of multiphoton intensity imaging and FLIM for the diagnosis of BCC, distinguishing them from a range of other skin lesions (Seidenari, Arginelli et al. 2012). A preliminary study of 35 BCCs and 35 healthy skin samples were imaged and morphological descriptors were identified using the resulting FLIM images. In the main study 63 BCCs, 66 other skin lesions (24 nevi, 8 melanomas, 15 inflammatory lesions and 19 skin tumours) and 63 samples of healthy skin were imaged and the presence or absence of each descriptor assessed by three independent observers. 15 FLIM images were acquired at different depths for each sample using an excitation wavelength of 760 nm. Cells with a longer fluorescence lifetime were always observed for BCCs and this descriptor provided the highest sensitivity/specificity (100/70%) of all of the descriptors investigated. The mean fluorescence lifetime values, calculated on three representative cells in the lower layers of each of the 98 (preliminary and main study samples combined) healthy skin lesions and each of the 98 BCC lesions were found to be 1012 ps and 1475 ps respectively (a significant difference at $p < 0.001$)i.e. longer and in agreement with earlier work on a smaller number of samples (Cicchi, Sestini et al. 2008). The mean number of BCC descriptors per lesion was higher in BCC (3.86 ± 1.45) compared to miscellaneous lesions (0.54 ± 0.86). The presence of at least one BCC descriptor was observed in all BCCs but only in 36% of other skin samples. An overall sensitivity for the diagnosis of BCC from other lesions and healthy skin of 97% was achieved when the diagnostic criterion was chosen to be the presence of two or more descriptors and this produced no false positives, either in other lesions or healthy skin. A specificity of 100% was obtained when considering the presence of five descriptors or more.

Seidenari's group then compared the morphological features seen in images from 16 BCCs acquired *in vivo* using reflectance confocal light microscopy to MPT FLIM images from the same lesion acquired *ex vivo* using the DermaInspect®(Manfredini, Arginelli et al. 2013). They concluded that there was a good concordance of morphological features between both modalities but found limitations in their ability to compare images directly due to the difference in field of view size between them.

3.6 Multiphoton spectroscopy and imaging of pigmented lesions

Teuchner et al. presented emission spectra and fluorescence lifetime measurements of synthetic melanin and melanin in *ex vivo* specimens of normal human skin (Teuchner, Freyer et al. 1999) reporting a complex fluorescence decay profile with a dominant short decay component at about 200 ps. Melanin excitation can also occur via a stepwise multiphoton excitation (Teuchner, Freyer et al. 1999), which allows for preferential excitation of melanin, particularly when using longer (nanosecond) NIR excitation pulses (Eichhorn, Wessler et al. 2009). In subsequent work, Teuchner et al. (Teuchner, Ehlert et al. 2000) studied the emission spectra of normal skin, naevi and melanoma

and noted a shift in the peak of the fluorescence emission spectrum of the melanoma sample (~550 nm) compared to naevi (~520 nm) and normal skin (~500 nm). The same group observed the same trends in a larger study of 10 specimens in each of the three lesion types (Hoffmann, Stucker et al. 2001).

Eichhorn et al. (Eichhorn, Wessler et al. 2009) exploited selective excitation of melanin using 2.5 ns excitation pulses at a wavelength of 810 nm to study the fluorescence emission spectra of melanin in formalin fixed paraffin embedded samples. A total of 27 lesions were studied, including 9 malignant melanomas. For common and junctional naevi, spectral emission peaks of ~480 and ~490 nm were observed respectively. For malignant melanoma, the autofluorescence was characterised by a peak at ~600 nm. A dysplastic compound naevus exhibited both peaks. Similar spectra were observed for a fresh unfixed specimen of malignant melanoma. These results were confirmed in a more detailed subsequent study by Leupold et al.(Leupold, Scholz et al. 2011), where the authors measured the emission spectra of 167 cases of naevi and melanomas. Melanoma gave a characteristic emission peak at 640 nm with common melanocytic naevi presenting a peak at 590 nm. This difference was thought to be due to changes in the ratio of eumelanin to pheomelanin. For each sample the emission spectrum was acquired for an array of 12×9 positions on the surface of the specimen that were spaced laterally in steps of 50 μm. The fluorescence signal at each point was compared in two bands (483-520 nm and 585-620 nm) in order to classify the measurement as benign or malignant. Overall, this study reported a sensitivity, specificity and diagnostic accuracy of 94, 80 and 83% respectively for distinguishing malignant melanoma from naevi.

Ehlers et al. (Ehlers, Riemann et al. 2007) used a DermaInspect® to investigate the fluorescence lifetime of human hair, which is rich in melanin. Fluorescence lifetime analysis of hair of different colours revealed differences in the lifetime between blond (0.4, 2.2ns) and black hair (0.2, 1.3ns) and these lifetimes were compared to pure melanin and melanin measured *in vivo* from a mole. When a fast multichannel plate photomultiplier tube providing a 24 ps response time was used to detect the fluorescence decays, eumelanin in black hair (0.03, 0.8ns) could be distinguished from pheomelanin in red/blonde hair (0.34, 2.3ns) and white hair (0.3, 2.1ns).

Cicchi et al. (Cicchi, Sestini et al. 2008; De Giorgi, Massi et al. 2009) applied spectrally resolved multiphoton imaging and FLIM to study 2 melanoma specimens with excitation at 740 nm. Melanomas were found to have a shorter fluorescence lifetime than normal skin and BCCs but were not compared to other pigmented lesions. Spectral analysis showed a reduction in fluorescence intensity below 520 nm for melanoma compared to normal skin. However, the shift towards longer

emission wavelengths for melanoma compared to normal skin reported by Teuchner et al. (Teuchner, Ehlert et al. 2000) was not seen.

Dimitrow et al. applied the DermaInspect® to study pigmented lesions. In their first study (Dimitrow, Ziemer et al. 2009), they initially studied 15 *ex vivo* specimens (healthy skin, melanocytic lesions and melanoma) using multiphoton imaging with excitation at 760 nm and identified 6 morphological features to distinguish melanomas from naevi. A further 83 lesions (42 both *in* and *ex vivo*, 11 only *in vivo* and 30 only *ex vivo*) were then imaged and the data assessed by four independent observers for the occurrence of each feature. The feature of 'large intercellular distance' provided the greatest sensitivity of 80% and 'dendritic cells' provided the greatest specificity of 96% (when considering all lesions). Binary logistic regression showed that the features of 'architectural disarray', 'poorly defined keratinocyte cell borders', 'pleomorphic cells', and 'dendritic cells' should also be included in diagnostic decisions, which yielded an overall diagnostic accuracy of 85/97% for analysis of images acquired *in*/*ex vivo*. MPT images of these features have been reproduced in figure 3.3 below.

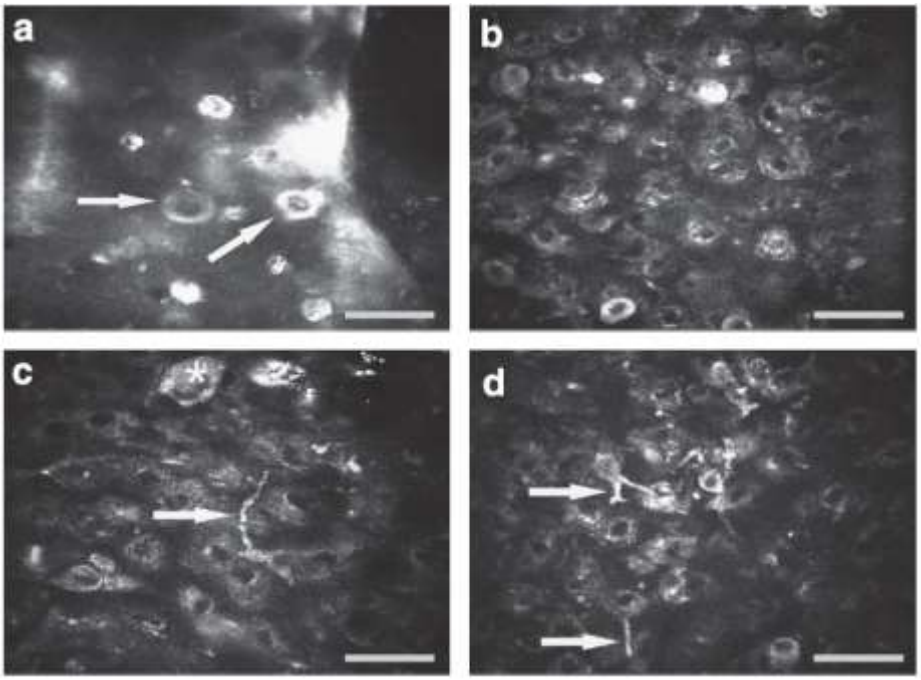

Figure 3.3. MPT features seen in melanomas (a) Ascending highly fluorescent melanocytes (white arrows) appear within the upper epidermal layers. (b) Large intercellular distance and poorly defined keratinocyte cell borders. (c,d) Cell fragments, pleomorphic cells (asterisk) and dendritic structures (white arrows) in the *s.spinosum*. Scale bar: 40 mm. Reprinted by permission from Macmillan Publishers Ltd: Journal of Investigative Dermatology 129(7): 1752-1758.Copyright (2009), (Dimitrow, Ziemer et al. 2009).

In a second study (Dimitrow, Riemann et al. 2009) Dimitrow et al. examined 13 naevi and 10 melanomas, mostly from *ex vivo* samples. In this study they found that multiphoton excitation at

800 nm enhanced many of the morphological features in the intensity images associated with melanoma, compared to excitation at 760 nm. Fluorescence lifetimes were calculated for a total of 84 manually selected pixels of the cytoplasm from either keratinocytes or melanocytes and a bi-exponential decay model was fitted to the data. The authors found that both the short/long decay components were shorter for melanocytes than keratinocytes (140/1076 ps vs. 445/2269 ps respectively) and that melanocytes had a more dominant short lifetime component than keratinocytes (93%/7% and 76%/24% respectively). The differences in the fluorescence decay parameters between the two cell populations were attributed to a dominant NAD(P)H fluorescence in keratinocytes and a dominant melanin fluorescence in melanocytes. The observed fluorescence lifetimes were able to distinguish keratinocytes from melanocytes but not naevi from melanomas. The authors also investigated the fluorescence emission spectrum of 4 lesions (two of normal skin, one naevus and one melanoma) and found a peak at 550 nm occurring in the melanoma sample, but not the naevus or normal skin. This peak was more pronounced when exciting at 800 nm compared to 760 nm.

Arginelli et al. performed a comparison of MPT FLIM images acquired *ex vivo* from 51 melanocytic naevi and compared them to 51 miscellaneous lesions with the aim to define diagnostic morphological features for melanocytic naevi (Arginelli, Manfredini et al. 2012). The miscellaneous lesions consisted of a wide variety of lesions including pigmented and non-pigmented diagnoses e.g. BCCs, SCCs, dermatofibroma, actinic keratosis and seborrhoeic keratosis. Initially images taken from 16 naevi *ex vivo* were used to define a number of morphological features. Their presence was then assessed blinded on the images acquired *ex vivo* from the 102 lesions. They determined that ‘small short-lifetime cells’ in the upper and lower epidermal layers, ‘edged papillae’, ‘junctional nests of short-lifetime cells’ and ‘dermal cell clusters’ as 5 sensitive and specific descriptors for diagnosing benign naevi, see figure 3.4. They also confirmed the presence of the descriptors for benign naevi defined by Dimitrow et al. of monomorphic cells with regular histo-architecture, evenly distributed keratinocytes, well defined cell borders and rarely seen dendritic cells (Dimitrow, Ziemer et al. 2009).

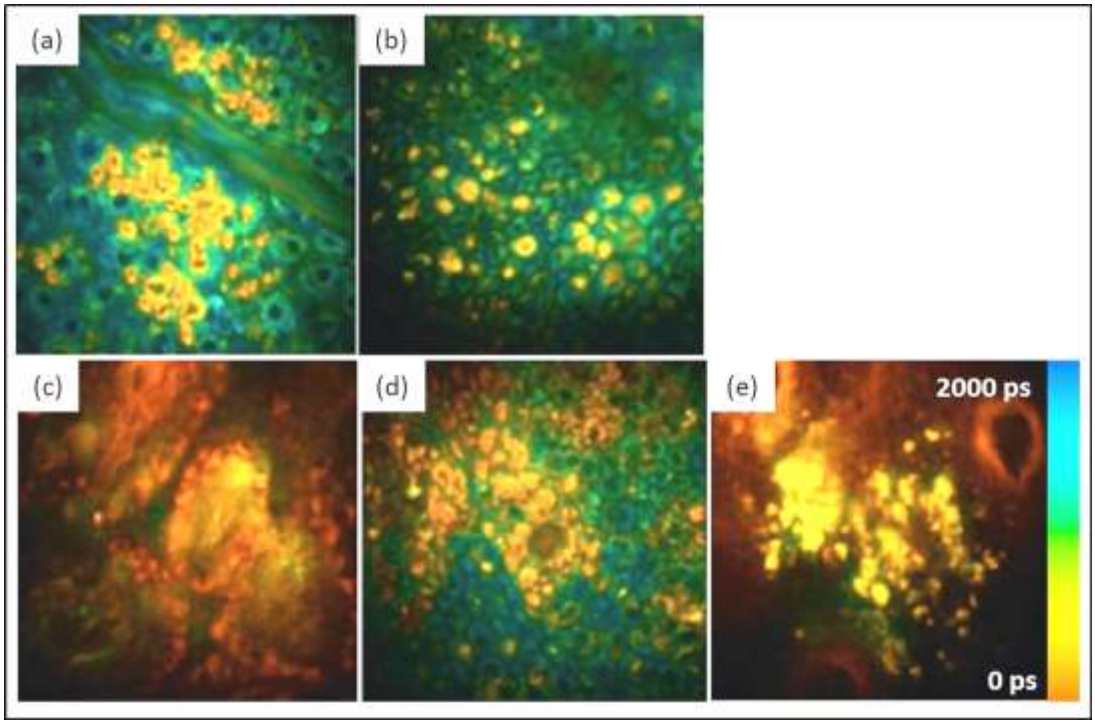

Figure 3.4. MPT FLIM images taken from benign naevi illustrating morphological descriptors for naevi defined by Arginelli et al. (a) Small cells with short lifetimes in the upper epidermis; acquired at 760 nm excitation wavelength. (b) Small cells with short lifetimes in the lower epidermis; acquired at 760 nm excitation wavelength. (c) 'edged papillae' constituted by a rim of short lifetime cells surrounding an oval space with collagen fibres; acquired at 800 nm excitation wavelength. (d)Junctional nest of short lifetime cells at the dermo-epidermal junction. acquired at 760 nm excitation wavelength. (e)'Dermal cell clusters' in the papillary dermis; acquired at 820 nm excitation wavelength. Reproduced from (Arginelli, Manfredini et al. 2012).

3.7 Multiphoton imaging of other skin diseases

3.7.1 Actinic keratosis

Keohler et al. (Koehler, Zimmermann et al. 2011) performed an *in vivo* study using the DermaInspect® to compare normal skin from 30 patients with actinic keratosis (AK) from 27 patients. The skin was excited at 760 nm and 820 nm for autofluorescence intensity (470 nm long-pass filter) and SHG imaging respectively. The authors observed wider inter-cellular spaces and the presence of a fluorescence perinuclear rim for AK. A number of cellular size parameters were compared, but only the nuclear to keratinocyte size ratio was deemed significantly different with AK. They also found an increase in the SAAID index with AK. In addition they observed increased thicknesses of the total and viable epidermis consistent with epidermal acanthosis seen histologically.

3.7.2 Atopic dermatitis

Huck et al. (Huck, Gorzelanny et al. 2010) presented results comparing the changes in autofluorescence intensity images and lifetimes seen with the inflammatory dermatosis 'atopic dermatitis' compared with normal skin *in vivo* using a DermaInspect® with an excitation wavelength

of 710 nm. In three patients with control, mild and severe atopic dermatitis, they found that the peak mean lifetime lengthened from ~1150 to ~1300 to ~1500 ps respectively. In addition, non-lesional skin in atopic dermatitis patients was found to have a longer mean lifetime than patients with normal skin (Huck, Gorzelanny et al. 2011).

3.7.3 Psoriasis

Pavone's group, based in Florence have used MPM to acquire images from the skin from patients with psoriasis *in vivo* (Kapsokalyvas, Cicchi et al. 2011; Kapsokalyvas, Cicchi et al. 2011). They noted an abnormal epidermis, smaller cells than normal in the *s.spinosum* and were able to detect the longer and larger dermal papilla, which is histologically characteristic of the disease.

In a review paper Roberts et al. also present FLIM images from the skin from patients with psoriasis but do not perform any analysis on them (Roberts, Dancik et al. 2011)

3.7.4 Scleroderma

Lu et al. (Lu, Chen et al. 2009) studied sclerodermatous skin *ex vivo* using frozen vertically sectioned tissue. Three samples from scleroderma patients and two from normal skin were imaged with multiphoton excitation at 810 nm, with SHG detected between 393-414 nm and autofluorescence between 430-650 nm. Intensity images from the dermis were analysed and general morphological differences were discussed. The net orientation of collagen bundles was assessed via the fast Fourier transform of the images and found to be higher in scleroderma compared to normal skin. In addition, the spacing of collagen fibrils and the epidermal thickness was found to be reduced in scleroderma. The SHG/autofluorescence ratio (similar to the SAAID index) was found to be increased in the lower dermis in scleroderma patients.

3.7.5 Scarring

Scarring of the skin occurs after full thickness epidermal injury and repair of the skin by the fibroblasts in the dermis. In some individuals this process becomes overactive and leads to the formation of raised hypertrophic scars or, if larger, keloid scars.

In 2004, Brewer compared multiphoton excited image depth stacks of an excised keloid scar with normal skin (Brewer, Yeh et al. 2004). In 2008 Cicchi et al. (Cicchi, Sestini et al. 2008) acquired 5 images for each of four different regions in one keloid specimen, showing that regions of fibroblastic proliferation and keloid demonstrated a strongly positive SAAID index compared to normal tissue.

Chen et al. (Chen, Chen et al. 2009) applied multiphoton imaging with 32 spectral channel detection to acquire multispectral image depth stacks from 5 hypertrophic scars and 1 sample of normal skin in frozen sectioned tissue excited at 850 nm. They recorded the SHG between 414-436 nm and

elastin autofluorescence between 457-714 nm, and presented the morphological features of the collagen and elastin fibres in normal and scar tissue. Their further work examined frozen sections from 5 freshly excised keloids. Tissue sections were excited at 810 nm and SHG was collected between 398-409 nm and elastin autofluorescence between 430-697 nm. In this paper they quantified the increase in collagen throughout the entire dermis of a keloid compared to normal skin and also measured an increase in elastin confined to the deep dermis (Chen, Zhuo et al. 2011).

Zhu et al. constructed mosaics of MPM images to assess scar margins from 15 normal scars on the abdomen of various ages using freshly frozen, sectioned samples of the scars (Zhu, Zhuo et al. 2011). The tissue was excited at 810 nm and fluorescence collected at 405 nm for collagen SHG and 430-697 nm for elastin autofluorescence. They were able to delineate scar margins based on the change in collagen and elastin morphology and signal. They also found a significant negative correlation with scar age/patient age and collagen/elastin content in the scar. i.e. the increased collagen and elastin found in fresh scars reduced with time. The sample was too small to conclude if this difference was caused by patient's age or the age of the scar.

3.8 Combining MPM with other modalities

MPM has for the first time allowed sub-cellular resolution depth resolved images to be acquired from skin *in vivo*. One deficiency of this modality is its limited depth of penetration in comparison to other non-invasive imaging modalities (which have poorer image resolutions). In recent years imaging with combined modalities has been reported with the aim to allow them to be used synergistically in the future. For example, MPM has been combined/compared with optical coherence tomography (König, Speicher et al. 2009), high frequency ultrasound (König, Speicher et al. 2010), reflectance confocal laser microscopy (Koehler, Speicher et al. 2011; Ulrich, Klemp et al. 2013) and epi-coherent anti-Stokes Raman scattering (CARS) (Breunig, Bückle et al. 2011) which images intercellular lipids and water.

3.9 Conclusions

Autofluorescence provides a rich range of contrast parameters for studying diseased human skin. These fluorescence signals have been investigated using a range of instrumentation including single-point fibre probes, wide-field imaging with single photon excitation and multiphoton imaging. Autofluorescence intensity can be complemented by measurements using multiple excitation wavelengths, multiple emission detection bands and measurements of fluorescence lifetime. This chapter aimed to summarise the key papers studying autofluorescence in the skin, focusing on multiphoton microscopy of both normal skin and skin malignancies.

Chapter 4. Materials, Methods & Analysis

4.1 Introduction

This chapter describes the details of patient recruitment and associated ethics approval, the instrumentation and its development, the imaging protocols, and the methods used for image analysis.

4.2 Patients

Patients were recruited from those attending the Dermatology Department at the Hammersmith Hospital site of Imperial College Healthcare NHS Trust.

Patients with the following criteria were excluded: age 18 years or less, in state custody, carrying a blood borne infection, having a photosensitive skin disorder, currently pregnant. In addition, patients unlikely to tolerate *in vivo* imaging were excluded from *in vivo* imaging. *In vivo* imaging of the skin not scheduled for excision were excluded from transplant patients to avoid any possible increased risk of genetic damage from the laser light source. Once recruited, all patients gave their written informed consent to participate in the study.

Patients with lesions clinically diagnosed as BCCs, naevi or melanomas were recruited for *in vivo* and *ex vivo* imaging from the skin cancer clinic. Patients attending non-cancer dermatology clinics were recruited for *in vivo* imaging of normal skin and SCCs in the pilot phase.

All patients were allocated a pseudo-anonymised identification number that identified the images and could be used to access the diagnostic histological slides without identifying the patient when lesions were excised. This was generated by either The Human Biomaterials Resource Centre of Imperial College Healthcare NHS Trust (Tissue Bank) or the clinical research team.

Once eligibility and pseudo-anonymisation had occurred, a minimum data set from each patient was collected, either from the medical records, clinical examination or verbally from the patient. Details included patient demographics, presence of a family history of melanoma, past history of skin cancer, if an organ transplant recipient, whether currently immunosuppressed, skin phototype, presence of solar lentigenies as a marker of actinic damage (none, few, numerous), number of melanocytic naevi (<50, 50-100, 100+) and current medication. In addition details regarding the site of imaging and clinical diagnosis for lesions were recorded.

Figure 4.1 (a) G10 Cannon Camera shown with dermatoscopic attachment. (b) DermliteFOTO® dermatoscopic lens detached from camera. (c) DermliteFOTO® ring light attachment for macroscopic imaging.

Finally a Cannon® G10 camera was used with a DermliteFOTO® macroscopic or dermatoscopic attachment to photograph the lesion, see figure 4.1.

The excitation wavelength, magnification, imaging depth, acquisition time (using the image save time) and a unique daily ID number was recorded for all FLIM images. The excision time for *ex vivo* samples was also recorded.

4.3 Ethics approval

4.3.1 *ex vivo* imaging

Application Title: Autofluorescence spectroscopy and fluorescence lifetime imaging (FLIM) of human tissues. (REC reference number: 09/H0706/28).

National Research Ethics Committee (NREC) approval was sought to acquire and image fresh *ex vivo* tissue using FLIM by Imperial College London. Provisional approval was granted on 16/3/2009 by the Riverside REC office. Local hospital trust approval from Imperial College Healthcare NHS Trust (LREC) was granted (project reference STAG1025) on 26/6/2009.

An amendment was requested to the study protocol including changes to the Chief Investigator's primary workplace (Professor G Stamp), amendment of the consent form for photography, changes to allow pseudo-anonymisation to be performed by clinical researches when necessary, the addition of Charing Cross Hospital (Imperial College Healthcare NHS Trust) and The Royal Marsden Hospital as recruitment sites, and changes to allow imaging using ultrasound and optoacoustic modalities in addition to FLIM. This was approved on 14/3/2011 by the LREC committee.

A further site specific approval was granted by the Research & Development office and LREC committee of The Royal Marsden Hospital on 10/8/2011 (CCR3610).

4.3.2 *in vivo* imaging

Application Title: 09/H0706/83.'Multimodal skin inspection with hybrid acoustic and optical spectroscopic imaging: SKINSPECTION A (REC reference number: 09/H0706/83)

NREC approval was sought by Imperial College London to image skin *in vivo* using FLIM. This application was provisionally approved on 22/1/2010 by the Riverside REC office. Local hospital trust approval from Imperial College Healthcare NHS Trust (LREC) was granted (project reference CHUA1039) on 08/3/2010.

A substantial amendment was submitted to allow modification and consolidation of consent forms, to allow peudo-anonmisation by clinical researchers when necessary and to add Charing Hospital (Imperial College Healthcare NHS Trust) as a recruitment site. This was approved by the LREC committee on 14/3/2011.

4.4 Instrumentation

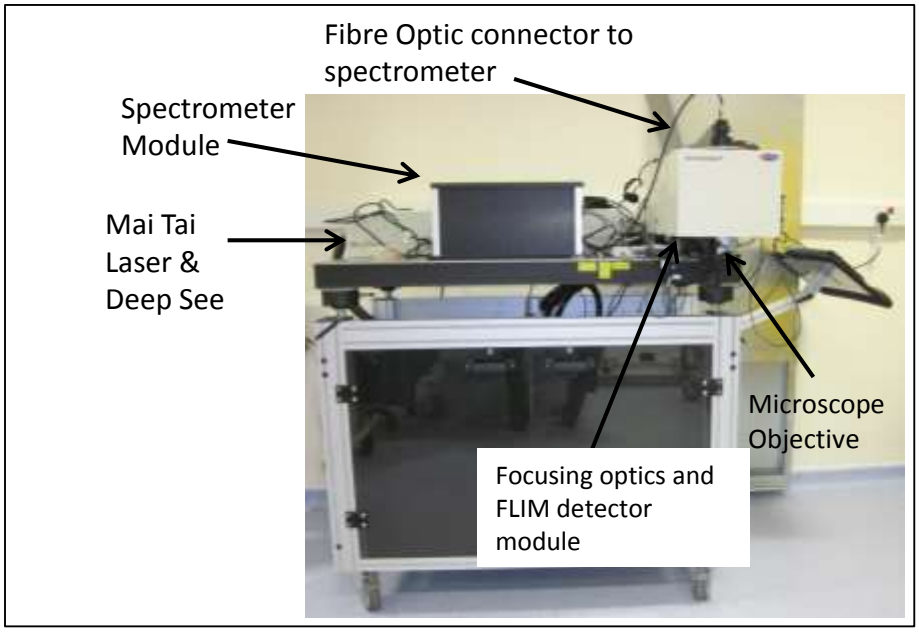

Figure 4.2. An annotated imaged of the modified DermaInspect®

The work in this thesis used a modified DermaInspect® instrument. The fluorescence detection module was adapted to allow fluorescence lifetime imges to be collected in four spectral channels and a spectrometer module was constructed to allow hyperspectral images to be acquired. The DermaInspect® (JenLab GmbH) is a CE marked, Class 1M femtosecond laser scanning system that allows non-invasive optical imaging, see figure 4.2. It incorporates a mode-locked 80 MHz Titanium:Sapphire laser (MaiTai, Spectra Physics®, CA, USA) equipped with a prism-based chirp compensation unit (DeepSee™ module, Spectra Physics®) generating femtosecond pulses with pulse

length <100fs, average power 1.3W, TEM_{00}, Noise <0.15% as its excitation light source. The laser has a tuning range between 710-920 nm with excitation power attenuated to a maximum of 50 mW at the sample (measured at 800 nm) by a step motor driven half-wave plate and polarising beam splitter system (software controlled). The excitation beam passes through two galvoscanners, allowing scanning in the x-y plane, before passing through a 40x/1.4NA oil immersion objective. The objective has a working depth of 200 µm in the z plane, with a lateral resolution of 0.7 µm and axial resolution of 1.5-2 µm for a maximum field of view of 350 x 350 μm^2.

Sliders, situated on the detector module casing allow the beam path for the emitted fluorescence to be directed either to the internal MPT fluorescence intensity PMT (BG39 filter & Hammamatsu H7732 PMT, Hamamatsu Photonics K.K., Japan), the FLIM detector module or the spectrometer.

4.4.1 FLIM detector module

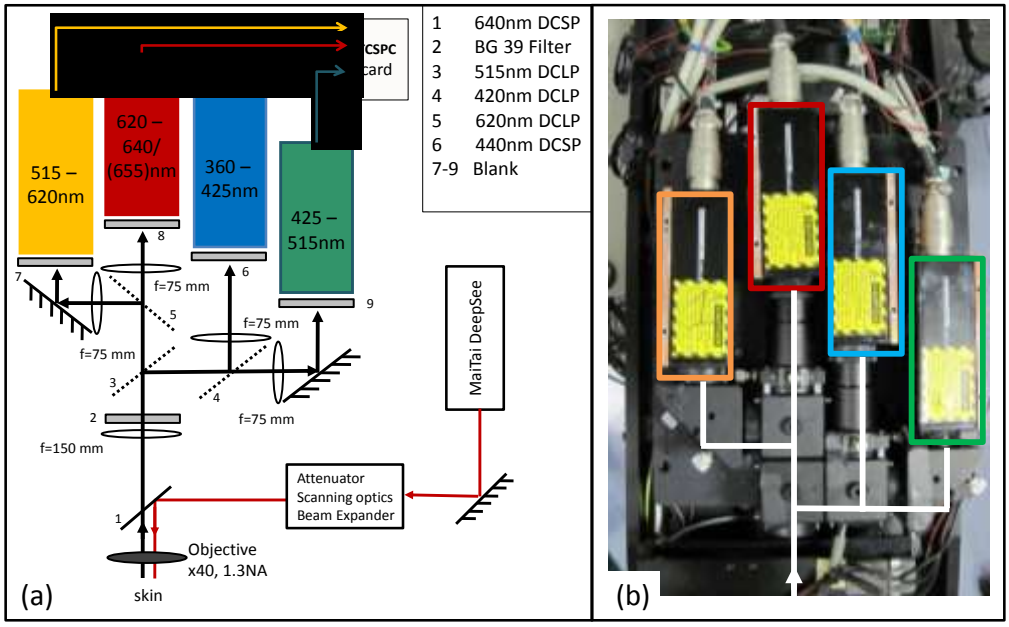

Figure 4.3 (a) A schematic of the original design of the 4 spectral channel FLIM detector unit. (b) A photograph of the completed unit with the module casing removed. Key –White line -The beam path. Colour of PMT outline- spectral range as per the schematic.

The FLIM detector module (see figure 4.3) was designed by Dr Clifford Talbot and had an optical transmission efficiency of 85% across 200 µm in the x-y plane. The figure 4.3(a) illustrates the excitation beam (in red) directed to the skin. The two photon fluorescence emitted from the skin passes through the excitation short pass dichroic filter (position 1), allowing fluorescence below 640 nm wavelength to pass to the FLIM detector module in the original configuration. The beam is then focused and spit into 4 spectral channels through a number of further filters and dichroic mirrors. The fluorescence is then collected by 4 Hammamatsu H7422P-40 PMTs (with peak quantum

efficiency of 40%) defining the spectral channels as blue (360-425 nm), green (425-515 nm), yellow (515-620 nm) and red (620-640 nm). Fluorescence decays are collected by time correlated single photon counting (TCSPC) using an SPC-830 module (Becker & Hickl, GmbH). The PMTs were controlled using a DCC-100 module (Becker Hickl) and wide band amplifiers with overload detection (Becker Hickl part number HFAC-26dB) were placed after each PMT. Routing of the timing signals from the four channels was achieved using a HRT-411 module (Becker Hickl). The spectral cut-off of the dichroic in position 1 was changed to 655 nm for the modified design and is discussed below in section 4.5.1, pp91.

4.4.2 Spectrometer Module

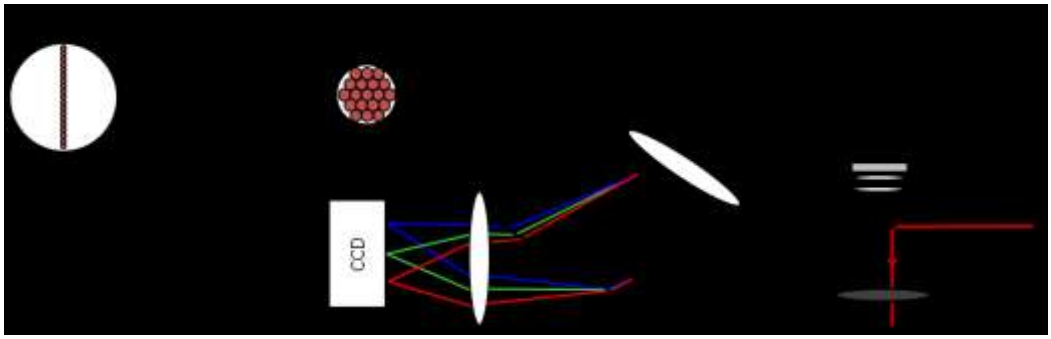

Figure 4.4. Schematic of the prism based spectrometer unit. The inset diagram illustrates the mapping of the fibres in the fibre bundle collecting the fluorescence of position (A) to those that relay it to the spectrometer at position (B).

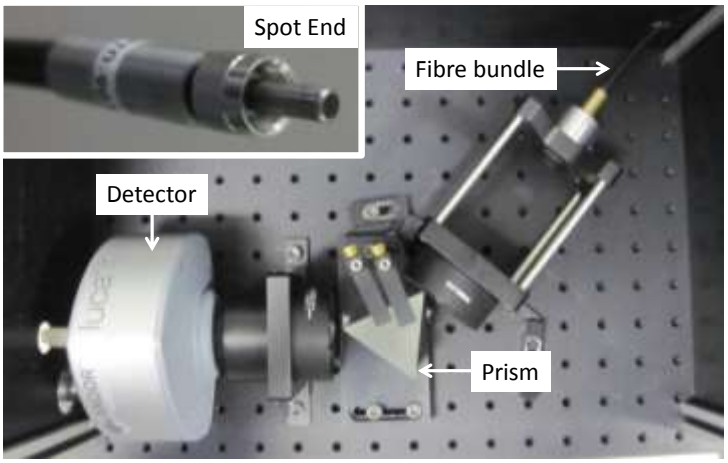

Figure 4.5 An annotated photograph of the prism-based spectrometer. The inset shows a detailed image of the spot end of the spot-to-line fibre bundle.

A prism based spectrometer that was designed and constructed by Dr Clifford Talbot allowed steady state fluorescence emission spectra to be collected from the plane of focus by the DermaInspect®, see Figures 4.4-4.5. The emitted fluorescence collected by the objective was initially relayed by two lenses onto spot-to-line fibre bundle (FiberTec Optica, Canada). This system had a geometric

transmission efficiency of 100% up to a calculated geometrical radial distance of 0.18mm from the centre of the field of view. The fibre bundle had an active area of 63% of the fibre spot end and was coupled into the prism based spectrometer, which used a LucaEM R (Andor™, Northern Ireland) EMCCD as the detector. The EMCCD camera had a detection spectral range between 360-877 nm with a quantum efficiency of between 40-65% in the range 380 – 655 nm. The EMCCD was configured to record the fluorescence signal into 50 spectral bins over this range. The start/stop signal and pixel clock from the DermaInspect® could be routed to the spectrometer, allowing a spectrum to be acquired from a pixel, line or frame of the imaged FOV. Image acquisition was performed using a user interface written in LabView™ 7.1 (National Instruments®,USA). Initially this was executed on a standalone laptop PC but was ultimately installed on the PC running the DermaInspect® control software.

When acquiring a spectrum from each pixel, the spectral image resolution was limited by the acquisition rate of the EMCCD camera. The image resolution was either 32x256 or 41x256 pixels in size and acquired over 49.9 seconds.

4.5 System Development

4.5.1 Spectral Channels of FLIM module

Minor modifications were made to the system during the study to improve the spectral separation between channels and to broaden the red channel's detection bandwidth from 620-640 to 620-655 nm. To achieve this, the 640 nm DCSP (Chroma Technology Corp., Vermont, USA; position 1, figure 4.3) was replaced with a 670 nm DCSP, the BG39 filter (position 2, figure 4.3) was replaced with a 680 nm short pass filter and a number of band pass filters were inserted, see table 4.1.

Installation date	Position	Manufacturer's Description
before 7/6/2010		As Above
07/06/2010	2	BG39 to 680 SPF
1-7/10/2010	6 (Blue)	Short pass 440nm
	1	640 DCSP to 670 DCSP
25/05/2011	8 (Red)	Band pass 601-657 nm
01/07/2011	7 (Yellow)	Band pass 506-594 nm
	9 (Green)	Band pass 420-520 nm

Table 4.1 Chronological list of the modification of the spectral filters made between then original design of the FLIM detector module and its final design. Position references to figure 4.3

As the spectral range of the optical filters inferred from the name given by the manufacturers had slight differences to their actual spectral ranges, a comparison of the listed spectral range and the 50% transmission spectral range of the filters used is given in table 4.2. Once the spectral sensitivities of the PMTs were accounted for, the overall detector efficiency for each channel following is illustrated in figure 4.6 for both before and after the modifications. Following the failure of a PMT, the red spectral channel was missing from FLIM images acquired between 27/7/11 and 6/10/11 and therefore data was collected for just three spectral channels over this time.

Channel	**Spectral range stated in Manufacture's filter description**	**50% transmission spectral range**
Blue	360-425 nm	370-429 nm
Green	425-515 nm	430-515 nm
Yellow	515-620 nm	517-600 nm
Red	620-655 nm	617-655 nm

Table 4.2 A comparison of the listed spectral range of filters used and their 50% transmission range.

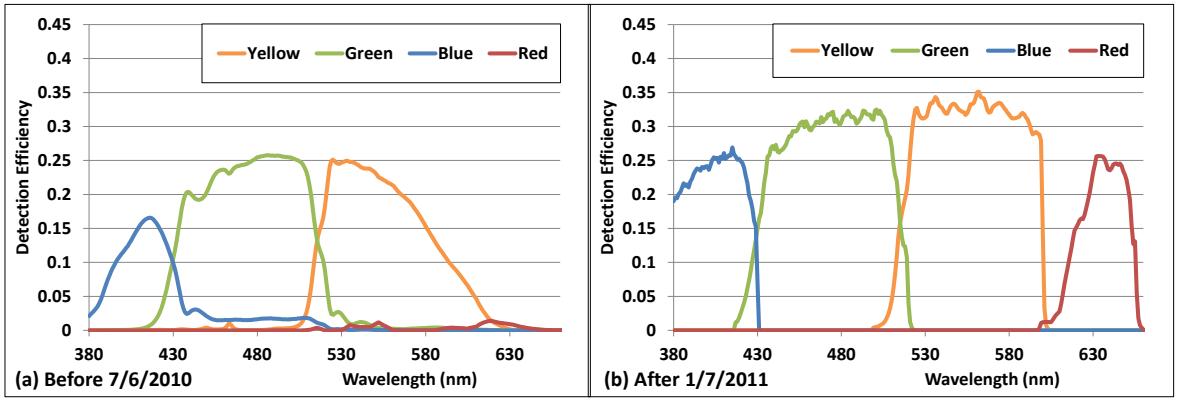

Figure 4.6 Wavelength range of detection for fluorescence for each spectral channel (a) in the original design and (b) following all modifications.

FLIM images were either 128 x128 pixels before the integration of TCSPC FIFO (first-in first-out) acquisition mode (occurred on 15/8/2011) or 256x256 pixels after, with all acquired over 25.5 seconds.

The changes to the dichroic filter in position 1 (figure 4.3) to increase the spectral range of the red channel, consequently meant that a greater spectral contribution came from the channel after the change. The remaining filter changes had a minimal effect on this parameter. The calculated lifetime parameters were independent from these changes as a calibrated spectral response of the system was made daily using a blue fluorescence slide as a reference (Chroma Technology Corporation, USA).

4.5.2 Articulated Arm

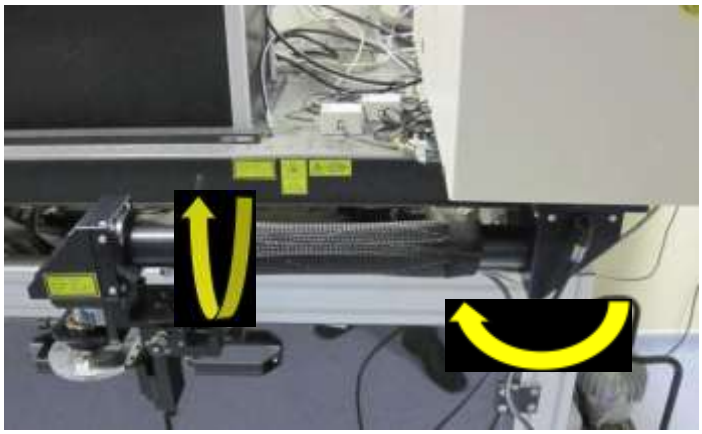

Figure 4.7 Photograph of the articulated arm with annotations of the two planes of rotation that can be made.

The fixed objective and its proximity to the edge of the optical bench significantly restricted the range of body sites that could be imaged *in vivo*. This was because of a number of reasons :-

- The physical restriction caused by the size and position of the optics.
- Insufficient comfort for the patient.
- Inability of microscope objective of the DermaInspect® to angle to the contour of a patient.

As a consequence imaging *in vivo* was effectively restricted to lesions on the extremities for most cases. On 25/5/2011 an articulated arm (JenLab GmbH) was installed to allow greater flexibility in positioning the objective, see figure 4.7. It could rotate in the horizontal plane about the detector module, and the objective head could rotate around the end of the arm, which allowed a greater range of body sites to be imaged.

4.5.3 Detector Overload Protection

Two safety mechanisms were incorporated into the system to protect the PMTs from potentially damaging high light levels caused by accidental exposed to room light or bright fluorescence. These electronic mechanisms were an internal overload trigger in the PMT and another inside the external amplifier. Images containing bright fluorescent spots (usually of from keratin or melanin) would trigger an overload circuit, resulting in a failed attempt to acquire a FLIM image. The internal overload circuit was very sensitive and typically triggered first. Unwanted triggering of either overload circuit increased the number of failed attempts to acquire a complete FLIM image and prolonged the time taken to obtain a complete image stack from a patient. This was especially noticeable when imaging lesions *in vivo*. As a result, over the period of July to September 2010, the internal PMT overload trigger was removed from all 4 detectors. This left the external overload trigger which was more tolerant of single bright pixels within an image.

4.5.4 Motorised Stage

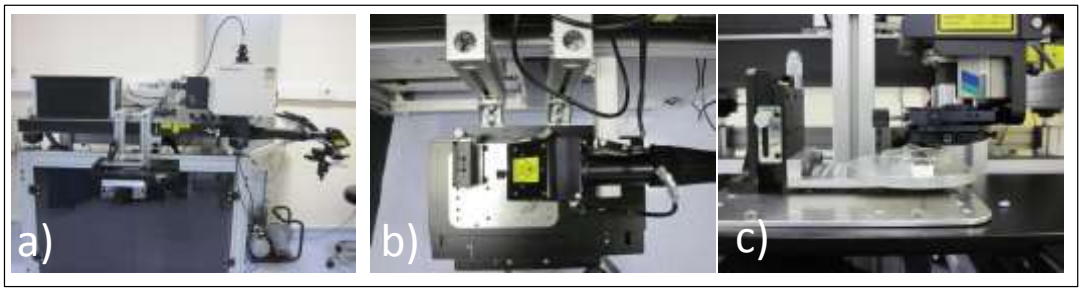

Figure 4.8 (a) An image of the DermaInspect® with the motorised stage and articulated arm attached. (b) An image from above the motorised stage illustrating the position of the microscope objective in relation to the stage. (c) A side image of the position of the microscope objective, tissue sample within a petri dish and motorised stage.

A motorised microscope stage (Scan IM 120 x 80, Märzhäuser Wetzlar Gmbh, Germany) , mounted on a custom built frame, attached to the DermaInspect® trolley was used for the sequential acquisition of data from several adjacent fields of view from *ex vivo* samples to create mosaic images, see Chapter 7.3.6. Course positioning of the sample in the z plane was made using a micrometer screw (figure 4.10f) in addition to the computer controlled piezo positioner controlled through the DermaInspect® acquisition software. The stage could be positioned in the horizontal tissue plane with a smallest step size of < 0.1 µm using a joystick or keyboard using software written in LabView™ running on a standalone laptop PC. The stage is illustrated in figure 4.8.

4.6 Tissue Imaging

4.6.1 Pre-Imaging Tissue Preparation

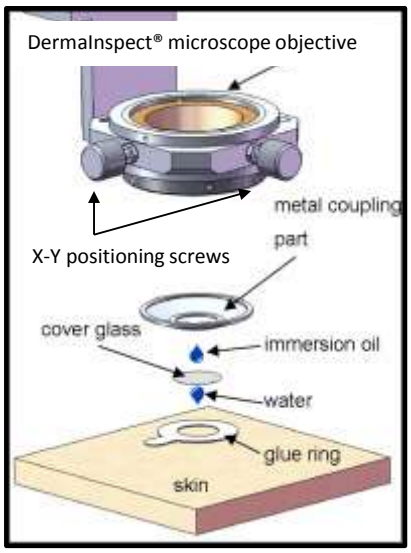

Figure 4.9 Illustration of how to attach the coupling ring to the skin and the microscope objective of the DermaInspect®. Adapted from the DermaInspect User Manual (JenLab 2009).

Once an area of skin was selected to be imaged *in vivo*, it was moistened with a drop of water. A coupling ring, with a size 0 (thickness 80-120 µm) and 18 mm diameter cover slip (Assistent®, Glaswarenfabrik Karl Hecht GmbH & Co KG,Germany) was then attached to the skin using double sided adhesive. Finally, a drop of Immersol ™ 518 F DIN 58.884 (Carl Zeiss Ltd., Germany) was placed on upper surface of the cover slip. The patient was then moved to magnetically couple the metal ring surrounding the DermaInspect® microscope objective (see figure 4.9).

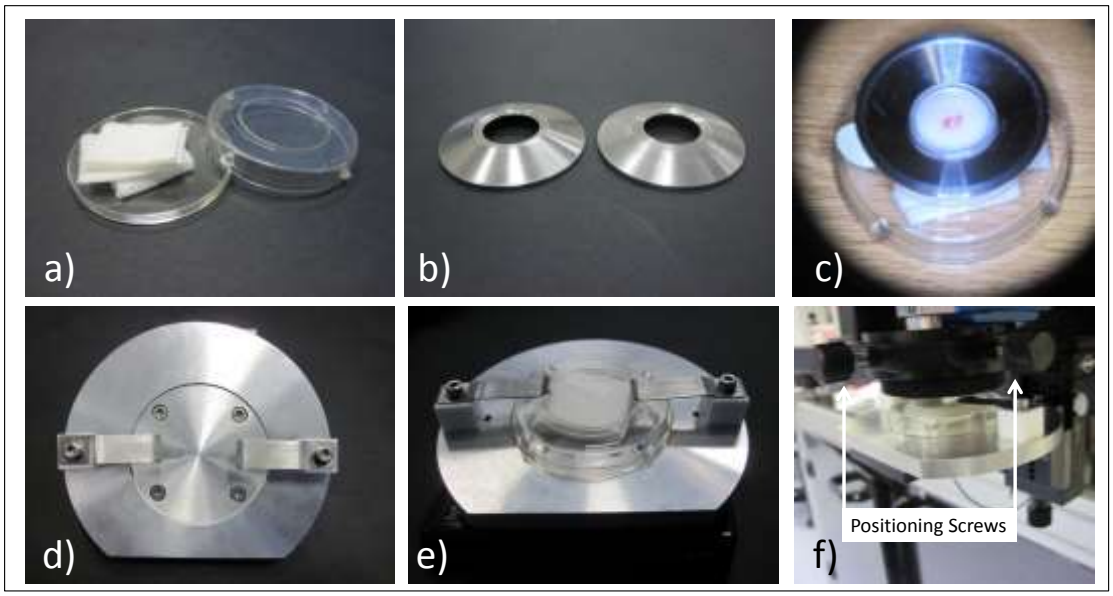

Figure 4.10 (a) Inverted glass bottomed petri dish used to image *ex vivo* samples. (b) Metallic coupling rings. Left- used for *in vivo* imaging. Right- coverslip groove removed to allow attachment to petri dish for *ex vivo* imaging. (c) Transparent plastic ring placed over metal coupling ring to indicate the centre of FOV that will be imaged. (d,e) Stage with clips to prevent lateral movement of the petri dish/sample during imaging. (f) Sample in petri dish mounted on stage ready to image.

Freshly excised *ex vivo* tissue was rinsed with Hanks Balanced Salt Solution buffer (HBSS) without phenol red, calcium or magnesium (Gibco®, Invitrogen™, CA, USA), its surface moistened with the buffer solution and placed on damp gauze in an inverted glass bottomed petri dish containing either a size 0 (thickness 80-130 µm) or size 1.5 (thickness 160-190 µm) cover slip (Matek®, USA), figure 4.10a. Once the lid (containing the cover slip) was replaced, a coupling ring (designed for *ex vivo* use), was adhered to the cover slip surface, so that the FOV of interest would align with the centre of the coupling ring and therefore the objective of the DermaInspect®, see figure 4.10b. This was aided by the use of a transparent plastic ring with a 1mm central hole (figure 4.10c) which indicated the centre of the coupling ring. A metallic plate was designed to accommodate the petri dish under the objective and prevent its movement during imaging which could be used with the motorised stage if necessary, for imaging *ex vivo* samples (figure 4.10d-f).

The objective could be adjusted to remain centred within the coupling ring by adjusting the positions of two screws shown in figure 4.10f, thereby ensuring that the image was taken from the centre of the FOV defined by the plastic ring.

Ex vivo samples imaged using the motorised stage to create mosaics required lateral movements of the petri dish in relation to the objective. Therefore, although the dish was fixed to the stage, it was not fixed to the objective using the coupling ring, as outlined above. Instead, a drop of the Immersol™ was placed on the surface of the cover slip, the objective was focused and the dish was allowed to move under the objective lens as controlled by the motorised stage.

4.6.2 FLIM Imaging Protocol

All FLIM images were acquired with the room lights off and the computer screen covered to minimise the background light.

Once the patient/tissue sample was in place, the *s.corneum* layer was visualised using the fluorescent intensity MPT detector by adjusting the depth of focus using the piezo driven objective positioner. Initially, the excitation power was restricted to < 12 mW for this layer (as per the DermaInspect® manual).

If required, imaging parameters such as excitation wavelength, magnification, x-y adjustment of the objective position were adjusted. The tissue depth reading on the control software was then reset to 0 µm in preparation for imaging the *s.corneum* layer.

The fluorescence beam path was then set to direct fluorescence to the FLIM detector module. The excitation power was adjusted to optimise the signal strength for the current imaging depth before a FLIM image was acquired (with the computer screen covered to further reduce the background light). Once acquired, the image was saved immediately and the objective was repositioned using the piezo positioner to image a different depth. Images were taken at approximately 10 µm depth intervals in the sample until the dermis was reached. The excitation power was adjusted for each image depth. Although most images were acquired using an excitation wavelength of 760 nm, paired images at two different wavelengths were taken for some samples.

FLIM images were acquired over 25.5 seconds. Images were initially acquired using 128 x 128 pixel resolution. From 15/8/2011 (from patient ID 4108) acquisition using FIFO FLIM mode was successfully implemented and allowed for images with an improved 256 x 256 pixel resolution. Most FLIM images were 107 µm x 107 μm^2 in size; however a range of sizes between 56 µm x 56μm^2 and 271 µm x 271 μm^2 were used. Fluorescence decays were collected with 256 time bins over 12.5 ns.

Should the emitted fluorescence from a pixel exceed the detector overload protection threshold, an audible warning was produced, the detectors would cut out and require resetting before the image could be re-acquired at a lower excitation power.

At the start of each session, two calibration fluorescence decay measurements were taken. One from a blue fluorescent slide (Chroma Technology Corp. USA) with a known lifetime of 0.9 ns for use as a lifetime standard and another from gold nanorods with an ultrafast response for use as an instrument response function (IRF), see section 4.10.1, pp103.

A time limit of 3 hours from surgical excision was set for imaging *ex vivo* samples for imaging i.e. before sample fixation in formalin for subsequent histology. This limit was chosen to maintain the tissue close to its *in vivo* state whilst still allowing sufficient time for imaging. Previously published studies vary considerably in this regard. For example, many do not define the length of time imaging was performed post excision (König and Riemann 2003; Dimitrow, Riemann et al. 2009; Dimitrow, Ziemer et al. 2009). In those that have, Benati et al. limited imaging to 45 minutes (Benati, Bellini et al. 2011), whilst some had imaging protocols extending from 3 to 6 hours post excision (Cicchi, Sestini et al. 2008; Ericson, Simonsson et al. 2008; Paoli, Smedh et al. 2008; De Giorgi, Massi et al. 2009).

In our studies a few samples were imaged longer than 3 hours to allow larger montaged mosaic images to be acquired. In these cases, images taken after this time limit were used for illustration of the image mosaic only and not for the lifetime analysis of the data.

It was difficult for patients to remain sufficiently still during the entire acquisition time of an image i*n vivo* for a number of reasons including the difficulty in maintaining many body sites correctly and the long duration of imaging (25 seconds). This caused many images to have significant movement artefacts. Improvement was seen after the addition of the articulated arm. However, despite its addition, many patients were unable to remain comfortable during imaging. The most successful images acquired *in vivo* were from patients seated in a chair with their arm resting on a couch. Further changes such as reducing the acquisition time were not found to make a significant difference.

4.6.3 Spectrometer Imaging Protocol

Hyperspectral images were always taken following FLIM image acquisition as they required greater excitation powers to acquire reasonable images. Typically, after a FLIM image was acquired and saved, the fluorescence and necessary electronic signals were directed to the spectrometer. Due to limitations in the frame rate of the spectrometer camera, images were acquired over 49.9 seconds

at either 32x256 or 41x256 pixel resolution. A background image, (using zero excitation power) was acquired in most cases for each individual FOV.

4.7 Histology

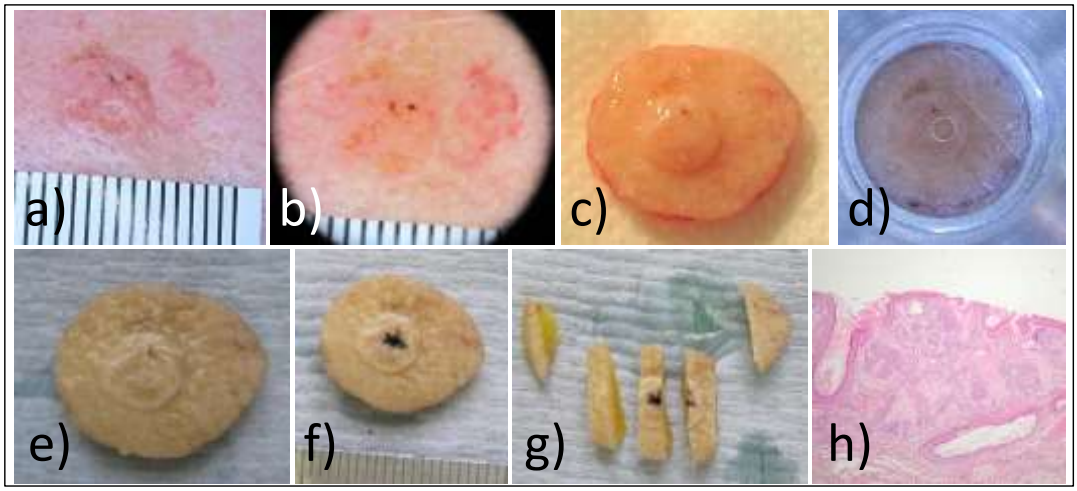

Figure 4.11 Images of sample 4126 recording the stages of the protocol. (a) Macroscopic image of a BCC taken *in vivo*. (b) Dermatoscopic image of BCC taken *in vivo* (c) Image of freshly excised BCC. (d) Image of sample attached to metallic coupling ring with plastic ring placed over to indicate the centre of the FOV/area of BCC to be imaged. (e) BCC after fixation with formalin. (f) Ink tattoo to indicate the area of BCC imaged, based on photograph d. (g) BCC cut into 5 sections prior to embedding, microtome sectioning and staining. (h) Photograph of stained vertically sectioned slides used to make the histological diagnosis.

Following imaging, *ex vivo* samples were placed in an aqueous solution of 10% formalin for fixation for at least 12 hours. Sectioning of the fixed tissue, prior to embedding was performed by myself or a histopathology technician. Following embedding, microtome sections were generated, mounted and stained with Haematoxylin & Eosin (H&E). The diagnosis of all *ex vivo* samples were confirmed histologically by a consultant pathologist. Figure 4.11 a-h shows a single lesion photographed at all the stages of the imaging and histological processing.

4.8 Image Co-registration

Dermatoscopic, FLIM and histological images are all viewed at scales of different orders of magnitude and orientation. Dermatoscopic and FLIM images are viewed *en face*, whilst histological slides are cut in vertical sections. These differences in scale and orientation created challenges when aligning the FLIM FOV with a specific skin surface feature and when correlating the FLIM images with histological structures. It was therefore important to develop a method to co-register the different types of images. A plastic ring, as described above and seen in figure 4.10 d, was found to be the best method to align the surface features of the lesion with the area being imaged. This method was tested and found to allow imaging to within 1x1 mm^2 of the defined spot.

The following procedure was used for co-registration of features seen in the FLIM images and sectioned slides. For samples that were cut-up by myself, the area imaged (as correlated with the photographs taken during imaging) was marked on the surface of the tissue by scoring superficially, perpendicular to the sectioning plane and tattooing with permanent ink. Histological sections were then aligned as accurately as possible using this tattoo. This is demonstrated in figure 4.11 f-g. For the majority of samples either the ink tattoo or the superficial score could be seen in the sectioned slides. When these markers could not be seen on the sectioned slides under the microscope, the slides from the sections nearest the area imaged (e.g. the 3rd and 4th sections in figure 4.11 g) were used as the closest correlate.

Prior to this method, a number of techniques were tried and were found to be less successful. These included marking the tissue with ink prior to imaging & collecting a reflected white light image of the sample through the DermaInspect® objective in order to orientate the position of the FOV within the sample. These methods were unsuccessful because the ink would often run over the surface of the tissue and/or it was very difficult to find the pre-marked spot, once the sample was under the DermaInspect®. The white light image was unsuccessful because of the difficulty in acquiring a focused image.

4.9 Experiences with the Modified DermaInspect®

4.9.1 DermaInspect® Characteristics

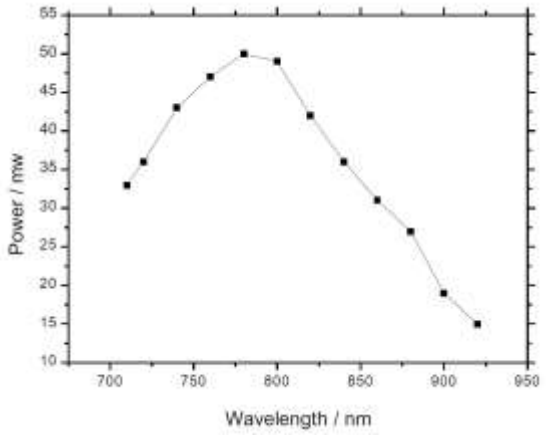

Figure 4.12 Graph of emitted power from the excitation laser of the DermaInspect® with software set to the maximum power of 50 mW.

Figure 4.12 plots the peak power output of the DermaInspect ® against excitation wavelength. It shows that the peak power of the instrument has been set to 50 mW which can only be achieved at 800 nm. The pulse length of the excited light is ~150 fs without the articulated arm. Breunig et al.

have shown that the pulse duration is maintained at ~150 fs in the image plane when the arm is attached (Breunig, Studier et al. 2010) over most wavelengths.

4.9.2 Detector Cross Talk

		% signal recorded			
		Blue	**Green**	**Yellow**	**Red**
Activated Detector	**Blue**		0	0.000891	0
	Green	0		0.023234	0
	Yellow	0	0		0
	Red	0	0	0.00049	

Table 4.3 shows the % of electrical crosstalk between the PMT detectors when the gold nanorod slide is excited and each detector it activated in turn with the photon count measured in all.

The electrical cross talk was assessed by measuring the luminescence decay in all 4 spectral channels when the gold nanorod IRF slide was excited at 760 nm. A reading was performed for each PMT activated in turn. Table 4.3 shows that the % electrical crosstalk between the detectors is <0.05%. The optical cross talk can be seen by the transmission curves previously shown in figure 4.6.

4.9.3 Clinical Experience

This section describes experiences using the DermaInspect® to acquire clinical images.

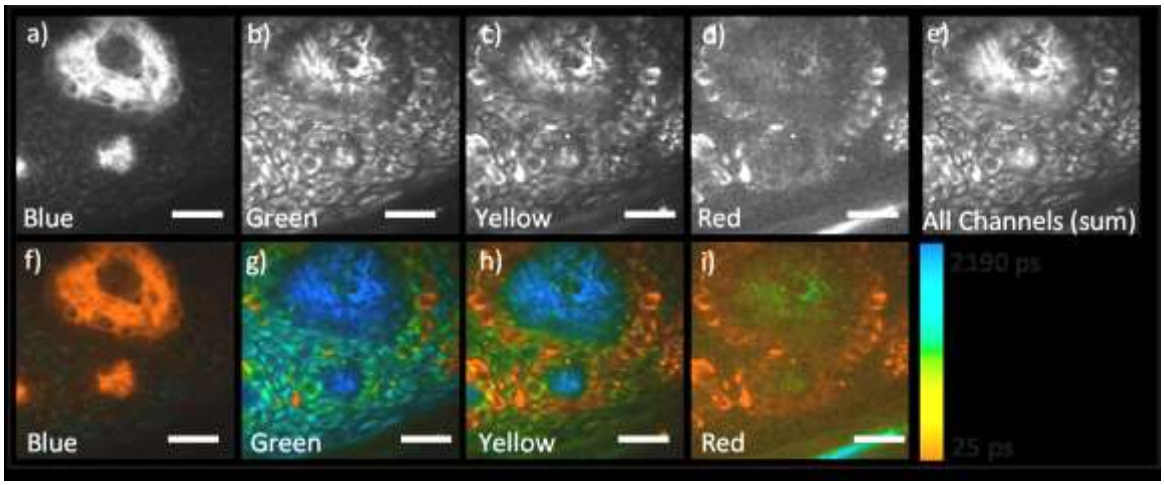

Figure 4.13 Fluorescence intensity & false colour FLIM images for each spectral channel are shown of an image taken at 110 μm depth of the basal layer of normal skin (ID 4117 fov3).

In the first instance, figure 4.13 is a typical image taken with the 4 spectral channels from normal skin and shows fluorescence intensity and FLIM images. All images have been taken from the same field of view of normal skin. It illustrates the increased contrast benefits of acquiring fluorescence lifetimes in more than one spectral channel. Figures 4.13a-d show that contrast between different structures can be seen in the fluorescence intensity images recorded in the 4 spectral channels that

is not visible in the calculated total fluorescence intensity image (Figure 4.13e). The second harmonic generation (SHG) signal from collagen, seen in the tips of the dermal papilla, dominates the blue spectral channel (Figure 4.13a) and can be visually separated from the weaker intracellular fluorophores (c.f. Figure 4.13b-d). It is however difficult to visually separate the multiple fluorophores contributing to the green, yellow and red channels (Figure 4.13b-d) using the fluorescence intensity images alone. The addition of the fluorescence lifetime information (Figures 4.13f-i) allows NAD(P)H autofluorescence (blue-green on false colour scale), dominant in the green spectral channel to be easily distinguished from melanin (short lifetime (Teuchner, Freyer et al. 1999) red on false colour scale), which is dominant in the red spectral channel. The yellow spectral channel includes fluorescence from flavins, NAD(P)H and melanin. The multiple FLIM spectral channels also allow SHG from collagen, (with an instantaneous decay) seen in the blue channel, and elastin (with a long fluorescence lifetime (König and Schneckenburger 1994)), seen in the green/yellow channels, to be distinguished from the same spatial location within the dermal papilla.

One disadvantage of the method of tissue preparation prior to imaging is that the useful imaging depth is reduced by the distance between the bottom surface of the cover slip and the *s.corneum*. For example, this can significantly affect the ability to image the epidermis when the surface of the tissue is not flat. Despite this, images with a good signal to noise ratio were obtainable to a tissue depth of 100 – 150 µm in the majority of cases. However, this restriction excluded imaging of lesions/normal skin that had significant hyperkeratosis (thick *s.corneum*), including many actinic keratosis and cutaneous squamous cell carcinomas. In these cases, only images from the *s.corneum* were possible.

A difficulty in developing the DermaInspect® was that software changes were difficult and costly to approve, as the CE marking of the device could not be compromised. It prevented the integration of all the software into a single user friendly interface. Instead, the following software tools were used to acquire the images presented in this thesis: JenLab GmbH software controlled the excitation parameters; Mai Tai laser software controlled the laser excitation wavelength; SPCM (Becker & Hickl) was used for FLIM acquisition; Spectometer control/acquisition software (Andor™) controlled the spectrometer; and in house software (written in LabVIEW®) was used to control the motorised stage. Some integration was instituted through AutoIT, an automating and scripting language for windows GUIs. For the future, improved software integration for image acquisition would reduce the risk of errors and allow images to be acquired *in vivo* more easily.

Over the project, the incremental changes made to the DermaInspect® improved the clinical experience both for the patient and the clinician. Initially, limited automation of the control software

using AutoIT (Jonathan Bennett & AutoIt Consulting Ltd), as described above, improved efficiency. This included code to automatically reset the PMTs once the overload protection was triggered and, code to co-ordinate the JenLab GmbH and Becker Hickl software to allow automatic image acquisition and automatic saving & standardised image file names. Much time was also saved by raising the internal PMT overload protection threshold, which reduced the likelihood that the overload trigger was tripped.

Finally the addition of the articulated arm had a significant impact on the number of body sites that could be imaged *in vivo*. Furthermore, as patients were no longer required to physically strain to be imaged, the extremities could be imaged for longer periods of time and less movement artefact was seen in the images acquired.

4.10 Analysis

4.10.1 Instrument Response Function

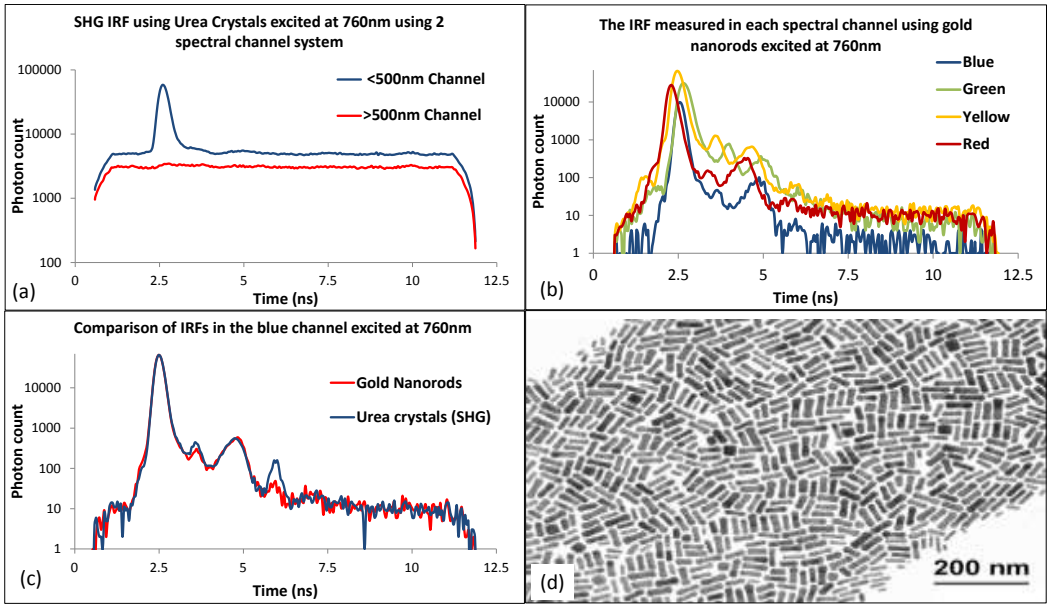

Figure 4.14 (a) A plot of the recorded SHG signal from Urea Crystals above and below 500 nm. (b) A plot of the measured luminescence of the signal from gold nanorods in each spectral channel. (c) A plot comparing the signals measured between urea crystals and gold nanorods using the DermaInspect®. (d) A electron microscope image of the gold nanorods used. Image courtesy of Fulvio Ratto. Inst. di Fisica Applicata, Consiglio Nazionale delle Ricerche, Fiorentino, Italy.

In order to accurately fit acquired fluorescence decay data, it is necessary to convolue the fluorescence decay model with an instrument response function (IRF).This process adjusts the model for the artefactual effects caused by the instrument itself. For this purpose, an IRF was collected by exciting a substance with a very short luminescence prior to each imaging session and allowed the fluorescence decay model to be adjusted as the system was modified over time.

For the preliminary studies using a modified DermaInspect® and 2 emission spectral channels (Patalay, Talbot et al. 2011), the IRF was measured by excited urea crystals to generate an SHG signal. This had the disadvantage that the SHG signal was only emitted at ½ the excitation wavelength and therefore was only detectable in a single spectral channel, see figure 4.14a.

Since that time, the method of collecting an IRF in multiple spectral channels by exploiting the broadband ultrafast luminescence (< 50fs) from gold nanorods was described by Talbot et al. (Talbot, Patalay et al. 2011). Gold nanorod luminescence provides a similar IRF to that emitted by urea crystals, as can be seen in figure 4.14c, and due to the broadband nature of their emission, they were better suited to providing an IRF in this multispectral system, see figure 4.14b.

4.10.2 Fluorescence Decay Models

In MPT of live biological tissue, the number of photons collected per pixel is limited because of restrictions on imaging duration and maximum allowed excitation power. This in turn restricts the complexity of the decay models that can be used to fit the data. Two fluorescence decay models were used for the work presented in this thesis – a single exponential decay model for generating FLIM images and a double exponential decay model for the FLIM analysis.

Fluorescence images were acquired at either 128 x 128 pixels or 256 x 256 pixels resolution, over 12 ns into 256 time bins.

4.10.3 Single Exponential Decay Model

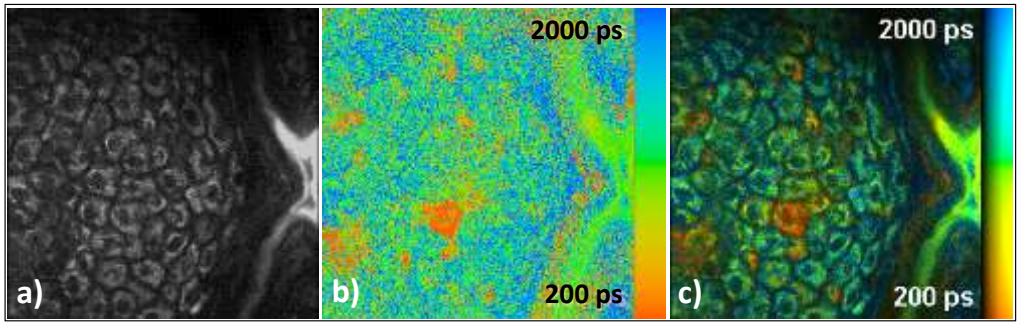

Figure 4.15 (a) Fluorescence intensity image (b) Colour map of the fluorescence lifetime calculated for each pixel (c) A merged fluorescence intensity and lifetime image taken from the green spectral channel (ID 4210 image 2).

For the purposes of displaying an image, a single exponential decay model was used to fit the fluorescence decay at each pixel of the images in each spectral channel, as insufficient photons were collected to calculate a more complex decay reliably. This was performed using fitting software written in C++ and Matlab® (R2010b, The Mathworks Inc., USA) by Sean Warren and with a user interface written by Dr Clifford Talbot.

For 128x128 resolution images the decay data was smoothed spatially using a 3x3 kernel prior to fitting each pixel. The fitting model accounted for effects of incomplete decays and the IRF obtained from gold nanorods was used with a temporal offset fixed to zero. The resulting FLIM map was then merged with the fluorescence intensity image.

Initially the 256x256 resolution images were binned to 128x128 prior to fitting. The FLIM image was then merged with the 128x128 resolution intensity image and upscaled using linear interpolation to 256x256 pixels again (see figure 4.15c). The final method used was to spatially smooth 256x256 resolution images using a 5x5 kernel without binning prior to fitting. The fitted FLIM image was then merged with the intensity image. This image could then be upscaled as necessary, depending on the monitor size and resolution to 384x384. This final method was chosen to allow FLIM images similar in resolution to that used in SPCImage (Becker & Hickl, GmbH) to be generated.

The intensity merged FLIM images were then used to assess the morphological features in the samples.

4.10.4 Manual Regions of Interest (ROI) segmentation

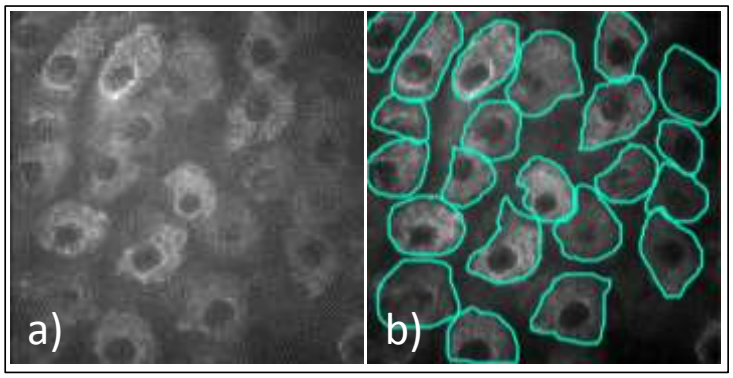

Figure 4.16 (a) Fluorescence intensity image (b) Intensity image with overlay indicating the manually defined ROIs corresponding to each cell in the image.

To allowing a more complex decay model to be used, images were segmented to combine the fluorescence from multiple pixels and increase the number of photons available for fitting. The photons were binned spatially for the area corresponding to each cell within each image into regions of interest (ROI), see figure 4.16.

ROI were defined manually using software written in Labview™ 7.1 by Dr Chris Dunsby, Dr Sunil Kumar and Dr Clifford Talbot. A threshold of 1000 photons in the total cell fluorescence decay was deemed sufficient to reliably fit a double exponential decay model for the lifetime analysis. Decay curves from a single spectral channel containing fewer than 1000 photons were therefore excluded from the analysis.

Although smoothing was used to increase the number of photons available to fit the single exponential decays used to generate the merged FLIM images, it was not used here. A disadvantage of smoothing is that it is performed over the entire image indiscriminately, counting light from both intracellular and extracellular regions and, for our data, would still have insufficient photons to fit a more complex decay model.

The use of ROI-integrated decays allowed sufficient photons to fit a double exponential decay model and the calculated lifetimes to reflect intracellular fluorophores only. This allowed each lifetime to be biologically meaningful by corresponding to a single cell. It further enabled analysis of different cell populations within a sample and comparison between different samples and disease states to be performed.

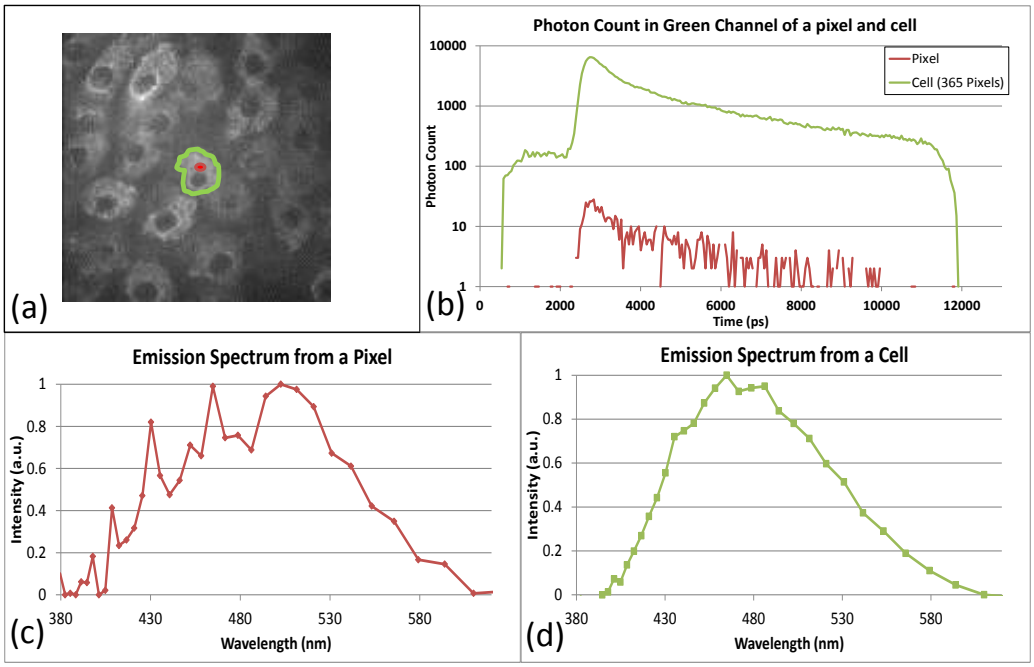

Figure 4.17 (a) A fluorescence intensity image with a pixel (red) and cell (green) highlighted. (b) Plot of the fluorescence decay curves of the pixel and cell shown in (a). (c) The fluorescence emission spectrum from the pixel shown in (a). (d) The fluorescence emission spectrum from the cell shown in (a).

Figure 4.17a shows a single pixel (red) within a cell (outlined in green) in a fluorescence intensity image. Figure 4.17b shows the resulting decays from the single pixel and cell ROI. Figure 4.17c-d demonstrates this same improvement with the emission spectra gained from the spectrometer from the same FOV.

4.10.5 Double Exponential Decay Model

For the fluorescence decay analysis, it was desirable to employ a more complex decay model than a single exponential decay. A double exponential decay model was chosen as it provided a reasonable

fit to the data and allowed information to be gleaned regarding the complex nature of the underlying fluorescence decay, which is considerably more complex. The skin autofluorescence originates from multiple fluorescent species, each of which are themselves likely to exhibit complex decay profiles. For example, free NADH in solution is known to have a double exponential decay and the fluorescence lifetimes of both components can change when they bind to proteins. Furthermore, there are a large number of potential protein binding partners and therefore more than 4 decay components are required for intracellular NADH alone (Vishwasrao, Heikal et al. 2005). Similarly, melanin is known to have at least 3 fluorescence decay components (Teuchner, Freyer et al. 1999).

Given the limited number of detected photons available, only two decay components were chosen to fit to the fluorescence signal from each ROI. Therefore, the short and long fluorescence decay components (τ_1 and τ_2) serve to summarise the changes occurring in a complex biological system exhibiting a multi-exponential decay.

The measured fluorescence decay per ROI for each channel was calculated by spatially summing the photons. This was then fitted to a double exponential model using non-linear least squares minimization (Levenberg-Marquardt method). Software was written in Matlab® by Dr Yuriy Alexandrov. Figure 4.18 illustrates a typical lifetime fitted to a double exponential decay model (the cell ROI signal highlighted in green in figure 4.17a).

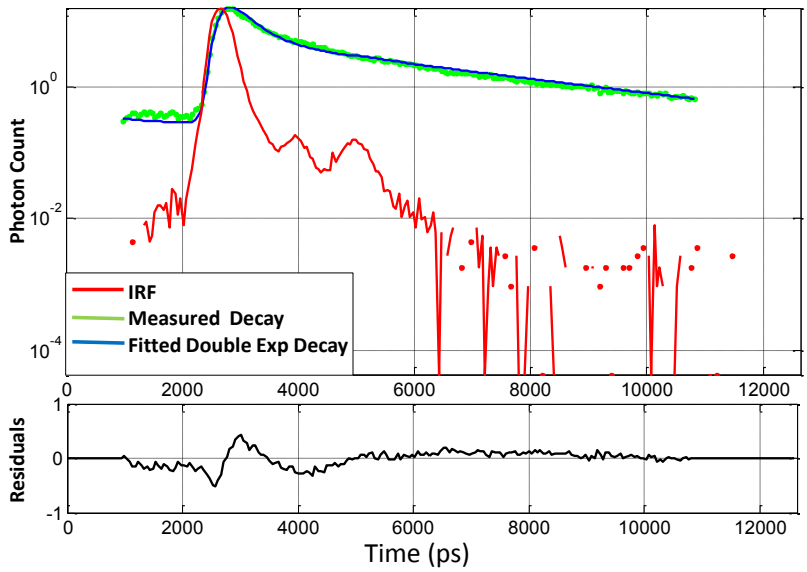

Figure 4.18 Illustration of a fluorescence decay fitted using a double exponential decay model with the residuals of the fit shown below.

The double exponential decay model used is described in Patalay et al. (Patalay, Talbot et al. 2012) and briefly below and was implemented using Matlab®. It accounted for incomplete exponential decays, background noise and detector after-pulsing. It was then convolved with the measured IRF to calculate a predicted fluorescence (Lakowicz 1999;P103), which was then used to fit to the measured data for each time point.

Prior to convolution, the IRF was pre-processed by subtracting the horizontal long-time asymptote or 'pedestal' and normalised to the unit area. The main contributing factors to this pedestal were a small signal-independent contribution from background noise (stray light, electronic noise and cosmic rays) and a much larger signal-dependent contribution from after-pulsing (caused by a delayed response of the PMT to a small fraction of preceding laser pulses) (Becker 2005 ;P233).

$$\chi^2 = \sum_{k=1}^{N_{bins}} \frac{\left[I_{predicted}(t_k) - I_{measured}(t_k)\right]^2}{I_{measured}(t_k)} \qquad \text{Equation 4.1}$$

The 'data-weighted' definition of the fitting error function χ^2 was used as it was found to be less biased when fitting a double exponential decay model, equation 4.1, see also (Lakowicz 1999 ;P119). Here, t_k is the time delay of the k^{th} bin (N_{bins} = 256 for our system), $I_{predicted}$ is the predicted fluorescence and $I_{measured}$ is the recorded fluorescence signal at each time delay. The fluorescence lifetime parameters fitted were τ_1, τ_2, and the f_1 (fractional component of τ_1). f_2 was calculated as 1-f_1. The fitting was implemented using the Matlab® "lsqnonlin" function to find the four fitting parameters $\{I_{tot}, f_1, \tau_1, \tau_2\}_{fitted} = \arg\min[\chi^2]$. Individual decays with fewer than 1000 photons per ROI per channel were discarded.

4.10.6 Fluorescence Decay Quantifiers

The following section lists the parameters that were calculated from the fluorescence decays.

a) The total fluorescence signal was calculated by first correcting for the PMT background and after-pulsing effects, and then calibrating against the signal acquired daily from a reference fluorophore with a known fluorescence emission spectrum (blue fluorescent slide from Chroma Technology Corp., Vermont, USA).
b) The relative fluorescence (RF) in each channel was calculated for each ROI using the total fluorescence (*F*) in each channel using the equation 4.2 below where the relative fluorescence and total fluorescence from each spectral channel in indicated by the subscript letter.

$$RF_b = \frac{F_b}{F_b + F_g + F_y + F_r} \qquad \text{Equation 4.2}$$

c) τ_1 is the short lifetime component. f_1 is the short lifetime component contribution. τ_2 is the long lifetime component. f_2 is the long lifetime component contribution. τ_{mean} is calculated using the equation 4.3 below

$$\tau_{mean} = f_1\tau_1 + (1 - f_1)\tau_1 \qquad \text{Equation 4.3}$$

d) The coefficient of variation (*CV*) was defined as the ratio of standard deviation of ROI pixels' intensities to their mean. In order to exclude the contribution of the Poisson pixel noise to *CV* values, the corrected formula was applied, where Var_{ROI} and E_{ROI} are the estimates of the variance and expectation (average) of the intensity of ROI pixels, respectively. See equation 4.4

$$CV = \left[Var_{ROI}(I) / E_{ROI}(I)^2 - 1 / E_{ROI}(I)\right]^{1/2} \qquad \text{Equation 4.4}$$

4.10.7 Cellular Morphological Quantifiers

Parameter	Description
Perimeter	Perimeter of ROI's boundary (µm)
Major Axis Length	The length of major axis of the effective ellipse (µm)
Minor Axis Length	The length of minor axis of the effective ellipse (µm)
Gyration Radius	A linear measure of distance of a point on the ROI from the centre, an indirect measure of effective linear size (µm)
Area	Area of ROI (μm^2)
Shape Factor	$Perimeter^2/(4\pi Area)$. A measure of how circular an object is (equals 1 for a circle and >1 for any other figure)
Solidity	Ratio of cell area to the area of a convex hull. A measure of negative curvature. Equals maximum of 1 for a shape with no concave parts e.g. a circle or square
Flattening Factor	Ratio of minor to major axis. A measure of flatness.

Table 4.4 Description of the cellular morphological quantifiers that were measured and calculated for the analysis.

The cellular morphology quantifiers were based on cell ROI geometry and are defined in table 4.4 above. A standard Matlab® morphometry routine "regionprops" was applied to obtain several geometric features such as Solidity and Major and Minor Axis Lengths. The dimensional geometric

parameters (e.g. area and distance measured in microns) were calculated taking into account image magnification.

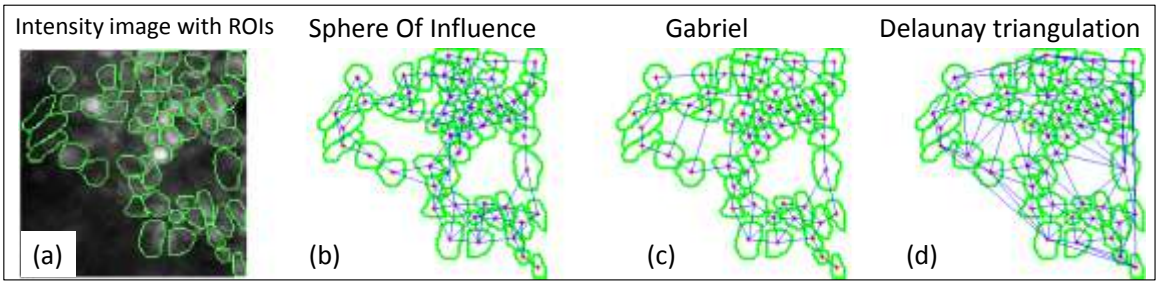

Figure 4.19 (a) Fluorescence Intensity image with ROI overlaid. (b-d) Adjacency graphs generated using 3 methods to define the nearest neighbour ROIs.

Another group of morphology features was designed to study properties of groups of neighbouring cells. These methods first define local neighbourhood relations via adjacency graphs in the image between a 'central' cell and its neighbouring cells. The Delaunay triangulation, Gabriel and Sphere of Influence (SOI) graphs (Bivand, Pebesma et al. 2008;P245) were constructed for this purpose for each field of view, see figure 4.19 .

Parameter	**Description**
Cell Density	The effective number of ROIs per μm^2
Cell Confluency	Relative area occupied in the image by a ROI and its neighbouring ROIs. Indirect measure of the area of cytoplasm present and therefore scales inversely with the amount of extracellular matrix present.
Orientation SD	Standard deviation of the angle of the major axis of a ROI and its neighbouring ROIs (degrees)
Number of Neighbours	The number of neighbouring ROIs
Distance to Neighbours	The average distance to a neighbouring ROI (µm)

Table 4.5 Description of the descriptors used to evaluate the density and relationship of ROIs/cell between each other.

The morphological features used to quantify the relationship of each cell with its neighbours are listed in table 4.5. Every cell was characterised (for every adjacency graph) by its number of

neighbours (n_{nb}) and average distance to the neighbour(d_{nb}). The local cell density and the cell confluency were estimated using the area of the effective influence circle as defined below in equation 4.5 where d_{nb} is the distance to neighbour.

$$A_{inf} = \pi {d_{nb}}^2 \qquad \text{Equation 4.5}$$

The cell density, defined below in equation 4.6 and is calculated using the number of neighbouring cells to a central cell and the area of influence, where A_{inf} is the effective influence circle and n_{nb} is the average number of nearest neighbours. It is independent of cell size.

$$Cell\ Density = \frac{1+\sum_{k=1}^{n_{nb}} \frac{1}{n_{nb(k)}}}{A_{\inf}} \qquad \text{Equation 4.6}$$

The calculation for cell confluency (equation 4.7) uses the area of a central cell ($Area_{cell}$) as a reference and calculates the ratio of average cell area of the neighbouring cells to the area of 'formal free space' for this cell, where A_{inf} is the effective influence circle and n_{nb} is the average number of nearest neighbours.

$$Cell\ Confluency = \frac{\frac{1}{n_{nb}+1}\left(\sum_{k=1}^{n_{nb}} Area_{(k)} + Area_{cell}\right)}{A_{inf}} \qquad \text{Equation 4.7}$$

Therefore, if cells have the same geometrical position but are larger in size, this ratio will be bigger, whereas cell density will not.

4.10.8 Automatic Segmentation

Manual segmentation of images was very time consuming for the number of images acquired. Therefore an algorithm to automatically segment images into ROIs was attempted. Automatic image segmentation was performed using size-tuned non-linear top-hat detection which has been previously used by Santos et al. (Santos, Zaltsman et al. 2008). This method applied a pixel-wise transformation to the image (formula A2.1 in Santos et al.) that enhanced the brightness of a pixel if its close vicinity was also bright and its distant vicinity was dim. A user defined threshold was then applied to the transformed image. The resulting binary images were then morphologically smoothed using the Matlab® 'imopen' function and spatially distinct regions identified. These regions were then size-sieved using standard Matlab® image processing functions to remove objects smaller than 35 μm^2. The same procedure, including all parameters, was applied uniformly across all images.

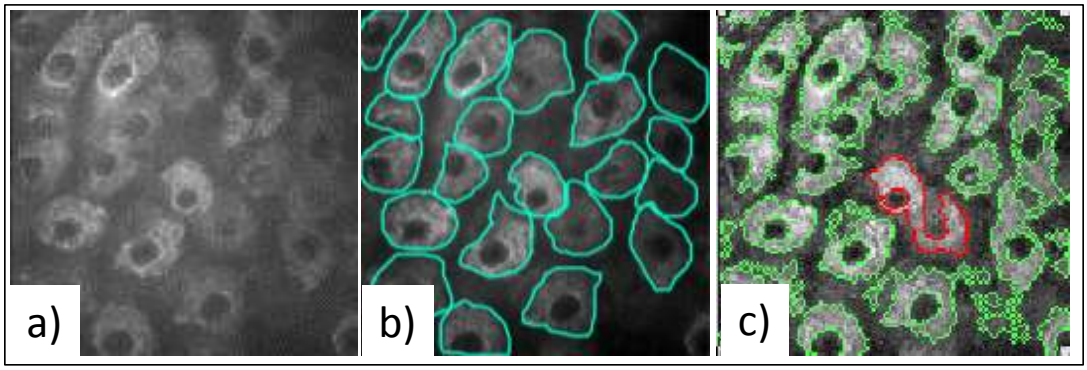

Figure 4.20 (a) Fluorescence Intensity Image and (b) Intensity image shown in (a) with manually segmented ROIs overlaid. (c) Intensity image with automatically segmented ROIs overlaid.

The automated approach was used to segment the images used for the analysis of normal skin to follow the changes in lifetime over time post excision, described in Chapter 5 (pp115). The application of the automatic ROI segmentation greatly reduced input from the user but was not found to be as accurate as defining individual cells as the manually defined ROIs, typically generating many more ROIs. This can be appreciated in figure 4.20c. As this analysis focused on the average changes in the lifetimes of cells over the whole FOV, the difference in the manual and automated segmentation was not important as long as each was internally consistent between images.

4.10.9 Statistics

The data within most summary tables were compiled using SPSS 18 (SPSS Inc. IL, USA).All the spectroscopic, lifetime and morphological parameters and the statistical calculations were performed by Dr Yuiry Alexandrov. The Wilcoxon Rank Sum test (Lupton 1993;P119-28) was applied to study the difference in distribution and their significance between BCC and normal skin or between pigmented lesions groups.

The discriminative ability of the individual spectroscopic and morphological ROI measurements were assessed using 2 parameters which were implemented using Matlab®

- Receiver Operator Characteristic Area Under the Curve (AUC,(Mathews 2010;P158)) which measures the probability that the source diagnosis of the cell/ROIs would be correctly identified.
- Cohen's d statistic (Gravetter and Wallnau 2009;P262) measures the difference between the means of two populations e.g. normal skin and BCC ROIs and is a marker for the discrimination between them.

To determine discrimination using multiple parameters, linear discriminant analysis (LDA) was performed. To reduce the dimensionality of the data, which included spectroscopic +/- cellular

morphology parameters, a correlation-matrix based principal component analysis (PCA) was performed first (Joliffe 2002;P24). The initial 4 principal components were then selected to be used in the LDA. To perform this, the Matlab® functions "cov" was used to get a covariation matrix. This was transformed into a correlation matrix before the Matlab® function "pcacov" was used to calculate PCA coefficients. The Matlab® function "classify" was then used to perform LDA for each ROI using a leave one out approach, to classify which diagnostic group it arose from e.g. either BCC or normal skin, or naevi or melanoma. Initially each patient was characterised by the fraction of malignant and Normal ROIs determined by LDA. These fractions could then be used to build ROC curves from which AUC could be calculated and sensitivities and specificities for a given diagnostic threshold to diagnose a patient correctly could be generated.

This process was applied using manually segmented ROIs, automatically segmented ROIs and for unsegmented images. Cellular morphological parameters were removed from the PCA when using automatically segmented images, due to its lack of accuracy defining individual cells, and for unsegmented images. Unsegmented images were analysed by first spatially integrating the fluorescence decay profiles over each field of view, fitting the resulting decays and then calculating the mean spectroscopic parameters for each patient.

Sensitivity and specificity were also calculated for the visual assessment of morphological features present in the FLIM images. For the example of BCC vs normal skin, the sensitivity was calculated as the number of patients correctly determined to have a BCC using a given threshold number of diagnostic features divided by the total number of patients with BCCs. The sensitivity was calculated as the number patients correctly determined not to have a BCC using this threshold divided by the total number of patients without BCCs.

4.11 Summary

This chapter has described the methods, instrumentation and the analytical techniques used to obtain the results discussed in this thesis.

In Section 4.2 the criteria for patient recruitment and the minimum data set collected from each is first described. This is followed by the details of the ethics approvals that were gained in order to perform this research.

Sections 4.4 – 4.5 describe the technical details of the original DermaInspect® and the modifications made over time to allow collection of FLIM in 4 spectral channels and of hyperspectral images.

Section 4.6 outlines the procedure used to prepare the skin (both *in vivo* and *ex vivo*) prior to imaging and the imaging protocol for acquiring FLIM and hyperspectral images.

A discussion can then be found of the methods used to process the tissue histologically to improve the co-registration of FLIM images with the dermatoscopic and histological images in section 4.7 and 4.8. The final section regarding methods (Section 4.9) outlines the characteristics of the DermInspect® and our clinical experiences using the device.

Finally the methods of analysis of the collected fluorescence and fluorescence lifetimes are discussed in section 4.10.

Chapter 5. An analysis of the effect of surgical excision on tissue autofluorescence of normal skin.

5.1 Aim

In this chapter, the changes in tissue autofluorescence and lifetime are monitored over a 3 hour time period after excision. This is the first time this has been performed using multispectral FLIM and the first time over this time period using human skin. The lifetimes from cells acquired *in vivo* vs. *ex vivo* are then compared directly.

5.2 Introduction

Multiphoton tomography (MPT) intensity imaging and multispectral MPT FLIM has been used to investigate changes in normal and cancerous skin, both *in vivo* and *ex vivo*. In many cases investigating skin *in vivo* is not possible for ethical reasons or practical concerns, e.g. motion artefacts and difficulty imaging highly curved surfaces. In these circumstances the use of excised, unfixed *ex vivo* skin is a necessary surrogate for *in vivo* imaging.

As soon as skin is excised, it is removed from its homeostatic environment. Hypoxia and hypercapnia start to occur immediately which affect the metabolism of the cells in the tissue sample, ultimately leading to cell death. The rate at which these changes affect intracellular metabolism (and therefore autofluorescence) is dependent on many factors, including cell type and origin and whether normal or malignant tissue is used.

The published studies performed using unfixed, excised skin have varied in the length of time post-excision imaging was performed. Some studies had imaging protocols extending from 3 to 6 hours post excision (Cicchi, Sestini et al. 2008; Ericson, Simonsson et al. 2008; Paoli, Smedh et al. 2008; De Giorgi, Massi et al. 2009), whilst other had no times reported (König and Riemann 2003; Dimitrow, Riemann et al. 2009; Dimitrow, Ziemer et al. 2009).

In this study, freshly excised normal human skin samples were taken and the changes seen in autofluorescence and lifetime were measured regularly up to 3 hours post excision. A further comparison was then made between normal skin *in vivo* and *ex vivo*.

5.2.1 Previous Literature

Two studies have been published to date to evaluate the changes in autofluorescence following ischaemia/excision of the skin. Sanchez et al. studied the changes in autofluorescence intensity and lifetimes of human skin daily over a 7 day time period (Sanchez, Prow et al. 2010). Palero et al.

investigated the changes in autofluorescence emission spectra emitted from mouse skin both *in vivo* and post euthanasia over a 3.3 hour time period (Palero, Bader et al. 2011). These studies will be described in detail below.

5.2.1.1 Sanchez et al. 2010

Following surgical excision, Sanchez et al. monitored the effect of ischaemic necrosis over time on tissue autofluorescence when incubated with/without culture medium and at different temperatures (-20 ^{o}C, 4 ^{o}C , 37 ^{o}C and room temperature) daily for 7 days. Up to 3 samples of human abdominal skin were tested in each environment and an *in vivo* control image was also acquired from the forearm of one volunteer. Tissue was excited using 740 nm at 25 mW and images of 52 x 52 µm in size were collected over 13.6 s. The *s.spinosum* was imaged using cellular morphology to assess when the correct depth of imaging was attained. Band pass filters were used to selectively collect autofluorescence from NAD(P)H (350-450 nm), keratin (450-515 nm) and FAD (515-620 nm).

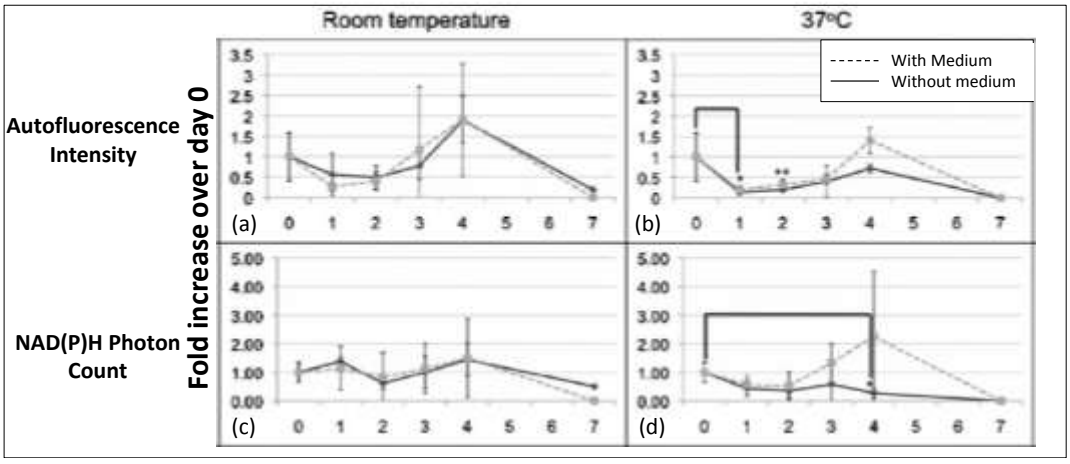

Figure 5.1 Change in autofluorescence of *ex vivo* human skin with time over 7 days relative to baseline. Total mean fluorescence intensity (350-620 nm) (a) at room temperature and (b) at 37^{o}C. Mean photon count from the NAD(P)H spectral channel (350-450 nm) (c) at room temperature and (d) at 37^{o}C. Key: Solid line – without culture medium. Dotted line - with culture medium. Reproduced from Sanchez et al. (Sanchez, Prow et al. 2010).

They found that without culture medium and storage at room temperature, tissue autofluorescence could still be detected after 7 days duration. The presence of culture medium accelerated changes in autofluorescence intensity seen over time, whilst reducing the temperature slowed them. The autofluorescence intensity for each day was calculated by averaging the photon counts for each image in the 3 samples and normalising by the image taken at day 0 from the excised skin. See figure 5.1 reproduced from the paper. Over the first 24 hours, when the tissue was incubated without culture medium (solid black line), the total autofluorescence intensity reduced to ~50% at room temperature (panel a) but to less than 25% at 37 ^{o}C (panel b). This drop in intensity plateaued over

the ensuing 24 hours and ultimately increased to 200% of its initial intensity on day 4 at room temperature. Although the same trend was seen at 37 ^{o}C, the intensity only recovered to 50% of its initial value.

Without medium, the NAD(P)H channel showed a slight increase in its fluorescence intensity after 24 hours at room temperature (panel c), and fluctuating around the baseline intensity over the remaining 6 days. At 37^{o}C (panel d), the same drop in intensity over time as that seen with total intensity (panel b) was found.

Fluorescence lifetimes for NAD(P)H were calculated for each pixel using a double exponential model using SPCImage (Becker & Hickl, GmbH). Some *ex vivo* samples showed a new lifetime peak at ~ 800 ps in τ_1 at day 0 in addition to the previously seen peak at ~400 ps seen *in vivo*. τ_2 showed a broadening of the peak at ~2500 ps seen *in vivo* following excision. τ_{mean} showed a progressive increase from ~1000 ps to 2000 ps with time whilst autofluorescence was still present over the 7 days period. No information was included in the paper of the time post-excision the images taken on day 0.

5.2.1.2 Palero et al. 2011

Palero et al. looked at NAD(P)H autofluorescence in the epidermis of mouse skin over 3.3 hours (Palero, Bader et al. 2011). They used MPT but recorded spectrally resolved fluorescence images, without lifetime information. The abdomens of two mice were imaged *in vivo* whilst anaesthetised. The changes following euthanasia of the mouse was monitored every 3 minutes for 3.3 hours whilst the animal was on a temperature-controlled stage. The epidermis was illuminated using an excitation wavelength of 765 nm and power of 5 mW. Images of 224 x 224 pixels covering 100 µm x 100 µm were acquired over a 2 minute period. The spectral resolution was 0.5 nm over 350 – 600 nm range i.e. sufficient to detect the small shift in the peak spectral emission between protein bound (445 nm) and free (460 nm) NAD(P)H, despite their large spectral overlap. Spectral changes were examined over a fixed area within the image sets covering approximately 25 cells from the *s.spinosum*. A spectral shift in the peak fluorescence emission wavelength was detected with time. An *in vivo* spectral peak of 456 nm seen at t= -29 minutes moved to 450 nm after 20 minutes, 455 nm at 80 minutes and 460 nm at 150 minutes. This suggested a shift from protein-bound to free NAD(P)H with time.

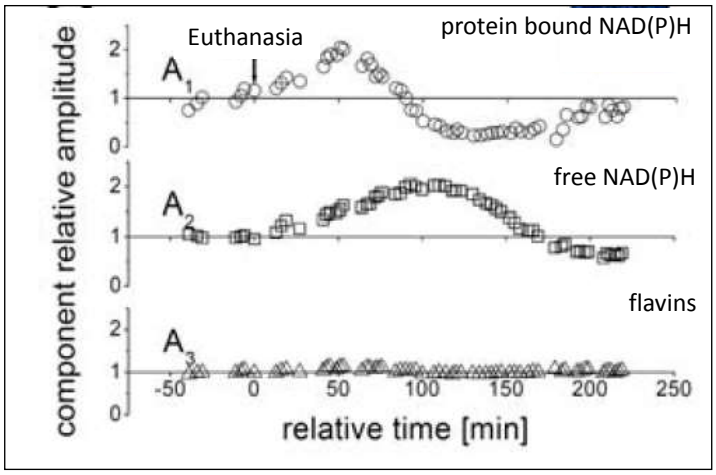

Figure 5.2 The change in relative amplitude of the fluorescence from a sample of mouse skin over time pre/post euthanasia. Key: A_1 -protein bound NAD(P)H component, A_2 - free NAD(P)H component, A_3 - flavins (in the figure). Reproduced from Palero et al. (Palero, Bader et al. 2011).

The total fluorescence intensity was seen to increase initially in all wavelengths, peaking at 80 mins (x1.7 fold). It then fell to below the initial intensity after 110 mins. Linear spectral unmixing was performed using 3 spectral components to estimate the changes in protein-bound peak (fixed at 448 nm), free NAD(P)H peak (fixed at 459 nm) and flavins peak (fixed at 528 nm), see figure 5.2. A good fit was obtained using this method and showed that flavins (A_3 in the figure) had the smallest contribution to the emission spectra of ~5% which remained unchanging over time. They found a doubling (x113%) in the amplitude of protein bound NAD(P)H component (A_1 in the figure) at 50 mins, which returned to baseline at 100 mins and remained reduced for the duration of the experiment (~70%). The free NAD(P)H component (A_2 in the figure) also increased with a broad peak at ~100mins (85%) which fell slowly to 25% of baseline amplitude. The greatest change in the free/bound NAD(P)H ratio was seen at ~50 mins.

5.3 Method

5.3.1 Instrumentation

Lifetime resolved imaging was performed using the instrument previously been described in Chapter 4.4. FLIM images were acquired by four emission spectral channels defined as blue (360-425 nm), green (425-515 nm), yellow (515-620 nm) and red (620- 655nm). All images were acquired at 760 nm excitation wavelength.

5.3.2 Tissue samples

Figure 5.3 An exemplar tissue sample used in our study (ID 4210). (a) Image of BCC *in vivo*. (b) Image of lesion excised. (c) Image following removal of peri-lesional normal skin prior to imaging.

Patients attending the Dermatology Department, Imperial College Healthcare NHS Trust, having suspected skin cancers requiring excision, consented to have their tissue imaged. Larger lesions with sufficient peri-lesional normal skin for imaging were selected for this study. 5 skin samples were collected, with a typical example presented in figure 5.3. Once excised, the peri-lesional normal skin was separated and prepared for imaging as previously outlined in Chapter 4.6.1 (pp95). Briefly, it was rinsed and moistened using HBSS and mounted on damp gauze in an inverted plastic petri dish containing an embedded cover slip. A field of view (FOV) centrally within the sample without obvious superficial blemishes was then selected for imaging. All imaging was conducted at room temperature.

5.3.3 Imaging protocol

Once the tissue was in focus, the *s.spinosum* layer of the epidermis was identified visually by cellular morphology and used for imaging in all samples. This layer is the thickest in the epidermis and therefore easiest to remain within in spite of the large degree of tissue movement that occurred in some samples during imaging. Images were acquired and saved as outlined previously in Chapter 4.6.2 (pp97). Initially, the excitation power was optimised in a plane of focus within 5 μm away from that used for imaging, to minimise possible photobleaching/ phototoxicity. Once the imaging plane of focus was selected, the excitation power was fixed throughout each experiment. Images were acquired over 25.5 seconds using excitation powers between 4-10 mW. All images had a field of view of 107 x 107 μm^2 and were taken with a resolution of 256x256 pixels with pixel size of 0.42 μm (FIFO images, zoom=800). Images were acquired until 3 hours post time of excision.

The time of excision was noted to the closest minute. Thereafter the time was recorded to the second using the PC clock on the DermaInspect®. The time post excision of each image taken was extracted from the save time of the FLIM image file. This save time included a delay of less than a minute between completion of image acquisition and the time stamp given to the saved file. This

time delay consisted of manually removing the shielding of the PC computer screen, activating the automated save macro following the emitted 'end of imaging' audible warning and a relatively fixed delay for the PC to save the 128 Megabyte image. The total delay was in the range of 30-60 seconds. This delay however was short compared to the time scale of the experiment.

When this imaging method was trialled, it was found that the tissue relaxed and moved away from the objective and therefore down in relation to the fixed depth of view of the microscope. This movement was most pronounced initially but continued to occur over the whole imaging period. To maintain a static FOV for the experiment, the depth of focus was adjusted as follows.

As a reference, the first FLIM image acquired was left on screen, adjacent to the imaging acquisition window on the DermaInspect® PC desktop. This reference image was compared by eye to every subsequent image taken to ensure the FOV remained static. During period of large tissue movement, typically within the initial hour, frames of 2.5 seconds were viewed (with no change to the excitation power) to confirm no change occurred from the reference FOV and adjust the FOV depth if necessary. Scans of 2.5 seconds were used for this purpose to minimising possible photobleaching effects to the tissue, before acquiring the actual FLIM image over 25.5 seconds. If the FOV of the reference image could not be found due to excessive movement, another reference image was taken and used for successive image acquisitions.

5.3.4 Image analysis

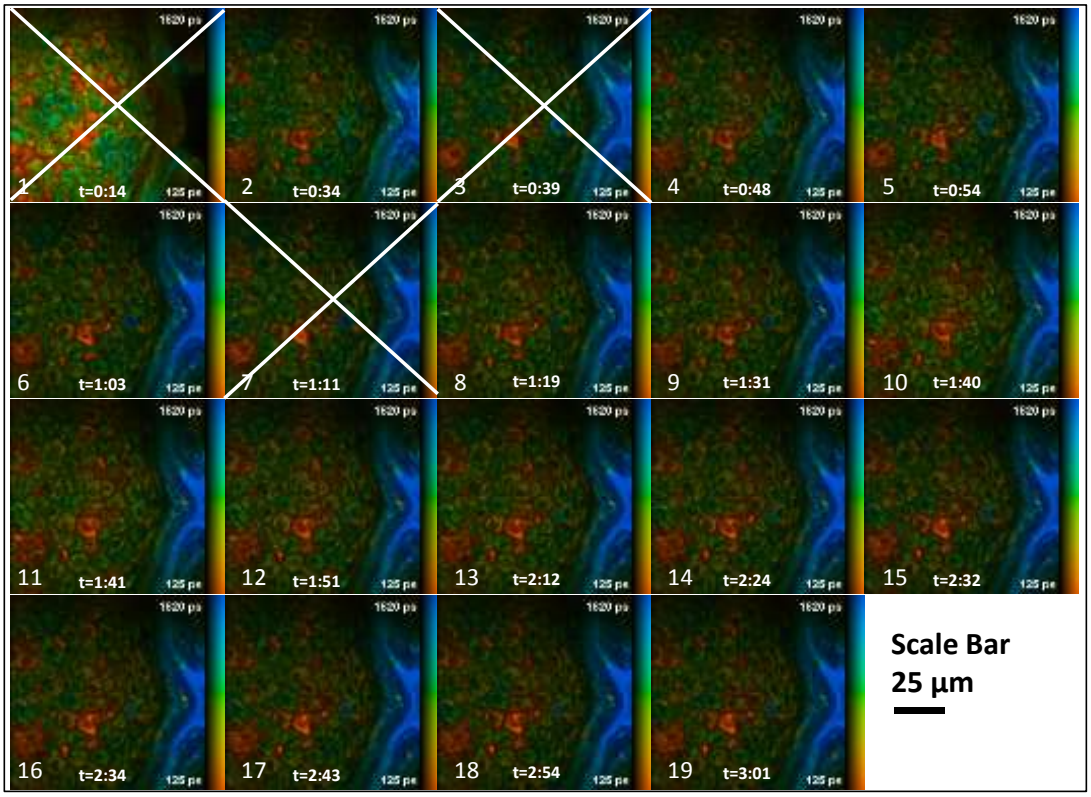

Figure 5.4. A series of sequentially taken FLIM images from sample 4210 taken in the yellow channel, numbered in the bottom left corner of each image. FLIM images 1,3,7 were discarded due to changes in FOV compared to the remaining images. The FLIM scale bar is shown on the right of each image. The image acquisition time given in min:seconds is shown centrally under each image.

FLIM images were generated, fitting each pixel with a single exponential decay model, as described in Chapter 4.10.3 (pp104). This allowed images with a difference in their FOV, not identified during image acquisition, to be discarded. An exemplar set of acquired images including those discarded from further analysis is presented in figure 5.4.

Due to the large number of images acquired and the variability of manually defining the same region of interests (ROIs) over a series of near identical images, an automated image segmentation algorithm was used. The segmentation was based on multiscale nonlinear local thresholding (Santos, Zaltsman et al. 2008) and is described further in Chapter 4.10.8 (pp111) and illustrated for a number of sequentially acquired images in figure 5.5. The fluorescence lifetimes parameters (τ_1, τ_2, f_1, τ_{mean}) of each ROI in the images were then fitted using a double exponential decay model as described in Chapter 4.10.5 (pp106).

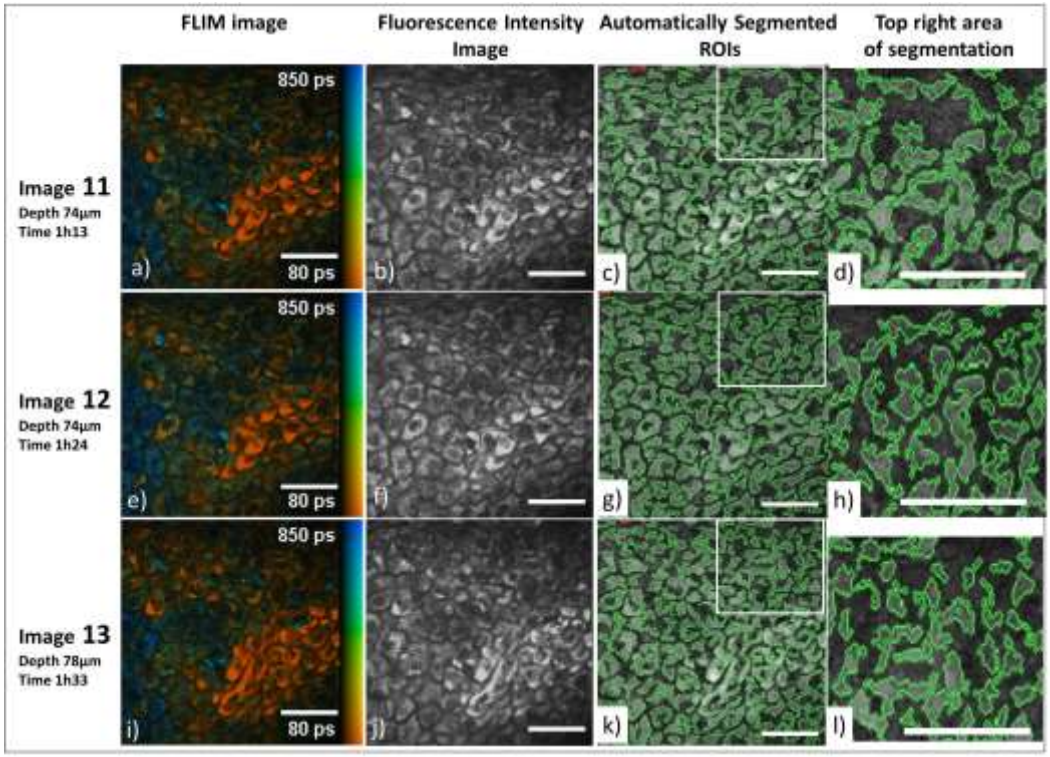

Figure 5.5 Set of sequentially acquired images (ID 11, 12, 13) taken in the yellow channel from sample 4117. 1st column (a,e,i) - FLIM images with lifetime scale bar on the right of each panel. 2nd column (b,f,j) – fluorescence intensity images. 3rd column (c, g,k) – automatically segmented ROIs overlaid on each intensity image. 4th column (g,h,l) – close up of top left hand corner of images of automatically segmented ROIs. Images 107 µm x 107 µm, 256x256 pixels. Scale Bar 25 µm.

In order to monitor the changes in lifetime between images, the average ROI lifetime parameters were calculated for each image.

5.4 Results

Tissue		Patient Details				Time (seconds)			
Sample	Lesional Diagnosis	Body Site	Sex	Age	Skin Type	Initial Image	1st Analysed Image	Last Analysed Image	Images Analysed
4117	Seborrhoeic Keratosis	Back	m	69	2	994	1354	9950	15
4120	Melanoma	Back	m	32	3	1356	2428	10208	14
4121	Seborrhoeic Keratosis	Lower Leg	m	75	2	1084	1434	10264	20
4122	BCC	Face	m	46	3	688	792	10068	18
4210	BCC	Back	m	50	3	868	2075	10881	16

Table 5.1 Details of the 5 tissue samples and imaging parameters used in the study.

The origin of the 5 tissue samples and imaging timings are shown in table 5.1. Although all samples originated from males, they varied in age (range 32-75 years), body site and lesional diagnosis.

The time taken to prepare tissue for imaging prevented immediate assessment following excision. The first image was taken an average of 16:38 minutes (range 11:28 - 22:36) after excision. Once prepared however, tissue movement prevented tracking a stable FOV until an average of 26:56 minutes (range 13:12 – 40:28) after excision. Once tracked, the average movement of this FOV was of 20 µm (range 5 – 33 µm) over the remaining imaging time. The tissue movement before this time was greater but could not be recorded.

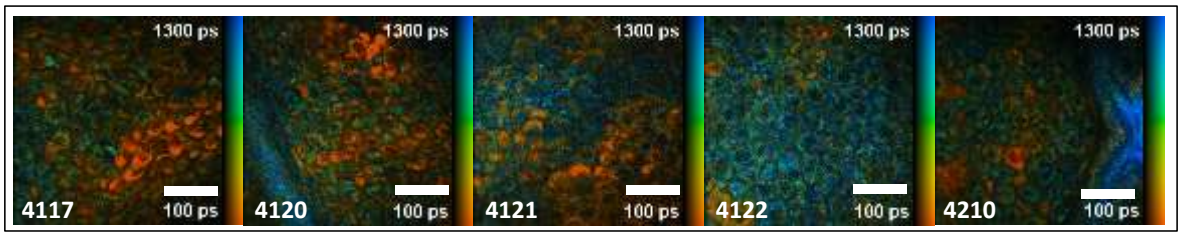

Figure 5.6. FLIM images of the *stratum spinosum* taken from each sample in the study (sample number labelled in the left lower corner) taken from the yellow spectral. Images 107 µm x 107 µm, 256x256 pixels channel. Lifetime scale bar shown to the right of each panel. Scale Bar 25 µm.

Exemplar FLIM images of the *s.spinosum* taken from each sample are illustrated in figure 5.6. Although the cells shown in this figure appear to have similar morphology, the FLIM images show that their melanin content varies between samples, indicated by its short fluorescence lifetime. No reduction in the signal to noise ratio was noticed in the images over time to suggest loss of cell

integrity and leakage of intracellular fluorophores into the extracellular space. This was assessed by visually assessing the images over time but was not quantitatively assessed.

5.4.1 Fluorescence Intensity

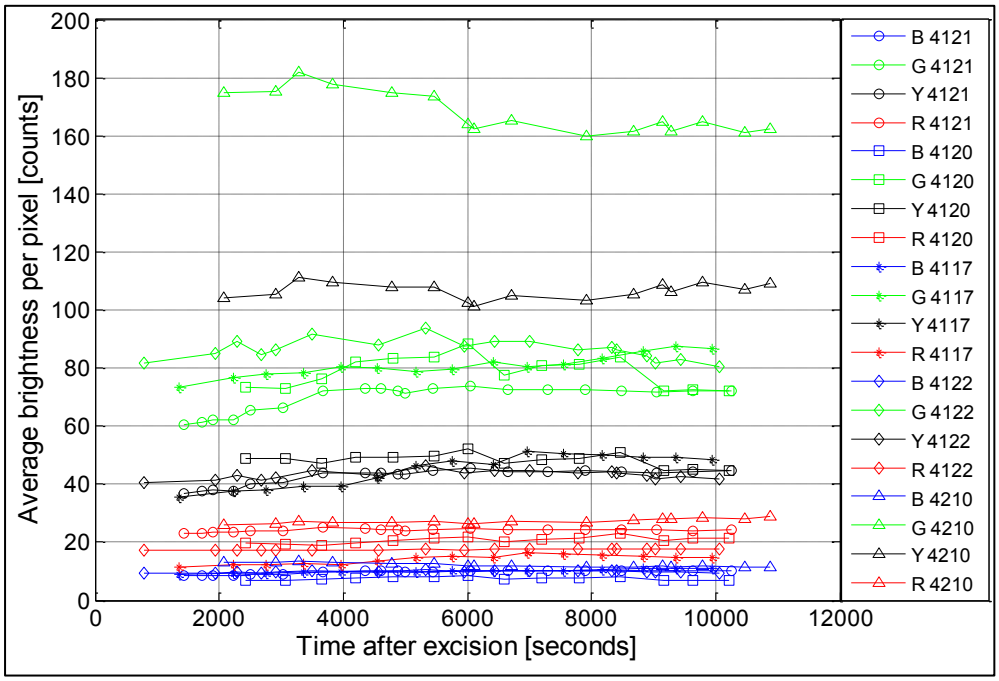

Figure 5.7 Change in average pixel brightness per image over time for each sample and spectral channel.

The mean pixel brightness was calculated for each time-point imaged by taking the sum of (time-integrated) counts over ROI pixels and dividing by the total number of ROI pixels. Only ROIs for which fluorescence lifetimes were fitted in all 4 channels, were considered. This is plotted for each spectral channel and sample in figure 5.7. The percentage change in the mean pixel brightness over all samples between the first and last image analysed were 106%, 105%, 112% and 112% for the blue, green, yellow and red spectral channels respectively. This indicates that no significant photobleaching was seen.

5.4.2 Fluorescence Lifetime

	Emission Spectral Channel			
Lifetimes	**Blue**	**Green**	**Yellow**	**Red**
τ1 (ps)	120	347	199	160
τ2 (ps)	4040	3610	2677	2928
f1	0.39	0.38	0.45	0.57
τ mean (ps)	2460	2366	1563	1343

Table 5.2 shows the average τ_1, τ_2, f_1 and τ_{mean} over all ROIs and images, by the emission spectral channel.

Table 5.2 summarises τ_1, τ_2, f_1 and τ_{mean} for all ROIs over all images by emission spectral channel. It shows that the lifetime parameters for ROIs are similar in the yellow and red spectral channels in comparison to the blue and green channels. A trend for the f_1 to increase and τ_{mean} to decrease with emission wavelength is also seen.

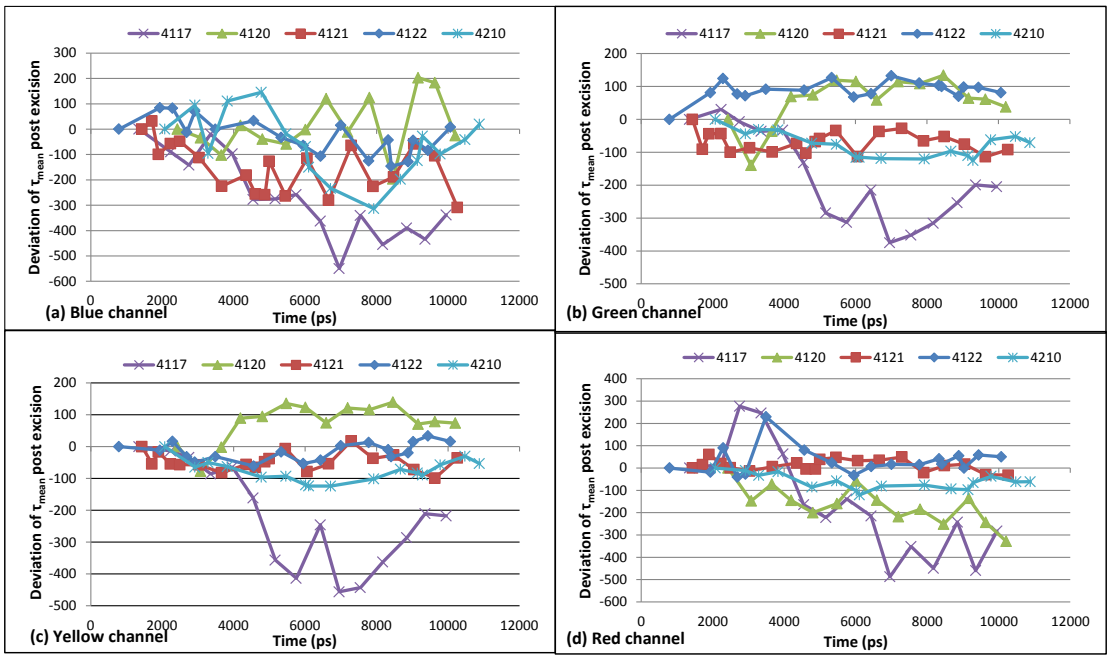

Figure 5.8 The average change in lifetime for all ROIs in each image from baseline over time, for each sample. (a) Blue channel (b) Green channel (c) Yellow channel (d) Red channel.

The deviation of τ_{mean} from baseline over time, for each sample and spectral channel is plotted in figure 5.8. On visual examination, although there are changes in lifetime over time seen, no clear trends could be identified.

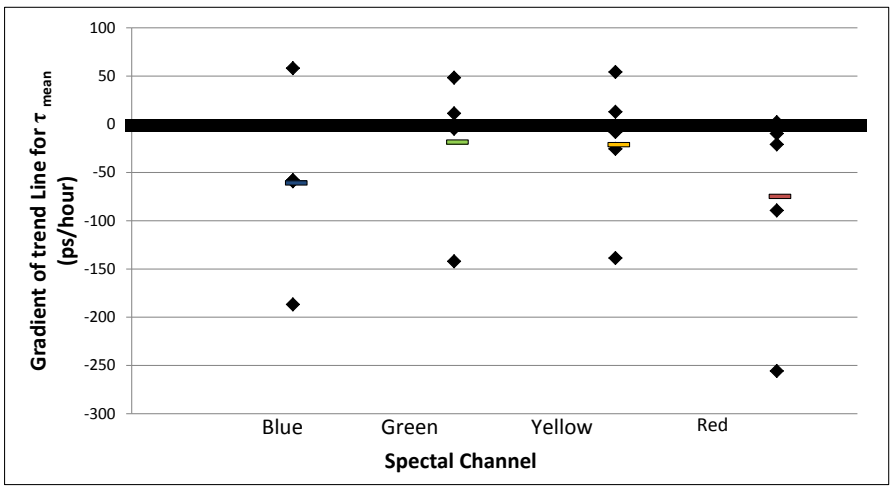

Figure 5.9 Dot Plot of average reduction in lifetime over time for each sample (diamonds) with the mean lifetime reduction per channel highlighted (dashes).

To evaluate the τ_{mean} over time further, linear regression was used to fit a trend line for each sample for each spectral channel. The slope calculated for each sample has been plotted in figure 5.9. It shows an average drop of 61, 18, 21 and 75 ps/hour in the blue, green, yellow and red spectral channels respectively over all samples. This small but consistent change in all spectral channels represents a 5.6%, 1.7%, 3.2% and 8.0% reduction in τ_{mean} from the baseline over the time period investigated. A summary of the variation in τ_{mean} for each spectral channel and the percentage change in lifetime broken down by sample and spectral channel is shown in table 5.3.

	Emission Spectral Channel			
	Blue	Green	Yellow	Red
Variation in mean lifetime from start(ps)	8 - 338	16 -218	38 - 205	32 - 283
Sample 4117 (% change)	-13.4	-9.0	-13.4	-13.0
Sample 4120 (% change)	-0.8	3.4	2.7	-22.6
Sample 4121 (% change)	-14.8	-1.5	-5.4	-2.8
Sample 4122 (% change)	0.3	0.6	4.6	4.2
Sample 4210 (% change)	0.7	-2.2	-4.5	-5.7
Mean % change from start	-5.6	-1.7	-3.2	-8.0

Table 5.3 Summary of the variation in τ_{mean} and percentage change in lifetime over time for each sample and spectral channel.

Table 5.3 shows that the percentage change in lifetime varies between 1.7-8.0% from the start of the experiment. However the variation in lifetime over this period is greater. This can be seen in the graphs shown in figure 5.8 that track the average lifetimes per FOV in each spectral channel over time and by the data in the first row of table 5.3. In an attempt to put this variation in context to the normal variation in lifetimes found in the skin, we calculated the variation in τ_{mean} between cells from images taken from the *s.spinosum* layer of the skin on a per FOV basis. This allowed the data to reflect intrapatient variation in the lifetimes of cells in this skin layer and exclude the variations caused by imaging different body sites and an interpatient comparison. Therefore ranges of τ_{mean} for all the cells imaged from the *s.spinosum* layer in normal skin on a FOV basis (and therefore patient) were calculated by subtracting the cellular τ_{mean} at 25^{th} from the 75^{th} percentile. The spread of ranges from all these FOVs are listed in Table 5.4 for each spectral channel. The results shown in this table indicates that the maximum variation in lifetime seen following excision of the skin (see row 1 in table 5.3) is close to the minimum intracellular variation in lifetime seen in this skin layer for normal skin.

Spectral Channel	FOVs	Minimum Lifetime Range (ps)	Maximum Lifetime Range (ps)
Blue	33	159	817
Green	33	105	779
Yellow	33	197	1651
Red	31	84	5171

Table 5.4 The range in τ_{mean} between cells found in the *s.spinosum* of normal skin. Calculated as the difference between the 75th and 25th percentile on a per FOV basis.

It has been previous described in Chapter 2.6.5 (pp58), that intracellular fluorescence from NAD(P)H is expected to dominate in the spectral range defined by the green spectral channel. Changes in free and protein bound NAD(P)H reflect changes in intracellular metabolism and are thought to be described by τ_1 and τ_2 respectively in this spectral range (Vishwasrao, Heikal et al. 2005).Table 5.3 has already shown that the change in τ_{mean} over all samples averaged 1.7% over time in the green channel, suggesting that there may not be a large change in τ_1, τ_2 or f_1. In order to investigate if this is the case τ_1, τ_2 and f_1 from the green channel are plotted in figure 5.10. This graph shows an average of -0.80%, +0.60% and +4.80% change in τ_1, τ_2 and f_1 respectively between the first and last plotted values. Therefore, as suggested by no significant change in τ_{mean}, no significant changes over time for any of these lifetime parameters was seen in the green channel.

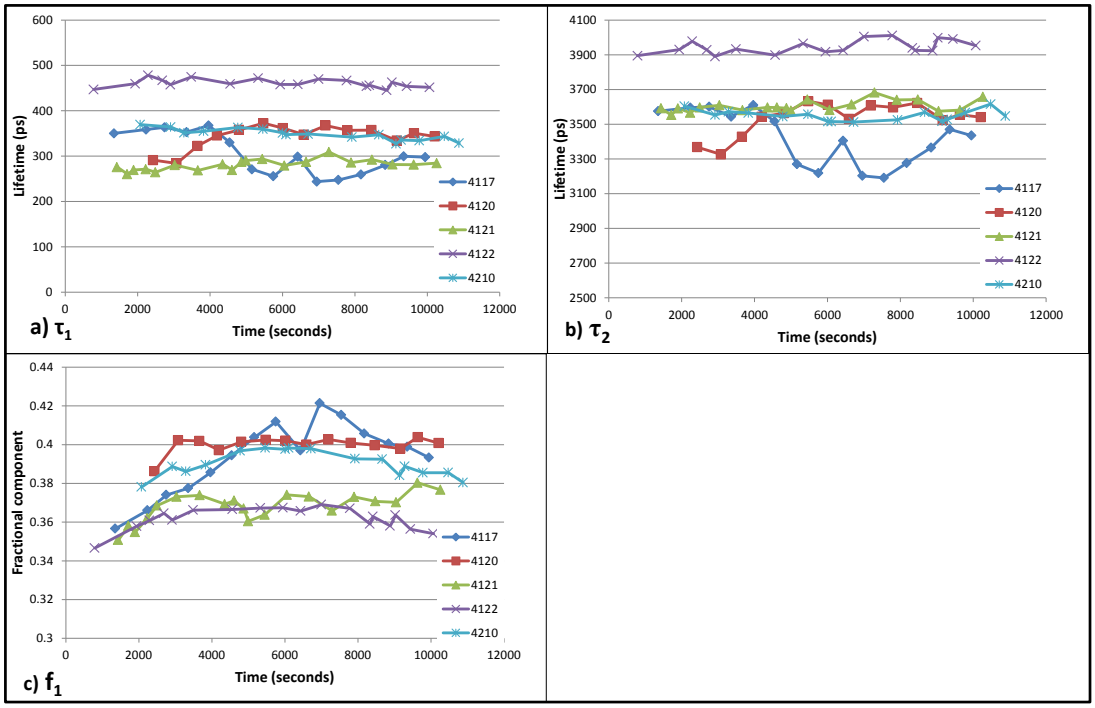

Figure 5.10 Graphs showing the change in ROI average fluorescence lifetime with time for the green spectral channel representing NAD(P)H fluorescence, illustrated per sample. (a) τ_1 (b) τ_2 (c) f_1.

5.4.3 Lifetimes *in vivo* vs *ex vivo*

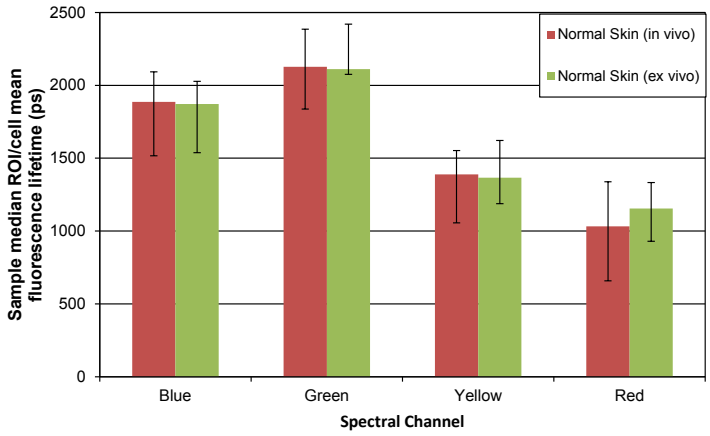

Figure 5.11 The difference in median τ_{mean} per sample per spectral channel for images acquired *ex vivo* and *in vivo*. Error bars show 25th and 75th percentiles.

Finally the median τ_{mean} from cells from normal skin are compared in images acquired *ex vivo* (n=8) and *in vivo* (n=19). The median τ_{mean} was recalculated per sample (not per cell) in an attempt to remove bias in the calculations from some samples having more cells than others. The median τ_{mean} for the samples were found to be 1886, 2127, 1389 and 1033 ps in the blue, green, yellow and red spectral channels respectively for samples imaged *in vivo*, see figure 5.11 The *ex vivo* samples were found to have a % difference in median τ_{mean} of -0.73%, -0.75%,-1.68% and +11.9% in the blue, green, yellow and red spectral channels respectively. This difference between *ex vivo* and *in vivo* measurements was not found to be statistically significant using the Wilcoxon rank sum test (p = 0.98, 0.70, 0.63 and 0.23 in the blue, green, yellow and red spectral channels respectively).

5.5 Discussion

5.5.1 Methods

In this study the changes that occur in tissue autofluorescence of normal skin over time following surgical excision has been investigated. An ideal study design would have allowed precisely the same area and depth in the skin to be measured continuously *in vivo* and following excision. Experience using the DermaInspect ® *in vivo* has shown that image acquisition is very sensitive to movement artefacts when attempting to acquire images at a fixed depth with submicron precision over 25.5 seconds. This difficulty tracking a set FOV *in vivo* and the difficulty in finding this set FOV *ex vivo,* made this 'ideal study' unachievable. In the literature, the images presented by Sanchez et al. show that they were not able to use identical FOV for sequential images either (Sanchez, Prow et al. 2010). Palero et al. only managed to both maintain a fixed FOV and monitor changes in autofluorescence

emission spectra *in vivo* and *ex vivo* in mouse skin by euthanising the mouse during monitoring (Palero, Bader et al. 2011).

The tissue movement that occurred during imaging also prevented the basal layer (which is a single cellular layer thick) from being monitored in this way consistently. This is the most metabolically active layer in the skin and most likely produced that greatest response following surgical excision.

One disadvantage of the method used in this study were the delays that occurred between excision of the tissue sample, tissue preparation and securing a trackable FOV to image. Although the time taken to prepare the samples for imaging did improve with practice to < 5 minutes, tissue movement within the petri dish caused a seemly random variation in the time to the first acquired image and first tracked image. This prevented any data being collected from any sample before 13 minutes 12 seconds (seen for sample ID 4122).

Lateral movements of the tissue within the petri dish were prevented by placing the sample on moistened gauze and firmly securing the petri dish under the microscope objective. These measures were successful as little lateral movement was seen. However, it is possible that the pressure required to close the petri dish lid, so as to ensure the embedded cover slip lay firmly against the sample, compressed the tissue. The compression may have acted on both the tissue itself, with the loss of extracellular fluid from the cut tissue margins, and supportive underlying gauze leading to a vertical shift away from the microscope objective. Another possible contributing cause for the tissue contraction is the cooling of the tissue from body temperature to room temperature during the investigation.

The methods used for fixing the FOV to within a micron during imaging are detailed in the methods section above. This method was necessary because movement by just a few microns in depth affected lifetimes. For example, a 5 µm shift in depth noted between 9060 and 9162 seconds after excision in sample ID 4120 caused a change of 29, 3, 2, 2 ps in τ_1, a 147, 70, 97, 77 ps in τ_2 and 9, 74, 86, 78 ps in τ_{mean} in the blue, green, yellow and red channels respectively. Some of these differences can be attributable to the automatic segmentation algorithm, as discussed in the following paragraph. However a true difference in the fluorescence lifetime may be accounted for by slight changes in quantity of fluorophores fluorescing between the images such as NAD(P)H and melanin. This lifetime change is small compared to the variability in lifetimes seen between cells in the *s.spinosum* (as shown in Table 5.4), however any artifactual changes affect the ability to detect small 'true' changes in lifetime.

The automatic segmentation algorithm for ROIs was also found to be sensitive to small changes in FOV between images. It resulted in slight changes in the defined ROIs between almost identical images. This has been illustrated in figure 5.5. It shows 3 consecutively taken images from sample ID 4117 (image 11, 12 and 13) taken at 5752, 6428 and 6956 seconds. As can be seen from the fluorescence intensity images (panels b, f, j), the images are almost identical. Panels d, h and I show a close up of the top left hand corner of the automatically segmented images. These pictures clearly highlight the differences in the segmentation process between these fluorescence images. These differences were not felt to significantly affect the average lifetime parameters per image used in the analysis. However, its influence is difficult to quantify and distinguish from changes in lifetimes for other reasons e.g. movement, change in cellular metabolism.

5.5.2 Fluorescence Intensity Changes

The results from this study have shown that no photobleaching occurred during the imaging process. The mean pixel brightness actually increased steadily over the period imaged between 105-112% dependent on spectral channel, as can be seen in figure 5.7. In comparison to the experimental set up by Sanchez et al., our study would be the equivalent to using no culture medium and at a temperature between 37 ^{o}C and room temperature (Sanchez, Prow et al. 2010). In contrast to our results, they found a drop in fluorescence intensity over the first 24 hours, followed by an increase until day 4. As only daily readings were taken, it is impossible to extrapolate what their findings at 3 hours might have been (the end time for this experiment). Palero et al. did demonstrate a peak in total fluorescence intensity at 80 minutes (x1.7 fold from baseline) followed by trough to below the initial intensity after 110 minutes (Palero, Bader et al. 2011) over the 3.3 hour time period they monitored the mouse skin. Although these results are more consistent with those found in this study, a large increase in intensity was not seen and no ensuing decrease was seen. Our data demonstrated a steady rise in the fluorescence intensity over time. The nature of this change was not investigated further in this study, but one can speculate it was caused by either a change in the metabolic state of the tissue as a direct result of the excision or a photochemical induced reaction.

5.5.3 Fluorescence Lifetime Changes

Table 5.2 shows that τ_1 and τ_2 in the yellow and red spectral channels are significantly shorter than in the remaining channels. This is likely to reflect an increase in the contribution of melanin to the fluorescence in these channels. The data shown in this table can also be used to summarise the fluorescence lifetime parameters found in normal human skin. A direct comparison of these lifetimes with the published literature is complicated by differences in the excitation parameters, emission spectral filters and spectral channels used and method of lifetime calculation used between studies despite imaging similar tissue with the same device (the DermaInspect®). Benati et al.

performed FLIM analysis of normal skin *in vivo* (Benati, Bellini et al. 2011). They also used 760 nm excitation power, 25.5 seconds acquisition times and similar sized FOVs. They used higher powers of 20-45 mW and only measured lifetimes in one very broad spectral channel. Cellular lifetimes calculated using a single exponential decay model for the lower epidermis (*s.spinosum*/basal layer) ranged between 882-1145 ps depending on age and body site. This was shorter than those calculated for our data for any spectral channel (range 1343-2460 ps). Breunig et al. also published lifetimes of each layer of human skin taken *in vivo* from the forearm (Breunig and König 2011). In keeping with our data, pixels were fitted with a double exponential lifetime model. Images were taken over 7-13 seconds but at 740 nm excitation wavelength, using excitation powers of 10 – 40 mW and the fluorescence was not separated into multiple spectral channels. τ_1 and τ_2 were found to be 450 ps and 3.0-3.2 ns respectively in the *stratum spinosum*. His co-author, Karsten König cites τ_2 of 2.3 ns for the lifetime of cells in this same skin layer *in vivo* (τ_1 fitting the SHG IRF) in his review article using the same equipment (König 2008). These published figures for lifetimes calculated using a double exponential decay model are most similar to the mean lifetimes calculated for the green channel of τ_1 of 347 ps and τ_2 of 2366 ps in our data and attributed to mainly NADP(H) fluorescence.

Figure 5.8 shows that there is change in τ_{mean} of the skin over time following excision in all spectral channels. The calculations presented in the first row of table 5.3 and in table 5.4 also show that this variation is small compared to the natural variation found in intracellular τ_{mean} between cells in this skin layer.

The results illustrated in figure 5.9 demonstrate a small but consistent drop in τ_{mean} of between 18-75 ps/hour over the time imaged, dependent on spectral channel. This trend was difficult to appreciate in the plots of τ_{mean} over time in figure 5.8 and represents between 1.7-8.0 % drop in lifetime over time over the study. To determine if this change could be due to changes in NAD(P)H fluorescence, lifetime parameters in the green spectral channel were examined, see figure 5.10. It shows that the reduction in lifetime over time was not a direct consequence to changes in NAD(P)H metabolism, as τ_1 and τ_2 changed by just < 1% over this time. These results do not support the findings by Sanchez et al. They noted a new peak in τ_1 at ~800 ps and a broadening of the lifetime peak of τ_2 following excision on day 0 in the fluorescence lifetime of their NAD(P)H spectral channel. Palero et al. did not measure lifetimes but did conclude that changes occurred in the free to protein bound NAD(P)H ratio over time, based on their analysis using spectral unmixing. As stated above, this was not seen in our data as no changes were seen in NAD(P)H metabolism based on the lifetimes from our green spectral channel.

The papers by Sanchez et al. and Palero et al. do have some similarities. They both describe increases in the total fluorescence intensity, followed by a decrease with time. They also both describe some change to the fluorescence from NAD(P)H over time. These changes may relate to the differences in the metabolic rates between the human skin and mouse skin used for these investigations. The human skin appears to have a slower metabolic rate than the mouse skin and therefore more resistant to the ischaemic changes caused by excision/euthanasia. It is possible that these changes may have been reproduced if the skin had been investigated over a longer time period.

Finally, images taken from 27 patient samples acquired from normal skin *in vivo* and *ex vivo* were analysed and compared. The median τ_{mean} per sample between *ex vivo* and *in vivo* measurements was not found to be statistically significant using the Wilcoxon rank sum test in any spectral channel.

5.6 Conclusions

In conclusion the changes in tissue autofluorescence of normal human skin following surgical excision between 11 minutes and 3 hours in 5 samples have been investigated using multispectral FLIM for the first time. The skin was excited at 760 nm wavelength and the autofluorescence was collected from the *s.spinosum* using four emission spectral channels. A steady increase in the mean pixel fluorescence intensity of 105-112% with time was demonstrated, dependent on spectral channel suggesting that photobleaching did not occur. A small but consistent drop in the τ_{mean} over time of 1.7-8.0% was also demonstrated. A <1% change was seen τ_1 and τ_2 in the green spectral channel in which NAD(P)H fluorescence dominates.

The changes described by Sanchez et al. in human skin over 7 days and those described by Palero et al. in mouse skin over 3.3 hours were not seen in this study. This difference may be caused by the difference in the metabolic rates between human skin and mouse skin.

It has then been shown that there is no statistical difference in lifetime between samples of normal skin acquired *in vivo* vs. *ex vivo*. These results support the use of freshly excised human skin as a surrogate for *in vivo* imaging for MPT and MPT FLIM investigations over the initial few hours post excision. It also validates the conclusions draw by previous authors using MPT whom have studied freshly excised skin to extrapolate changes seen *in vivo*.

Chapter 6. An analysis of cellular morphology and FLIM of normal human skin using MPT.

6.1 Introduction

In this chapter multiphoton tomography (MPT) FLIM images and spectral images taken from normal skin both *in vivo* and *ex vivo* are examined. The results & discussion section of this chapter can be divided into 3 sections. This is the first time a detailed analysis has been performed on normal skin using multispectral FLIM.

A- Morphological features seen in multispectral MPT images from normal skin are presented and discussed. Emission spectra from depth resolved images and spectrally resolved images are then presented and correlated with the lifetime resolved images.

B- Investigation of the differences in cell morphology and lifetimes between cells from different epidermal skin layers within normal skin.

C- Investigation of the differences in cell morphology and lifetimes between cells from normal skin in patients with differing age, sex, skin type and body site.

6.2 Methods

6.2.1 Instrumentation

The instrument used and the minor modification made during the acquisition of data analysed in this section have previously been described in chapter 4. The FLIM detection module acquired FLIM images using time correlated single photon counting (TCSPC) using 256 time bins. The emitted fluorescence was spectrally separated using four emission spectral channels, defined as blue (360-425 nm), green (425-515 nm), yellow (515-620 nm) and red (620- 640/655nm). The emission spectral filter in the red channel was altered so that its long edge was broadened from 640 to 655 nm over the period of data collection and 5/30 samples were imaged prior to this alteration. This could be accounted for by daily calibrating by acquiring an IRF and fluorescence decay from a blue fluorescence slide. A spectrometer module was used to collect the steady state hyperspectral images separately.

6.2.2 Tissue preparation

For this investigation imaging was performed both *in vivo* (n=18) and on freshly excised *ex vivo* samples (n=12). Patients attending the dermatology clinic at the Hammersmith site of Imperial College London Healthcare NHS Trust gave written informed consent to participate.

In vivo imaging was performed on either the inside (medial) and/or outside (lateral) forearm of patients. An area was selected without skin pathology or obvious skin blemishes for imaging of 'normal skin'.

Excised samples of suspected malignancies with sufficient normal peri-lesional skin were selected for imaging of *ex vivo* 'normal skin'. The peri-lesional normal skin was separated from the lesion using a surgical blade immediately following excision of the lesion. Freshly excised tissue was rinsed with Hanks Balanced Salt Solution buffer without phenol red, calcium or magnesium (Gibco®, Invitrogen™, CA, USA), its surface moistened with the buffer solution and placed on damp gauze in an inverted glass bottomed petri dish (80-170 μm cover slip Matek®, MA,USA) following excision. A field of view (FOV), sited centrally within the sample, without obvious superficial blemishes, was then selected for imaging.

6.2.3 Imaging protocol

Imaging was performed as outlined previously in Chapter 4.6 (pp95). Image stacks were typically taken from each FOV at 10 μm depth intervals until the dermis was reached. In 10/144 images tissue movement had occurred, rendering the depth readout inaccurate.

All images were taken using 760 nm excitation wavelength, unless specifically stated otherwise. FLIM images were acquired over 25.5 seconds. These images were taken using either 128 x 128 pixel or 256 x 256 pixel resolution with FOV varying between 56 μm x 56μm^2 and 203 μm x 203 μm^2 (usually 107 μm x 107 μm^2). Therefore pixel size ranged from 0.42-0.84 μm between images. The *ex vivo* cells/ROIs used in the analysis were imaged on average ±SD of 60 ±41 minutes from excision.

Hyperspectral images acquired using the spectrometer required higher excitation powers to achieve an adequate photon count and were always taken following FLIM image acquisition. Images were either 32x256 or 41x256 pixels in size and acquired over 49.9 seconds.

6.2.4 Image Analysis

A detailed description of the lifetime analysis is outlined in chapter 4.10 (pp103). In summary, FLIM images in each channel were generated by fitting a single exponential decay to the fluorescence in each pixel in the image. For the lifetime analysis fluorescence decays for each ROI (not pixel) in each channel were fitted to a double exponential decay model. ROI fluorescence decay curves from a single spectral channel containing fewer than 1000 photons were felt to have insufficient photons to allow the double exponential decay fitting to be sufficiently reliable and so were excluded from the analysis. The number of ROIs (± SD) per patient was 230 (±179).

For the analysis of lifetime changes with depth, each image containing cells was defined as originating from the *stratum granulosum*, *stratum spinosum* or the basal layer based on the morphology of the cells in the image. The keratinocyte morphology from MPT images from each epidermal layer published by Koehler et al. (Koehler, Zimmermann et al. 2011) was used as a guide to label the epidermal layer of each image and is reproduced in Chapter 3.4. The actual depth recorded by the piezo objective positioner was not felt to be sufficiently accurate or reliable as great variability existed in the thickness of all cellular layers of the epidermis between patients. The undulated shape of the basal layer also meant that the cell layer would vary for a given depth within a small area, even within the same patient, depending on the depth of the dermal papilla.

As the *stratum corneum* is acellular in normal skin, no ROIs were defined from this layer. Due to the angle of the sectioned images and the undulating nature of the basal layer, a number of images spanned more than one layer. In such cases images were labelled according to the layer of the majority of the cells in the image.

Morphological features in the images were identified from the MPT intensity and FLIM images.

6.3 Results & Discussion

The results and discussion have been separated into 3 distinct sections that examine different aspects of normal skin fluorescence.:- Sections A-C.

6.4 SECTION A – Image Analysis

The results presented in section A show that depth resolved spatially co-registered multispectral fluorescence intensity and FLIM images can be acquired using this instrument. Initially a complete set of fluorescence images from a single sample of *ex vivo* skin is presented. The data sets acquired were sufficiently detailed to perform an analysis of emission spectra and lifetimes from user defined ROIs within each image, which is also demonstrated.

Following this, specific features seen in the acquired images and an analysis of the spectral images & FLIM images of the dermis is presented.

6.4.1 Fluorescence Images

Figure 6.1 is split over two pages demonstrating a montage of images taken from a sample of *ex vivo* normal skin. Both multispectral FLIM images and hyperspectral images were taken in succession from the same FOV at each depth. The FLIM images were acquired using the FLIM detector module and were 107 µm x 107 μm^2 in size, 256x256 pixels in resolution and taken over 25.5 seconds. The hyperspectral images were acquired using the spectrometer module (described in Chapter 4.6.3) over 49.9 seconds. They were from the same area but were 32x256 pixels in resolution. For each depth, the following images are presented:- a combined fluorescence intensity image from the four FLIM module PMTs; false colour FLIM/intensity images from the blue, green, yellow and red channels; a total fluorescence intensity image collected from the spectrometer camera and a false colour hyperspectral/intensity image.

From figure 6.1, little structure can be seen from the *s.corneum* layer (column a). Cells in the epidermis can be seen in the *s.granulosum* (column b &c) & *s.spinosum* (column d &e). An increase in the nuclear to cytoplasm ratio can then be seen with depth. Cells with increased melanin content have shorter τ_{mean} and appear redder in colour in the FLIM images (rows 2-5). The images from the basal layer (column f) demonstrate the transition from the basal layer (identified by the cellular areas on the bottom left of the images in column f, except f2) to the dermis (identified by the lack of cells in the top right of the images, except f2). Panel f2 shows the images taken from the blue FLIM channel and identifies collagen fibres by their SHG signal. The emission wavelength spectral range in the blue channel is too short for cellular fluorescence to be detected and is therefore relatively 'selective' for dermal collagen, except for some melanin fluorescence, which has a broad emission spectrum. Melanin fluorescence can be seen in panel d2, whilst dermal collagen is seen in panel g2 clearly. Panels g3 and g4, also taken from the dermis, show cord like structures. The emission spectra from these structures (i.e. in the green and yellow channels), their shape and their presence in the dermis would suggest dermal elastin fibres. However, the lifetime of these fibres from the

FLIM images would suggest that their lifetime is ~1-1.5 ns with is shorter than a τ_{mean} ~2-3 ns found in previous studies of elastin (see Chapter 2.6.3). One explanation is the presence of other fluorophores in proximity to the fibres affecting the calculated lifetimes due to the binning and smoothing that occurs to generate the FLIM images. When elastin fibres are imaged in isolation (see section 6.4.4), their lifetime is closer to that found in the literature.

Rows 6 and 7 in figure 6.1 show the images acquired from the spectrometer. The images in row 7 merge the wavelength of peak intensity with the intensity image. The cell outlines appear less well defined than the merged FLIM images (in rows 2-5) because they have a reduced horizontal resolution, as described above. Despite this, the resolution remains sufficient to co-register individual cells from images taken using the FLIM PMTs and the spectrometer. The images in row 7 of the spectral images illustrate the low spectral contrast between the cellular and acellular areas in the images, ranging from ~425 -450 nm.

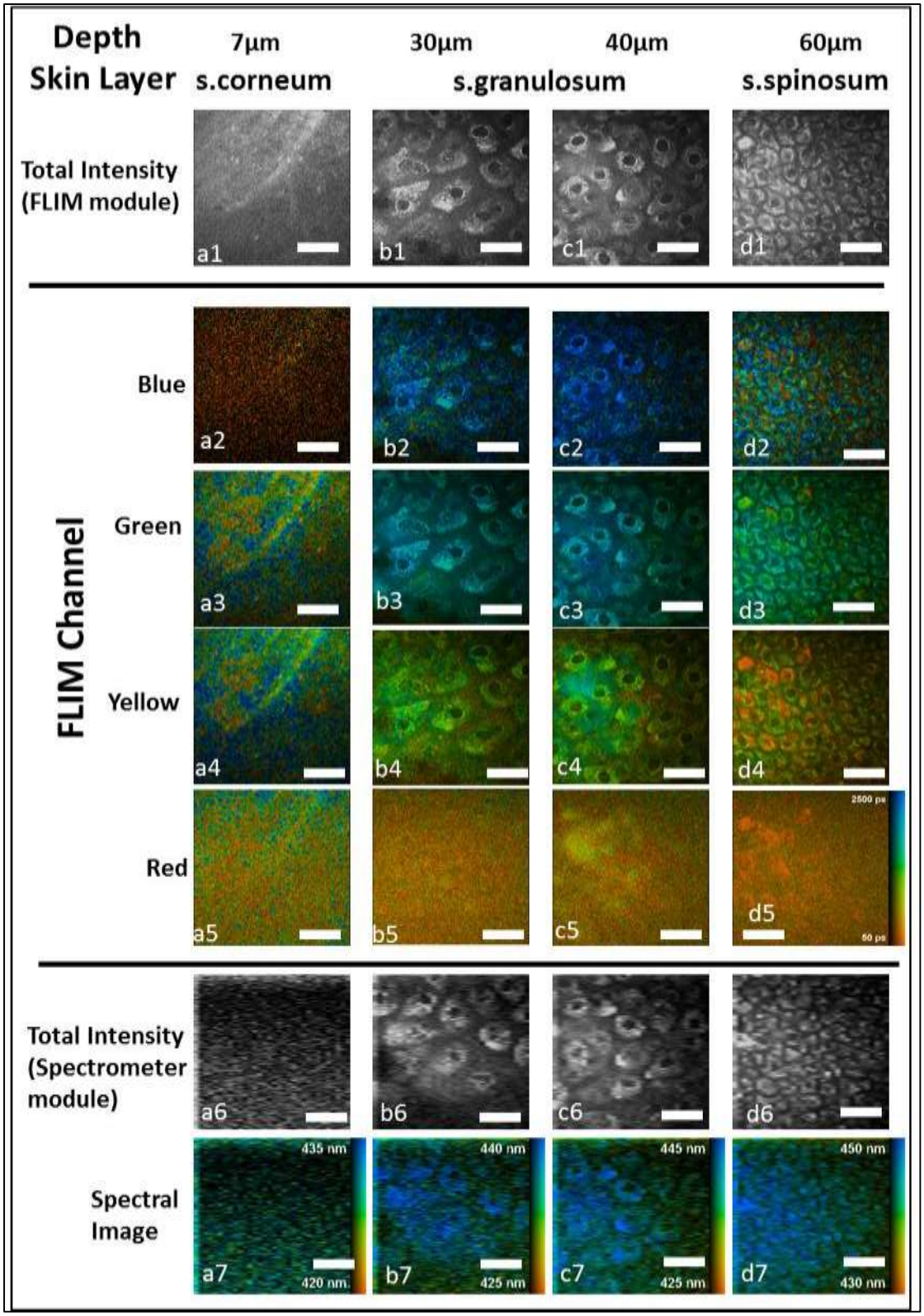
Depth
Skin Layer
7µm
s.corneum
30µm
40µm
s.granulosum
60µm
s.spinosum
Total Intensity (FLIM module)
a1
b1
c1
d1
FLIM Channel
Blue
a2
b2
c2
d2
Green
a3
b3
c3
d3
Yellow
a4
b4
c4
d4
Red
a5
b5
c5
d5
2500 ps
50 ps
Total Intensity (Spectrometer module)
a6
b6
c6
d6
Spectral Image
435 nm
420 nm
a7
440 nm
425 nm
b7
445 nm
425 nm
c7
450 nm
430 nm
d7

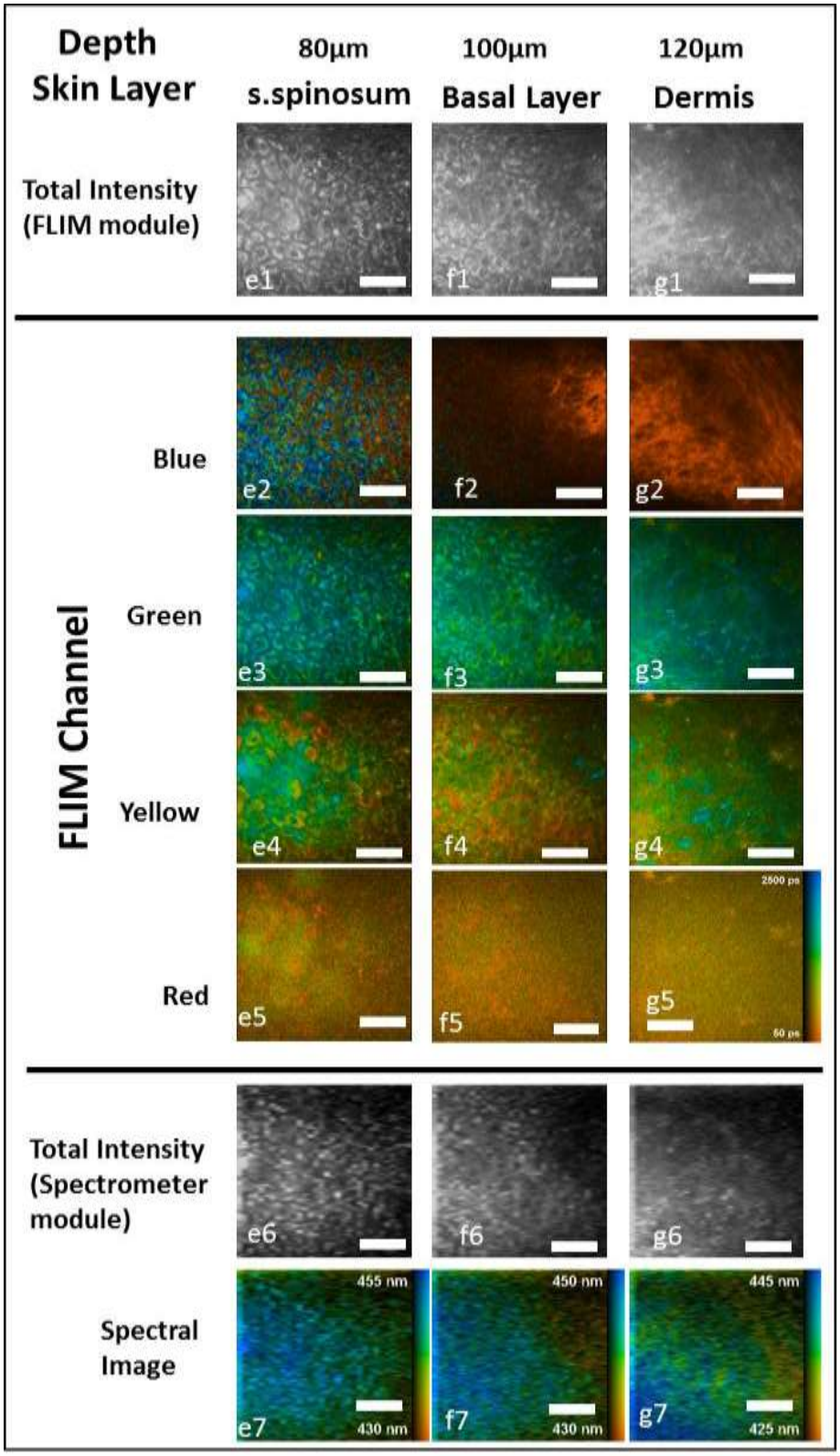

Figure 6.1 Fluorescence images from a number of depths from a sample of normal skin acquired *ex vivo*. Images were acquired using the FLIM module detectors and the hyperspectral camera in the spectrometer module of the DermaInspect®. Scale Bar 25 µm. FLIM scale shown to right of each row for each spectral channel. Spectral images plot the mean spectral emission wavelength.

6.4.2 Cellular Emission Spectra and lifetimes

The software allows the emission spectrum from manually defined ROIs within the spectral images to be extracted from the data collected. This allows the emission spectra from individual cells at different depths to be compared.

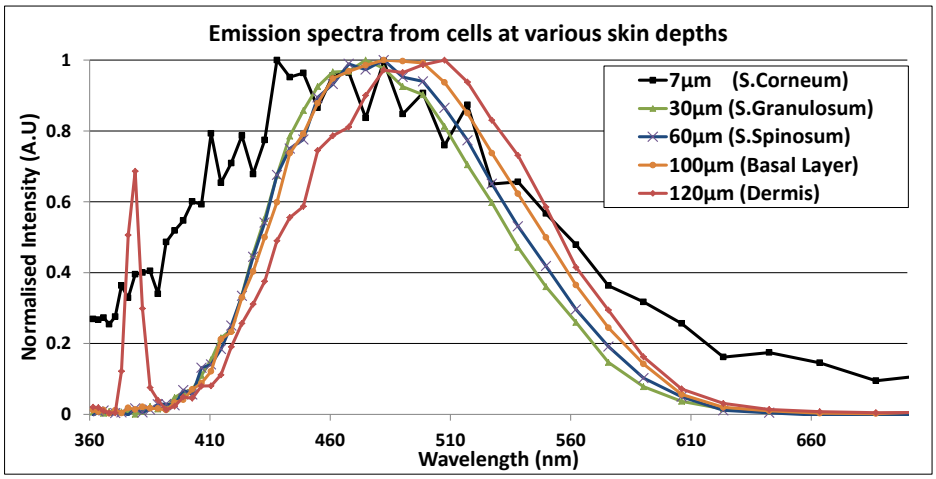

Figure 6.2 Figure plotting the emission spectra from cells at different depths taken from the sample of freshly excised normal skin illustrated in figure 6.1 using the hyperspectral depth resolved images.

Figure 6.2 shows emission spectra from ROIs taken from the spectral images illustrated in figure 6.1. The emission spectrum taken from the *s.corneum* (7 µm) combined the fluorescence signal from the entire image. The spectra shown for the remaining layers were taken by drawing a ROI around either single cells or small groups of cells in an image, depending on their size.

The figure shows that the emission spectrum acquired from the *s.corneum* (7 µm layer) is noticeably shorter than the remaining layers. A peak intensity between 440-480 nm can be seen which is expected to arise from keratin fluorescence, since this is the major constituent in this layer. It correlates well with the emission spectrum published for keratin in solution, which peaks at 450 nm when excited at 750 nm (Pena, Strupler et al. 2005) and ~465 nm when excited at 760 nm (Palero, de Bruijn et al. 2007).

The cellular fluorescence from the *s.granulosum* (depths 30 µm) and *s.spinosum* (60µm) have similar emission spectral shapes and peak intensities ~470 nm. This is at the upper limit of the range expected for NAD(P)H and may be longer because of contributions from flavins that have a spectral peak ~525 nm. A shift in the emission spectrum towards longer wavelengths in the basal layer and dermis (depths 100 µm and 120 µm) can also be seen in figure 6.2. This might represent a greater contribution from melanin autofluorescence or a different metabolic rate of the cells in these lower layers affecting the emission spectra of NAD(P)H between bound and unbound fractions (Palero,

Bader et al. 2011).The fluorescence emission spectrum taken from the cells in the dermis (120 µm depth) has a large peak present at 365 nm. This wavelength corresponds to SHG from extracellular collagen when excited at 760 nm which should have been rejected by the manually defined ROIs used for the lifetime analysis. It proves that, although a cluster of cells in this layer were defined, some collagen was also selected. As collagen is ubiquitous in the dermis and its SHG signal is very strong, this signal is not surprising.

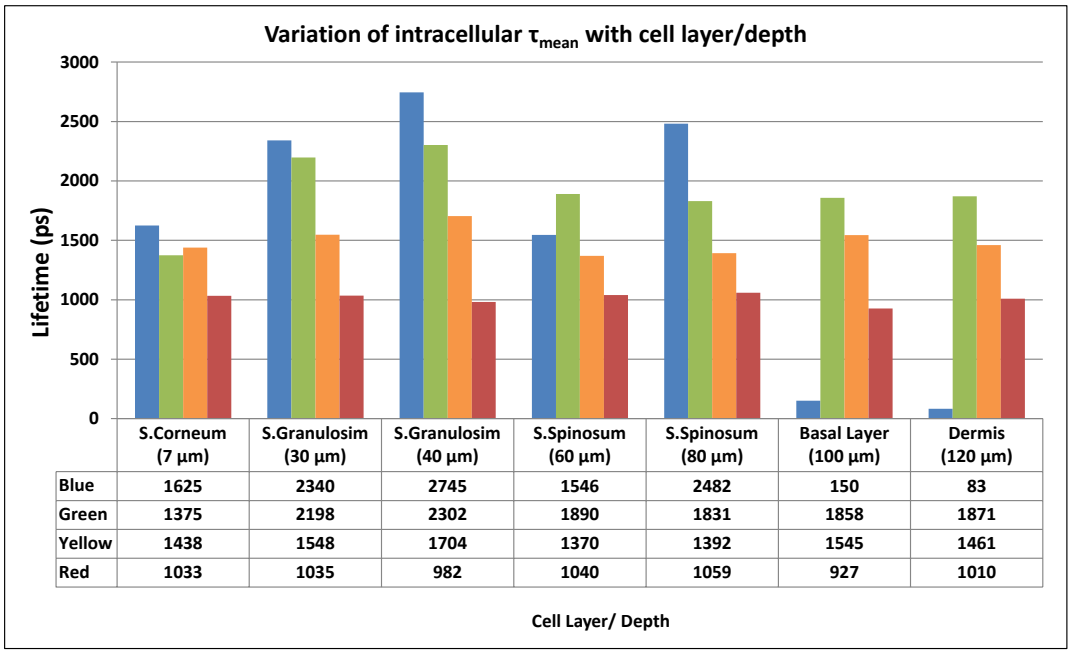

	S.Corneum (7 µm)	S.Granulosim (30 µm)	S.Granulosim (40 µm)	S.Spinosum (60 µm)	S.Spinosum (80 µm)	Basal Layer (100 µm)	Dermis (120 µm)
Blue	1625	2340	2745	1546	2482	150	83
Green	1375	2198	2302	1890	1831	1858	1871
Yellow	1438	1548	1704	1370	1392	1545	1461
Red	1033	1035	982	1040	1059	927	1010

Figure 6.3 The variation of τ_{mean} acquired from cells/cell clusters plotted according to spectral channel and cell layer/depth in the sample from the *ex vivo* skin illustrated in figure 6.1.

As paired spectral and FLIM images were acquired from the same FOV, intracellular fluorescence lifetimes could also be calculated from these cells/cell clusters. The results of τ_{mean} of these ROI are shown in figure 6.3. As stated in the previous section, the greatest contribution to the lifetime in the *s.corneum* is from keratin. The lifetimes calculated from this layer in the 4 spectral channels (1033-1625 nm) are in keeping with the lifetime for pure keratin taken from a single spectral channel of 1400 ps (Ehlers, Riemann et al. 2007). Also as stated in the previous section, a SHG signal from extracellular collagen in the cellular ROIs from the basal layer and dermis (100 µm, 120 µm depth) accounts for the spuriously short intracellular lifetimes calculated for these layers in the blue channel.

The lifetimes from the green channel in the *s.granuolsum*, *s.spinosum* and basal layer are expected to to be dominated by NADP(H) but also include a contribution from flavins. The τ_{mean} of NAD(P)H is dependent on environment and has been reported to vary between 444-948 ps, with the protein bound component (τ_2) calculated to vary between 2.03 and 6.04 ns (Vishwasrao, Heikal et al. 2005;

Skala, Riching et al. 2007). The lifetime of free flavins varies between 2.3-5.2 ns when free and ~250 ps when protein bound (Nakashima, Yoshihara et al. 1980; König and Schneckenburger 1994; Yang, Luo et al. 2003). These values compare with an average τ_{mean} calculated from the data presented above over all the images of 2.02 ns. This figure is in reasonable agreement with the published values. We suggest that the drop in τ_{mean} between the *s.granulosum* and the deeper layers either reflects an increased melanin contribution to the fluorescence in this channel or reflects a difference in fluorescence arising from NAD(P)H & flavin in these metabolically more active cells deeper in the epidermis.

The cellular lifetimes in the red spectral channel shows little variation with depth and an average τ_{mean} of 1.01 ns over the cellular layers (30-100 μm). The lifetime of melanin is expected to dominate in this channel and this value is consistent with a τ_{mean} of 1.23 ns reported for synthetic melanin (Teuchner, Freyer et al. 1999).

6.4.3 Epidermal Cytoplasmic Autofluorescence

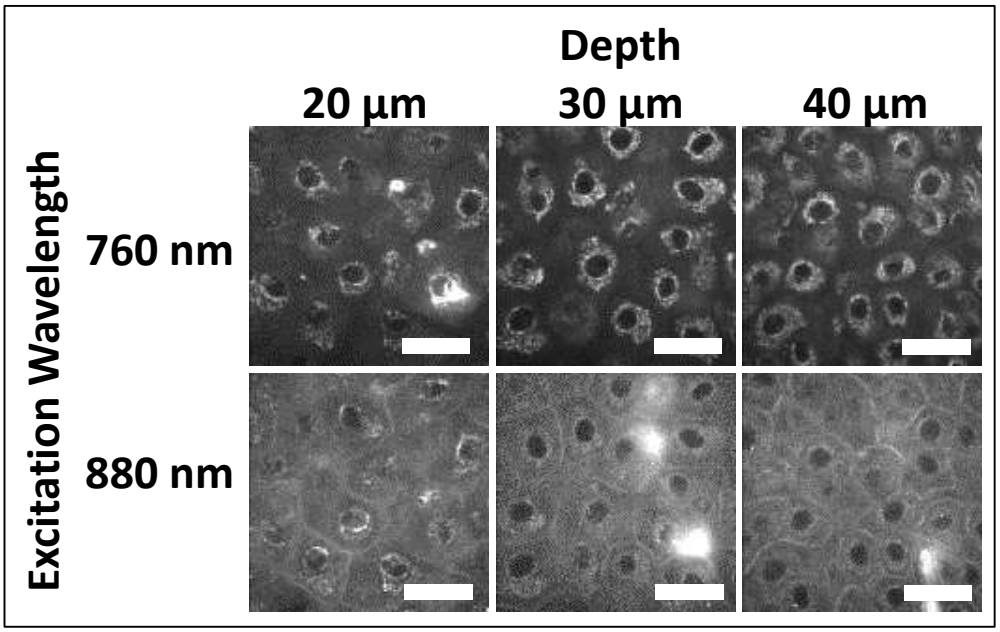

Figure 6.4 Illustrates paired images of the same FOV within the *s.spinosum* using different excitation wavelengths and acquired from the green spectral channel. Scale Bar 25μm

Figure 6.4 shows a selection of paired images taken in the green channel, from identical FOVs and depths, but using different excitation wavelengths (760 and 880 nm). The images were taken from the *s.spinosum* from an *ex vivo* sample of normal skin (ID 4038 fov1). The images taken using an excitation wavelength of 760 nm illustrate the typical appearance of non-fluorescent nuclei, fluorescent peri-nuclear cytoplasm and the presence of apparent intercellular spaces with little/no

fluorescence. The brighter ring of autofluorescence around the nucleus of the cell may reflect the higher concentration of mitochondria, and therefore NAD(P)H in this area of the cell.

Different contrast can be seen in the images shown when excited at 800 nm. This reflects the different fluorophore absorption and emission profiles at 880 nm compared to 760 nm. These images appear to now show the cell membrane, which was absent from the images taken at 760 nm. They show that the cells are in fact confluent. The appearance of intercellular spaces was therefore an artefact of low/absent autofluorescence from the peripheral cellular cytoplasm in images when excited using 760 nm. This is consistent with images of the skin acquired *in vivo* using confocal microscopy, which show cellular confluence in the epidermis (Rajadhyaksha, Grossman et al. 1995).

It is noted that this artefact will therefore affect all morphological assessments of cells, including calculations of the cell size and shape when images acquired at 760 nm are used. This artefact was not as apparent in the images acquired from the basal layer. It is postulated that the cytoplasmic volume for cells in the basal layer was sufficiently small compared to the size of the nuclei and their cytoplasm was sufficiently metabolically active, that the artefact of spaces between cells was not seen for images from this layer.

6.4.4 The Dermis

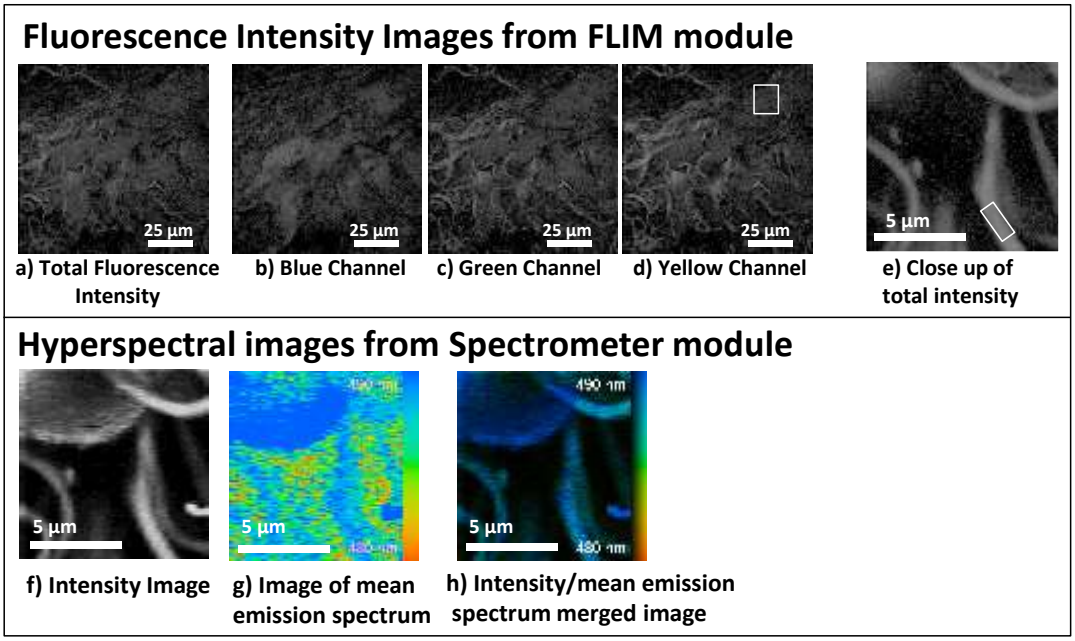

Figure 6.5 (a-d) Fluorescence images of the reticular dermis taken using the FLIM detector module, with close up image (e). Box in (d) indicates a representative area of collagen for ROI analysis. Box in (e) indicates representative area of elastin for ROI analysis. (f-h) Corresponding images taken using spectrometer detector module from FOV (e).

Figure 6.5 shows both intensity and spectral images taken from the underside of a sample of normal skin (the reticular dermis). The top images (a-e) show a combined fluorescence intensity images and the intensity images taken from three spectral channels (b-d, no red channel image taken). The last panel (e) shows a close up image of the same FOV. These images are of collagen and elastin. Collagen SHG is very strong in the blue channel (b), appearing as the only visible feature. As collagen fibres are fine, individual fibres cannot be resolved at this image resolution and they appear as diffusely fluorescent. The remaining spectrally segmented images (c,d) show a weaker collagen autofluorescence compared to a more dominant elastin fluorescence in this spectral range. The elastin fibres are coarser, allowing individual fibres to be distinguished.

Figure 6.5e-h show images taken at a higher magnification of an elastin fibre. The spectral images mapping the mean emission spectrum (g,h) suggest that elastin has a mean emission spectrum ~490 nm.

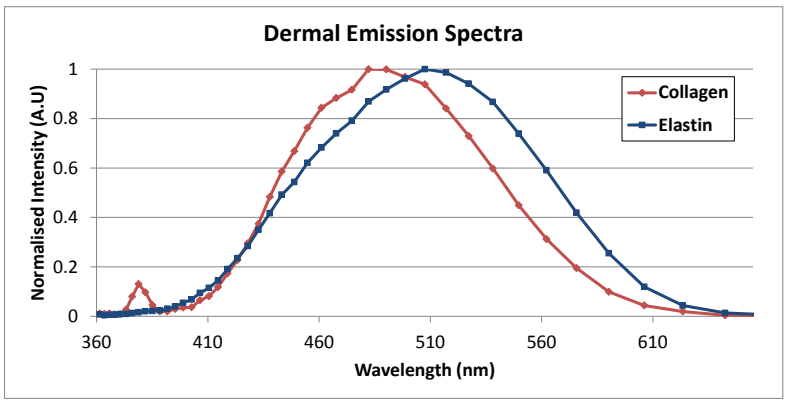

Figure 6.6 Emission spectra from areas of collagen and elastin from image FOV shown in figure 6.5

To examine these dermal structures further, emission spectra were extracted from the hyperspectral images from areas representative of collagen and elastin, e.g. highlighted boxes in figure 6.5d,e. These are plotted in figure 6.6. The emission spectrum of elastin shows a peak spectral intensity at 507 nm. This is slightly higher than those found in the literature of peak emission spectrum between 445-500 nm (Pena, Strupler et al. 2005; Palero, de Bruijn et al. 2007).

Collagen has two signals evident from this graph. The emission spectrum shows a small peak at 360 nm consistent with its SHG signal when excited at 760 nm. This SHG peak is smaller than expected as the signal is known to be very strong compared to autofluorescence. It is not clear from the data why this is the case. It may have been caused by a low excitation power used to acquire the preceding FLIM image and not sufficiently increased prior to acquiring the spectral image. Figure 6.2 showed a significantly larger SHG peak when the dermis was imaged on another occasion suggesting again that a user defined parameter was suboptimal.

The collagen autofluorescence spectrum has a peak ~490 nm. This is longer than that reported in the literature by Lutz et al. who excited purified collagen at 750 nm using the DermaInspect® and saw a spectral peak ~460 nm (Lutz, Sattler et al. 2012). This longer peak may be related to the slight changes in emission spectra associated with collagen subtype, its post-translational modification with additional proteins or its environment. Another contributing factor could be autofluorescence from the brighter elastin fibres.

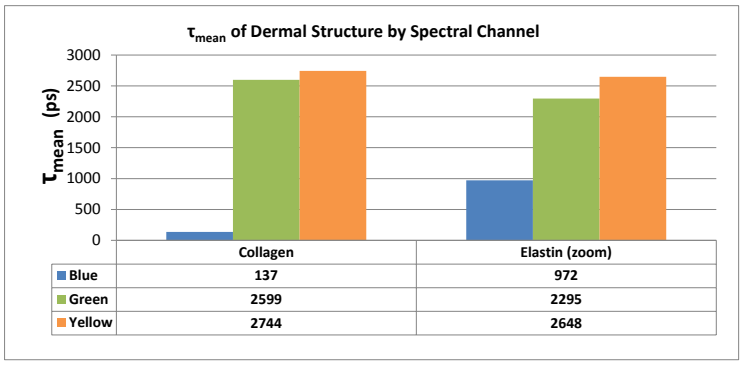

Figure 6.7 Bar Graph of τ_{mean} from ROIs corresponding to collagen and elastin derived from the FLIM images illustrated in figure 6.5 b-e, categorised by spectral channel.

Figure 6.7 show the τ_{mean} for selected ROI within the FLIM images illustrated in figure 6.5 of collagen in the unmagnified FLIM images (figure 6.5b,c,d), and elastin from the set of magnified images (of which the total intensity images is shown in figure 6.5e). The lifetime from collagen in the blue channel is short (137 ps) due to the dominance of its SHG signal in this channel. The average collagen lifetime calculated from ROIs in the green & yellow channels were τ_1 =568, τ_2= 3186 and τ_{mean} =2672 ps. This is consistent with lifetimes reported in the literature. As discussed in the introduction ~80% of dermal collagen is type I that has a reported τ_{mean} ranging between 2466-2335 ps (Marcu, Cohen et al. 2000; Lutz, Sattler et al. 2012).

The lifetime calculated for elastin in the blue channel is also short and probably reflects contaminant signal from the much stronger collagen SHG signal in this channel. The average lifetime for an elastin fibre averaged between the green and yellow channel is τ_1 =437, τ_2= 2869, τ_{mean} =2471 ps. The τ_{mean} is close to that found for collagen in these channels so contaminating fluorescence from collagen cannot be excluded. This lifetime is also longer than that reported in the literature of 2.05 ns for elastin (Fang, Papaioannou et al. 2004).

6.5 SECTION B - Epidermal Cell Layers

In this section MPT FLIM data is used to investigate differences in lifetimes between the cellular layers of the epidermis. The MPT images taken from the skin were initially acquired as controls against images taken of skin cancers. Therefore, the data presented in sections B and C was not collected with this analysis in mind. The analysis focuses on the data that has been collected, not necessarily that needed to perform a conclusive study.

6.5.1 Introduction

As described in detail in the introduction chapter 1.2 (pp27), the epidermis can be subdivided into a number of layers based on cell morphology in normal skin. The *stratum corneum* lies on the surface and is acellular. Beneath this are the cellular layers, namely the *stratum granulosum*, the *stratum spinosum* and finally the basal layer. These layers become progressively more metabolically active with depth.

A number of groups have published lifetime data from different layers in the skin previously. For example, Cicchi et al.(Cicchi, Massi et al. 2007) performed a pixelwise fit using a single exponential decay model to images taken from various depths from *ex vivo* normal skin, excited at 740 nm. They found an increase in the lifetime to 50 μm depth, followed by a sharp decrease with a maximum positive shift of ~+90 ps and negative shift of -10 ps from zero depth. In their conference proceedings, Breunig et al. performed a pixelwise fit using a double exponential decay model to images taken from different layers in the skin after excitation using 720 nm *in vivo* (Breunig and König 2011). The data was not spectrally separated so τ_1 was dominated by collagen SHG and may have masked a fluorescence decay arising from free NAD(P)H in their results. They found τ_2 shorter in the basal layer (2700 ps) compared to the *s.spinosum* (3000 ps) which they felt in keeping with the lifetime for protein bound NAD(P)H.

The only systematic analysis was performed by Benati et al. (Benati, Bellini et al. 2011). They compared the lifetimes between the upper and lower epidermis in two age groups and body sites (forearm, thigh). They performed a single exponential decay fit to a pixel within a cell (after binning 5x5 pixels) and made an average over 5 cells for each group. In the 20-35 year old age group, they found a statistically significant differences in the lifetimes between layers in all body sites e.g. 1171±116 upper vs 935±174 ps lower epidermis on the outside forearm (difference of 236 ps). However, this was not found in the >60 years age group. They suggested that the reduction in lifetime with depth related to the cellular melanin content of the cells and speculated that differences in the metabolic activity between the layers also contributed to these differences.

6.5.2 Methods

The differences in lifetime with depth in the epidermis using the MPT FLIM images collected from normal skin has been investigated. Images of normal skin acquired both *in vivo* and *ex vivo* have been investigated and it has already been shown in Chapter 5 (pp115) that fluorescence lifetime does not alter significantly post excision over the initial few hours.

To combine data from multiple patients, images were categorised by cell layer and not absolute depth. The thickness of each cellular layer in the epidermis varies widely between patients and body sites. This renders the absolute depth of the images taken (in relation to the *s.corneum*) unhelpful. Therefore the skin layer of each image of normal skin analysed was manually assigned. This was based on the MPT exemplar images and definitions of each layer described by Koehler et al. (Koehler, Zimmermann et al. 2011) and illustrated in figure 3.1 in Chapter 3.4 (pp69).

Number of Patients		30
Demographics	Male/Female	17/13
	Age (Range)	45.1 (17-88)
	Skin Type (Range)	2.5 (1-4)
In vivo/Ex vivo		18/12
FOV by body site	Inner Forearm	17
	Outer Forearm	8
	Back	8
	Face	3
	Lower Leg	1
Images Taken		144
Total Cells/ROIs		6904
Cells/ROIs per Skin Layer (%)	S.Granulosum	973 (14.1%)
	S.Spinosum	3647 (52.8%)
	Basal Layer	2284 (33.1%)

Table 6.1 Summary of the images taken from normal skin that were analysed.

Table 6.1 outlines the images that were analysed in this section. It lists details of the patients from which the images were taken, whether the images were acquired *in vivo* or *ex vivo* and the number of images and ROIs analysed. As previously stated, all images were acquired with an excitation wavelength at 760 nm. The table shows that more than ½ of the cells arise from the *s.spinosum*, the thickest layer in the epidermis.

6.5.3 Change in cell size with depth

It is known that cells in the epidermis reduce in size with depth (i.e. reducing from the *s.granulosum* to the basal layer. It should also be noted that the elongated polygonal cells in the *s.granulosum* and *s.spinosum* are orientated horizontally (with their long axis parallel to the skin), whilst the columnar cells of the basal layer lie vertically (with their long axis perpendicular to the skin). It might therefore be expected that a sharp reduction in the measured size of cells from the *s.spinosum* would be seen, when imaged *en face*, (as is the case in MPT images compared) to the basal layer due to the change cell orientation.

To investigate this, the shapes and sizes of the manually defined ROIs were analysed. It has already been shown in Section 6.4.3 (pp142) that the autofluorescence does not extend to the cell periphery for the larger cells seen in the *s.granulosum* and upper *s.spinosum*. The size of cells in these layers will therefore be underestimated, making it difficult to make an accurate comparison. In addition, the cell density between cell layers has been compared, which is not subject to the inaccuracy outlined above.

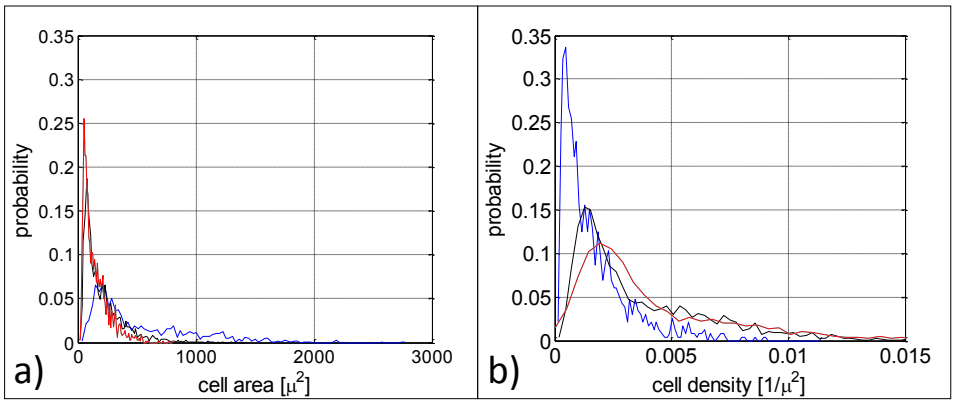

Figure 6.8 Plots the distribution of (a) cell area and (b) cell density (calculated using the Gabriel method) of cells categorised by cell layer. Key: Blue-*S.Granulosum*, Black- *S.Spinosum*, Red- Basal Layer.

Figure 6.8 shows histograms of the cell area and density of the analysed ROIs by cell layer. Figure 6.8a shows that a small proportion of cells in the *s.granuosum* are very large in size compared with cells in other layers. As the sizes of cells in the *s.spinosum* are underestimated, it is not possible to assess for a sharp reduction in the cell area from the *s.spinosum* compared to the basal layer.

Figure 6.8b shows the density of the cells between layers. The methods used to calculate the density have been outlined in Chapter 4.10.7 (pp109). The histogram shows a smoother progression of increased density with depth between the layers with a median density of 0.00221, 0.00522 and 0.00561 cells/μm^2 for the cells in the *s.granulosum*, *s.spinosum* and basal layer respectively.

However, this too does not demonstrate a sharp decrease between the *s.spinosum* and the basal layer.

6.5.4 Change in lifetime with depth

Previous groups have found a decrease in fluorescence lifetime with depth of between 236-300 ps (Benati, Bellini et al. 2011; Breunig and König 2011). It is suggested that this drop in lifetime with depth reflects an increase in melanin content from melanocytes and keratinocytes. Melanin has a short lifetime with components as short as 200 ps (Teuchner, Freyer et al. 1999) and is expected to contribute most to fluorescence detected in the yellow and red spectral channels, based on its emission spectrum (refer to figure 2.7,pp51; & figure 2.11;pp57 of the emission spectrum of melanin). However changes are likely to be seen in all spectral channels as melanin has a broad emission spectrum that covers the whole detection emission spectral range.

An increase in the melanin content would therefore be expected to present as a decreasing τ_1 (& possibly τ_2) and an increasing f_1, reflecting a greater contribution and increasing quantity of melanin to the shorter lifetime component. This would result in a progressive shortening in τ_{mean} with depth that would predominantly affect the yellow and red spectral channels.

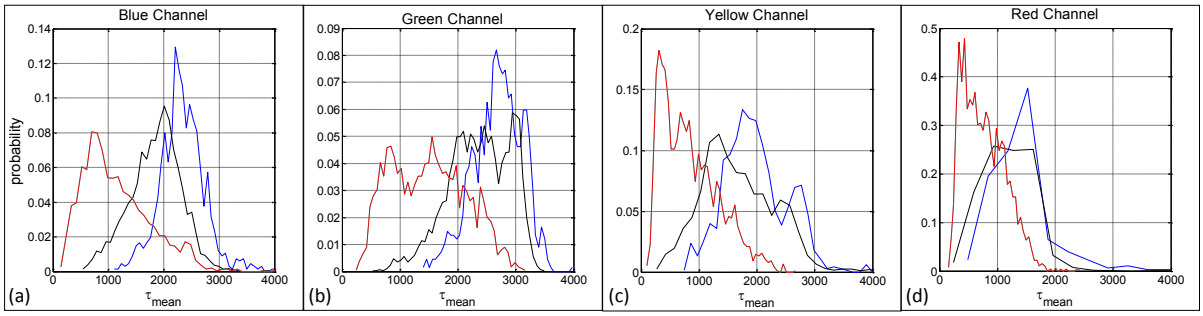

Figure 6.9 Distribution of τ_{mean} with epidermal cell layer. Key: Blue-*S.Granulosum*, Black- *S.Spinosum*, Red- Basal Layer.

Figure 6.9 shows the distribution of τ_{mean} in all spectral channels categorised by cell layer. A trend towards shorter lifetimes can be seen in all channels as the cell layer progresses from the *s.granulousm* to *s.spinosum* to the basal layer.

			Percentile		
	Channel	**Level**	**25**	**50**	**75**
τ_{mean} (ps)	Blue	S.Granulosum	2087	2313	2575
		S.Spinosum	1563	1892	2157
		Basal Layer	696	1027	1513
	Green	S.Granulosum	2411	2705	2990
		S.Spinosum	1999	2393	2826
		Basal Layer	937	1499	1981

Yellow	S.Granulosum	1616	1925	2346
	S.Spinosum	1220	1594	2132
	Basal Layer	428	755	1163
Red	S.Granulosum	1079	1410	1620
	S.Spinosum	851	1204	1548
	Basal Layer	456	719	1035

Table 6.2 Distribution of τ_{mean} with epidermal cell layer, categorised by spectral channel

This can be confirmed by the median τ_{mean} for each layer in each channel, listed in table 6.2. It shows a decrease in the median τ_{mean} between the *s.granulosum* and the basal layer of 1286, 1206, 1169 and 691 ps for the blue, green, yellow and red spectral channels respectively. This difference is significantly larger than has been previously reported of up to 300ps and is consistent with the presence of increased melanin content with cell layer.

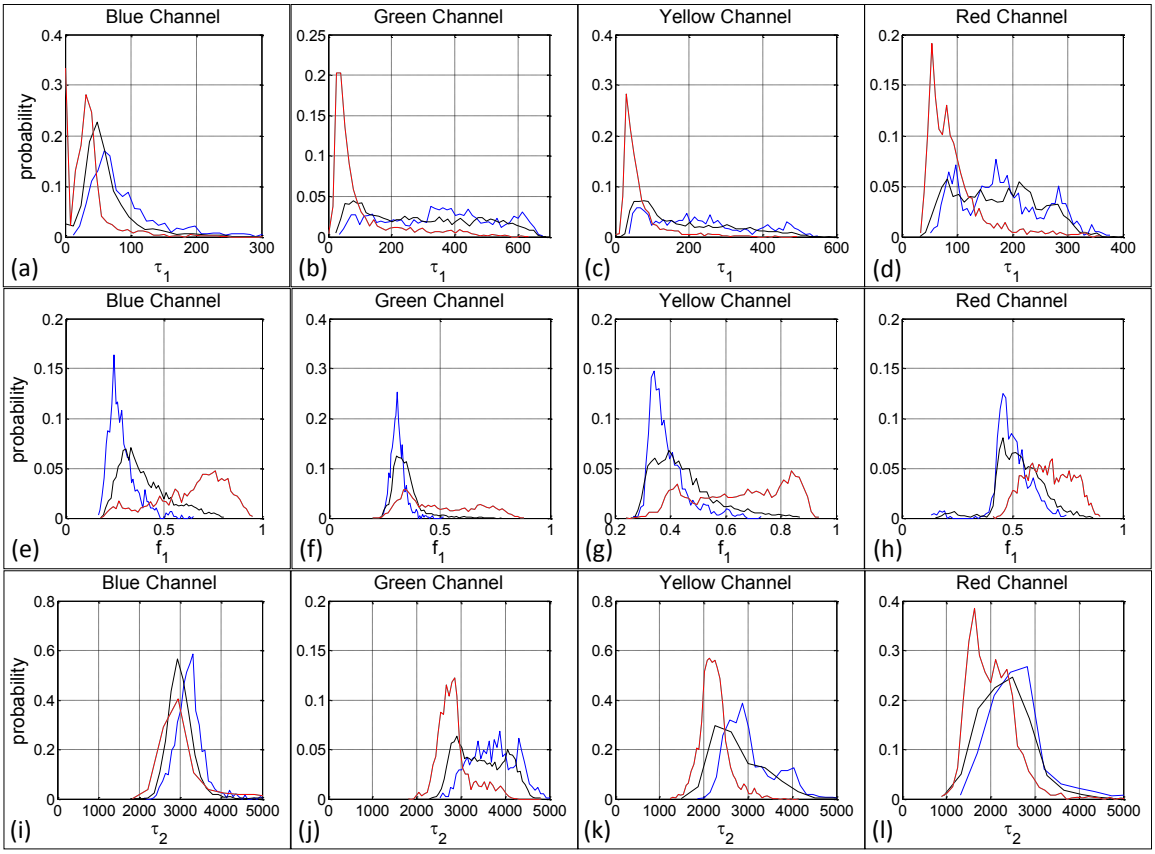

Figure 6.10 Histograms showing the changes seen in τ_1, f_1 & τ_2 with cell layer. Key: Blue-*S.Granulosum*, Black- *S.Spinosum*, Red- Basal Layer.

To explore this trend further, individual lifetime parameters can be examined. Changes to τ_1 and τ_2 will reflect differences in the contributions to each lifetime component of each intracellular fluorophore between layers.

Figure 6.10a-d shows the distribution of τ_1 categorised by cell layer. The median τ_{mean} is very short (between 31-73 ps) in the blue channel for all cell layers (not just the basal layer). This suggests that melanin fluorescence contributes significantly to this channel, as other tissue fluorophores have significantly longer lifetimes. This short lifetime is not thought attributable to collagen SHG because no collagen should be seen in the upper cell layers and a large peak ~0 ps can be seen for the basal layer that is distinct from the other peaks and would account for collagen SHG.

The τ_1 lifetime component of the cells in the basal layer, tend to be the shortest for all spectral channels. The peaks seen for the basal layer with a median τ_1 ~ 50 ps in the green and yellow channels cannot be attributed to collagen SHG, as this should only be detected in the blue channel. This finding strongly suggests that the shorter lifetimes of cells in the basal layer are caused by an increased presence of melanin. Interestingly, a median τ_1 of 80 ps in the red channel for cells in the basal layer is longer than the median τ_1 for other channels, despite the dominance of melanin in this channel. One would expect the lifetime to be even shorter. It has been shown previously that the emission spectrum and lifetime of melanin can depend of the size of its aggregates (Nofsinger and Simon 2001), see Chapter 2.6.4 (pp56). This discrepancy might therefore be attributable to melanin aggregates that have longer emission spectra (i.e. 1000 – 10,000 MW) also having longer lifetimes. Unfortunately, Nofsinger et al. did not correlate the lifetime differences with emission spectra to support this theory. It might also be accounted for by the presence of another fluorophore that emits strongly in the red spectral channel with a longer lifetime than melanin contributing to the fluorescence e.g. porphyrins.

Figure 6.10 e-h show the contribution of the short lifetime component (f_1) to τ_{mean}. These histograms confirm a greater f_1 seen for the basal layer for all spectral channels. As τ_1 has already been shown to be more strongly influenced by melanin in the basal layer, a high f_1 strongly supports the conclusion that these cells have higher cellular melanin content.

Figure 6.10 i-l shows τ_2 for all channels categorised by cell layer. These histograms show many of the trends described above for τ_1. For example, cells in all layers exhibit similar lifetimes in the blue channel and cells from the basal layer have a shorter τ_2 than the other layers for all spectral channels. These features are consistent with an increased melanin content in cells from the basal layer.

6.5.5 Change in metabolism with depth

The basal layer of the epidermis is metabolically more active than the layers above. It was investigated if this might be detected as a change in the autofluorescence from NAD(P)H and FAD which fluoresce in the green and yellow spectral channels respectively. The assumption that the

changes in NAD(P)H and FAD autofluorescence associated with the increased metabolism in normal skin mimic those seen with epidermal malignancy has been made.

Skala et al. studied malignancy in a hamster cheek pouch model and found these changes to include a decrease in the contribution and lifetime of the protein bound component of NAD(P)H (f_2 & τ_2 in the green channel), a less significant decrease in the lifetime of the free component of NAD(P)H (τ_1 in the green channel), increase in the lifetime of protein bound FAD (τ_1 in the yellow channel) and a decrease in its contribution (f_1 in the yellow channel) (Skala, Riching et al. 2007). The changes in NAD(P)H fluorescence could therefore be screened for by a decrease in τ_{mean} in the green channel.

It has been suggested above (section 6.5.4) that melanin strongly influences the lifetimes in many channels. As the highest melanin content has been suggested to be in the basal layer, our ability to use lifetime to detect changes in metabolic rate in this layer is adversely affected. One method to account for this is to attempt to separate the cells that have high melanin content. This might allow other trends in fluorescence lifetime to be detected more easily in the remaining cells.

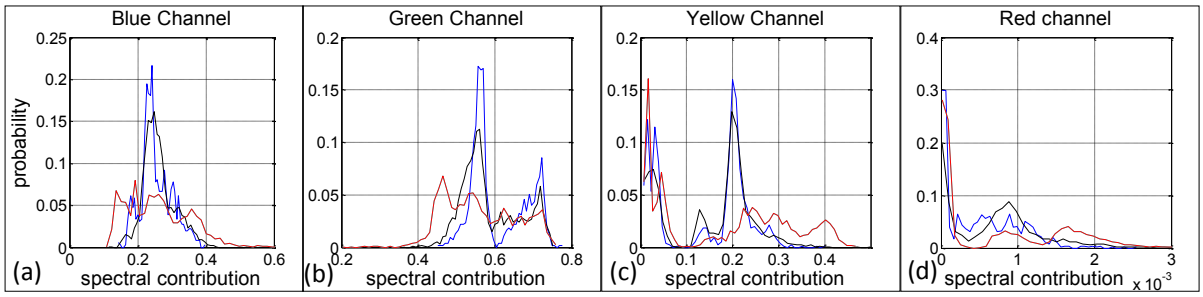

Figure 6.11 The distribution of spectral contributions from each channel categorised by cell layer. Key: Blue-*S.Granulosum*, Black- *S.Spinosum*, Red- Basal Layer.

Figure 6.11 a-d are histograms that show the distribution of spectral contributions for each spectral channel, separated by cell layer. The histograms in yellow and red channels show 2 peaks for the *s.granulosum* and *s.spinosum*. Further analysis (not shown) show that these peaks represent two distinct populations of cells. By assuming that these populations differ primarily in their melanin content all cells can be described as having a low melanin content (with < 0.1 contribution in the yellow channel) or a high melanin content (with > 0.1 contribution in the yellow channel).

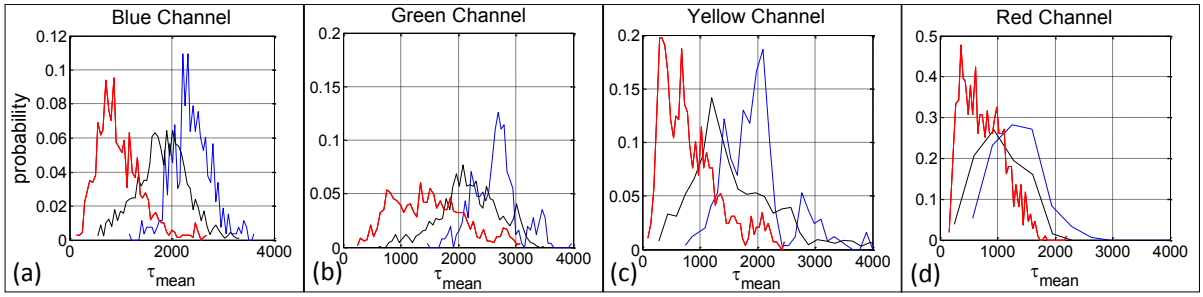

Figure 6.12 The distribution of τ_{mean} for 'low melanin content' cells with a spectral contribution in the yellow channel <0.1, categorised by cell layer and spectral channel. Key: Blue-*S.Granulosum*, Black- *S.Spinosum*, Red- Basal Layer.

Figure 6.12 replots τ_{mean} for all spectral channels for this population of cells that have a spectral contribution in the yellow channel <0.1 and have been described as having a low melanin content. These histograms for τ_{mean} are very similar to those shown in figure 6.9. Slight changes in the distribution and size of the peaks can be seen but the overall trends have not changed. A reduction in τ_{mean} in the green channel with depth is not seen, which could be caused by a higher metabolic rate affecting NAD(P)H fluorescence. However, as no significant changes are seen in the histograms between figure 6.9 and 6.12, melanin cannot be excluded as the cause for all the trends seen and are unable to confidently attribute any findings to changes in NAD(P)H fluorescence . The individual lifetime parameters have therefore not been analysed further because confident conclusions cannot be made.

6.5.6 Section B - Conclusions

In this section it has been shown that the cell density increases with cell layer for normal skin. In addition we have demonstrated a shortening in τ_{mean} with increasing depth which is summarised in table 6.2. The data demonstrated a decrease in the median τ_{mean} between cells in the *s.granulosum* and the basal layer of 1286, 1206, 1169 and 691 ps for the blue, green, yellow and red spectral channels respectively. This is a larger difference detected than previous groups, whom have found lifetime changes of between 236-300 ps (Benati, Bellini et al. 2011; Breunig and König 2011). Evidence has then been presented that this change can be attributed to increasing melanin with depth. Like Benati et al., we also proposed that the shorter lifetime with depth is contributed to by increased metabolic activity. However, the data collected in this study does not support this.

Also, melanin was expected to be the most dominant fluorophore in the red channel, especially for τ_1. An interesting finding from the data is that the lifetimes seen for τ_1 in the red channel (figure 6.10d) had longer than expected lifetimes for all cell layers, especially the basal layer, which is

expected to have the highest melanin content. The cause for this difference remains unclear and was not investigated further. It may represent aggregates of melanin with longer lifetimes fluorescing in this channel or may be attributable to another fluorophore such as porphyrin.

6.6 SECTION C- Changes with demographics

In this section the variation in fluorescence lifetimes between patients is examined. Despite inter-patient variation, the presence of distinct populations of cells are presented and discussed. Finally a more detailed analysis of the changes in lifetime with patients age, sex and skin type and body site is made.

As previously stated, the MPT images taken from normal skin, both *in vivo* and *ex vivo*, were initially acquired as controls against images taken of skin cancer. Therefore, the images were not collected with the purposes of this analysis in mind. As a result, the analysis focuses on the trends seen in the data collected, not the ideal data set.

6.6.1 Lifetime variability by patient

Initially intrapatient vs interpatient variability in fluorescence lifetimes is evaluated. Intrapatient variation was made by comparing MPT FLIM images taken from a patient (ID 5010) *in vivo*, from their outer forearm in 2 separate FOVs (1 & 3). As lifetimes have been shown to alter with cell layer in section B, the comparison has been restricted to cells from the *s.spinosum*.

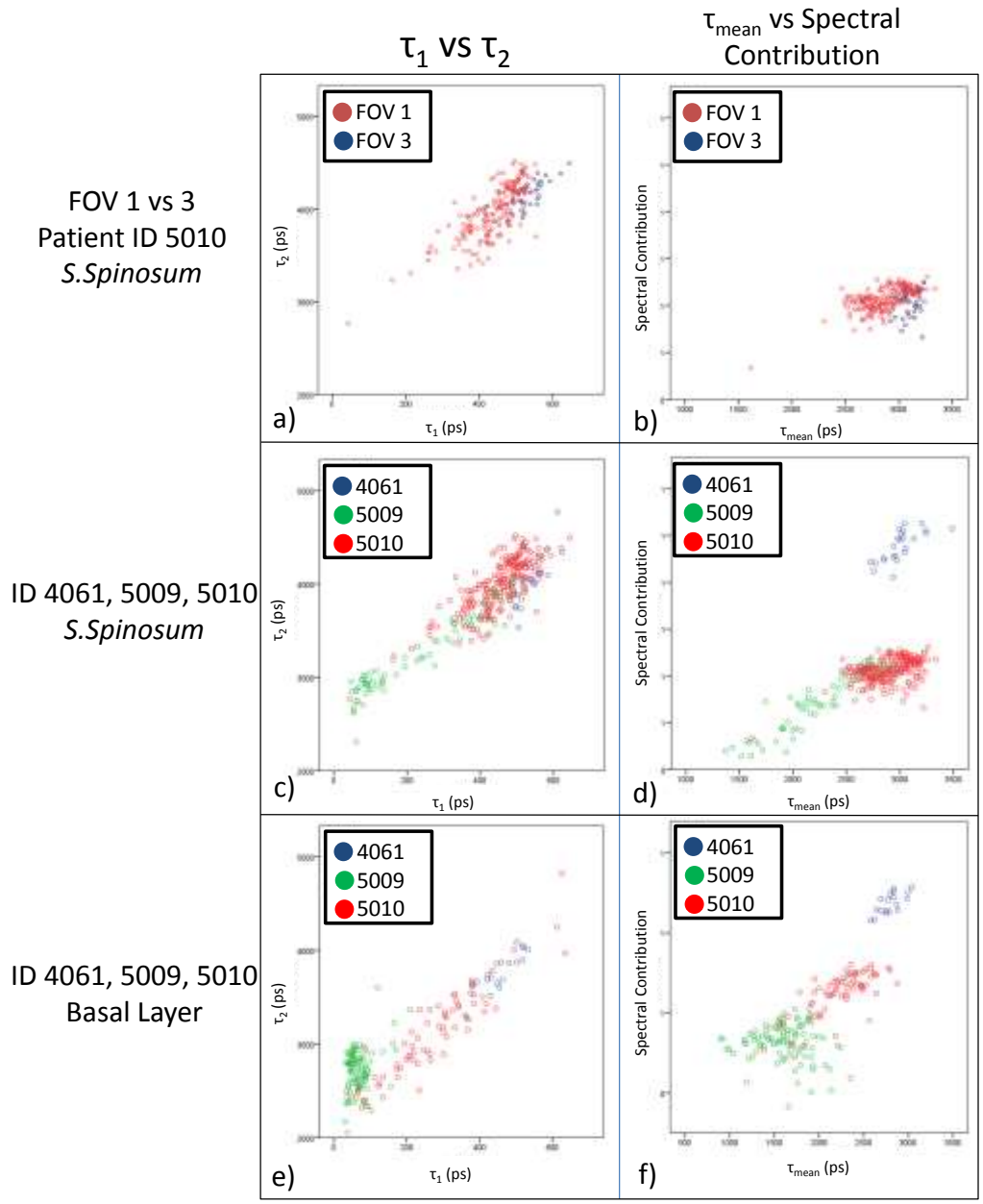

Figure 6.13 Scatter plots comparing various lifetime parameters in images acquired in the green spectral channel from cells from (a,b) 2 FOVs within the same patient. (c,d) Cells from the s.spinosum between patients. (e,f) Cells from the basal layer between patients.

Figure 6.13 a,b are scatter plots contrasting the fluorescence parameters from these two FOVs. Two sets of parameters calculated for the green spectral channel were chosen for this comparison, τ_1 vs τ_2 and τ_{mean} vs the spectral contribution. In the plots, cells from each FOV are distinguished by colour (blue vs red). Both scatter plots show that the cells have similar fluorescence profiles, however distinct clusters of points derived from each FOV exist, despite matching all possible parameters.

To assess interpatient variability, two further patients (ID 4061 and 5009)with normal skin imaged *in vivo* were matched for sex, skin type, body site to patient 5010. Ages were similar but not matched

(29, 36, 43 years). Figure 6.13c,d shows scatter plots of cells from the *s.spinosum* between these patients using the same lifetime parameters as figure 613a,b. ROIs from each patient (not FOV) are distinguished by colour in these plots. Figure 6.13e,f plots cells from the basal layer between these patients.

In the plot of τ_1 vs. τ_2 of cells from the *s.spinsoum* (panel c), the distribution from patient 4061 (blue) are very similar to those from patient 5010 (red). However, the plot of τ_{mean} vs. spectral contribution (panel d) clearly distinguishes the cells from these patients. The plots of the cells from the basal layer (panel e,f) show greater separation between them than the cells from the *s.spinosum*.

In conclusion, the plots (panels c-f) show a greater interpatient variability between lifetimes than the intrapatient variability shown between FOVs. The cells from the *s.spinosum* between patients (panels c,d) do demonstrate some interpatient overlap between clusters and the plots also demonstrate that the spectral contribution parameter seems to contrast cell fluorescence more than either τ_1 or τ_2.

These findings are consistent with those described previously by our group using a 2 spectral channel detector module with the DermaInspect® (Patalay, Talbot et al. 2011). In this paper, greater separation of cells was seen on scatter plots of τ_{mean} vs spectral contribution between FOVs taken from dysplastic naevi within the same patient than between different patients. This trend was not detected in images taken from basal cell carcinomas.

6.6.2 Cell Populations

In section 6.6.1, we have shown the clustering of cells between FOVs from the same patient on scatter plots of lifetime parameters. Figures 6.13c,d also demonstrate some overlap between clusters of cells between patients. It is known from the anatomy and physiology of the cells in the epidermis that cells have specific structural and functional properties. The finding that cells from different patients exhibit similar fluorescent properties raises the possibility that cells types with similar properties may be distinguished by their spectral properties. To investigate this, fluorescence from all cells and all patients were plotted.

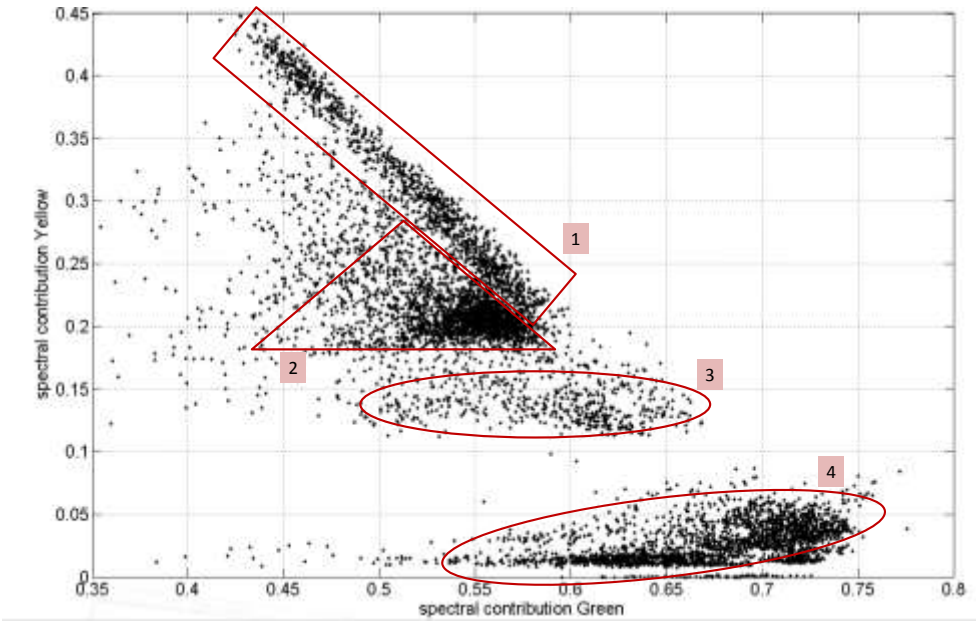

Figure 6.14 Scatter plot of spectral contribution from the green and yellow spectral channels for all cells from normal skin. 4 distinct clusters of cells have been identified.

Our research group has previously found the spectral contribution parameter to maximally contrast the autofluorescence between cells in section 6.6.1 above. Figure 6.14 shows that a number of spectrally separated clusters of cells can clearly be defined when plotting the spectral contribution in the green against the yellow channel for all cells from normal skin in all patients. These channels have been selected to find clusters of cells with similar metabolism as NAD(P)H is the brightest fluorophore in the green channel and melanin & FAD are the brightest fluorophores in the yellow channel.

It could be speculated that cells clusters with a similar spectral contributions in these channels (i.e. clusters 2 & 3) would have similar NAD(P)H and melanin (&FAD) quantities and function. The remaining clusters (1 & 4) appear to be distributed in a linear arrangement. This might represent a structural link between the cells. For example cluster 4 has low contribution from the yellow channel, which would suggest that these cells contain little melanin. The range of contribution to the green channel of these cells might represent variation in NAD(P)H fluorescence (secondary to metabolism) or the effect of other fluorophores that emits in the blue or red spectral channels.

In summary, distinct clusters of cells could be identified from the plot in figure 6.14. One method to assess these clusters further is to see how these vary with the origin of the normal skin imaged. Figure 6.14 has therefore been re-plotted, but colour coded the data based on sex, skin type, age group and body site. These can be seen in figure 6.15.

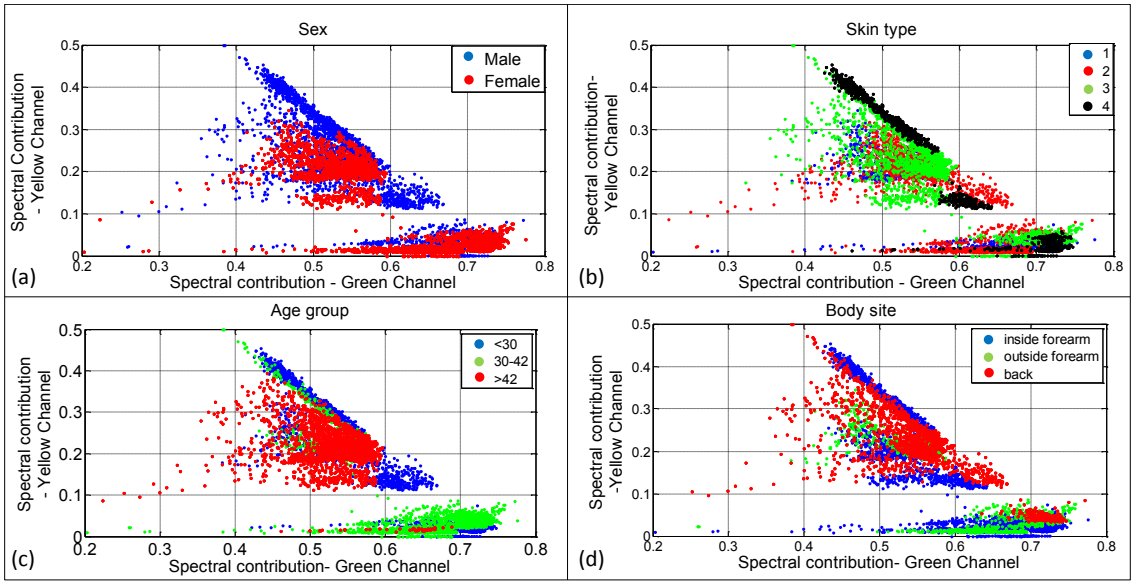

Figure 6.15 Scatter plots of the spectral contribution from all cells from normal skin, categorised by (a) sex (b) skin type (c) age group (d) body site.

These plots show that the cells from all sexes, age groups, skin types and body sites (panel a-d) contribute to clusters 2 and 4 (defined in figure 6.14). Cells from every cell layer of the epidermis are also found to contribute to all clusters (data not shown). Cluster 1 contains cells from all sexes and age groups but appears not to contain cells from the outer forearm (panel d) or from skin type 1 (panel b). As no cells from skin type 1 are seen in cluster 1, cells in this cluster might represent melanocytic cells. Contrary to this would be our expectation that the cells from the outside forearm have more melanin that those on the inside forearm which is the opposite of our findings.

Finally the presence of cells into cluster 3 varies with category. Patients from the 30-42 year old age group and cells from the outside forearm are absent from group 3. Also, cells plotted on the right side of group 3 seem to be restricted to cells from males, patients <30 years old and those with skin type 4. Similarly the left of this group only contains cells from females, >42 years old and those with skin type 3. These findings are difficult to explain easily from the data collected and require further work in the future.

In conclusion, different populations of cells based on their spectral characteristics have been identified. Although it has been speculated that these differences are based on cell pigmentation and metabolism, no definitive conclusions can be drawn from our data alone. These findings would benefit from further investigation such as using a larger population of cells or using cells grown in culture so the biological basis for the spectral changes described could be observed more directly and investigated.

6.6.3 Age

In this sub-section trends in the fluorescence lifetime from the cells from normal skin with the age of the patient are examined. Although Keohler et al. have shown a statistically significant increase in the fluorescence lifetime of the dermis with age (Koehler, Preller et al. 2011), just one publication has attempted to quantify the changes in lifetime of the epidermis with age. Benati et al. (Benati, Bellini et al. 2011) compared the lifetimes of skin *in vivo* between patients aged 20-35 and >65 years. They showed that a statistical increase in fluorescence lifetime with age for comparisons between the upper and lower epidermal layers. When fitted using a single exponential decay model, a lifetime of 1171±116 ps vs 1280±85 ps was found in the upper epidermis for the younger (n=21) and lower age groups (n=21) respectively (difference of +109 ps with age). For the lower epidermis lifetimes of 935±174 ps vs 1145±167 ps were found between the age groups (difference of +210 ps with age).

Our aim was to compare the cells from patients with different age groups and determine if a similar trend in lifetime existed with our cohort of patients. Initially patients were allocated into 3 roughly equal age group categories :- <30, 30-42 and >42 years.

		Age Group (years)			
		< 30	**30 - 42**	**> 42**	**Total**
Patient Numbers		9	9	12	**30**
Demographics	**Sex (M/F)**	6/3	4/5	7/5	**17/13**
	Skin Type (Range)	2.4 (1-4)	2.4 (1-4)	2.6 (1-4)	
In vivo/Ex vivo		8/1	7/2	3/9	**18/12**
FOV by body site	**Inner Forearm**	7	7	3	**17**
	Outer Forearm	2	5	1	**8**
	Back	1	2	5	**8**
	Face	0	0	3	**3**
	Lower Leg	0	0	1	**1**
Images Taken		41	50	53	**144**
Total Cells/ROIs		1897	2300	2707	**6904**
Cells/ROIs per Skin Layer (%)	**S.Granulosum (%)**	262 (13.8)	335 (14.6)	376 (13.9)	**973**
	S.Spinosum (%)	912 (48.1)	1007 (43.8)	1728 (63.8)	**3647**

Basal Layer (%)	723 (38.1)	958 (41.7)	603 (22.3)	**2284**

Table 6.3 Characteristics of samples used and images taken for comparison of ages with fluorescence lifetime.

Table 6.3 summarises the characteristics from the 3 age groups and shows that all are broadly matched. The eldest group includes samples from a wider variety of body site and a slight bias towards *ex vivo* samples. They also have slightly more cells from the *s.spinosum* than other groups (63.6% vs. 48.1% & 42.8%) with a corresponding fall in the proportion of cells from the basal layer.

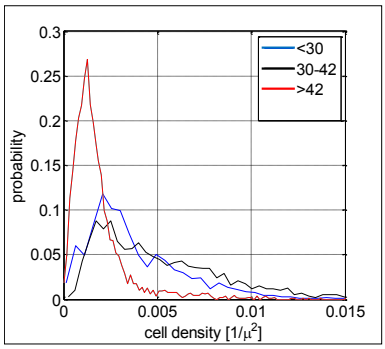

Figure 6.16 Histogram of the distribution of densities of cells from images of normal skin, categorised by age group calculated using the Gabriel method.

In section 6.5.3 (pp148) it has already been shown that cell density is a more reliable surrogate indicator for cell size. The cell density of the cells by age group has therefore been plotted in figure 6.16. The median density is 0.00301, 0.00435 and 0.00141 cells/μm^2 for the <30, 20-42 and >42 year old age groups respectively. It shows that the density of cells is similar for the age groups <42 year. The median density would appear lower for the eldest age group. From this sample, it is not clear if this difference is a true finding or caused from a lower proportion of cells arising from the basal layer in the eldest age group. Fewer cells in this layer, which have already been shown to have a higher density, would have the effect of decreasing the density measured (see figure 6.8 in section 6.5.3).

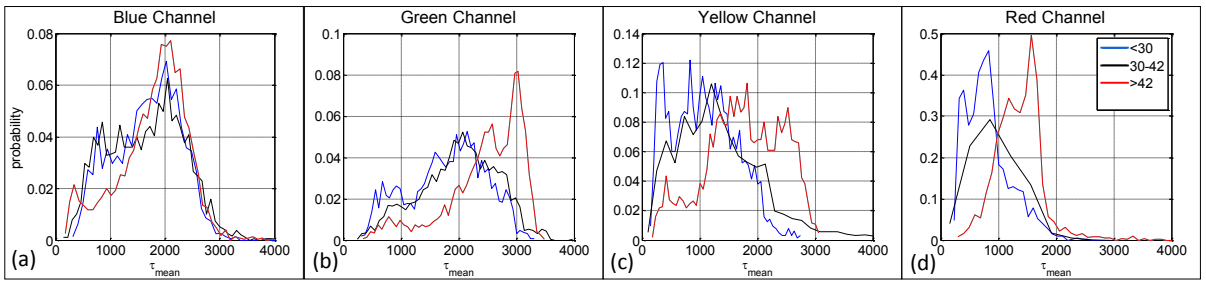

Figure 6.17 Distribution of τ_{mean} with spectral channel categorised by age group.

Figure 6.17 shows the distribution of τ_{mean} for all spectral channels categorised by age group. Like the cell densities, the distribution is very similar between the 2 age groups below 42 years. However, the >42 years group shows longer lifetimes in the green, yellow and red channels. Apart from the blue

channel, there is an increasing median τ_{mean} with age group seen in all channels. The increase in the median τ_{mean} between the 30-42 and >42 year old groups are +199, +550, +514 and +417 ps in the blue, green, yellow and red channels respectively. This is a larger lifetime difference between closer age groups than the difference of +109 and +210 ps found between patients 25-35 years and >65 years old seen by Benati et al. using a single spectral detection channel (Benati, Bellini et al. 2011). The differences in τ_{mean} between all age groups was found to be significant when analysed on a per cell basis but was not found to be statistically significant when compared on a per patient basis using the Wilcoxon rank sum test.

It has already been discussed in section 6.5.5 (pp151) that Skala et al. had associated specific lifetime changes from the fluorescence of NAD(P)H (green channel) and FAD (yellow channel) with an increased metabolism associated with dysplasia (Skala, Riching et al. 2007). By inference the reverse of these changes might suggest a decrease in cellular metabolism. The individual lifetime components from our data were therefore examined to look for clues to the underlying cause for this increase in lifetime with age. However no changes were seen in the lifetime components with age consistent with either a faster or slower cellular metabolism.

In conclusion, a decrease in the cell density was found in the >42 year old age group. However, it was not clear if this change was caused by a reduced proportion of the smaller cells from the basal layer in this category. Also a trend of longer median τ_{mean} was found with age. Between the 30-42 and >42 year old groups a lifetime difference of +199, +550, +514 and +417 ps in the blue, green, yellow and red channels respectively was found. The data supports the trends found by Benati et al., but our data does not demonstrate a significant difference in median τ_{mean} between age groups.

6.6.4 Sex

In this sub-section the changes in lifetime between the sexes is investigated. No work has previously been published on this and no difference is expected.

		Sex		
		Male	**Female**	**Total**
Patient Numbers		17	13	**30**
Demographics	**Age (Range)**	45.4 (18-81)	44.7 (17-88)	
	Skin Type (Range)	2.5	2.5	
In vivo/Ex vivo		7/10	11/2	**18/12**
FOV by	**Inner Forearm**	7	10	**17**

body site	**Outer Forearm**	1	7	**8**
	Back	8	0	**8**
	Face	1	2	**3**
	Lower Leg	1	0	**1**
Images Taken		74	70	**144**
Total Cells/ROIs		3559	3345	**6904**
Cells/ROIs per Skin Layer (%)	**S.Granulosum (%)**	300 (8.4)	673 (20.1)	**973**
	S.Spinosum (%)	1978 (55.6)	1669 (49.9)	**3647**
	Basal Layer (%)	1281 (36.0)	1003 (30.0)	**2284**

Table 6.4 Characteristics of samples used and images taken for comparison of sexes with fluorescence lifetime.

Table 6.4 summarises the characteristics from the two sexes. From the table, it can be seen that there are a significant proportion of samples from the back in males and a similar proportion from the outer forearm in females. Also, a greater proportion of ROIs arise from the *s.granulosum* in females compared to males (20.1 vs 8.4%).

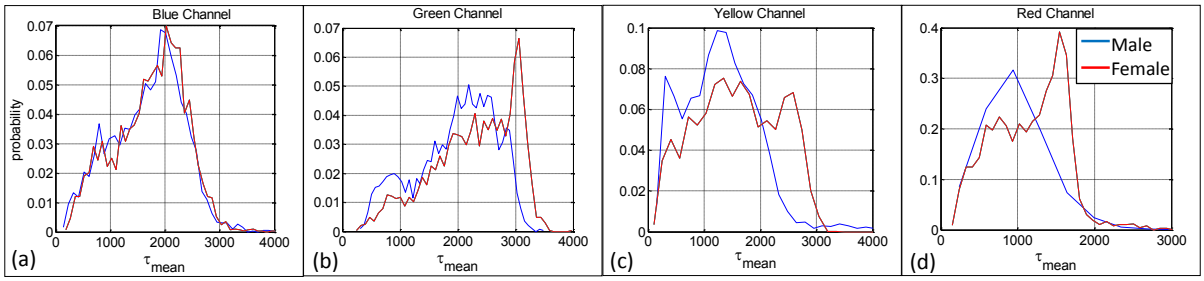

Figure 6.18 Distribution of τ_{mean} with spectral channel categorised by sex.

Figure 6.18 shows the distribution of τ_{mean} in all spectral channels, categorised by sex. Although histograms are similar, there is a noticeable population of cells with a longer lifetime in the green, yellow and red channels in the female group. In particular there is a population of cells with a τ_{mean} of 1500 ps in the red channel.

Further analysis found that 50% of the cells above a threshold of 1250 ps for τ_{mean} in the red channel arose from a single tissue sample (id 5010). The sample came from a patient who was skin type 1 and images were taken from both the inside and the outside forearm. The remaining cells arose from a further 8 samples, pointing against an outlier data set i.e. from id 5010, as the sole cause for this finding.

It was also found that the cells above this threshold in the red channel accounting for the peak seen for females were also the cells that formed the highest peak in the green channel (above threshold

of 2750 ps) and the peak with the longest τ_{mean} for females in the yellow channel (above threshold of 2250 ps). Further analysis was performed as it was not clear what the underlying cause for this finding was.

		% of ROIs		
Red Channel τ_{mean} threshold	**Layer**	**Male**	**Female**	**Difference**
<1250 ps	s.granulosum	6.46	13.57	**7.11**
	s.spinosum	49.68	40.16	**-9.51**
	basal layer	43.87	46.26	**2.40**
>1250 ps	s.granulosum	15.37	27.93	**12.56**
	s.spinosum	76.37	61.51	**-14.86**
	basal layer	8.26	10.56	**2.30**

Table 6.5 Percentage of cells in each cell layer categorised by sex, above and below a threshold of 1250 ps for τ_{mean} in the red channel.

To investigate if this could be explained by an increased proportion of cells arising from the *s.granulosum* (where cells have longer lifetimes) in the female group, the % of cells above and below a threshold of 1250 ps for τ_{mean} in the red channel for each sex and categorised by cell layer was calculated, see table 6.5. If this was a cause, it would be expected that the population of cells above this threshold in the female group would have a greater proportion of cells from the *s.granulosum*. The table shows that 27.93% of cells vs 13.57% cells arose from the *s.granulosum* above and below the threshold respectively for females. The table also shows that there is an increase in the % of cells in the *s.granulosum* for females compared to males above this threshold (7.11 to 12.56%). The net effect would be a rise in the median τ_{mean} in the population of cells above the threshold for females because it has been shown in section 6.5.4 (pp149) that lifetimes increase with distance from the basal layer.

In summary, a difference in the lifetime was found between the sexes. However, further analysis revealed that this difference was heavily contributed to by a single 'outlier' patient's data and may have arisen from the differences in the proportion of cells from each cell layer.

6.6.5 Skin type

The difference in lifetime with the Fitzpatrick skin type of patients was then investigated. The Fitzpatrick skin type measures the skin pigmented by clinical phenotype and its ability to tan and burn in the sun. The scale extends from 1 (pale skin, blue eyes, blond/red hair, always burns and never tans) to 6 (dark brown or black skin, easily tans and never burns). FLIM images have been taken from patients of skin type 1-4. Although the number of melanocytes in the basal layer remains

similar for all skin types, their activity increases with skin type. One would therefore expect to see an increase in melanin content in both the melanocytes and keratinocytes in the epidermis with skin type and thus expect to see a decrease in τ_1, τ_{mean} and increase in f_1, with a possible increase in spectral contributions from the yellow and red channels. Although studies have investigated the differences in fluorescence between skin types *in vivo* (Krasieva, Stringari et al. 2013), to our knowledge, a detailed investigation of fluorescence lifetime has not been performed before. Dancik et al. measured arms from patients with each skin type using colourimetry and MPM. They noted a positive correlation of b* (a measure of colour along the blue-yellow axis), which also correlates with skin type, to τ_1 with R^2 of 0.71 for the inside forearm and R^2 of 0.81 for the outside forearm (Dancik, Favre et al. 2013).

		Skin Type				
		1	**2**	**3**	**4**	**Total**
Patient Number		5	10	10	5	**30**
Demographics	**Age (Range)**	30.8 (18-43)	50.9 (21-88)	51.5 (17-81)	35 (25-60)	
	Sex (M/F)	2/3	7/3	5/5	3/2	**17/13**
In vivo/Ex vivo		5/0	4/6	4/6	5/0	**18/12**
FOV by body site	**Inner Forearm**	4	4	4	5	**17**
	Outer Forearm	3	3	1	1	**8**
	Back	0	4	4	0	**8**
	Face	0	1	2	0	**3**
	Lower Leg	0	1	0	0	**1**
Images Taken		31	50	37	26	**144**
Total Cells/ROIs		1578	2246	1849	1231	**6904**
Cells/ROIs per Skin Layer (%)	**S.Granulosum (%)**	327 (20.7)	322 (14.3)	182 (9.8)	142 (11.5)	**973**
	S.Spinosum (%)	922 (58.4)	1313 (58.5)	917 (49.6)	495 (40.2)	**3647**
	Basal Layer (%)	329 (20.8)	611 (27.2)	750 (40.6)	594 (48.3)	**2284**

Table 6.6 Characteristics of samples used and images taken for comparison of skin type with fluorescence lifetime.

Table 6.6 summarises the characteristics from the different skin types. The sample size is small (n=30) for this number of categories and the 4 groups are not of equal size which may confound the

results. For example, the table shows skin types 1 and 4 have ½ the number of patients compared to skin types 2 and 3. In addition they are younger, all images were taken *in vivo* and taken from the forearm only. Also, a greater proportion of ROIs were taken from the *s.granulosum* and *s.spinosum* for skin types 1 and 2 with smaller contribution from the basal layer, compared to skin types 3 and 4.

To summarise, groups with skin type 1 and 4 are younger (decreasing the expected median τ_{mean}, see section 6.6.3, pp160) and skin type groups 1 and 2 have ROIs from higher skin layers (increasing the expected median τ_{mean} , see section 6.5.4, pp149).The net effect is difficult to predict.

			Percentile		
Index	**Channel**	**Skin Type**	**25**	**50**	**75**
τ_{mean} (ps)	Blue	1	1571	1928	2256
		2	1149	1659	2126
		3	1232	1915	2202
		4	1021	1642	2081
	Green	1	2456	2926	3079
		2	1867	2277	2587
		3	1490	2084	2493
		4	921	1590	2045
	Yellow	1	1649	2254	2564
		2	1072	1464	1838
		3	778	1287	1685
		4	388	818	1232
	Red	1	1246	1484	1611
		2	885	1150	1491
		3	604	867	1141
		4	403	569	742

Table 6.7 Summary of the distribution of $\tau_{mean}$for each spectral channel, categorised by skin type.

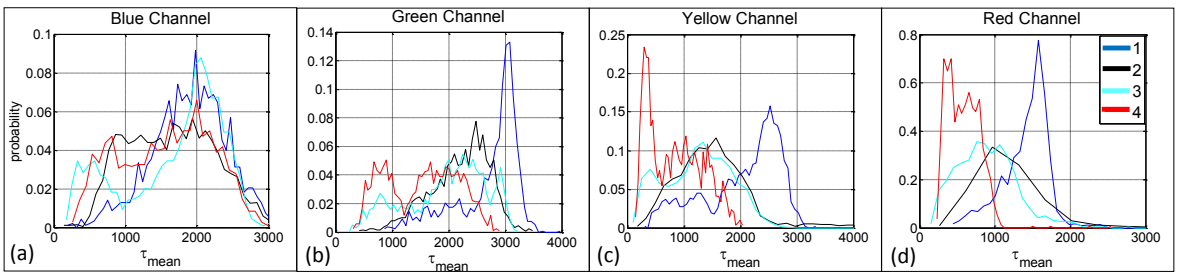

Figure 6.19 Distribution of τ_{mean} with spectral channel categorised by skin type.

The quartiles of τ_{mean} for each skin type and spectral channel is listed in table 6.7. Figure 6.19 illustrates the distribution of τ_{mean} with channel and skin type. All groups have similar distributions of τ_{mean}in the blue channel. There is also a consistent trend (that can be confirmed in table 6.7) that the median τ_{mean} decreases with increasing skin type (i.e. darker skin colour) across the remaining channels. The median τ_{mean} decreases between skin type 1 and 4 by 286, 1336, 1436 and 915 ps in the blue, green, yellow and red channels respectively. This difference was found to be statistically significant when τ_{mean} was averaged and comparing on a per patient basis using the Wilcoxon rank sum test for the green (p=0.016), yellow (p=0.016) and red (p=0.016) spectral channels.

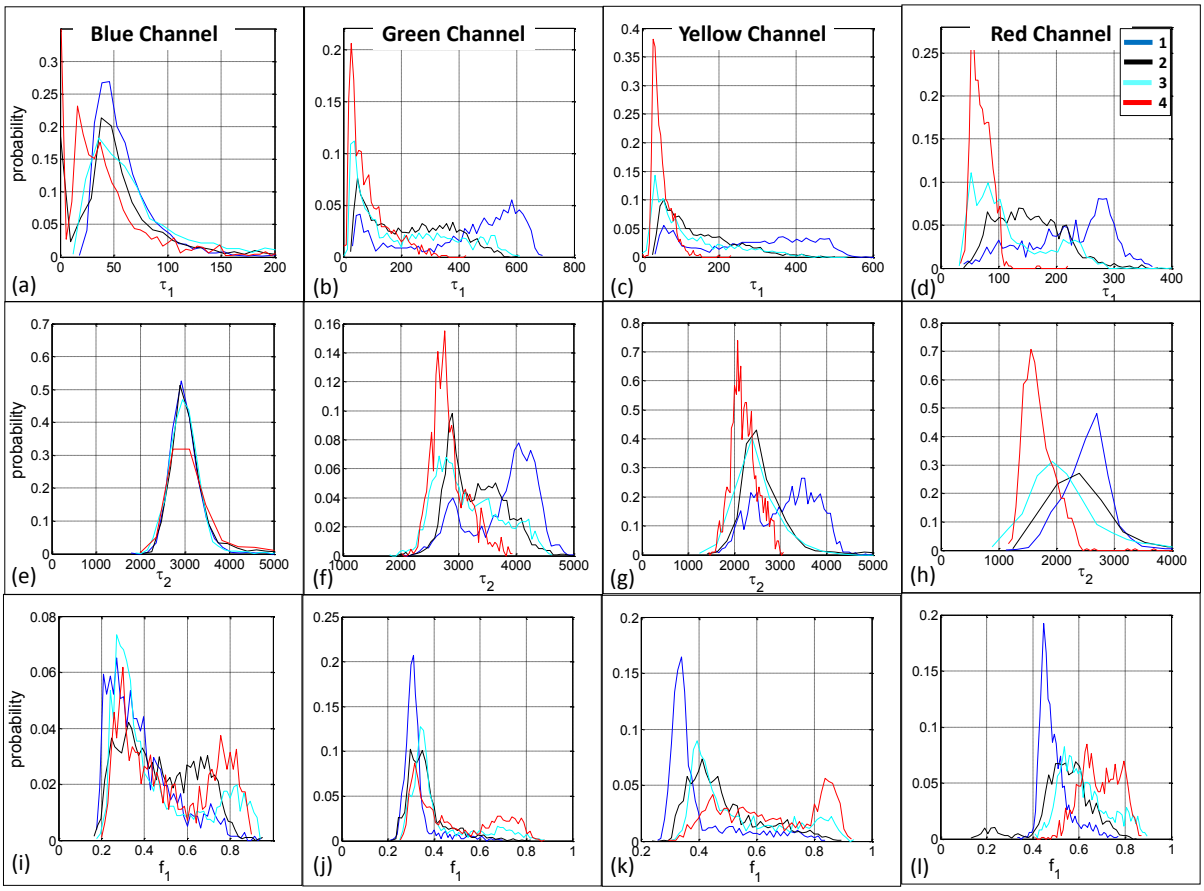

Figure 6.20. The distribution of τ_1, τ_2 and f_1 by spectral channel for each skin type.

To investigate this trend further, histograms of the distribution of $\tau_1$and τ_2 and f_1 in all spectral channels for each skin type were plotted, see figures 6.20. Again, there is very little difference between the skin types in the blue channel. In the remaining channels there is a progressive shift towards shorter lifetimes with skin type for both τ_1 and τ_2. f_1 shows an increased contribution from the shorter lifetime component with increasing skin type.

Can these changes be attributable to differing melanin content between patients with different skin types? A large population of cells with a τ_1 of <100 ps in all channels from all skin types suggests that melanin is a dominant fluorophore for the short lifetime component. Therefore the progressively

higher f_1 with skin type supports the conclusion that an increased melanin content accounts for the changes seen in τ_{mean} with skin type.

As noted previously in section 6.5.4 (pp149), either a particular melanin aggregate or contribution from a fluorophores other melanin may account for a population of cells, with a τ_1 >200 ps in the red channel. This lifetime is most noticeably from patients with skin type 1 (whom have lower baseline melanin quantities in their skin and a greater pheomelanin: eumelanin ratio in their pigment) and raises a further possibilities as to the origin of this difference.

In summary a progressive shortening of the median τ_{mean} was seen with skin phototype. This was greatest between type 1 and 4 skin and caused a 286, 1336, 1436 and 915 ps decrease in the median τ_{mean} in the blue, green, yellow and red channels respectively. This trend was reflected in τ_1, τ_2 and f_1 and felt to arise from increasing melanin content of the cells with increasing skin type. As a clear trend was detected, the biases described above between the groups known to affect lifetime i.e. age and cell layer do not appear to have affect the results significantly.

6.6.6 Body site

In this section, the differences in the fluorescence lifetime between body sites is investigated. Dancik et al. measured the fluorescence intensity and lifetimes from the forearms from 5 patients with different skin types from the inside and outside forearms (Dancik, Favre et al. 2013). They were unable to measure a difference in the fluorescence intensity between these sites in African skin, but measured between 1.4-2 times increase from Asian skin in the outside compared to the inside forearm. They also compared the fluorescence lifetimes from the skin against the fluorescence intensity within the images for body site and skin type, but did not make a direct comparison of the fluorescence lifetimes between body sites.

Benati et al. did study the fluorescence lifetime variation with body site (Benati, Bellini et al. 2011). They recorded the lifetimes of skin *in vivo* in 21 patients aged 20-35 years from the inside forearm, outside forearm and the thigh. They fitted single pixels (after binning 5x5) using a single exponential decay model. They found that the average lifetimes were found to be 1215±100, 1171±116 and 1080±103 ps from cells in the upper skin layers and 882±201, 935±174 and 931±101 ps from the lower skin layers in the inside forearm, outside forearm, and thigh respectively. The only statistically significant difference in lifetime they found was between the inside forearm and the thigh in the upper skin layers.

No explanation was offered for these differences in the paper. One may have expected less sun exposure to the skin on the thigh and possibly the inside forearm leading to a longer τ_{mean} than the

outside forearm. As this was not seen, one could conclude that either the melanin induction from photo-exposure does not have a significant contribution towards the changes seen between body sites, or differences between the patients, such as skin type, obscure this effect.

		Body Site			
		Inside Forearm	**Outside Forearm**	**Back**	**Total**
FOV imaged		17	8	8	**33**
Demographics	**Age (Range)**	34.1 (17-60)	35.6 (25-43)	58 (28-81)	
	Sex (M/F)	7/10	1/7	8/0	
	Skin Type (Range)	2.6 (1-4)	2 (1-4)	2.5 (2-3)	
In vivo/Ex vivo		17/0	8/0	0/8	**25/8**
Images Taken		72	26	34	**132**
Total Cells/ROIs		3295	1288	1560	**6143**
Cells/ROIs per Skin Layer (%)	**S.Granulosum (%)**	511 (15.5)	290 (22.5)	67 (4.3)	**868**
	S.Spinosum (%)	1699 (51.6)	493 (38.3)	859 (55.1)	**3051**
	Basal Layer (%)	1085 (32.9)	505 (39.2)	634 (40.6)	**2224**

Table 6.8 Characteristics of samples used and images taken for comparison of body site with fluorescence lifetime

From our data sets, the greatest numbers of images were taken from the inside forearm, outside forearm and the back, see Table 6.8. As more than one body site was imaged from some patients (inside and outside forearm), the number of sites imaged (n=33) is greater than the number of patients (n=30). There are a number of key differences between the groups. The images taken from the back were all taken from *ex vivo* tissue, all tissue originated from males who were older than the remaining groups. The skin type of the inner forearm group was higher (i.e. darker skin) than those of the outside forearm group, potentially obscuring changes of melanin related to photo-exposure. Finally, apart from the different number of images taken & ROIs between groups, the proportion of cells in the *s.granulosum* and *s.spinosum* varied.

			Percentile		
Index	**Channel**	**Body Site**	**25**	**50**	**75**
τ_{mean} (ps)	Blue	Back	1194	1820	2155
		Inside Forearm	1208	1741	2145
		Outside Forearm	1167	1823	2257
	Green	Back	1670	2148	2463

	Inside Forearm	1486	2070	2636
	Outside Forearm	1709	2337	2825
Yellow	Back	923	1320	1676
	Inside Forearm	747	1298	1933
	Outside Forearm	873	1434	2026
Red	Back	823	1053	1496
	Inside Forearm	579	866	1447
	Outside Forearm	831	1156	1393

Table 6.9 Distribution of τ_{mean} with body site, categorised by spectral channel

Table 6.9 shows the distribution of τ_{mean} by body site for each spectral channel. The median cell densities were 0.00174 cells/μm^2 for the back, 0.00323 cells/μm^2 for the inside forearm and 0.00286 cells/μm^2 for the outside forearm. The median cell density taken from the back was lower than those taken from the forearm. Table 6.9 shows a progressive reduction in the median τ_{mean} from the outside forearm to the back to the inside forearm for in all spectral channels. This decrease was found to be 82, 267, 136 and 291 ps between the outside and inside forearm in the blue, green, yellow and red spectral channels respectively. This difference was not found to be statistically significant when lifetimes were averaged and compared on a per patient basis using the Wilcoxon Rank Sum Test. This compares to an increase of +44 ps in the upper skin layer and a decrease of -53 ps in the lower skin layer between these same body sites found by Benati et al. (Benati, Bellini et al. 2011). There is no clear explanation for this finding.

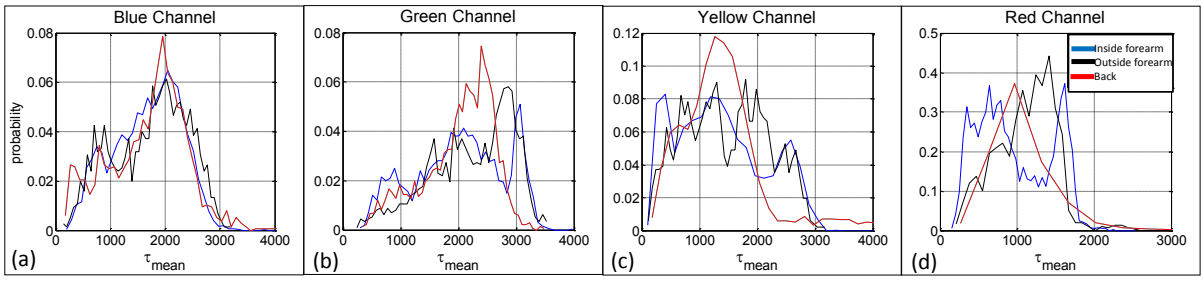

Figure 6.21 Distribution of τ_{mean} with spectral channel categorised by body site.

On closer analysis of the data, the trends in τ_{mean} detailed above and seen in the table are not as clearly visible from the histograms of τ_{mean}, shown in figure 6.21. These histograms suggest a more complex picture than originally implied by table 6.9. It has already been noted that the groups are not ideally matched and although real differences in lifetime may have been detected with our data, a more carefully controlled study would be necessary to investigate further.

One method to minimise such discrepancies is to analyse paired data taken from different body sites but from the same patient. In this way each patient acts as their own control for all parameters

except the number of cells arising from each cell layer. It is a more sensitive approach and might therefore be more successful with our small sample size. This approach was tried for 5 patients who were imaged *in vivo* from the inside and outside forearm. The results showed that no trends could be seen in τ_{mean} between pairs.

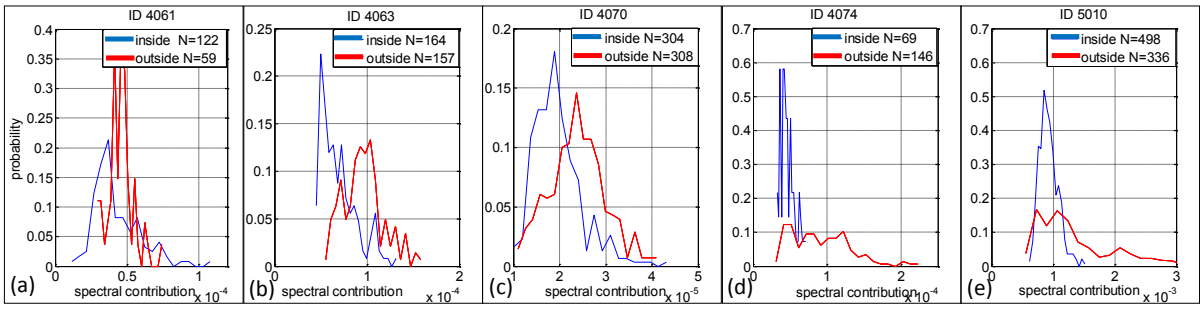

Figure 6.22 The spectral contribution in the red channel from 5 patients imaged from inside and outside forearm *in vivo*. Patient ID and number of cells indicated.

The only consistent change found was a larger spectral contribution from the outside forearm in the red channel in all patients. This is illustrated in figure 6.22 which shows the spectral contribution of the red channel from the 5 patients. This difference was not detected in the unpaired data. It was not possible to attribute this to increased melanin in the skin from the outside forearm as no consistent reduction in τ_{mean} or increase in f_1 in the yellow or red channels was seen, which might be expected with increased melanin. Therefore this trend also requires further study in order to verify it and investigate its origin.

In conclusion, a decrease in fluorescence lifetime was found between the outside and inside forearm of 82, 267, 136 and 291 ps in the blue, green, yellow and red spectral channels respectively. However, as the groups of cells analysed were not well matched, it was not clear if this difference represents a true finding. A difference in the fluorescence lifetime was also not found when paired images taken from the same patient of the inside and outside forearm. The only consistent difference detected in the paired images was a larger spectral contribution in the red channel from the outside forearm. This is of uncertain significance and should be confirmed in future studies.

These findings are in agreement with those reported by Benati et al. (Benati, Bellini et al. 2011), that no difference could be concluded between the 2 sides of the forearm. The fact that differences were seen in the lifetimes between the inside forearm, outside forearm and the back suggests that a larger, more controlled study may find statistically significant differences that our study did not have the power to detect.

6.6.7 Section C- Conclusions

In the first half of section C the intra and interpatient variability in lifetimes in normal skin has been evaluated. It has been shown that cells from the same patient have a tendency to cluster together in respect to their spectral and lifetime properties. A greater interpatient variability between lifetimes has also been shown than the intrapatient variability shown between the FOV.

When all cells were plotted by their spectral contribution in the green and yellow channels, the appearance of distinct cell populations that transcend individual patients emerged. Although it was speculated that the differences in these populations were based on cell pigmentation and metabolism, no definitive conclusions could be drawn.

The second half of section C investigated the changes in the fluorescence lifetime with a number of parameters including age, sex, skin type and body site. A longer median τ_{mean} was found between the 30-42 and >42 year old groups of +199, +550, +514 and +417 ps in the blue, green, yellow and red channels respectively. The data supports the trends found by Benati et al., but our data demonstrate a significantly longer median τ_{mean} between age groups than their cohort, although not statistically significant.

Although a difference in the fluorescence lifetime between the sexes was initially seen, it became unclear if this was a true finding and further work was suggested to investigate this.

A progressive shortening of the median τ_{mean} was seen with skin phototype of 286, 1336, 1436 and 915 ps in the blue, green, yellow and red channels respectively between skin type 1 and 4. This trend was reflected in τ_1, τ_2 and f_1 and felt to arise from increasing melanin content of the cells with increasing skin type and was found to be statistically significant using the Wilcoxon Rank Sum Test for the green ($p=0.016$), yellow ($p=0.016$) and red ($p=0.016$) spectral channels.

Finally, a decrease in fluorescence lifetime was found between the outside and inside forearm of 82, 267, 136 and 291 ps in the blue, green, yellow and red spectral channels respectively. However, as the groups of cells analysed were not well matched, it was not clear if this difference represented a true finding and further work was suggested.

6.7 Summary

The results in this chapter are the first study of normal skin using multispectral FLIM. This conclusions section aims to highlight the findings from all sections in this chapter.

In section A the morphological features seen in MPT images from normal skin are presented and discussed. An example of paired multispectral MPT FLIM images is presented with hyperspectral

images taken from the same FOV using a modified DermaInspect®. It is then demonstrated that a detailed spectral and lifetime analysis can be performed from these images using a set of epidermal and dermal images as an example. Following this, a number of morphological features noted in the FLIM images are discussed.

Section B specifically investigates the fluorescence lifetime changes seen between the different cell layers of the epidermis. In conclusion the cell density was found to increase with depth in the epidermis. A decrease in the median τ_{mean} between the *s.granulosum* and the basal layer of 1286, 1206, 1169 and 691 ps for the blue, green, yellow and red spectral channels respectively was then found, which is significantly longer than the difference reported previously (300ps). Further analysis of the lifetime parameters support the conclusion that this related to increased melanin content in the cells from the basal layer. There was however insufficient evidence from this data that a change in NAD(P)H lifetime (reflecting an increased metabolic activity) accounted for some shortening of the lifetime with depth.

On a number of occasions the lifetime seen in the red channel, especially for τ_1, had a longer than expected lifetime than could be expected for melanin. The cause for this difference remains unclear and might be attributable to an aggregate of melanin of a size that has a longer emission spectrum and a longer than average lifetime than other aggregate sizes. Another possibility is the presence of another fluorophore in the red spectral channel, other than melanin.

Section C evaluated intra- and interpatient variability in fluorescence lifetimes of normal skin. A greater variability between lifetimes has been shown between patients than the intrapatient variability shown between the FOV. The presence of distinct cell populations has also been demonstrated, for the first time using cellular fluorescence from the green and yellow channels. Although it has been speculated that the differences in these populations were based on cell pigmentation and metabolism, no definitive conclusions could be drawn without further investigation.

The changes in the fluorescence lifetime with age, sex, skin type and body site was then investigated. A longer median τ_{mean} was found between the 30-42 and >42 year old groups of +199, +550, +514 and +417 ps in the blue, green, yellow and red channels respectively which was larger than found by previous groups. Although this was a significant difference when analysed on a per cell basis, it was not found to be statistically difference on a per patient basis.

A progressive shortening of the median τ_{mean} was also seen with skin phototype of 286, 1336, 1436 and 915 ps in the blue, green, yellow and red channels respectively between skin type 1 and 4. This

trend was reflected in τ_1, τ_2 and f_1 and felt to arise from increasing melanin content of the cells with increasing skin type. This difference was found to be statistically significant when comparing on a per patient basis using the Wilcoxon Rank Sum Test for the green (p=0.016), yellow (p=0.016) and red (p=0.016) spectral channels which has not been recorded in the literature previously.

Finally, a decrease in fluorescence lifetime was found between the outside and inside forearm of 82, 267, 136 and 291 ps in the blue, green, yellow and red spectral channels respectively. However, as the groups of cells analysed were not well matched, it was not clear if this difference represented a true finding and further work was suggested.

Chapter 7. The use of autofluorescence to evaluate Basal Cell Carcinoma

7.1 Aim

The aim of the work described in this chapter was to evaluate MPT FLIM as a means to discriminate basal cell carcinomas (BCCs) from normal skin. Fluorescence intensity and FLIM images were collected from normal skin (*in & ex vivo*) and freshly excised BCCs using four emission spectral channels. This is the first time images from BCCs have been analysed using multispectral MPT FLIM and the first detailed analysis of their lifetime parameters.

A selection of FLIM images is initially presented and the visual architectural features associated with BCCs (basal cell carcinoma) are discussed. The diagnostic accuracy of using these features is then calculated. Next the diagnostic accuracy and degree of discrimination provided by the spectroscopic, lifetime and automatically calculated cellular morphological parameters are then explored.

7.2 Introduction

Basal cell carcinoma is most common in Caucasian populations and has a high prevalence in the western world (Diepgen and Mahler 2002; Demers, Nugent et al. 2005) with a rising incidence in all age groups (Christenson, Borrowman et al. 2005; Staples, Elwood et al. 2006). They are tumours that are thought to arise from the basal layer of the epidermis and can manifest as a number of clinically and histologically defined sub-types. A further introduction can be found in Chapter 1.3.1, pp30.

Initial assessment of a possible BCC is currently made on clinical examination. If a lesion arises on the face (the most common site of presentation), a diagnostic biopsy is typically performed to confirm the diagnosis. The biopsy rate is driven by the desire for a high threshold of diagnostic certainty and different subtypes can be treated differently e.g. superficial BCCs can be treated with topical cream instead of surgical excision which has cosmetic implications for the patient. This threshold for biopsy is higher for BCCs on the body and definitive excisions are more often performed based on a clinical diagnosis alone. Sometimes a biopsy may not be fully diagnostic e.g. superficial biopsies may miss the presence of deeper infiltrative components of tumour. Furthermore, identifying recurrence on biopsy may be challenging and skin with lots of adnexal elements and actinic change can add to the difficulty in the interpretation of the biopsy slides.

As a result, a large proportion of suspected BCCs have diagnostic biopsies. This involves a portion of the tumour first being excised, fixed, processed, sectioned and stained before it can be reviewed. Biopsies can be both uncomfortable, cosmetically disfiguring to the patient, time-consuming and

expensive to the clinician. As the biopsy does not always confirm a BCC or other lesion that requires further treatment, it can be seen an unnecessary in some cases.

In these circumstances a non-invasive imaging modality capable of producing optically sectioned images *in situ* with high spatial resolution and correlation with histology would be highly desirable in terms of time, cost and patient experience. Such a device could also, for the first time allow real time monitoring of the response to topical chemotherapy. The assessment of clearance or recurrence following non-invasive topical therapy is also only performed on clinical judgement, with only clinically apparent recurrences being biopsied/treated. Real time non-invasive monitoring would allow recurrences to be diagnosed earlier and facilitate more lesions to be treated with topical chemotherapy i.e. without surgery. Therefore modalities such as multiphoton tomography (MPT) FLIM have the potential to be relevant in the clinical management for patients with BCCs.

7.3 Methods

Further details regarding all aspects of the methods are outlined in Chapter 4, pp87.

7.3.1 Instrumentation

MPT was performed using the modified DermaInspect®, as described in Chapter 4.4 & 4.5, pp89,92. Fluorescence was recorded using time correlated single photon counting (TCSPC) into 256 time bins and 4 spectral channels. The spectral channels were defined as 360-425nm (blue), 425-515nm (green), 515-620nm (yellow) and 620-640/655nm (red). Minor modifications were made to the system during the study to broaden the longest wavelength channel's detection bandwidth from 620-640 to 620-655 nm and to improve the spectral separation between the 360-425 nm and 425-515 nm channels.

A motorised microscope stage (Scan IM 120 x 80, Märzhäuser Wetzlar Gmbh, Germany) was used for the sequential acquisition of data from several fields of view in a number of *ex vivo* samples (without the use of the metallic coupling ring) to allow image mosaics to be created.

Ex vivo specimens in an inverted glass bottomed petri dish were coupled to the DermaInspect® magnetically using a metallic coupling ring, attached to the dish with an adhesive tape prior to imaging. For *in vivo* imaging, a glass coverslip was attached to the metallic ring and then attached to the patient using an adhesive tape.

7.3.2 Patients and Samples

Patients attending clinics at the Department of Dermatology at Imperial College Healthcare NHS Trust were recruited. Patients gave written informed consent to participate. Images were collected

from normal skin (*in & ex vivo*) and freshly excised BCCs. Further details of the patient selection and sample preparation are described in Chapter 4.2 & 4.6 (pp87,95).

Freshly excised BCCs were rinsed with Hanks Balanced Salt Solution buffer without phenol red, calcium or magnesium (Gibco®, Invitrogen™, CA, USA), its surface moistened with the buffer solution and placed on damp gauze in an inverted glass bottomed petri dish (80-170 μm cover slip Matek®, MA,USA) immediately following excision.

Ex vivo normal skin was acquired from the margins of larger surgical excisions for suspected skin cancers. This normal skin was sufficiently distant from the tumour site to not be affected and appeared normal by clinical inspection of the surface. *Ex vivo* samples were kept at room temperature and imaged 66±38 minutes (mean±SD) after excision and prepared for imaging as outlined above for BCC samples. Images of normal skin *in vivo* were taken from patients from areas without cutaneous disease or malignancy.

The diagnoses of all excised suspected BCCs were confirmed histologically.

7.3.3 Imaging

The excitation wavelength was fixed at 760 nm. The power was adjusted according to the depth of imaging (<50 mW) and was restricted by the manufacturers to <12 mW for imaging the *s.corneum*. Each FLIM image was either 128×128 or 256x256 pixels and was acquired over 25.5 s. The mean depth imaged per sample and range (25^{th} - 75^{th} centile) was 65 μm (range 40-85 μm) for the BCCs and 62 μm (range 40-72μm) for normal skin, i.e. within the lower epidermis for most samples of normal skin. All images from BCCs were acquired from intact skin and not areas of ulceration.

7.3.4 Data Analysis

FLIM images were generated by fitting a single exponential decay to the fluorescence from each spectral channel of each pixel in the image using software written in Matlab® (R2010b, The Mathworks Inc.,USA). Regions of interest (ROI) were defined manually in each image corresponding to each cell. An example is illustrated in Chapter 4.10.4, pp105. Each ROI in each channel was then fitted to a double exponential decay model. ROI fluorescence decay curves from a single spectral channel containing fewer than 1000 photons were excluded from the analysis as they contained too few photons to reliably fit to a double exponential mode for that channel. Morphological parameters were calculated from the manually segmented ROIs within each image. These included descriptors of each ROI individually and how these relate to each other spatially. A full description of the parameters can be found in Chapter 4.10.7, pp109.

The linear discriminant analysis (LDA) was initially performed on the data using the manually segmented ROIs. ROIs containing <1000 photons in any spectral channel were also excluded from the analysis in addition to the photon threshold criteria outlined above. All the ROIs from two patients (one normal, one BCC) had <1000 photons in all spectral channels and so were excluded from the LDA entirely. Finally, the LDA was repeated using ROIs defined by automatic image segmentation as described in Chapter 4.10.8 (pp111) and using unsegmented images.

7.3.5 Image montaging

The motorised microscope stage was used to image a total of 12x8 FOVs. Each image in the montage was acquired over 25.5 s with an image resolution of 256x256 pixels. The total acquisition time for the montage was ~100 minutes. Fitting a single exponential decay model to every pixel in an image required approximately 2.5 s using an 8-core, 3.16 GHz PC with 32 GB RAM running MATLAB R2011a under Windows 7, 64 bit. Therefore the FLIM decay fitting process required a total of ~4 minutes for the entire montage in one spectral channel. Due to backlash when reversing the direction of stage motion, fully automatic image stitching using the programmed stage translation distance did not provide satisfactory results. Therefore, semi-manual image registration was employed using a software package developed in-house in LabVIEW, which required approximately 1 hour aligning the whole montage.

7.3.6 Statistics

It should be noted that all the spectroscopic, lifetime and morphological parameters and the statistical calculations were performed by Dr Yuiry Alexandrov. The Wilcoxon Rank Sum test (Lupton 1993;P119-28) was applied to study the difference in distribution of lifetimes parameters between BCC and normal groups and assess their significance. The discriminative ability of the spectroscopic and morphological ROI measurements were assessed using 2 parameters: Receiver Operator Characteristic Area Under the Curve (AUC,(Mathews 2010;P158)) and the Cohen's d statistic (Gravetter and Wallnau 2009;P262).

As described in Chapter 4.10.9 (pp112), principal component analysis (PCA) was used to reduce the dimensionality of the large number of spectroscopic and cellular morphological parameters. The first 4 principal components were then used in the linear discriminant analysis (LDA).

The LDA was performed for each ROI to classify it as arising within a BCC or normal skin. The fraction of cells classified as BCC could then be determined for each patient and an AUC and sensitivity and specificity for the correct diagnosis of each patient was then calculated.

All spectroscopic and cellular morphology parameters were included for the analysis of the manually segmented ROIs. For the automatically segmented data, only the spectroscopic parameters were included as the ROIs correlated less accurately to individual cells compared to the manually defined method, as illustrated in Chapter 4.10.8 (pp111). Unsegmented images were binned per FOV analysed by first spatially integrating the fluorescence decay profiles over each field of view, fitting the resulting decays and then calculating the mean spectroscopic parameters for each patient. These mean parameters were then included in a PCA and the first 4 components were selected for the LDA, as previously described in Chapter 4.10.9 (pp112).

7.4 Results & Discussion

					Median τ_{mean} (ps) (Inter-quartile range)			
Diagnosis	**Patients (M/F)**	**Mean Age (Range)**	**Images**	**ROIs/ Cells**	**Blue**	**Green**	**Yellow**	**Red**
BCC	19 (11/8)	64 (44-86)	110	4259	2419 (1759-2773)	2624 (2412-2819)	1908 (1582-2200)	1448 (1240-2013)
Normal Skin	27 (15/12)	42 (17-80)	122	6203	1797 (1282-2175)	2189 (1656-2709)	1380 (888-1974)	1036 (709-1428)
% difference from Normal					34.6	19.9	38.3	39.8

Table 7.1 Patient characteristics and median lifetimes for each spectral channel.

Table 7.1 summarises the patients and data used in the analysis. 19 patients with normal skin were imaged *in vivo*, the remaining samples in the study were imaged *ex vivo*. Patients had skin phototypes I-IV with a mean of 2.5 and 2.2 for normal skin and BCCs respectively. All BCCs except 2 had nodular components and 8 were mixed subtypes including infiltrative and superficial. Skin was imaged from the scalp, face, neck, chest, forearm and back for BCCs and face, forearm, back and lower leg for normal skin. The difference in median τ_{mean} between BCC and normal samples (compared on a per patient basis) was found to be statistically significant to $p<0.01$ using the Wilcoxon rank sum test ($p = 0.0013, 0.0049, 0.0061, 0.0006$ in the blue, green, yellow and red channels respectively). The fluorescence lifetimes are further discussed in section 7.4.3 (pp187). Figure 7.1 shows an exemplar image stack taken from a BCC.

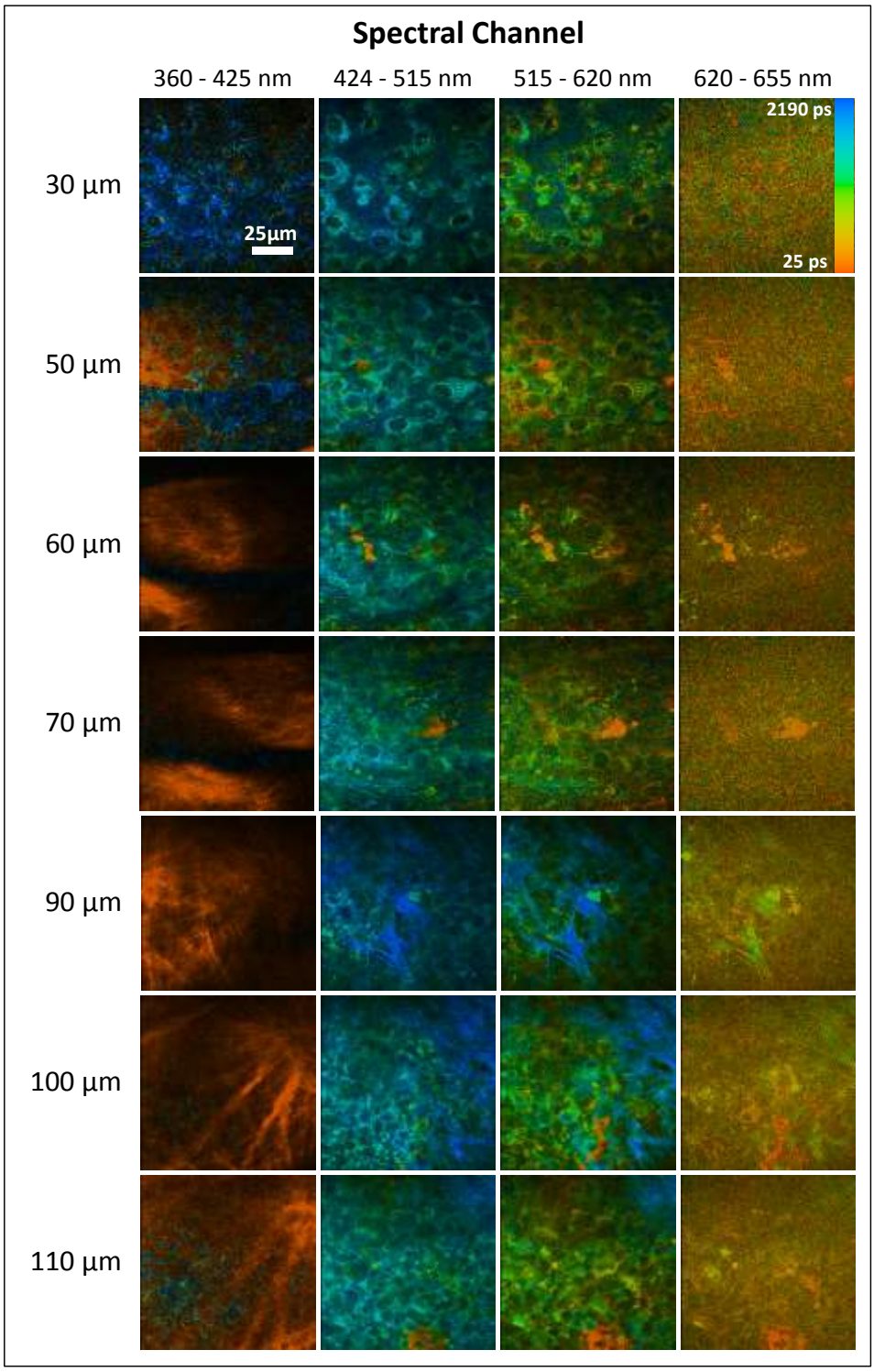

Figure 7.1 Multispectral FLIM images taken at multiple depths from a nodular/superficial BCC.

7.4.1 Visual Morphological Analysis

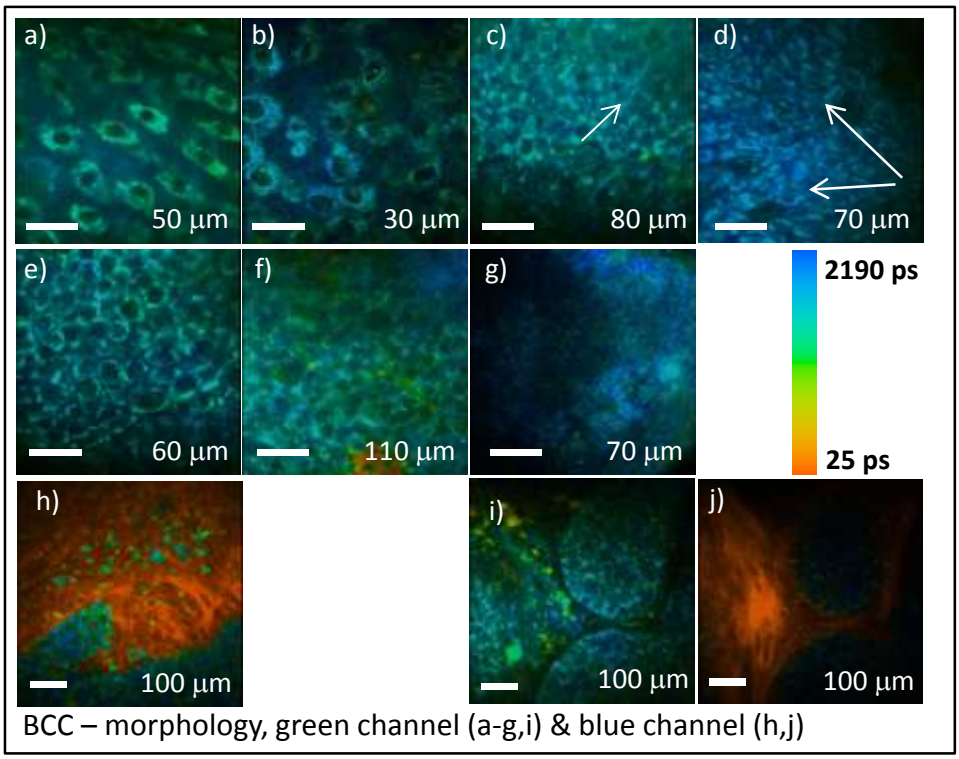

Figure 7.2 FLIM images acquired from BCCs. (a-g) FLIM images taken from the green channel illustrating visual architectural features seen in BCC using MPT. (h) FLIM image taken from the blue channel of a BCC. (i,j) paired FLIM images taken from the green and blue channels respectively of a BCC nest. Depth of image acquisition stated in bottom left corner of each panel. Scale bar 25 µm.

Figures 7.2a-j illustrates architectural changes seen in BCCs using MPT. These were identified by comparing the differences between the MPT FLIM images taken from BCCs to those from normal skin. A number of features described previously (Paoli, Smedh et al. 2008; Seidenari, Arginelli et al. 2012) (images from Seidenari et al. reproduced in Chapter 3.5, pp78) were observed. These include 'detached cells with enlargement of intercellular spaces' (panel a), 'cells with irregular contours' and 'random arrangement of cells' (both seen in panel b), 'aligned elongated cells' (panel c, white arrow), 'double alignment of monomorphous cells' (panel d, white arrows), 'palisading' (panel i) and 'sheets of cells intermingled with fibres' (panel h). The paired images in panel i, j are taken from the green and blue channels respectively and show the proximity of BCC nests to the surrounding collagen fibres ('cell islands surrounded by fibres').

In addition to these features, a pattern of monomorphous cells, often heterogeneous in size, with large nuclear/cytoplasmic ratios, poorly defined cell margins and appearing to overlap was repeatedly observed. This new feature of 'merging cells' can be seen in Figure 7.2 c,e,f,g.

Criteria for BCCs	BCC (N=19)	Normal Skin (N=27)	Sensitivity	Specificity
Random arrangement of cells	1	0	5.3	100
Cells with irregular contours	0	0	N/A	N/A
Detached cells with enlargement of intercellular spaces	2	0	10.5	100
Aligned elongated cells	6	1	31.6	96.3
Double alignment of monomorphous cells	1	0	5.3	100
Palisading	2	0	10.5	100
Sheets of cells intermingled with fibres	4	0	21.1	100
Cell islands surrounded by fibres	1	0	5.3	100
Merging Cells	8	1	42.1	96.3

Table 7.2 The sensitivity and specificity for the diagnosis of BCC listed by individual morphological feature.

Blinded to the diagnosis, all FLIM images were assessed for the presence of the MPT diagnostic morphological features for BCC described above. The results are outlined in table 7.2 which outlines the specificity and sensitivity of each feature individually. The sensitivity and specificity have been calculated as follows:-

$$\text{Sensitivity} = \frac{True\ \ Positive}{True\ \ Positives + False\ \ Negatives} = \frac{Positives\ detected\ by\ test}{Total\ positives} \quad \text{(Equation 7.1)}$$

$$\text{Specificity} = \frac{True\ Negative}{True\ \ Negatives + False\ \ Positives} = \frac{Negatives\ correctly\ identified\ by\ test}{Total\ \ Negatives} \quad \text{(Equation 7.2)}$$

As can be seen from Table 7.2 the frequency that each individual morphological feature is present in both samples of normal skin and BCCs is low. The highest frequency was the presence of 'merging cells' that was detected in 8/19 samples of BCC (42.1%).

In situations where multiple diagnostic criteria have been identified, using a threshold number of positive criteria to positively identify a disease is commonly used. . For example, this approach has been applied to diagnose systemic lupus erythematosus (threshold of 4 out of 11 criteria) (Tan, Cohen et al. 1982). More recently it has been applied to optimize the accuracy of the diagnosis of BCCs using confocal microcopy (threshold of 4 out of 5 criteria) (Nori, Rius-Diaz et al. 2004). Table 7.3 outlines the sensitivity and specificity of these criteria using several example thresholds and shows a sensitivity/specificity of 79%/93% for the presence of at least one feature.

Number of features present	BCC (N=19)	Normal Skin (N=27)	Sensitivity (%)	Specificity (%)
>=1	15	2	78.94	92.59
>=2	6	0	31.58	100
>=3	2	0	10.53	100

Table 7.3. The number, sensitivity and specificity for the diagnosis of BCC by the presence of multiple morphological features.

Although the incidence of each morphological criterion was low in our images, the presence of more than one per sample was only detected in BCCs. As a result, no images from normal skin reached the increased threshold of 2 or more criteria present, leading to a high specificity for the test. We can speculate that this arises from sampling bias in the location the images were taken within the BCC, as tumours are heterogeneous in structure.

Similarly, the number of BCC images that also have more than 2 criteria present is also lower (but not zero). Consequently the sensitivity also reduces from 15/19 for 1+ criterion to 6/19 for 2+ criteria (as calculated from equation 7.1). The sensitivity reduces further for 3 or more criteria as only two specimens meet this condition.

An alternate but similar method of expressing the presence of the morphological criteria is to list the actual score and not the threshold. This data has been listed in Table 7.4. Clearly the greater the score, the higher the probability that the images are from a BCC. Using this method and for this data, we can select a threshold of 1 for diagnosis of a BCC. This ultimately calculates the same sensitivity/specificity as above of 78.94% / 92.59%.

Score	BCC (N=19)	Normal Skin (N=27)
0	4	25
1	9	2
2	4	0
3	1	0
4	0	0
5	1	0

Table 7.4. Outline of numerically scoring the presence of morphological features in images of BCCs and normal skin.

In summary, it has been shown that the morphological features described by Seidenari et al. (Seidenari, Arginelli et al. 2012) together with the newly proposed feature of 'merging cells' provide a good specificity and sensitivity for identifying BCCs from FLIM images using a visual architectural analysis. The presence of at least one morphological feature was able to diagnose BCCs from the images taken by a sensitivity/specificity of 79%/93%.The added contrast provided by the colour FLIM

images and the spectral selectivity of features using multispectral FLIM, aided the identification of many features, especially when assessing cells within fibres, e.g. see Figure 7.2 h, j.

7.4.2 Spectroscopic & morphological analysis

			Percentile		
Index	**Channel**	**Diagnosis**	**25**	**50**	**75**
τ_{mean} (ps)	Blue	BCC	1759	2419	2773
		Normal	1282	1797	2175
	Green	BCC	2412	2624	2819
		Normal	1656	2189	2709
	Yellow	BCC	1582	1908	2200
		Normal	888	1380	1974
	Red	BCC	1240	1448	2013
		Normal	709	1036	1428
f_1	Blue	BCC	0.268	0.312	0.428
		Normal	0.299	0.397	0.589
	Green	BCC	0.326	0.349	0.380
		Normal	0.307	0.342	0.415
	Yellow	BCC	0.378	0.406	0.448
		Normal	0.374	0.455	0.617
	Red	BCC	0.490	0.532	0.585
		Normal	0.488	0.564	0.652
τ_1 (ps)	Blue	BCC	56	115	302
		Normal	34	47	71
	Green	BCC	325	418	470
		Normal	67	178	397
	Yellow	BCC	187	293	368
		Normal	53	94	232
	Red	BCC	200	263	388
		Normal	80	130	208
τ_2 (ps)	Blue	BCC	3053	3379	3766
		Normal	2800	2986	3205
	Green	BCC	3512	3857	4122
		Normal	2812	3141	3786
	Yellow	BCC	2630	3058	3476
		Normal	2217	2475	2985
	Red	BCC	2301	2917	3790
		Normal	1803	2211	2634
Spectral Contribution	Blue	BCC	0.2533	0.2740	0.3149
		Normal	0.2263	0.2527	0.2964
	Green	BCC	0.5269	0.5633	0.5923
		Normal	0.5301	0.5653	0.6633
	Yellow	BCC	0.1199	0.1601	0.1994
		Normal	0.0314	0.1828	0.2185
	Red	BCC	0.0002	0.0006	0.0036

		Normal	0.0001	0.0005	0.0011
Total Photons per ROI	Blue	BCC	5722	11739	22650
		Normal	2363	5540	11220
	Green	BCC	32062	66009	120605
		Normal	17529	31816	58006
	Yellow	BCC	15051	28605	54824
		Normal	10994	20143	37669
	Red	BCC	743	3822	24041
		Normal	4386	8837	15841

Table 7.5 – Summary of all spectroscopic parameters calculated for each ROI/cell.

A number of spectroscopic and cellular morphology parameters were calculated using code written in MATLAB to process the manually defined regions of interest (ROI), as described and illustrated in Chapter 4.10.7 (pp109). The median ROI τ_{mean} is summarised for each spectral channel in Table 7.1. The complete table of the calculated lifetime parameters, categorised by diagnosis and spectral channel is shown in Table 7.5

Parameter	Index	Channel	Cohen's d	AUC
Fluorescence Intensity	Spectral Contribution	Blue	0.45	0.63
	Spectral Contribution	Red	0.73	0.61
	Fluorescence Coefficient of Variation	Yellow	0.17	0.59
	Spectral Contribution	Green	0.48	0.58
	Fluorescence Coefficient of Variation	Blue	0.17	0.53
	Spectral Contribution	Yellow	0.03	0.52
	Fluorescence Coefficient of Variation	Red	0.20	0.52
	Fluorescence Coefficient of Variation	Green	0.06	0.51
Fluorescence Lifetime	τ_1	Red	1.44	0.82
	τ_1	Blue	1.22	0.80
	τ_1	Yellow	1.00	0.77
	τ_2	Red	0.20	0.74
	τ_2	Green	0.87	0.73
	τ_2	Blue	0.38	0.73
	τ_1	Green	0.83	0.72
	τ_2	Yellow	0.53	0.71
	f_1	Blue	0.40	0.63
	f_1	Yellow	0.57	0.62
	f_1	Red	0.34	0.59
	f_1	Green	0.29	0.52

Table 7.6 The AUC for Spectroscopic parameters.

Parameter	Index	Adjacency Calculation Method	Cohen's d	AUC
Cellular morphology	Number of Neighbours	Delaunay	0.14	0.66
	Number of Neighbours	Gabriel	0.12	0.64
	Number of Neighbours	SOI	0.17	0.62
	Cell Confluency	Gabriel	0.02	0.60
	Cell Confluency	SOI	0.02	0.60
	Cell Confluency	Delaunay	0.29	0.60
	Solidity		0.27	0.58
	Area		0.00	0.58
	Cell Density	Delaunay	0.29	0.57
	Cell Density	SOI	0.02	0.57
	Distance to Neighbours	SOI	0.14	0.57
	Distance to Neighbours	Delaunay	0.11	0.56
	Cell Density	Gabriel	0.02	0.56
	Distance to Neighbours	Gabriel	0.11	0.56
	Distance to Neighbours	SOI	0.13	0.56
	Distance to Neighbours	Delaunay	0.04	0.55
	Distance to Neighbours	Gabriel	0.02	0.54
	Orientation SD	Gabriel	0.12	0.53
	Orientation SD	Delaunay	0.14	0.53
	Orientation SD	SOI	0.13	0.53
	Flattening Factor	SOI	0.18	0.53
	Flattening Factor	Gabriel	0.17	0.52
	Gyration Radius		0.16	0.52
	Flattening Factor	Delaunay	0.16	0.52
	Shape Factor		0.05	0.52

Table 7.7 The AUC for cellular morphology parameters.

The discriminating parameters of area under the curve (AUC) the Cohen's d statistic were then calculated for individual spectroscopic and morphological parameters. The results are listed in table 7.7 and 7.7. Although the Cohen's d suggests that many of the morphological parameters are poor discriminators between BCCs and normal skin, differences can be seen in some cases.

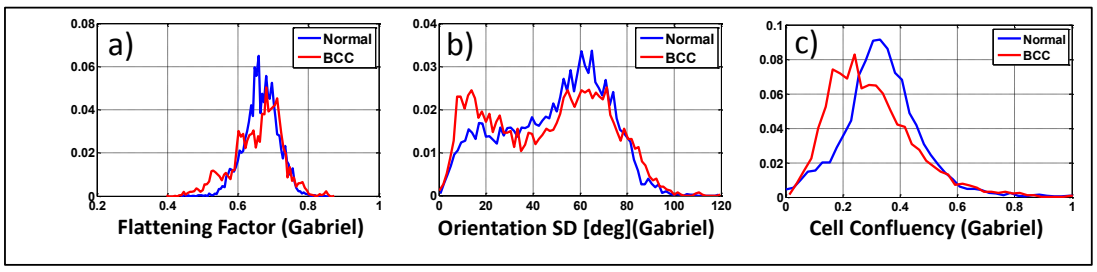

Figure 7.3 Histograms of cellular morphology features demonstrating the difference between normal skin (Blue) and BCCs (Red).

Figure 7.3a-c present histograms of the three cellular morphology parameters, namely the flattening factor (ratio of minor to major axis length), orientation SD (the standard deviation of the ROI major axis angle of a cell and its neighbours), and the cell confluency (combined area of ROI and adjacent ROIs relative to intercellular space). The difference in the median value for the orientation SD and cell confluency between BCC and normal samples was found to be statistically significant at the 5% level using the Wilcoxon rank sum test ($p = 0.03$, 0.05 respectively), but was not significant for the flattening factor ($p = 0.33$). The difference in orientation SD reflects the increase in BCCs of aligned and elongated cells and of "palisade"-like structures. The differences seen in cell confluency suggest that cells from BCCs are, on average, more sparsely arranged in an x-y plane than those from normal skin. These differences are in accordance with visual assessments of tissue morphology discussed by Seidenari et al. (Seidenari, Arginelli et al. 2012).

7.4.3 Fluorescence Lifetime

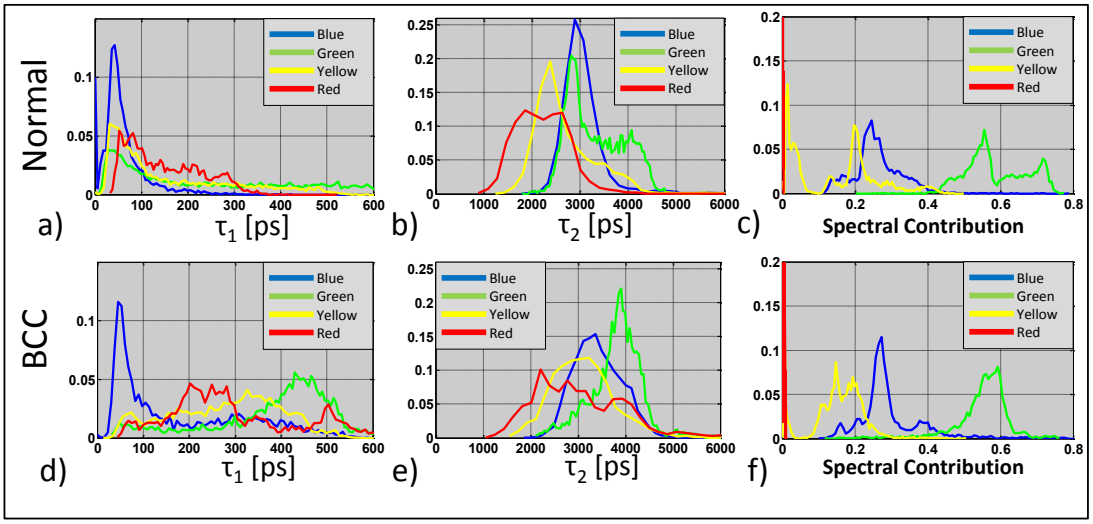

Figure 7.4 Histograms of τ_1, τ_2, spectral contribution for all spectral channels for BCC and normal skin. Curves are color-coded according to channel.

Histograms of fluorescence lifetime parameters (Figure 7.4a-f) show a shift toward longer lifetimes for BCCs in τ_1 and τ_2 for all channels compared with normal skin. Strong peaks are seen in the BCC histograms at $\tau_1 = 450$ ps and $\tau_2 = 4000$ ps in the green channel, the peak in τ_2 shifts from 2400 ps to 3000 ps in the yellow channel and new peaks in τ_1 around 250 and 500 ps are present in the red channel in BCCs. The difference in median τ_{mean} between BCC and normal samples were compared on a per patient basis and was found to be statistically significant to $p<0.01$ using the Wilcoxon rank sum test ($p = 0.0013$, 0.0049, 0.0061, 0.0006 in the blue, green, yellow and red channels respectively).

Analysis with respect to the fraction of the total fluorescence signal in each spectral channel (spectral contribution, Figure 7.4c) indicates a population of cells with a high contribution in the green channel in normal skin and a broader distribution in the yellow channel in normal skin compared to BCC (figure 7.4f). There is also an increase in spectral contribution in the red channel for BCCs which can also be seen from table 7.5.

In the cell-based spectroscopic analysis, longer τ_{mean} in all spectral channels for BCC compared to normal were observed, in agreement with earlier non-spectrally resolved FLIM MPT studies of BCC (Cicchi, Massi et al. 2007; De Giorgi, Massi et al. 2009; Seidenari, Arginelli et al. 2012). It is important to note that since normal keratinocytes are present within BCC, many cells/ROIs in the BCC FLIM images will have actually been normal cells, yet statistically significant differences were observed between groups in spite of this. From a spectroscopic perspective, it could be argued that the observed fluorescence lifetime contrast is due to a higher concentration of melanin (with a short fluorescence lifetime) in normal samples. It was not believed to be the case in this instance because the BCC dataset includes some pigmented BCCs and well matched spectral contributions were observed between groups in the melanin dominated yellow and red spectral channels (see Table 7.4). It is interesting to note that the spectroscopic parameters providing the highest discrimination (AUC) between groups are the fluorescence lifetimes of the red and yellow channels. It is possible that increased porphyrins, a dominant fluorophore in this spectral range, may account for finding. Policard originally described increased endogenous autofluorescence due to porphyrins associated with cancer in 1924 (Policard 1924). This phenomenon has since been described and commented on by others (Wagnieres, Star et al. 1998) in other tumour types. Further research is required to verify if this is the case for BCCs and if not, to elucidate the origin of this contrast.

Previous *in vivo* measurements in a hamster cheek pouch model of oral cancer by Skala et al.(Skala, Riching et al. 2007) show a decrease in the fluorescence lifetime of NAD(P)H and flavins associated with malignancy. The measurements found in our study have the opposite trend. This which may be due to differences between animal model and human, in disease pathophysiology or the absence of melanin in mucosal epithelium.

Potential confounding factors in fluorescence lifetime measurements include (Benati, Bellini et al. 2011) imaging depth in the skin (τ_{mean} decreases with depth) and patient age (τ_{mean} increases with age). In this study, image depths were well matched between groups (62 v. 65 µm mean cell/ROI depth) and are not expected to influence the results significantly. In a previous study of two very distinct age populations (20-35 and >60 years) using a single spectrally broad FLIM channel (Benati, Bellini et al. 2011), lifetimes were observed to differ between age groups by 109 ps for upper skin

layers and by 210 ps for lower layers. In this study the age disparity was much lower (mean age 42 v. 64, Table 7.1) and the observed changes in fluorescence lifetime between normal and BCC are much larger (412-622 ps, Table 7.1).

7.4.4 Lifetime variation of BCC vs normal skin

It has already been shown in Chapter 5 that there is no significant difference in the fluorescence lifetimes between *in vivo* and *ex vivo* samples over the time scale of these experiments. One factor that was explored was the variation in the median τ_{mean} for BCCs compared to normal skin.

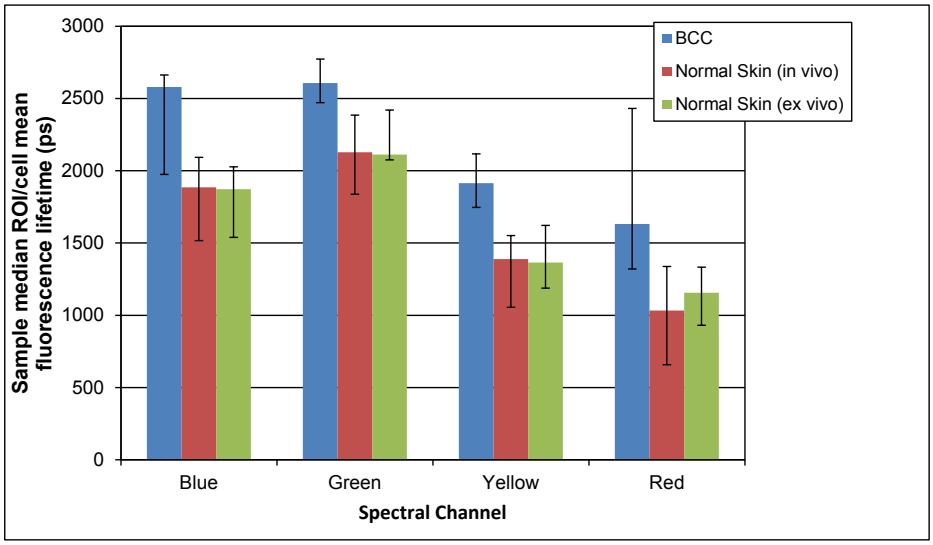

Figure 7.5 Bar chart showing sample median ROI/cell mean fluorescence lifetime per sample for BCCs, *in vivo* normal and *ex vivo* normal skin for the four spectral detection channels. Error bars indicate value of 25th and 75th percentile.

Figure 7.5 illustrates the median and variation in τ_{mean} between samples (not ROIs) of normal skin (*in vivo* and *ex vivo*) compared to BCCs. It highlights that the lifetimes calculated for BCCs are significantly longer than those seen in either *in vivo* or freshly excised normal skin in all channels, despite the range in lifetimes calculated.

7.4.5 Discrimination

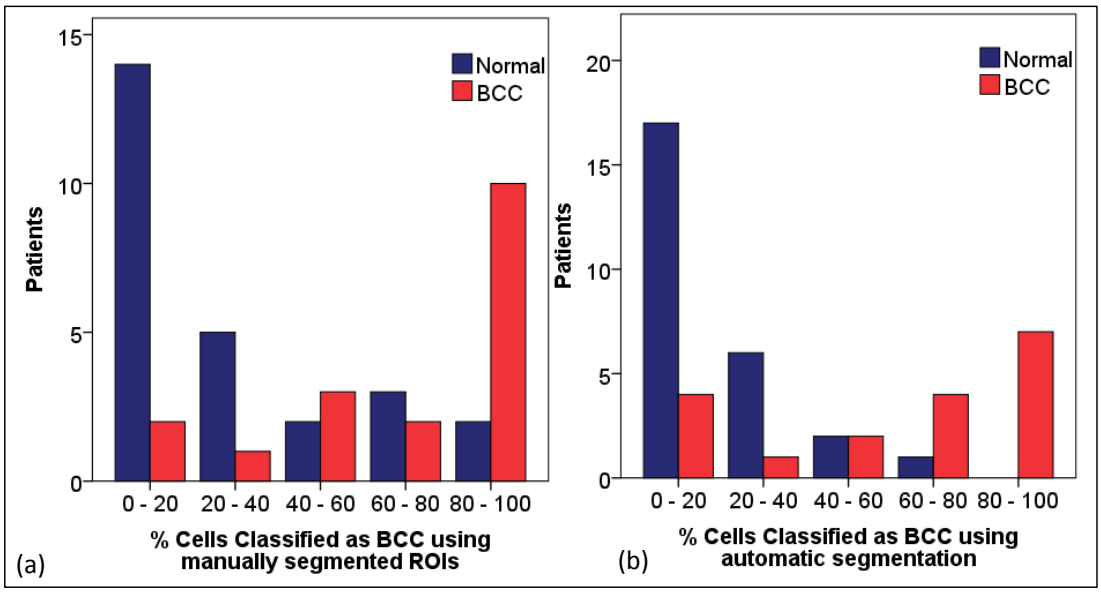

Figure 7.6. Histograms of the fraction of cells classified as BCC for the samples of actual BCCs and of those from normal skin. This analysis was performed using (a) manually segmented ROIs & spectroscopic and morphological parameters or (b) automatically segmented ROIs & spectroscopic parameters only.

In this section the use of LDA to discriminate between normal skin and BCCs is explored. PCA-based dimensionality reduction was employed to develop a diagnostic algorithm using all of the spectroscopic and cellular morphology parameters, as discussed in section 7.3.4 (pp177). LDA was then applied to the first 4 principal components of the data. This allowed each ROI to be classified as either 'Normal' or 'BCC'. The fraction of cells/ROIs classified as 'BCC' was then determined for all patients and is illustrated in figure 7.6a. The separation of these variables' distributions as measured using the AUC, was 0.83. For example, if the threshold for classifying a patient as having BCC is set at having ≥30% of cells classified as BCC, then this yields a sensitivity/specificity of 89%/73%.

To further automate the discrimination, the step of manual segmentation was replaced by automatic ROI segmentation. This procedure identified 2343 BCC and 4034 normal ROIs. Here, the cellular morphology parameters were not included in the PCA because the automatic ROI detection did not provide a clean outline of the cells and did not always correctly identify individual cells. Examples are illustrated in Chapter 4.10.8 (pp111) and Chapter 5.3.4 (pp119). However, the cellular morphology parameters only provide very weak discrimination between normal and BCC, as illustrated by the low AUC and Cohen's d values seen in table 7.6, so their exclusion was not expected to significantly affect the outcome.

Although the resulting fraction of cells/ROI's classified as 'BCC' using automatic segmentation (see Figure 7.6b) is different to that obtained with manual segmentation, the separation of these two distributions also yielded an AUC of 0.83. One might expect the discrimination based on automatically segmented ROIs to score lower than the one based on manual segmentation, due to the loss of information on the cellular morphology, the occasional grouping of more than one cell into the same ROI and erroneous inclusion of some extracellular fluorescence by the segmentation algorithm. In practice, however, the exact shape of the ROI around a single cell was not expected to greatly affect the spatially integrated fluorescence decay from that ROI or the derived fluorescence lifetime parameters. This is because the fluorescence decay profile is reasonably uniform across individual cells and the erroneous inclusion of extracellular fluorescence makes only a small contribution to the total signal analysed. Although the automatic segmentation is not perfect, it did allow bi-exponential fluorescence decay parameters to be measured at multiple regions across an image and was much less time-consuming than manual segmentation. Further work and larger numbers of patients/samples will be required to compare the relative performance of these two methods more precisely. An analysis that did not include any image segmentation was also performed for comparison and resulted in a reasonable sensitivity/specificity of 72%/84% respectively.

7.4.6 Mosaic

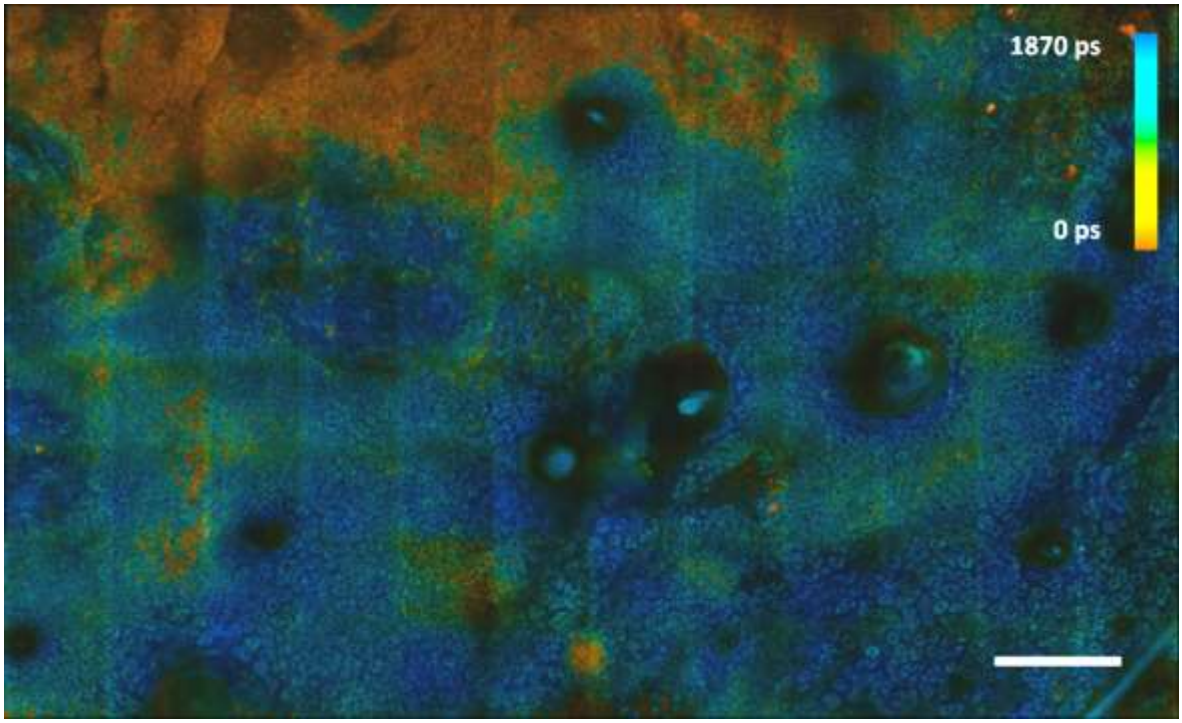

Figure 7.7 False colour mosaic FLIM image from the green channel of a BCC consisting of 12x8 FOVs covering an area of 1.86x1.24 mm^2. Bar 0.2 mm.

To observe the variation of spectroscopic and morphological parameters of a lesion across a larger field of view than is possible with the MPT instrument (350 µm x 350 μm^2), a motorised stage was employed to move *ex vivo* samples within the x-y plane and mosaics of high resolution images were then assembled. Figure 7.7 shows an example comprising 12x8 individual FLIM images from the green spectral channel acquired from a BCC. It illustrates the potential of this technique to be used for high resolution label-free histology over a large field of view.

Combining the subcellular resolution of multispectral MPT FLIM with a motorised stage to facilitate imaging over large fields of view provides a means to identify small nests of BCCs in normal skin, such as those seen with infiltrative BCCs, whose margins are notoriously difficult to define. Currently the manual acquisition and processing of montage data is slow with data acquisition, FLIM data analysis and montaging requiring approximately 100, 4 and 60 minutes respectively for 12x8 images. In the future, full automation of the image acquisition process would reduce the image acquisition time to ~45 minutes. Further reductions in image acquisition time may be possible by reducing the time required to acquire each sub-image, at the expense of signal-to-noise ratio in the final image. A wide range of sophisticated image stitching algorithms exist that could be used to greatly speed up the montaging compared to the current manual image stitching. While the current depth of penetration of MPT is too limited to assess the margins of many infiltrative BCCs *in vivo*, its high sensitivity, specificity and high spatial resolution can be exploited by stitching multiple images together to provide an extended multidimensional mosaic of such lesions. This could be useful for clinical *ex vivo* margin assessment for the future, e.g. during Mohs procedures where currently, assessment of fresh frozen sectioned tissue can take several hours.

7.5 Conclusions

This chapter presents a detailed study using multispectral MPT FLIM imaging to differentiate BCCs from normal skin for the first time. Images were acquired from 19 freshly excised BCCs and 27 samples of normal skin (*in & ex vivo*).

In this chapter existing MPT morphological features have been assessed and, together with a newly proposed feature (‘merging cells’), demonstrated that visual assessment of the images provides a sensitivity/specificity of 79%/93%. Statistically significant increases were found in the fluorescence lifetimes of cells from BCCs in all spectral channels, ranging from 19.9% (425-515 nm spectral emission) to 39.8% (620-655 nm emission). These differences are greater than those found between *in vivo* and *ex vivo* normal skin.

In addition, a detailed analysis of the discrimination between BCCs and normal skin has been performed using a number of spectroscopic and cell-based morphologic parameters for the first time. They have then been ranked them by their discriminatory power.

The first semi- and fully-automated diagnostic algorithms based on manual and automatic segmentation of MPT FLIM images is also reported. Segmentation of images into ROIs followed by principal component analysis based dimensionality reduction yielded an AUC of 0.83 for the discrimination of BCC from normal skin using LDA with both methods of segmentation.

Finally, a mosaic of BCC fluorescence lifetime images covering >1mm^2 is also presented for the first time, demonstrating the potential for tumour margin delineation.

In the future, the combination of automatically calculated spectroscopic information together with manually identified visual architectural features could lead to higher diagnostic accuracies. This work demonstrates the diagnostic potential of multispectral MPT FLIM for the evaluation of BCC and its margins.

Chapter 8. The use of autofluorescence to investigate pigmented lesions: Dysplastic Naevi & Melanoma

8.1 Aim

This chapter describes the evaluation of melanocytic lesions using MPT multispectral FLIM. To achieve this, clinically dysplastic naevi and melanomas were imaged *ex vivo* and the images analysed. Morphological features are identified that characterise melanomas from naevi and an analysis of the cellular lifetimes comparing naevi with melanomas is made with a quantitative discrimination of lifetime parameters being made, for the first time. Also mosaic MPT FLIM images acquired from both naevi and melanomas are presented for the first time.

8.2 Introduction

A naevus can be defined as benign collection of melanocytes in the skin. Melanocytes are the cells in the skin that synthesise melanin. Naevi can be subdivided into congenital naevi (those present at birth) and acquired. The acquired naevi arise from a proliferation of melanocytes at the dermo-epidermal junction after birth. Over time the natural evolution of some acquired naevi is to migrate into the dermis (Burns, Breathnach et al. 2010). This can be seen clinically as a change in appearance such as decrease in pigment and increase in nodularity. During this process they are described as compound naevi (when part of the naevus has migrated) or intradermal naevi (when the naevus has completed its migration into the dermis).

When the proliferation of a naevus deviates from that described above, its clinical appearance can be described as atypical or dysplastic in regards to size, shape and colour compared to benign naevi. These naevi are typically >5 mm in size and have some asymmetry in shape or colour. Ultimately, most of these naevi cease to proliferate and revert to the path of maturation outlined above. Their significance is that they are likely to be a precursor to and often indistinguishable from early melanoma i.e. a malignant naevus.

A clinical history from the patient and clinical examination of the lesion can help evaluate the likelihood that a dysplastic naevus is malignant. However many cases cannot be distinguished clinically and a definitive diagnosis can only be made from a histological examination of the lesion, which requires the lesion to be surgically removed. The prognosis of melanoma is critically dependent on its depth of invasion at diagnosis. Clinicians therefore have a low index of suspicion for surgical excision because the consequences of clinically monitoring a growing melanoma by a few millimetres can impact on the prognosis significantly (Roberts, Anstey et al. 2002).

In recent decades, the use of a dermatoscope, to more clearly visualise the epidermis and upper dermis, has made a significant impact on a clinician's ability to diagnose melanomas at the bedside compared to clinical examination alone (Kittler, Pehamberger et al. 2002). A number of diagnostic algorithms have been validated such as the ABCD system (asymmetry, boarder irregularity, colour, diameter) (Nachbar, Stolz et al. 1994), pattern analysis (Argenziano, Soyer et al. 2003), 7 point score (Dal Pozzo, Benelli et al. 1999) and the Menzies method (Menzies, Ingvar et al. 1996). These have been shown to have a high sensitivity (range 83-86%) and specificity (range 70-83%) for identifying melanomas from other pigmented lesions (7 point score, Menzies method) or from pigmented melanocytic lesions (ABCD system, pattern analysis). They have allowed more melanomas to be diagnosed at the bedside, and by confidently excluding melanoma, reduce the rate of unnecessary biopsies.

Despite this tool, the number of naevi excised for every melanoma still range from 8.7 to 29.4 between specialist and non-specialist dermatology centres respectively (Argenziano, Cerroni et al. 2012). This range highlights the continued importance of clinical experience, even between dermatologists for the recognition of melanomas, despite the use of a dermatoscope. This number of 'unnecessary' excisions creates a physical and financial burden on hospital services and causes unnecessary, potentially disfiguring scars for patients.

A number of non-invasive imaging modalities have been used to assess pigmented lesions, including high frequency ultrasound, optical coherence tomography and reflectance confocal light microscopy. The studies examining pigmented lesions using these modalities have been previously summarised in Chapter 1.4 (pp33-42).

This work used MPT FLIM to assess dysplastic naevi and melanomas and attempts to distinguish them using spectroscopic and morphological parameters. Although other groups have presented studies investigating lesion margins and the thickness using other non-invasive imaging modalities, this has not been measured here due to the limited penetration depth of MPT.

8.2.1 Prior studies investigating autofluorescence of pigmented lesions

Previous studies investigating tissue autofluorescence from pigmented lesions are limited with most studies investigating the emission spectra and/or fluorescence intensity images only. In 1988 Lohmann et al. (Lohmann and Paul 1988) used excitation at 366 nm (bandwidth of 11 nm) and recorded the emission spectrum from melanomas and naevi in 82 patients *in vivo*. They found that melanomas had a maximum emission peak at 475 nm wavelength which was not present in benign moles or the other inflammatory skin diseases that were measured.

Ten years later Chwirot et al. used similar equipment and an identical excitation wavelength to record fluorescence images from 408 pigmented lesions that included 90 melanomas and 205 naevi *in vivo* (Chwirot, Chwirot et al. 1998). Images were acquired through a transmission filter centred at 475 nm and were used to distinguish melanomas from naevi with as sensitivity of 82.5% and specificity of 78.6%.

In contrast Sterenborg et al. were unable to detect a difference when comparing fluorescence intensity images and emission spectra from 8 melanomas and 8 benign pigmented lesions, using and excitation wavelength of 375 nm (Sterenborg, Motamedi et al. 1994).

In 2007 De Beule et al. published the autofluorescence lifetime taken from melanocytic lesions *(De Beule, Dunsby et al. 2007)*. They used picosecond pulsed lasers to excite various freshly excised skin lesions, including 2 melanomas and 6 benign naevi at 355 nm and 435 nm wavelength. The autofluorescence was collected using a fibre optic point probe and was spectrally and time resolved. They found that melanomas exhibited a redshift in the emission spectrum and a lower average fluorescence lifetime than benign neavi when excited at 435 nm. However this was not quantified in the paper and the sample size was too small to perform any statistical evaluation.

The investigation of melanocytic lesions using MPT has been reported by three groups. Pavone's group published spectral and lifetime resolved fluorescence histograms from samples of normal skin, BCCs and a single melanoma (Cicchi, Sestini et al. 2008; De Giorgi, Massi et al. 2009).

Arginelli et al. used MPT images from 16 *ex vivo* benign naevi to define descriptors for naevi. These were then tested blindly on 102 lesions that were imaged *ex vivo*, of which 51 were melanocytic naevi and 51 were a miscellaneous group of conditions, both malignant and benign (Arginelli, Manfredini et al. 2012). They determined that 'small short-lifetime cells' in the upper and lower epidermal layers, 'edged papillae', 'junctional nests of short-lifetime cells' and 'dermal cell clusters' were 5 sensitive and specific descriptors for diagnosing benign naevi. These have been reproduced in figure 3.4 in Chapter 3 (pp.83) They also fitted the lifetimes from 3 cells per image using a single exponential decay model for images taken from 48 naevi and 48 areas of normal skin imaged *ex vivo*. They recorded a lifetime ± SD for normal skin of 1000±200 ps and 360±120 ps for naevi.

König et al. have published both a morphological analysis (Dimitrow, Ziemer et al. 2009) and a lifetime analysis (Dimitrow, Riemann et al. 2009) comparing melanocytic lesions using MPT. In the former study, 83 melanocytic lesions were imaged both *in vivo* and *ex vivo* using the DermaInspect® with an excitation wavelength of 760 nm. They found the following morphological features to be statistically significant for the diagnosis of melanoma: architectural disarray of the epidermis, poorly

defined keratinocyte cell boarders, the presence of pleomorphic cells and the presence of dendritic cells. These features are reproduced in figure 3.3 in Chapter 3 (pp81) and were found to have sensitivities ranging from 71-95% and specificities between 69-97% for each feature individually. The features of large intercellular distance and ascending melanocytes were also noted but not found to be statistically significant. The feature of pleomorphic cells associated with melanomas was also illustrated in Seidenari et al.'s review paper (Seidenari, Arginelli et al. 2012).

In Dimitrow et al.'s second paper, fluorescence lifetimes (13 naevi, 10 melanomas) and emission spectra (4 lesions) were collected from pigmented lesions. Images from lesions were taken both *in vivo* and just after excision using both 760 nm and 800 nm excitation wavelengths. They found that although FLIM could distinguish between the keratinocytes and melanocytic cells within the images, it was unable to distinguish between benign naevi and melanoma (Dimitrow, Riemann et al. 2009).

8.3 Methods

The methods for patient recruitment, image acquisition, image analysis are outlined in Chapter 4 (pp 87). In summary, patients were recruited from those attending the dermatology department at the Hammersmith Hospital site of Imperial College Healthcare NHS Trust, London. Those patients with clinically suspicious dysplastic naevi that required surgical excision were invited to participate in the study. Only lesion that were histologically confirmed as naevi or melanomas were then included in the analysis. Only image sets with all 4 spectral channels present and for which a gold nanorod IRF could be applied to the analysis were included.

All images were acquired *ex vivo*, from freshly excised samples. The time from excision for all melanomas and 26/32 naevi were recorded, allowing the imaging time post excision to be calculated for 92.9% of the cells (ROIs). The mean±SD of the acquisition time post excision were 80.6±35 minutes for the cells from naevi and 81.9±34 minutes for the cells from melanomas.

All images were acquired at 760 nm excitation wavelength with the power (<50mW) adjusted according to the depth of the image and restricted to <12mW for the *s.corneum*. A number of samples were imaged from more than field of view (FOV) with images acquired at ~10 μm intervals for most samples. The mean depth imaged was 45.5 μm for naevi and 59.0 μm for melanomas.

The FLIM images were generated by fitting a single exponential decay to the fluorescence from each spectral channel of every pixel in the image, as outlined in Chapter 4.10.3 (pp104). The FLIM analysis used ROI defined manually in each image corresponding to each identifiable cell. A double exponential decay was then fitted to the spatially integrated fluorescence from each ROI for each channel independently, as outlined in Chapter 4.10.5 (pp106). For each ROI in each spectral channel,

the total fluorescence was recorded and a τ_1, τ_2, f_1, f_2 , and τ_{mean} were calculated. ROIs with fewer than 1000 photons in a channel had insufficient photons to reliably fit a double exponential decay and were excluded. 90.5%, 100%, 100% and 98.6% of the ROIs were fitted for melanoma and 85.3%, 99.1%, 98.4%, 95.9% of the ROI for naevi were fitted for the blue, green, yellow and red channel respectively.

In addition the ROIs were used to make assessments of the cell shape, area and the spatial orientation between them. The parameters calculated are outlined in Chapter 4.10.6 (pp108).

The image montages presented in this chapter were acquired using the methods outlined in the Chapter 4.5.4 (pp95).

A more detailed description of the statistical methods used can be found in Chapter 4.10.9 (pp112). The statistical tests were performed using MATLAB®.

The discrimination between melanomas and naevi was made using the first 4 components of a principle component analysis (PCA) of the spectral, lifetime and morphological parameters. This was then categorised using linear discriminant analysis (LDA). Only ROIs that had >1000 photons for all spectral channels were included for this analysis. 89.3% and 81.2% of ROIs for melanoma and naevi respectively had sufficient ROIs in all spectral channels to be included in the analysis.

8.4 Results Summary

Diagnosis	Patients (M/F)	Mean Age (Range)	Images	ROIs/Cells
Melanoma	8 (5/3)	38.3 (27-73)	81	2177
Naevus	32 (11/21)	34.6 (20-65)	221	12632

Table 8.1 Summary of the patients and images taken from pigmented lesions used.

Table 8.1 summarises the data used in the analysis. 40 patients with histologically confirmed dysplastic naevi or a melanoma were selected for the analysis. The mean skin phototype was 2.5 for the patients with naevi and 1.9 for those with melanomas. The site of origin of the 32 naevi were as follows : 14 from the back, 6 from the arms, 4 from the legs, 4 from the abdomen, 2 from the chest and 2 from the shoulder. These were histologically classified as 14 junctional, 6 intradermal and 8 compound naevi. The sites of origin of the 8 melanomas were 4 from the back, 2 from the lower leg, 1 from the chest and 1 from the forearm. They were histologically classified as 2 in situ melanomas, 6 superficial spreading malignant melanomas of which 1 containing a nodular component. The mean Breslow thickness of the 6 invasive melanomas was 1.03 (range 0.7-1.4) mm.

8.5 Manual Morphological Analysis

8.5.1 Naevi

Figure 8.1 (4207 fov1) shows a typical image stack from a junctional neavus. Melanocytes lining the basal layer around the dermal papilla can most clearly be seen in the images taken between 80-100 μm by their short lifetimes (false colour coded in red).

Minimal differences in architectural features were seen between the FLIM images taken from dysplastic naevi and those from normal skin. One difference between FLIM images from normal skin and those from the pigmented lesions was the presence of increased melanin within the cells of the lower epidermis and basal layer in the pigmented lesions.

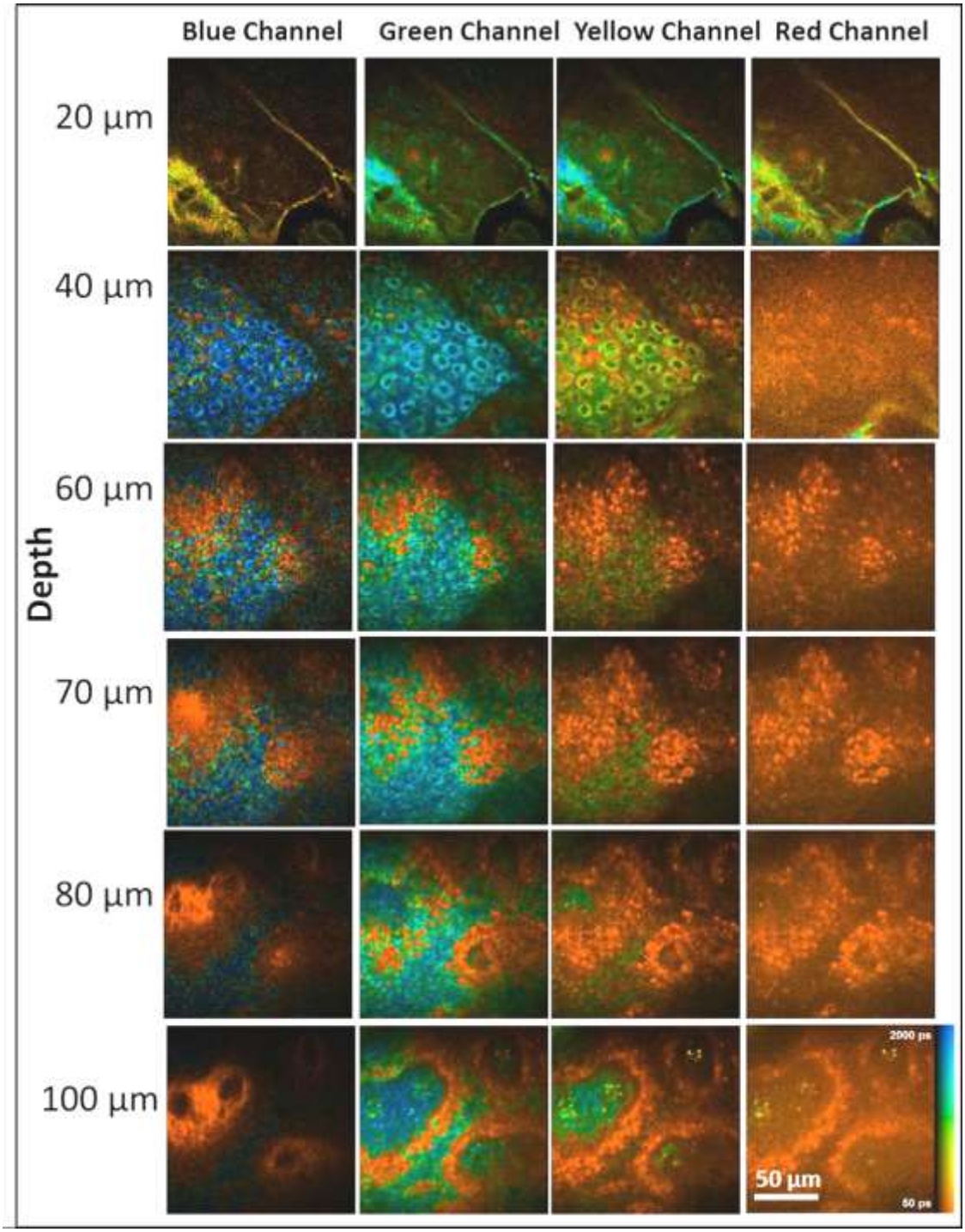

Figure 8.1 illustrates MPT FLIM images of a junctional naevus (4207 fov1) acquired using the DermaInspect® showing images taken from each spectral channel at various depths of the epidermis.

8.5.2 Melanomas

Figure 8.2 (4205 fov1) shows an image stack including all spectral channels from a superficial spreading melanoma. These images demonstrate the lack of architectural order with depth and the transition between the different layers within the epidermis has been lost.

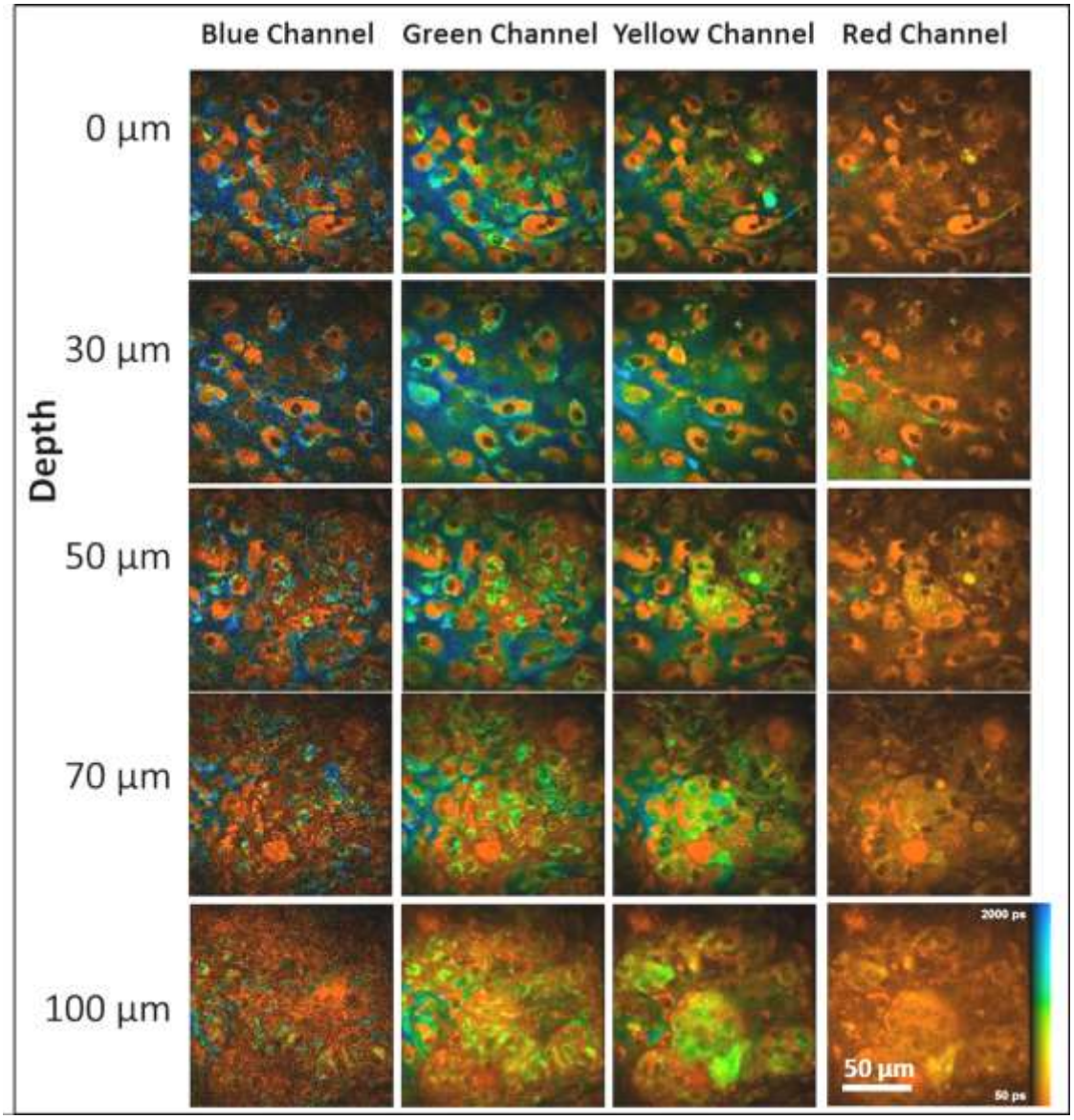

Figure 8.2 illustrates MPT FLIM images of a superficial spreading melanoma (4205 fov1) acquired using the DermaInspect® showing images taken from each spectral channel at various depths of the epidermis.

A selection of characteristic features of melanoma seen from our MPT FLIM images can be seen in figure 8.3. The identification of a number of features defined by Dimitrow et al. for the diagnosis of melanoma was difficult, particularly the presence of pleomorphic cells and poorly defined cell borders, due to the subjective nature of their identification (Dimitrow, Ziemer et al. 2009).

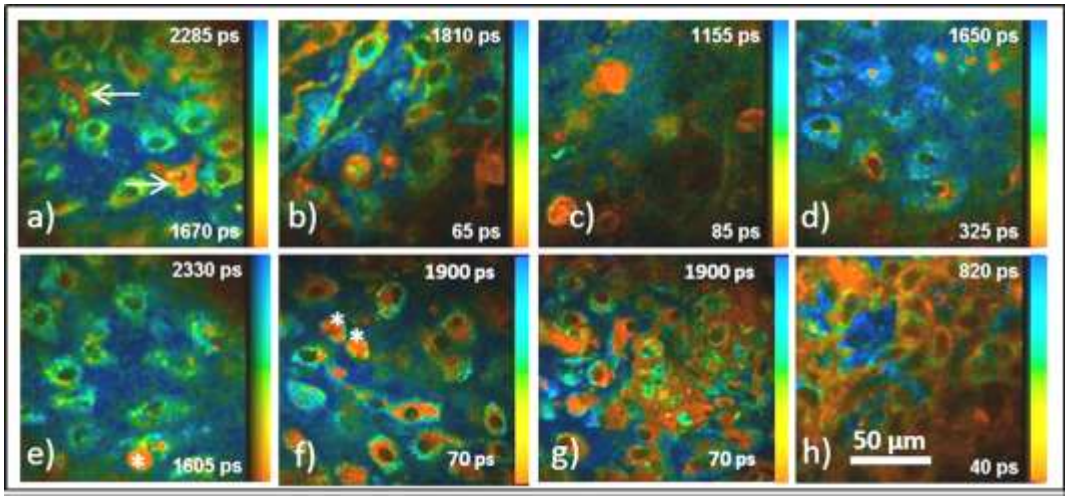

Figure 8.3 illustrates characteristic features found in melanomas. All MPT FLIM images were acquired from the green channel at various depths.(a) Melanocyte dendritic cell (arrow). (b) Multiple melanocytic dendritic cells. (c) Ascending melanocytes. (d,e) Cells with poorly defined cell borders and large intercellular distance. (e,f) Pleomorphic cells (asterisk).(g,h) Areas of fragmented cells and architectural disarray.

In Figure 8.3a a melanocyte and melanocytic dendrites (arrows) can be seen. The short lifetime (colour coded red) of the cell body and the dendrite highlighted by the arrows identify these structures as containing melanin and distinguish them from other dendritic cells that may be present in the epidermis, such as Langerhans cells. This distinction and the identification of the dendrite would be difficult without the lifetime information merged with the fluorescent intensity image. Figure 8.3b shows many dendritic cells with varying melanin content and exhibiting architectural disarray. The image in figure 8.3c was taken from the *s.corneum* and illustrates the presence of ascending melanocytes. Figure 8.3d,e illustrate images of cells with poorly defined boarders and large intercellular distance. It has been our experience that these two features co-existed together in 6/8 cases of melanoma.

It has previously been discussed in chapter 6.4.3 (pp142) that the feature of large intercellular distance is an artefact of fluorescence imaging and represents a lack of cellular autofluorescence at the cell periphery. Cells in figure 8.3e and 8.3f are pleomorphic cells (asterisk), as defined by the description and fluorescence images provided in the paper by Dimitrow et al. (Dimitrow, Ziemer et al. 2009). Figure 8.3g and 8.3h illustrate areas of fragmented cells, architectural disarray and cells with unusually morphology and increased heterogeneity of intracellular lifetimes.

8.5.3 Quantification of morphological features

The accuracy of the morphological diagnostic criteria for melanomas discussed and illustrated above (Dimitrow, Ziemer et al. 2009) were then assessed using our data. The presence of the six defined

features was assessed from the MPT FLIM images taken from each lesion. This assessment was blinded to the histological diagnosis and performed by myself.

	Melanoma (N=8)	Naevi (N=32)	AUC	Sensitivity %	Specificity %
Large intercellular distance	5	1	0.797	62.5%	96.9%
Dendritic cells	5	2	0.781	62.5%	93.7%
Ascending melanocytes	3	2	0.656	37.5%	93.7%
Poorly defined cell boarders	3	2	0.656	37.5%	93.7%
Architectural disarray	2	2	0.594	25.0%	93.7%
Pleomorphic cells	1	2	0.531	12.5%	93.7%

Table 8.2 summarises the frequency of each morphological feature identified in images from melanomas and naevi and the calculated area under the curve (AUC), sensitivity and specificity for each feature for the diagnosis of melanoma. n=40.

Table 8.2 lists the number of times that each of the morphological features was identified in the images from melanomas and naevi. The diagnostic accuracy for each feature is then calculated for each feature. The table shows that all features appear specific to the diagnosis of melanoma but have poorer sensitivities. In part, this disparity arose through the difference in the numbers of patients with each diagnosis (melanoma n=8, naevi n=32). The number of patients with melanoma is small. Therefore small differences in the number of times a morphological feature is detected translate into a large difference in the sensitivity. For example, the sensitivity for ' large intercellular distance' is calculated as 5/8 = 62.5%. If another 2 patients were included with melanoma and this feature was seen in both sets of images (likely), the sensitivity would increase to 7/10 = 70%. In contrast, the number of naevi is comparitatively large. If another 2 patients were included with naevi and this feature was seen (unlikely) then the specificity would change from (32-1)/32 = 96.9% to (34-3)/34=91.2%. This is a smaller percentage difference.

These results compares to a sensitivity range of 90-95% and specificity range of 69-86% found by Dimitrow et al. for pigmented lesions imaged *ex vivo* (n=72)(Dimitrow, Ziemer et al. 2009). In comparison our data had a similarly high specificity but lower sensitivity. Dimitrow et al. used logistic regression to determine the optimal discriminatory features. They agreed with our findings that the presence of dendritic cells was important but did not find large intercellular distance a good discriminator. However, they found that architectural disarray, poorly defined keratinocytes and the presence of pleomorphic cells as important discriminators, whilst this was not found from our data, assessed by AUC.

The study population appeared to be similar between the studies and therefore not likely to have caused the differences in the results seen between the studies. Both studies imaged naevi that were sufficiently dysplastic/suspicious to require surgical excision. Dimitrow et al. imaged melanocytic

lesions either *in vivo* or *ex vivo* or both. Although 26/83 (31.3%) patients had melanomas in the Dimitrow et al. paper, compared to 8/40 (20%) in our data (all imaged *ex vivo*), the proportion of these were imaged *ex vivo* was not explicitly stated.

	Melanoma (N=8)	**Naevi (N=32)**	**sensitivity %**	**specificity %**
N>=1	6	6	75.0%	81.3%
N>=2	5	3	62.5%	90.6%
N>=3	4	2	50.0%	93.8%
N>=4	2	0	25.0%	100.0%
N>=5	2	0	25.0%	100.0%
N=0			Negative Predictive Value of 92.8%	

Table 8.3 shows the effect of changing the threshold of the number of features necessary for the diagnosis of melanoma to be made. .

Another approach was to assess the presence of 1 or more of the diagnostic criteria for melanoma in the images from each lesion. The results are outlined in Table 8.3. It shows that the presence of 1 or more features would have a sensitivity and specificity of 75.0% and 81.3% respectively. This compares with a sensitivity and specificity of 93% and 74% respectively by Dimitrow et al.

The sensitivity significantly reduces as the number of features required increases. When tests have a high specificity but lower sensitivity, as is the case for the presence of multiple features, they are useful in clinical practice to exclude a condition confidently. In this case, the absence of all 6 features has a negative predictive valve against melanoma of 92.8%.

In summary the morphological features defined by Dimitrow et al. for the identification of melanomas from MPT intensity images has been applied to MPT FLIM images successfully. In many instances the false colour coded FLIM images facilitated the identification of the features. The features were found to have high specificities but varied in their sensitivities for the diagnosis of melanoma. Importantly the absence of all features had a negative predictive value of 92.8%.

8.5.4 Mosaics

Figure 8.4 and 8.5 are image mosaics made from images taken in the green spectral channel from junctional naevi. The image in figure 8.4 has been manually assembled and arranged within Microsoft® Powerpoint whilst the image in figure 8.5 has be semi-automatically stitched together, as described in Chapter 7.3.5 (pp178) for the BCC image montage. Figure 8.4 illustrates the distribution of the melanocytes around the dermal papilla. The lifetime information in the image allows the

keratinocytes between the dermal papilla (coloured green), the melanocytes (coloured red) and the elastic fibres in the dermis (coloured blue) to be easily distinguished. The two green vertical lines toward the right of the image the mosaic are hair follicles. Figure 8.5 (4201 fov2) shows a larger mosaic taken higher within the epidermis, above the level of the dermal papilla and shows individual cells clearly. These two image mosaics demonstrate the ability of this device to assess large areas of skin.

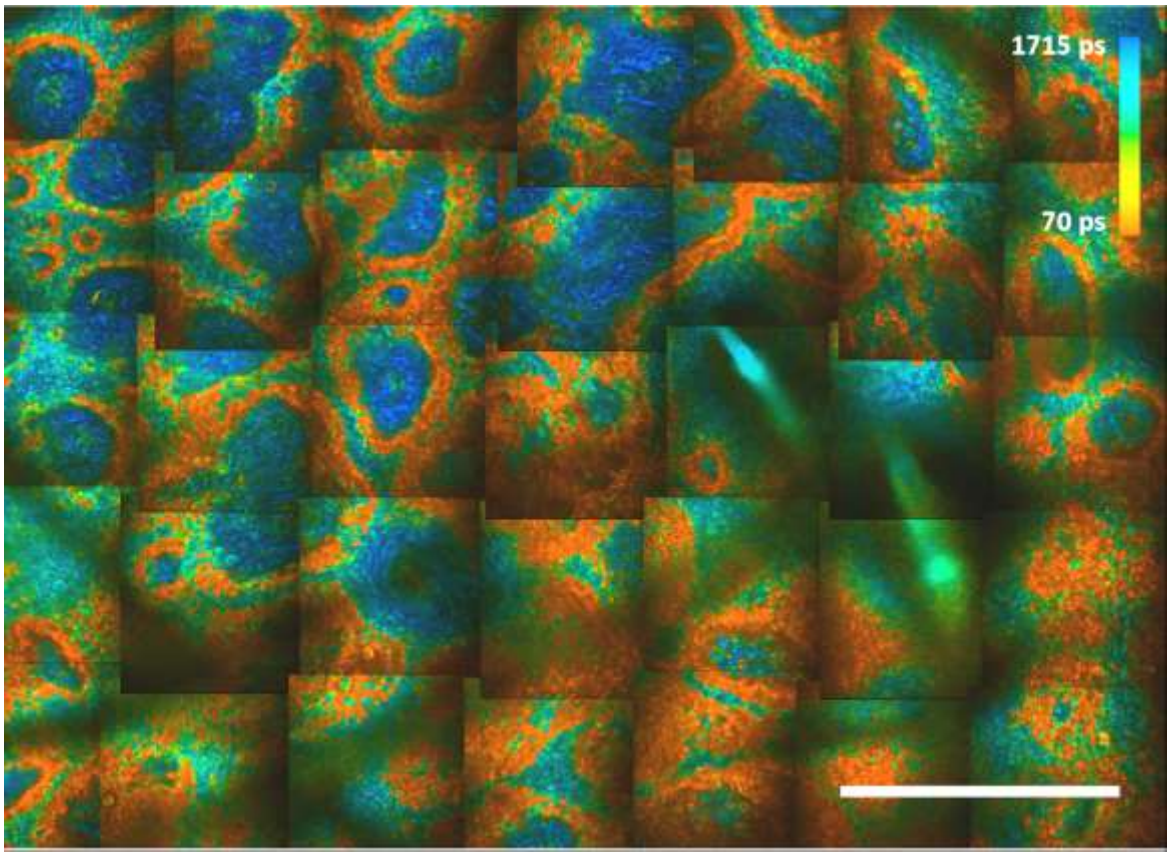

Figure 8.4 shows a montage of 7x5 MPT FLIM images taken from the green channel at a depth of 95 μm from a junctional naevus (4207 fov2). It represents an area of 1055 x 715 μm^2. Scale Bar 250 μm.

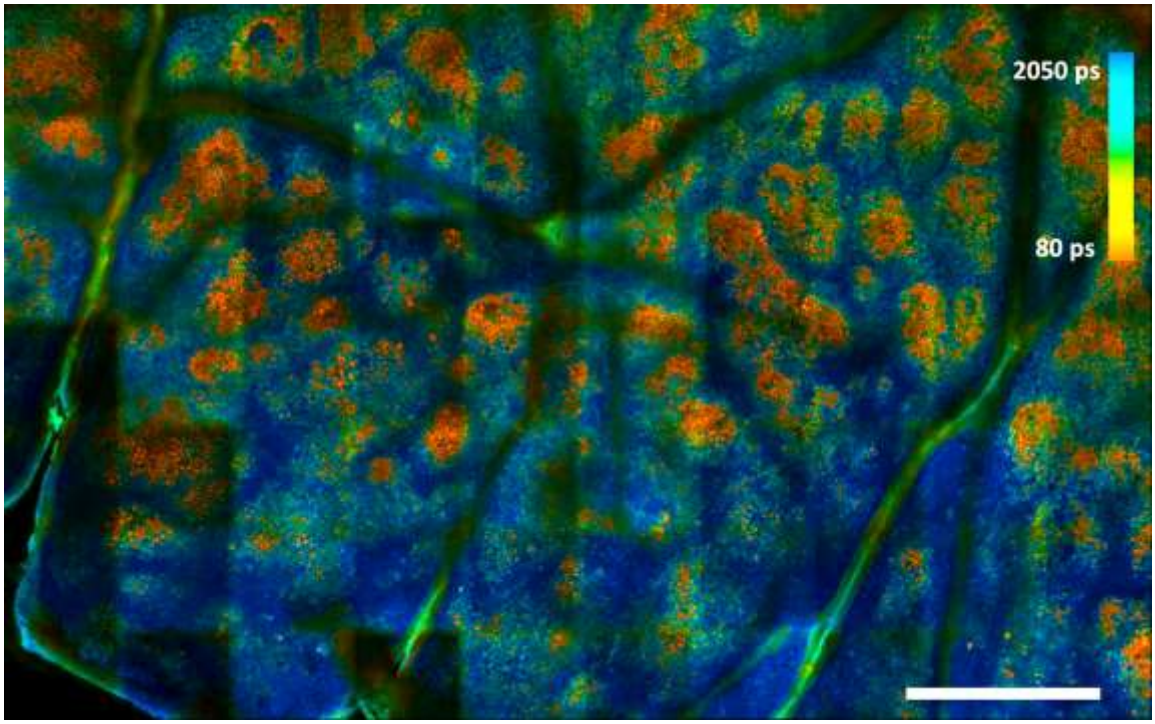

Figure 8.5 shows a montage of 10x7 MPT FLIM images taken from the green channel at a depth of 50 μm from a junctional naevus (4201 fov2). It represents an area of 1055 x 715 μm^2. Scale Bar 250 μm.

Figure 8.6 (4205 fov3) shows a mosaic generated manually within Microsoft ® PowerPoint taken from the green channel at a depth of 100 μm from a superficial spreading malignant melanoma. Many of the features described and illustrated in figure 8.3, can be seen within this mosaic.

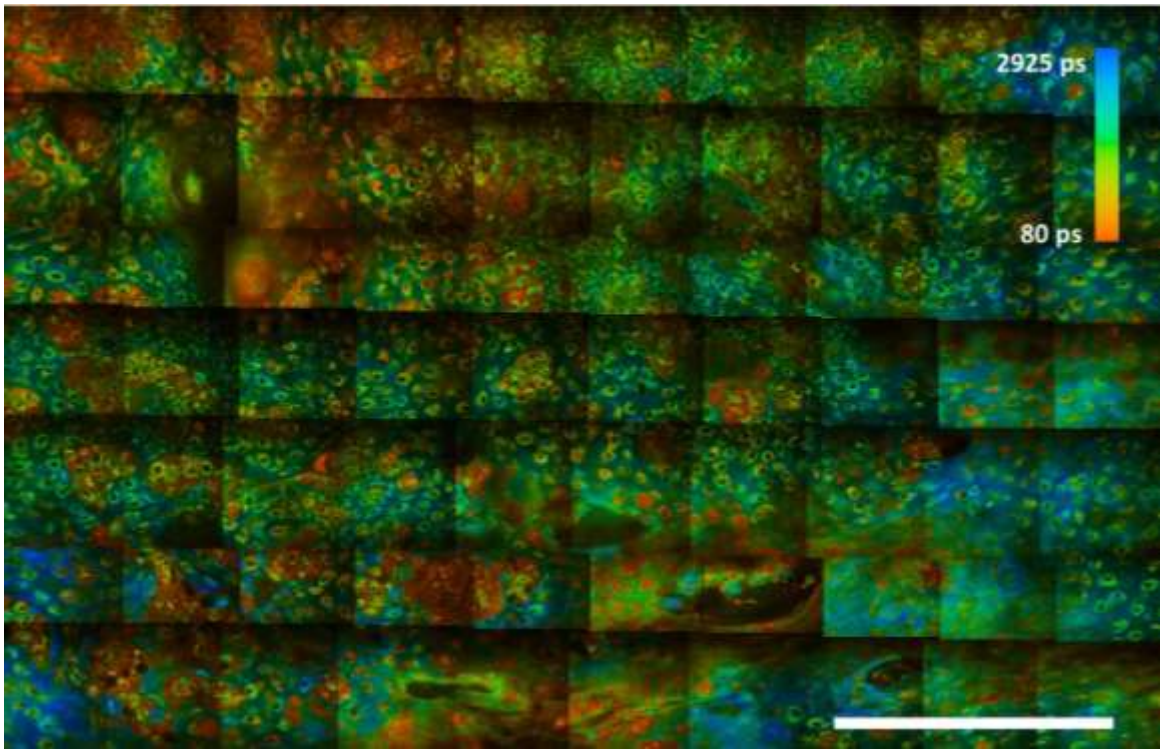

Figure 8.6 shows a montage of 10x7 MPT FLIM images taken from the green channel at a depth of 100 μm from a superficial spreading melanoma (4205 fov3). It represents an area of 1055 x 715 μm^2. Scale Bar 250 μm.

8.6 Analysis of calculated morphological and lifetime parameters

A comparison of the autofluorescence from manually segmented ROIs from images of naevi and melanomas was then performed.

8.6.1 Morphological Comparison

The morphological parameters and parameters describing the relationship between cells, previously outlined in Chapter 4.10.7 (pp109) were calculated using the manually defined ROIs. Table 8.4 lists these parameters in descending order of their discriminatory ability using AUC (area under the curve), which is a combined measure of the sensitivity and specificity and Cohen's d, a measure of discrimination between two populations.

Parameter	Index	Adjacency Calculation Method	Cohen's d	AUC
Morphology	Gyration Radius		1.38	0.85
	Area		1.27	0.75
	Cell Density	SOI	0.02	0.74
	Distance to Neighbours	SOI	1.36	0.74
	Cell Density	Gabriel	0.06	0.74

Distance to Neighbours	Gabriel	1.23	0.74
Cell Density	Delaunay	0.61	0.73
Distance to Neighbours	Delaunay	0.96	0.73
Distance to Neighbours SD	SOI	1.15	0.72
Shape Factor		0.58	0.68
Distance to Neighbours SD	Delaunay	0.36	0.66
Distance to Neighbours SD	Gabriel	0.50	0.66
Flattening Factor	Delaunay	0.55	0.62
Flattening Factor	Gabriel	0.55	0.62
Flattening Factor	SOI	0.54	0.62
Solidity		0.01	0.54
Orientation SD	Delaunay	0.12	0.54
Number of Neighbours	Gabriel	0.25	0.54
Orientation SD	Gabriel	0.09	0.53
Orientation SD	SOI	0.07	0.53
Cell Confluency	SOI	0.02	0.52
Number of Neighbours	Delaunay	0.35	0.52
Number of Neighbours	SOI	0.31	0.52
Cell Confluency	Gabriel	0.01	0.51
Cell Confluency	Delaunay	0.04	0.51

Table 8.4 lists the morphological parameters with corresponding spectral channel showing the greatest discrimination between melanoma and naevi as measured by the area under the curve (AUC) and Cohen's d.

The gyration radius (an indirect linear measure of size), area, cell density, distance to neighbour and distance to neighbour standard deviation all having a AUC of > 0.65. The gyration radius and cell area have a high Cohen's d, suggesting that they are good parameters for distinguishing melanomas from naevi. However, it has previously been shown that the manually defined ROI using the fluorescence intensity images can underestimate the cell area, especially in the *s.granulosum* (see Chapter 6.4.3) and is not a reliable parameter to use for discrimination. As the cell density parameter has been shown to be a more reliable surrogate marker for cell area, the discrimination for this was expected to be even higher. However, Table 8.4 shows that in contrast to the gyration radium and area, discrimination using cell density has less discrimination between the two groups (Cohen's d of 0.06 using the Gabriel calculation method).

The manual assessment of morphological features above in section 8.5.3 found larger intercellular spaces to show the best discrimination between melanomas and naevi with an AUC of 0.797. The

cell confluency (the closest equivalent measure), might be expected to give a similar result. However, this parameter was the worst discriminating index with an AUC of 0.51- 0.52, depending on the adjacency method used.

In conclusion, the calculated morphological and architectural parameters vary in their ability to distinguish melanomas from naevi using the AUC and Cohen's d measures of discrimination. They appear to be less sensitive at highlighting the differences observed in the FLIM images than by eye. This could be improved on in the future by using more sophisticated image analysis methods that are better able to detect the six morphological criteria defining melanomas automatically.

8.6.2 Lifetime Comparison

Table 8.5 below lists the 25th, 50th and 75th centiles for the distribution of the calculated lifetime parameters for the manually defined ROIs for melanomas and naevi.

			Percentile		
Index	**Channel**	**Diagnosis**	**25**	**50**	**75**
τ_{mean} (ps)	Blue	Melanoma	1440	1860	2300
		Naevus	1105	1480	1919
	Green	Melanoma	1525	1948	2417
		Naevus	1286	1735	2207
	Yellow	Melanoma	1027	1293	1635
		Naevus	698	1027	1410
	Red	Melanoma	580	748	1002
		Naevus	516	711	922
f_1	Blue	Melanoma	0.303	0.390	0.520
		Naevus	0.378	0.515	0.645
	Green	Melanoma	0.346	0.397	0.463
		Naevus	0.351	0.409	0.521
	Yellow	Melanoma	0.395	0.447	0.532
		Naevus	0.452	0.560	0.677
	Red	Melanoma	0.568	0.628	0.689
		Naevus	0.583	0.659	0.733
τ_1 (ps)	Blue	Melanoma	53	70	106
		Naevus	37	46	63
	Green	Melanoma	90	147	239

		Naevus	58	92	202
	Yellow	Melanoma	69	97	143
		Naevus	56	73	112
	Red	Melanoma	71	83	102
		Naevus	75	94	125
τ_2 (ps)	Blue	Melanoma	2781	3070	3424
		Naevus	2687	2942	3284
	Green	Melanoma	2780	3111	3561
		Naevus	2609	2843	3206
	Yellow	Melanoma	2087	2353	2694
		Naevus	2025	2253	2505
	Red	Melanoma	1608	1908	2322
		Naevus	1584	1850	2157
Spectral Contribution	Blue	Melanoma	0.12127	0.15324	0.19174
		Naevus	0.18247	0.20841	0.23530
	Green	Melanoma	0.44752	0.51903	0.58275
		Naevus	0.52299	0.55204	0.59021
	Yellow	Melanoma	0.18264	0.31657	0.42360
		Naevus	0.16768	0.22879	0.26678
	Red	Melanoma	0.00048	0.00104	0.00152
		Naevus	0.00056	0.00084	0.00131
Total Photons per ROI	Blue	Melanoma	1725	3578	6667
		Naevus	1347	2417	5029
	Green	Melanoma	23340	49433	84359
		Naevus	14572	24976	42678
	Yellow	Melanoma	23276	49273	97096
		Naevus	10821	19508	36582
	Red	Melanoma	4334	10982	27808
		Naevus	3124	5585	12173

Table 8.5 outlines the 25th, 50th and 75th centiles of the fluorescence intensity, fluorescence lifetime of melanomas and naevi imaged. Fluorescence parameters are subcategorised by spectral channel.

Using the data summarised in Table 8.5, histograms of the τ_{mean} and f_1 for each spectral channel were plotted between the naevi and melanomas (figure 8.7a-h). The histograms of τ_{mean} show a tendency for τ_{mean} to be longer in all spectral channels for melanomas than naevi. This consistent

difference between spectral channels reflects a longer τ_1 and τ_2 in the melanoma group for all channels except τ_1 in the red channel. The shorter median f_1 for all spectral channels for melanoma also contributes to the differences in τ_{mean} seen (see table 8.5), with a noticeable difference in its distribution seen in the blue and yellow channels (see figure 8.7e,g).

This change in distribution of f_1 between naevi and melanomas would suggest the presence of cells with a different fluorophore mix favouring the fluorophores contributing to the long lifetime component.

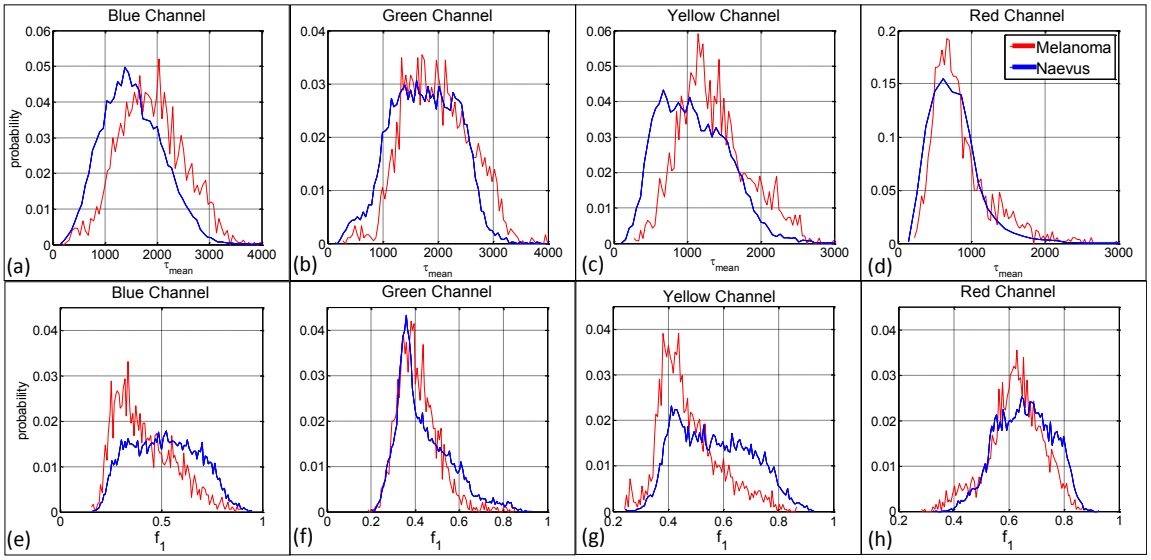

Figure 8.7 shows the τ_{mean} and f_1 for each spectral channel comparing fluorescence between naevi and melanomas.

The difference between the median τ_{mean} of naevi and melanoma are +380, +213, +266 and +37 ps for the blue, green, yellow and red spectral channels respectively and were found to be statistically significant using the Wilcox Rank Sum Test with P<0.001 for all spectral channels when compared on a per cell basis. However, when the median τ_{mean} was averaged per patient and compared, no statistically statistical difference was found between patients with melanoma and naevi.

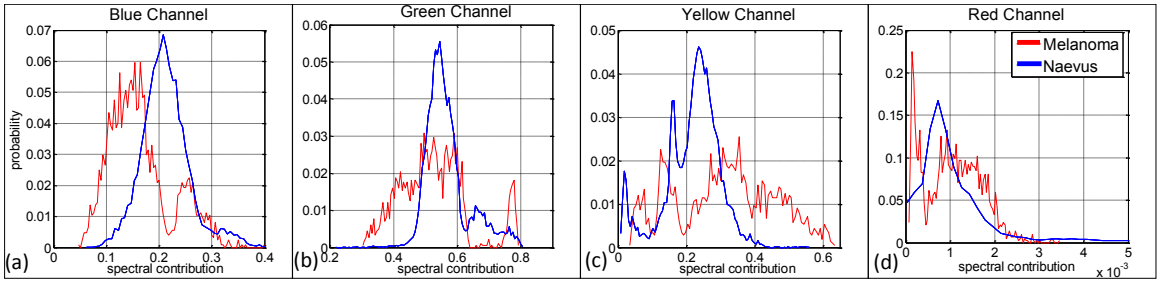

Figure 8.8 The distribution of the spectral contribution for the ROIs between the spectral channels comparing naevi with melanomas.

To investigate further the spectral contribution from each channel was analysed and can be seen in figure 8.8. The histograms in figure 8.8 show that the distribution of spectral contribution differs

significantly between the groups for all channels. The multi-peaked distribution of the histograms for melanoma, again suggest the presence of different population of cells contributing to the 'melanoma' group. As the spectral contribution in the red channel remains almost identical between groups (difference in median τ_{mean} of 0.0002), the increase in spectral contribution in the yellow channel for melanomas of 0.0878 is matched by a decrease in the blue and green channels. It shows that melanomas fluoresced relatively more brightly in this channel (515-620 nm). This increased peak in fluorescence intensity is slightly longer in wavelength than the increased fluorescence intensity commented on in Section 8.2.1 (pp198), and seen at ~475 nm by Lohmann et al. (Lohmann and Paul 1988).

The increased spectral contribution seen in the yellow channel for melanomas supports the supposition that melanoma cells have increased melanin content, which increases the relative fluorescence intensity above 500 nm. However, against this is the finding that the median τ_{mean} is increased for melanomas in the yellow channel from 1027 to 1293 ps, which does not support this theory.

The underlying cause for the differences in τ_{mean} and spectral contribution is not clear from the data collected and warrants further study for more biological correlation and to investigate further the possibility of multiple cell populations.

Parameter	Index	Channel	Cohen's d	AUC
Fluorescence	Fluorescence Coefficient of Variation	Red	1.05	0.79
Intensity	Fluorescence Coefficient of Variation	Blue	0.98	0.78
	Fluorescence Coefficient of Variation	Green	0.89	0.76
	Spectral Contribution	Blue	0.83	0.75
	Fluorescence Coefficient of Variation	Yellow	0.86	0.75
	Spectral Contribution	Yellow	1.03	0.71
	Spectral Contribution	Green	0.37	0.64
	Spectral Contribution	Red	0.05	0.55
Fluorescence	τ_1	Blue	0.58	0.74
Lifetime	f_1	Yellow	0.74	0.71
	f_1	Blue	0.60	0.67
	τ_2	Green	0.41	0.63
	τ_1	Green	0.19	0.63
	τ_1	Yellow	0.16	0.62
	τ_1	Red	0.36	0.60

f_1	Red	0.34	0.59
τ_2	Yellow	0.26	0.58
τ_2	Blue	0.02	0.56
f_1	Green	0.27	0.56
τ_2	Red	0.10	0.55

Table 8.6 lists the fluorescence intensity and lifetime parameters with corresponding spectral channel showing the greatest discrimination between melanoma and naevi as measured by the area under the curve (AUC) and Cohen's d.

The ability of the fluorescence and fluorescence lifetime to discriminate between naevi and melanomas can also be evaluated. Table 8.6 lists the florescence intensity and lifetime parameters. The results in the table support the findings above that the spectral contribution and the coefficient of variation (a measure of the variability of the fluorescence intensity) differ between the groups and can be used to discriminate between them. It also shows that although f_1 is ranked amongst the highest fluorescence lifetime parameters for discrimination using Cohen's d, overall they rank poorly compared to the fluorescence intensity and morphological parameters.

If all calculated fluorescent and morphological parameters are ranked in order of Cohen's d, morphological parameters account for the top 6/10 and fluorescence intensity for the remaining 4. The highest ranking fluorescence lifetime parameters rank 13th, 15^{th} and 16^{th} out of 45.

These results mirror the findings of Dimitrow et al. who concluded that lifetimes were unable to distinguish between melanoma and naevi (Dimitrow, Riemann et al. 2009).

8.6.3 Discrimination of combined parameters

The methods used to assess discrimination have treated each ROI as independent data and assigned it to either the naevi or melanoma categories. Whilst this approach is the most simple and appropriate for this sample size, it does not account for ROIs being clustered into distinct samples/patients, i.e. the sample identification for each ROI is discarded.

Therefore, to combine the discriminatory ability of combining multiple parameters (based on the manually defined ROIs) and making an assessment of diagnosis at the patient level, a linear discriminant analysis (LDA) was employed. The methods are described further in Chapter 4.10.9 (pp112). In brief, principle component analysis (PCA) was initially performed to reduce the dimensionality of the data using the calculated parameters. The first 4 components where then selected for inclusion in the LDA. The proportion of ROIs identified as malignant for each patient could then be used to calculate an AUC.

Using the manually segmented ROI data, when all spectral intensity, fluorescence lifetime and morphological parameters were included for the PCA, an AUC of 0.66 was calculated for the discrimination on a per patient basis. This reduced to 0.54 when the morphological parameters were excluded. This reduction in AUC is consistent with the results above that each individual fluorescence parameter has a poor discriminatory ability.

As a comparison, just the spectral intensity and fluorescence lifetime parameters were used for the LDA using automatically segmented images, as described in Chapter 4.10.8 (pp111). The AUC calculated on a per patient basis was 0.65. Finally, these parameters were used to compare non-segmented images using LDA. An AUC of 0.65 was also found for this comparison. Although this suggests segmentation is unnecessary, the large difference in the number of images included between melanomas and naevi (43 vs 145) makes this a less valid comparison to make and further work would need to be undertaken to quantify this difference further.

These calculations show that although the discrimination using manually characterised images for features of melanomas is good, the spectral, lifetime and automatically defined morphological features are poor at discriminating them.

8.7 Conclusions

In conclusion, a detailed qualitative and quantitative assessment of the autofluorescence and autofluorescence lifetime from pigmented lesions has been made for the first time. Fluorescence lifetime images acquired *ex vivo* using multispectral MPT FLIM between 8 melanomas and 32 dysplastic naevi were compared. A number of exemplar image stacks from naevi and melanomas including mosaic images taken from both naevi and melanomas of larger fields of view are shown.

A sensitivity and specificity for identifying melanomas using 6 features previously identified by Dimitrow et al. (Dimitrow, Ziemer et al. 2009) was made. Specificities ranging between 93.7 – 97% were calculated for all parameters, with only the sensitivity of 'large intercellular distance' and the presence of dendritic cells reaching >50%. However, when the presence of 1 or more feature was assessed, a sensitivity and specificity of 75% and 81% respectively was found, with the absence of all 6 features having a negative predictive valve against melanoma of 92.8%.

A qualitative and quantitative analysis of the morphological/architectural features calculated from the manually segmented ROIs was then performed. These parameters varied widely in their ability to distinguish between the two groups, as measured by AUC and Cohen's d.

For the first time, a detailed analysis of the cellular fluorescence intensity and lifetimes was made between naevi and melanomas using multispectral FLIM. Although no statistical difference was seen comparing the τ_{mean} between the two groups when compared on a per patient basis, differences in the distribution of fluorescence lifetime parameters on a per cell basis were clearly detectable. However, the degree of separation between these distributions was insufficient for most fluorescence intensity and lifetime parameters to be used for discrimination. These differences, detected for the first time, do raise interesting questions as to their biological origin, for which further work is suggested.

Chapter 9. Conclusions

9.1 Aims

The aim of the work presented in this thesis was to investigate the skin and skin disease by measuring tissue autofluorescence and fluorescence lifetime using multiphoton microscopy (MPM). In particular we have focused on the differences in autofluorescence and fluorescence lifetime found in normal skin compared to those found in skin malignancies such as basal cell carcinoma (BCC) and melanoma.

9.2 Instrumentation

In order to achieve this aim, a clinically licensed device for *in vivo* imaging of the skin using multiphoton excitation (the DermaInspect®, JenLab, Germany) was adapted. The Mai-Tai laser remained the excitation light source allowing a range between 710-920 nm to be selected. The focusing optics also remained unchanged, allowing an image resolution of 0.7 μm in the X-Y plane and <2 μm in the Z plane to be achieved to a working distance of 200μm depth. In addition to the ability to record fluorescence intensity images, fluorescence could be diverted to a detector module allowing FLIM to be achieved in four spectral channels simultaneously i.e. a blue channel (360-425 nm), green channel (425-515 nm), yellow channel (515-620 nm) and red channel (620-655 nm) with an image resolution of up to 256x256 pixels. Dr Clifford Talbot designed this to achieve an optical transmission efficiency of 85% and the H7722P-40 PMTs used allowed a high peak quantum efficiency of 40%.

In addition a prism-based spectrometer using an EMCCD detector was designed to allow steady state hyperspectral images to be acquired in the spectral range of 380-655 nm with a high quantum efficiency of 40-65% and an image resolution of up to 41x256 pixels.

The results, demonstrated in Chapter 6 (figure 6.1, pp138-9), show that sets of depth resolved FLIM images can be acquired from unfixed, unsectioned tissue with corresponding hyperspectral images and emission spectra. The analysis described in section 6.4 (pp136) then demonstrate that the information within these images can be used to made a detailed analysis of the fluorescence of the skin. This instrument therefore provides a powerful and versatile tool for investigating the skin.

MPM and fluorescence lifetime imaging microscopy (FLIM) of the skin using modified versions of the DermaInspect® has been reported elsewhere. For example, the research group of Dr Roberts et al. in Brisbane, Australia have described measuring multispectral FLIM using a DermaInspect® in up to four spectral channels. Their work initially used the instrument to monitor the penetration of Zinc

Oxide into the skin (Roberts, Roberts et al. 2008). Subsequently they have investigated the changes in autofluorescence over time following excision (Sanchez, Prow et al. 2010) and skin pigmentation (Dancik, Favre et al. 2013).

Similarly, Professor König's group have presented depth resolved paired FLIM images and emission spectra from normal skin by measured the fluorescence emission with a DermaInspect® and using an attached spectrometer (Breunig and König 2011). However, the instrument described in this thesis is the first time both multispectral FLIM and hyperspectral images have been acquired from a significant number of patients.

A motorised stage was attached to the modified DermaInspect® for the acquisition of image mosaics from BCCs, naevi and melanomas. Although a large mosaic image of a BCC acquired using MPM has been presented previously by Lin et al. (Lin, Jee et al. 2006), they measured autofluorescence intensity from fixed, sectioned tissue. In contrast, for the first time, the images presented in this thesis of a BCC (figure 7.7, pp191), naevi (figures 8.4, 8.5, pp206/7) and a melanoma (figure 8.6, pp209) were acquired using MPM using freshly excised, unfixed, unsectioned tissue and of FLIM images taken with multiple spectral channels.

9.3 Analysis

The analysis of the fluorescence lifetime from the skin presented in this thesis has attempted to define the cellular fluorescence on a cell by cell basis using the FLIM images acquired. The aim of this approach was to exclude extracellular fluorescence from adversely affecting the lifetime analysis, which may have occurred if each field of view (FOV) was analysed as a whole. In addition it could allow the identification of subpopulations of cells within the skin, based on their autofluorescence signature. In contrast to previous studies using FLIM to investigate the skin, most images were acquired at comparatively high magnification (107μm x107μm) so as to be able to delineate individual cells within the image and, where possible, every cell from every image has been manually defined as a region of interest (ROI). This prevents possible selection bias compared to manually choosing specific cells from the FLIM images or manually selecting individual pixels from within a cell to analyse. This approach has allowed differences in the intra- and interpatient variation in cellular lifetimes to be evaluated (Chapter 6.6.1, pp155) and subpopulations of cells based on autofluorescence to be described (Chapter 6.6.2, pp157) for the first time.

9.4 Normal skin following excision

Chapter 5 (pp115) describes the changes in autofluorescence and autofluorescence lifetimes seen over time following surgical excision of normal human skin (n=5, *s.spinosum* layer) over a 3 hour

time period for the first time. Previous studies have reported changes over this time period in mouse skin, using fluorescence spectral imaging (Palero, Bader et al. 2011) and in human skin daily, over seven days using multispectral FLIM (Sanchez, Prow et al. 2010).

In this study, a steady increase in the mean pixel fluorescence intensity of 105-112% with time was demonstrated, dependent on spectral channel which suggests that the imaging parameters outlined in Chapter 5.3 (pp118) did not cause photobleaching.

A small but consistent drop in the τ_{mean} over time of 1.7-8.0% was also demonstrated, dependent on the spectral channel. Further analysis showed that a <1 % change was seen τ_1 and τ_2 in the green spectral channel in which NAD(P)H fluorescence dominates, suggesting that the cellular metabolism remains minimally affected over this time period. As a comparison, the variation found in lifetime over time was compared to the range in variation in lifetime between field of views from cells in the *s. spinosum* (n=31-33 depending on spectral channel). This showed that the changes seen in lifetime over time for all spectral channels was small compared to the variation found between cells. In addition, it has been shown that there is no statistical difference in lifetime acquired *in vivo* from samples of normal skin (n=19) and from freshly excised *ex vivo* samples (n=8) over the initial 3 hours.

In summary the study showed that the fluorescence lifetimes remained fairly constant over the initial 3 hours post excision. We were not able to detect the changes described by Sanchez et al. described over a 7 day period, as expected, or the changes seen in mouse skin over a 3 hour period by Palero et al. It can be speculated that this difference may be caused by the difference in the metabolic rates between human and mouse skin but further work would be necessary to validate this supposition.

These results support the use of freshly excised human skin as a surrogate for *in vivo* imaging for MPT and MPT FLIM investigations over the initial few hours post excision. It also validates the conclusions draw by previous authors using MPT whom have studied freshly excised skin to extrapolate changes seen *in vivo* (Cicchi, Sestini et al. 2008; Ericson, Simonsson et al. 2008; Paoli, Smedh et al. 2008; De Giorgi, Massi et al. 2009).

9.5 Normal Skin

A detailed analysis has also been presented in Chapter 6 (pp133) of the variation seen in lifetimes in normal skin with cell layer, age, sex, skin phototype and body site. For this analysis, although the patient numbers were sub-optimal for a definitive comparison, an attempt has been made to match each comparative group. To date, Benati et al. have published the only report to evaluate the

changes systematically in fluorescence lifetime of normal skin with age and skin layer (Benati, Bellini et al. 2011).

In the analysis of cell layer, a decrease in the median τ_{mean} between the *s.granulosum* and the basal layer of 1286, 1206, 1169 and 691 ps for the blue, green, yellow and red spectral channels respectively was found, which is significantly longer than the decrease reported previously of 236 ps between the upper and lower epidermis of the forearm (Benati, Bellini et al. 2011) and of 300 ps between the *s.spinosum* and the basal layer (Breunig and König 2011). The data supported the conclusion that this change relates to increased melanin content in the cells in the basal layer.

The cellular lifetime was found to increase with age. A longer median τ_{mean} was found between the 30-42 and >42 year old groups of +199, +550, +514 and +417 ps in the blue, green, yellow and red channels respectively. These results support the trend reported by Benati at al., who detected a smaller increase in lifetime with age of 109-210 ps (Benati, Bellini et al. 2011) but the data presented here was not found to be statistically different.

A progressive shortening of the median τ_{mean} was also seen with skin phototype of 286, 1336, 1436 and 915 ps in the blue, green, yellow and red channels respectively between skin type 1 and 4. This trend was reflected in τ_1, τ_2 and f_1 and felt to arise from increasing melanin content of the cells with increasing skin type. This difference was found to be statistically significant using the Wilcoxon rank sum test in the green ($p=0.016$), yellow ($p=0.016$) and red ($p=0.016$) spectral channels and has not been recorded in the literature previously.

No difference in lifetime was detected between the sexes. Finally, when the lifetimes from the skin from different body sites were compared, a decrease in the median τ_{mean} was found between the outside and inside forearm of 82, 267, 136 and 291 ps in the blue, green, yellow and red spectral channels respectively. However, this finding may have been affected by sub-optimal matching of the patient groups and further work is suggested to determine if this represents a true finding. In comparison, Benati et al. did not detect a difference in lifetimes between the inside and outside forearm, but did detect a significant difference between the inside forearm and the thigh (Benati, Bellini et al. 2011).

9.6 Basal Cell Carcinoma

Chapter 7 (pp175) presents a detailed *ex vivo* study using multispectral FLIM imaging to differentiate BCCs from normal skin. Previously defined morphologically features for the identification of BCCs in MPT images were tested (Seidenari, Arginelli et al. 2012) and a newly proposed feature of 'merging cells' was defined (illustrated in figure 7.2, pp181). These features allowed image stacks from BCCs

to be identified correctly with a sensitivity/specificity of 79%/93%. The fluorescence lifetimes of cells from BCCs were also found to be statistically significantly longer in all spectral channels compared to normal skin ranging from 19.9% (425-515 nm green spectral emission channel) to 39.8% (620-655 nm red emission spectral channel).

The fluorescence lifetime changes measured using MPT associated with BCCs have been investigated by a number of groups previously. For example, Cicchi et al. to record a modest increase in lifetime of 90 ps from BCCs compared to normal skin (Cicchi, Massi et al. 2007; Cicchi, Sestini et al. 2008). Seidenari et al. repeated the comparison of lifetimes taken from BCC cells and cells from normal skin (Seidenari, Arginelli et al. 2012) and confirmed an increase in lifetime between normal skin and BCCs of 463 ps. The study of BCCs presented in this thesis, and now published (Patalay, Talbot et al. 2012), represent the most comprehensive analysis of fluorescence lifetimes of BCCs and the only study to use multispectral FLIM and the results are in agreement with these previous studies.

In addition, cell-based morphological parameters and the relationship between cells and their neighbours could be calculated as all cells were manually identified and delineated in the FLIM images. This allowed comparisons to be made in the distributions of these parameters between normal skin and BCCs. For the first time also, a quantitative discrimination index of individual spectroscopic and cell-based morphologic parameters have been calculated. The discriminatory ability of using multiple parameters were then assessed using principal component analysis (PCA) based dimensionality reduction and linear discriminant analysis (LDA). This yielded an AUC of 0.83 for the discrimination of BCC from normal skin.

Finally, the discrimination using PCA and LDA was repeated using a fully automated image segmentation algorithm ‘define’ each cell automatically from the FLIM images. This also yielded an AUC of 0.83 for the discrimination of BCC from normal skin and is the first time that this image segmentation technique has been applied to this application.

9.7 Pigmented melanocytic lesions

Chapter 8 (pp195) investigates the application of multispectral FLIM to pigmented melanocytic lesions, namely comparing the fluorescence lifetimes from dysplastic naevi to melanomas. A detailed qualitative and quantitative assessment of the autofluorescence and autofluorescence lifetime from pigmented lesions has been made for the first time using multispectral FLIM detection. A sensitivity and specificity for identifying melanomas using previously defined morphological features in MPT intensity images was made (Dimitrow, Ziemer et al. 2009). Specificities ranging between 93.7 – 97% were calculated for all parameters. However the sensitivity for these morphological features using

this data was generally poor, with only the sensitivity of 'large intercellular distance' and the presence of dendritic cells reaching greater than 50%. However, when the presence of 1 or more feature was assessed, a sensitivity and specificity of 75% and 81% respectively was found and the absence of all 6 features had a negative predictive valve against melanoma of 92.8%.

Cell-based morphological parameters and the relationship between cells and their neighbours were calculated for all cells using the manually defined ROIs and this was this first time this was performed for these diagnostic groups. Although differences in these parameters could be seen between dysplastic naevi and melanomas, they generally had a poor ability to discriminate between dysplastic naevi and melanomas.

Some differences in the distribution of fluorescence lifetimes between the two groups was found, however no statistical difference was seen comparing the median τ_{mean}. The degree of separation between these distributions was insufficient however for most fluorescence intensity and lifetime parameters to be used for discrimination. These differences raise interesting questions as to their biological origin, for which further work is suggested.

These findings regarding the fluorescence lifetime are consistent with and build upon the work by Dimitrow et al. whom also performed a lifetime comparison of naevi with melanomas (Dimitrow, Riemann et al. 2009). They were also unable to detect a difference between naevi and melanomas based on lifetime but could distinguish keratinocytes from melanocytes.

9.8 Future Work

The work presented in this thesis has used multispectral MPT FLIM to investigate tissue autofluorescence and fluorescence lifetime variability in normal skin, between normal skin and BCCs and between dysplastic naevi and melanomas.

The modifications made to the DermaInspect® have produced a useful tool to investigate skin disease. Its application could extend to the wide variety of skin diseases, including inflammatory dermatoses, which were not possible within the time constrains of this project.

Future work has been suggested in Chapter 6.6.1 (pp155) to extend the sample size and scope to investigate the variability seen in lifetimes in normal skin. Only limited data could be collected to delineate the extent of changes in lifetime seen within patients e.g. between body sites and between patients e.g. changes with age.

The fluorescence data collected from normal skin identified population of cells with distinct fluorescence characteristics. Further work is suggested to correlate these populations with their

morphological appearance in the MPT FLIM images and to correlate the biological basis for the changes seen. The greater understanding gained about the autofluorescence of normal skin would aid the interpretation of changes detected with malignancy.

An important result was gained using the automatically segmented images instead of the manually segmented images when calculating the discrimination index between BCCs and normal skin. This finding is promising because it potentially allows the labour intensive manual segmentation step to be automated. This advance would be necessary for high throughput of FLIM images in the future, as MPT FLIM becomes increasingly clinically used.

Finally, as MPT matures as a clinical imaging modality, like reflectance confocal microscopy, the barriers to its use will be the availability and clinical awareness of large, blinded, randomised controlled trials assessing its usefulness in clinical practice

References

Andersson-Engels, S., G. Canti, et al. (2000). "Preliminary evaluation of two fluorescence imaging methods for the detection and the delineation of basal cell carcinomas of the skin." Lasers in Surgery and Medicine **26**(1): 76-82.

Argenziano, G., L. Cerroni, et al. (2012). "Accuracy in melanoma detection: A 10-year multicenter survey." Journal of the American Academy of Dermatology **67**(1): 54-59.e51.

Argenziano, G., H. P. Soyer, et al. (2003). "Dermoscopy of pigmented skin lesions: results of a consensus meeting via the Internet." Journal of American Academy of Dermatology **48**(5): 679-693.

Arginelli, F., M. Manfredini, et al. (2012). "High resolution diagnosis of common nevi by multiphoton laser tomography and fluorescence lifetime imaging." Skin Research and Technology **19**(2): 194-204.

Armstrong, B. K. and A. Kricker (2001). "The epidemiology of UV induced skin cancer." Journal of Photochemistry & Photobiology B **63**(1-3): 8-18.

Avi-Dor, Y., J. M. Olson, et al. (1962). "Fluorescence of pyridine nucleotides in mitochondrion." Journal of Biological Chemistry **237**: 2377-2383.

Bader, A. N., A.-M. Pena, et al. (2011). "Fast nonlinear spectral microscopy of in vivo human skin." Biomedical Optics Express **2**(2): 365-373.

Becker, W. (2005). Advanced Time-Correlated Single Photon Counting Techniques. Berlin, Springer.

Benati, E., V. Bellini, et al. (2011). "Quantitative evaluation of healthy epidermis by means of multiphoton microscopy and fluorescence lifetime imaging microscopy." Skin Research and Technology **17**(3): 295-303.

Berezin, M. Y. (2010). "Fluorescence lifetime measurements and biological imaging." Chemical Reviews **110**(5): 2641.

Bivand, R. S., E. J. Pebesma, et al. (2008). Applied Spatial Data Analysis with R, Springer Science & Business Media.

Blackwell, J., K. M. Katika, et al. (2008). "In vivo time-resolved autofluorescence measurements to test for glycation of human skin." Journal of Biomedical Optics **13**(1): 014004.

Boone, M. A. L. M., S. Norrenberg, et al. (2012). "Imaging of basal cell carcinoma by high-definition optical coherence tomography: histomorphological correlation. A pilot study." British Journal of Dermatology **167**(4): 856-864.

Brancaleon, L., A. J. Durkin, et al. (2001). "I*n vivo* fluorescence spectroscopy of nonmelanoma skin cancer." Photochem Photobiol **73**(2): 178-183.

Breunig, H. G., R. Bückle, et al. (2011). "Combined in vivo multiphoton and CARS imaging of healthy and disease-affected human skin." Microscopy Research and Technique: n/a-n/a.

Breunig, H. G. and K. König (2011). Spectral characteristics of two-photon autofluorescence and second harmonic generation from human skin in vivo. Proceedings of SPIE, San Francisco, California, USA, SPIE.

Breunig, H. G., H. Studier, et al. (2010). "Multiphoton excitation characteristics of cellular fluorophores of human skin in vivo." Optics Express **18**(8): 7857-7871.

Brewer, M. B., A. T. Yeh, et al. (2004). Multiphoton imaging of excised normal skin and keloid scar: preliminary investigations, SPIE.

Brinckmann, J., Y. Açil, et al. (1995). "Collagen synthesis in (sun-)aged human skin and in fibroblasts derived from sun-exposed and sun-protected body sites." Journal of Photochemistry and Photobiology B: Biology **27**(1): 33-38.

Buehler, C., K. Kim, et al. (2005). "Single-Photon Counting Multicolor Multiphoton Fluorescence Microscope." Journal of Fluorescence **15**(1): 41-51.

Burns, T., S. Breathnach, et al. (2010). Rook's Textbook of Dermatology, Wiley-Blackwell.

Busam, K. J., C. Charles, et al. (2001). "Morphologic features of melanocytes, pigmented keratinocytes, and melanophages by in vivo confocal scanning laser microscopy." Modern Pathology **14**(9): 862-868.

CancerResearchUK. (2010). "Cancer Statistics." Retrieved 30/03/2010, from http://info.cancerresearchuk.org/cancerstats/types/skin/.

Chance, B., B. Schoener, et al. (1979). "Oxidation-reduction ratio studies of mitochondria in freeze-trapped samples. NADH and flavoprotein fluorescence signals." Journal of Biological Chemistry **254**(11): 4764-4771.

Chen, G., J. Chen, et al. (2009). "Nonlinear spectral imaging of human hypertrophic scar based on two-photon excited fluorescence and second-harmonic generation." British Journal of Dermatology **161**(1): 48-55.

Chen, J., S. Zhuo, et al. (2011). "Multiphoton microscopy study of the morphological and quantity changes of collagen and elastic fiber components in keloid disease." Journal of Biomedical Optics **16**(5): 051305-051306.

Chen, J. X., S. M. Zhuo, et al. (2006). "Spectral characteristics of autofluorescence and second harmonic generation from ex vivo human skin induced by femtosecond laser and visible lasers." Scanning **28**(6): 319-326.

Christenson, L. J., T. A. Borrowman, et al. (2005). "Incidence of basal cell and squamous cell carcinomas in a population younger than 40 years." Journal of the American Medical Association **294**(6): 681-690.

Chwirot, B. W., S. Chwirot, et al. (1998). "Detection of melanomas by digital imaging of spectrally resolved ultraviolet light-induced autofluorescence of human skin." European Journal of Cancer **34**(11): 1730-1734.

Chwirot, B. W., S. Chwirot, et al. (2001). "Fluorescence in situ detection of human cutaneous melanoma: study of diagnostic parameters of the method." Journal of Investigative Dermatology **117**(6): 1449-1451.

Cicchi, R., D. Massi, et al. (2007). "Multidimensional non-linear laser imaging of Basal Cell Carcinoma." Optics Express **15**(16): 10135-10148.

Cicchi, R., S. Sestini, et al. (2008). "Nonlinear laser imaging of skin lesions." Journal of Biophotonics **1**(1): 62-73.

Coleman, A. J., T. J. Richardson, et al. (2012). "Histological correlates of optical coherence tomography in non-melanoma skin cancer." Skin Research and Technology: n/a-n/a.

Cubeddu, R., D. Comelli, et al. (2002). Clinical system for skin tumour detection by fluorescence lifetime imaging. Engineering in Medicine and Biology. 24th Annual Conference and the Annual Fall Meeting of the Biomedical Engineering Society.

Cubeddu, R., A. Pifferi, et al. (1999). "Fluorescence lifetime imaging: An application to the detection of skin tumors." Ieee Journal of Selected Topics in Quantum Electronics **5**(4): 923-929.

Cubeddu, R., A. Pifferi, et al. (1999). "Fluorescence lifetime imaging: An application to the detection of skin tumors." IEEE J. Select. Topics Quantum Electron. **5**(4): 923-929.

Cunha, D., T. Richardson, et al. (2011). "Comparison of ex vivo optical coherence tomography with conventional frozen-section histology for visualizing basal cell carcinoma during Mohs micrographic surgery." British Journal of Dermatology **165**(3): 576-580.

DaCosta, R. S., H. Andersson, et al. (2003). "Molecular fluorescence excitation-emission matrices relevant to tissue spectroscopy." Photochemistry and Photobiology **78**(4): 384-392.

Dal Pozzo, V., C. Benelli, et al. (1999). "The seven features for melanoma: a new dermoscopic algorithm for the diagnosis of malignant melanoma." European Journal of Dermatology **9**(4): 303-308.

Dancik, Y., A. Favre, et al. (2013). "Use of multiphoton tomography and fluorescence lifetime imaging to investigate skin pigmentation in vivo." Journal of Biomedical Optics **18**(2): 026022-026022.

De Berker, D., J. M. McGregor, et al. (2007). "Guidelines for the management of actinic keratoses." British Journal of Dermatology **156**(2): 222-230.
De Beule, P. A., C. Dunsby, et al. (2007). "A hyperspectral fluorescence lifetime probe for skin cancer diagnosis." Review of Scientific Instruments **78**(12): 123101.
De Giorgi, V., D. Massi, et al. (2009). "Combined non-linear laser imaging (two-photon excitation fluorescence microscopy, fluorescence lifetime imaging microscopy, multispectral multiphoton microscopy) in cutaneous tumours: first experiences." Journal of the European Academy of Dermatology and Venereology **23**(3): 314-316.
Demers, A. A., Z. Nugent, et al. (2005). "Trends of nonmelanoma skin cancer from 1960 through 2000 in a Canadian population." Journal of the American Academy of Dermatology **53**(2): 320-328.
Denk, W., J. H. Strickler, et al. (1990). "Two-photon laser scanning fluorescence microscopy." Science **248**(4951): 73-76.
Desai, T. D., A. D. Desai, et al. (2007). "The use of high-frequency ultrasound in the evaluation of superficial and nodular basal cell carcinomas." Dermatologic Surgery **33**(10): 1220-1227; discussion 1226-1227.
Diepgen, T. L. and V. Mahler (2002). "The epidemiology of skin cancer." British Journal of Dermatology **146 Suppl 61**: 1-6.
Dimitrow, E., I. Riemann, et al. (2009). "Spectral fluorescence lifetime detection and selective melanin imaging by multiphoton laser tomography for melanoma diagnosis." Experimental Dermatology **18**(6): 509-515.
Dimitrow, E., M. Ziemer, et al. (2009). "Sensitivity and specificity of multiphoton laser tomography for in vivo and ex vivo diagnosis of malignant melanoma." Journal of Investigative Dermatology **129**(7): 1752-1758.
Ehlers, A., I. Riemann, et al. (2007). "Multiphoton fluorescence lifetime imaging of human hair." Microscopy Research and Technique **70**(2): 154-161.
Eichhorn, R., G. Wessler, et al. (2009). "Early diagnosis of melanotic melanoma based on laser-induced melanin fluorescence." Journal of Biomedical Optics **14**(3): 034033.
Elwood, J. M. and J. Jopson (1997). "Melanoma and sun exposure: An overview of published studies." International Journal of Cancer **73**(2): 198-203.
Ericson, M. B., C. Simonsson, et al. (2008). "Two-photon laser-scanning fluorescence microscopy applied for studies of human skin." Journal of Biophotonics **1**(4): 320-330.
Fang, Q., T. Papaioannou, et al. (2004). "Time-domain laser-induced fluorescence spectroscopy apparatus for clinical diagnostics." Review of Scientific Instruments **75**(1): 151.
Fassihi, H., T. Wong, et al. (2006). "Target proteins in inherited and acquired blistering skin disorders." Clinical and Experimental Dermatology **31**(2): 252-259.
Favazza, C. P., O. Jassim, et al. (2011). "In vivo photoacoustic microscopy of human cutaneous microvasculature and a nevus." Journal of Biomedical Optics **16**(1): 016015.
Fuchs, E. (2008). "Skin stem cells: rising to the surface." Journal of Cell Biology **180**(2): 273-284.
Fuchs, E. and D. W. Cleveland (1998). "A Structural Scaffolding of Intermediate Filaments in Health and Disease." Science **279**(5350): 514-519.
Galletly, N. P., J. McGinty, et al. (2008). "Fluorescence lifetime imaging distinguishes basal cell carcinoma from surrounding uninvolved skin." British Journal of Dermatology **159**(1): 152-161.
Gambichler, T., G. Moussa, et al. (2007). "Preoperative Ultrasonic Assessment of Thin Melanocytic Skin Lesions Using a 100-MHz Ultrasound Transducer: A Comparative Study." Dermatologic Surgery **33**(7): 818-824.
Gambichler, T., A. Orlikov, et al. (2007). "In vivo optical coherence tomography of basal cell carcinoma." Journal of Dermatological Science **45**(3): 167-173.

Gambichler, T., P. Regeniter, et al. (2007). "Characterization of benign and malignant melanocytic skin lesions using optical coherence tomography in vivo." Journal of the American Academy of Dermatology **57**(4): 629-637.
Gerger, A., R. Hofmann-Wellenhof, et al. (2008). "In vivo confocal laser scanning microscopy of melanocytic skin tumours: diagnostic applicability using unselected tumour images." British Journal of Dermatology **158**(2): 329-333.
Gerger, A., M. Horn, et al. (2005). "Confocal examination of untreated fresh specimens from basal cell carcinoma: implications for microscopically guided surgery." Archives of Dermatology **141**(10): 1269-1274.
Gerger, A., S. Koller, et al. (2006). "Sensitivity and specificity of confocal laser-scanning microscopy for in vivo diagnosis of malignant skin tumors." Cancer **107**(1): 193-200.
Ghadially, F. and W. Neish (1960). "Porphyrin fluorescence of experimentally produced squamous cell carcinoma." Nature **188**: 1124.
Giorgi, V. d., M. Stante, et al. (2005). "Possible histopathologic correlates of dermoscopic features in pigmented melanocytic lesions identified by means of optical coherence tomography." Experimental Dermatology **14**(1): 56-59.
González, S. and Z. Tannous (2002). "Real-time, in vivo confocal reflectance microscopy of basal cell carcinoma." Journal of the American Academy of Dermatology **47**(6): 869-874.
Göppert-Mayer, M. (1931). "Über Elementarakte mit zwei Quantensprüngen." Annalen der Physik **401**(3): 273-294.
Gravetter, F. J. and L. B. Wallnau (2009). Statistics for the Behavioral Sciences, Wadsworth.
Grootendorst, D. J., J. Jose, et al. (2012). "First experiences of photoacoustic imaging for detection of melanoma metastases in resected human lymph nodes." Lasers in Surgery and Medicine **44**(7): 541-549.
Guitera, P., S. W. Menzies, et al. (2012). "In vivo confocal microscopy for diagnosis of melanoma and basal cell carcinoma using a two-step method: analysis of 710 consecutive clinically equivocal cases." Journal of Investigative Dermatology **132**(10): 2386-2394.
Hayashi, K., H. Koga, et al. (2009). "High-frequency 30-MHz sonography in preoperative assessment of tumor thickness of primary melanoma: usefulness in determination of surgical margin and indication for sentinel lymph node biopsy." International Journal of Clinical Oncology **14**(5): 426-430.
Hinz, T., L. K. Ehler, et al. (2012). "Preoperative characterization of basal cell carcinoma comparing tumour thickness measurement by optical coherence tomography, 20-MHz ultrasound and histopathology." Acta Dermato-Venereologica **92**(2): 132-137.
Hinz, T., L. K. Ehler, et al. (2011). "Assessment of Tumor Thickness in Melanocytic Skin Lesions: Comparison of Optical Coherence Tomography, 20-MHz Ultrasound and Histopathology." Dermatology **223**(2): 161-168.
Hoffmann, K., M. Stucker, et al. (2001). "Selective femtosecond pulse-excitation of melanin fluorescence in tissue." Journal of Investigative Dermatology **116**(4): 629-630.
Holme, S. A., K. Malinovszky, et al. (2000). "Changing trends in non-melanoma skin cancer in South Wales, 1988-98." British Journal of Dermatology **143**(6): 1224-1229.
Huang, S., A. A. Heikal, et al. (2002). "Two-photon fluorescence spectroscopy and microscopy of NAD(P)H and flavoprotein." Biophysical Journal **82**(5): 2811-2825.
Huck, V., C. Gorzelanny, et al. (2011). Intravital multiphoton tomography as an appropriate tool for non-invasive in vivo analysis of human skin affected with atopic dermatitis, San Francisco, California, USA, SPIE.
Huck, V., C. Gorzelanny, et al. (2010). Intravital multiphoton tomography as a novel tool for non-invasive in vivo analysis of human skin affected with atopic dermatitis, San Francisco, California, USA, SPIE.
JenLab (2009). User Manual DermaInspect® Version 2.2.1e. GmbH.
Joliffe, I. T. (2002). Principal Component Analysis. New York, Springer-Verlag.

Kaatz, M., A. Sturm, et al. (2010). "Depth-resolved measurement of the dermal matrix composition by multiphoton laser tomography." Skin Research and Technology **16**(2): 131-136.
Kapsokalyvas, D., R. Cicchi, et al. (2011). In-vivo optical investigation of psoriasis, Proc. SPIE.
Kapsokalyvas, D., R. Cicchi, et al. (2011). In-vivo morphologic and spectroscopic investigation of Psoriasis, Proc SPIE.
Karen, J. K., D. S. Gareau, et al. (2009). "Detection of basal cell carcinomas in Mohs excisions with fluorescence confocal mosaicing microscopy." Br J Dermatol **160**(6): 1242-1250.
Katika, K. M., L. Pilon, et al. (2006). In vivo time-resolved autofluorescence measurements on human skin. Photonic Therapeutics and Diagnostics II, San Jose, CA, USA, SPIE.
Kielty, C. M., M. J. Sherratt, et al. (2002). "Elastic fibres." Journal of Cell Science **115**(14): 2817-2828.
Kierdaszuk, B., H. Malak, et al. (1996). "Fluorescence of reduced nicotinamides using one- and two-photon excitation." Biophysical Chemistry **62**(1–3): 1-13.
Kittler, H., H. Pehamberger, et al. (2002). "Diagnostic accuracy of dermoscopy." Lancet Oncology **3**(3): 159-165.
Koehler, M. J., S. Hahn, et al. (2008). "Morphological skin ageing criteria by multiphoton laser scanning tomography: non-invasive in vivo scoring of the dermal fibre network." Experimental Dermatology **17**(6): 519-523.
Koehler, M. J., K. König, et al. (2006). "In vivo assessment of human skin aging by multiphoton laser scanning tomography." Optics Letters **31**(19): 2879-2881.
Koehler, M. J., A. Preller, et al. (2011). "Non-invasive evaluation of dermal elastosis by in vivo multiphoton tomography with autofluorescence lifetime measurements." Experimental Dermatology **21**(1): 48-51.
Koehler, M. J., A. Preller, et al. (2009). "Intrinsic, solar and sunbed-induced skin aging measured in vivo by multiphoton laser tomography and biophysical methods." Skin Research and Technology **15**(3): 357-363.
Koehler, M. J., M. Speicher, et al. (2011). "Clinical application of multiphoton tomography in combination with confocal laser scanning microscopy for in vivo evaluation of skin diseases." Experimental Dermatology **20**(7): 589-594.
Koehler, M. J., T. Vogel, et al. (2010). "In vivo measurement of the human epidermal thickness in different localizations by multiphoton laser tomography." Skin Research and Technology **16**(3): 259-264.
Koehler, M. J., S. Zimmermann, et al. (2011). "Keratinocyte morphology of human skin evaluated by in vivo multiphoton laser tomography." Skin Research and Technology **17**(4): 479-486.
Kollias, N., G. Zonios, et al. (2002). "Fluorescence spectroscopy of skin." Vibrational Spectroscopy **28**: 17-23.
Konig, K. (2000). "Multiphoton microscopy in life science." Journal of Microscopy **200**: 83-104.
König, K. (2008). "Clinical multiphoton tomography." Journal of Biophotonics **1**(1): 13-23.
König, K., G. Flemming, et al. (1998). "Laser-induced autofluorescence spectroscopy of dental caries." Cellular and molecular biology (Noisy-le-Grand, France) **44**(8): 1293-1300.
König, K., A. P. Raphael, et al. (2011). "Applications of multiphoton tomographs and femtosecond laser nanoprocessing microscopes in drug delivery research." Advanced Drug Delivery Reviews **63**(4-5): 388-404.
König, K. and I. Riemann (2003). "High-resolution multiphoton tomography of human skin with subcellular spatial resolution and picosecond time resolution." Journal of Biomedical Optics **8**(3): 432-439.
König, K. and H. Schneckenburger (1994). "Laser-induced autofluorescence for medical diagnosis " Journal of Fluorescence **4**(1): 17-40.
König, K., M. Speicher, et al. (2009). "Clinical optical coherence tomography combined with multiphoton tomography of patients with skin diseases." Journal of Biophotonics **2**(6-7): 389-397.

König, K., M. Speicher, et al. (2010). "Clinical application of multiphoton tomography in combination with high-frequency ultrasound for evaluation of skin diseases." Journal of Biophotonics **3**(12): 759-773.
Konig, K., U. Wollina, et al. (2002). Optical tomography of human skin with subcellular spatial and picosecond time resolution using intense near infrared femtosecond laser pulses, SPIE.
Krasieva, T. B., C. Stringari, et al. (2013). "Two-photon excited fluorescence lifetime imaging and spectroscopy of melanins in vitro and in vivo." Journal of Biomedical Optics **18**(3): 31107.
Kricker, A., B. K. Armstrong, et al. (1995). "A dose-response curve for sun exposure and basal cell carcinoma." International Journal of Cancer **60**(4): 482-488.
Laiho, L. H., S. Pelet, et al. (2005). "Two-photon 3-D mapping of ex vivo human skin endogenous fluorescence species based on fluorescence emission spectra." Journal of Biomedical Optics **10**(2): 024016.
Lakowicz, J. (1999). Principles of Fluorescence Spectroscopy. New York, Kluwer Academic/Plenum Publishers.
Lakowicz, J. R., Ed. (2006). Principles of Fluorescence Spectroscopy, Springer.
Lakowicz, J. R., H. Szmacinski, et al. (1992). "Fluorescence lifetime imaging of free and protein-bound NADH." Proceedings of the National Academy of Sciences **89**(4): 1271-1275.
Langley, R. G., M. Rajadhyaksha, et al. (2001). "Confocal scanning laser microscopy of benign and malignant melanocytic skin lesions in vivo." Journal American Academy of Dermatology **45**(3): 365-376.
Langley, R. G., N. Walsh, et al. (2007). "The diagnostic accuracy of in vivo confocal scanning laser microscopy compared to dermoscopy of benign and malignant melanocytic lesions: a prospective study." Dermatology **215**(4): 365-372.
Leupold, D., M. Scholz, et al. (2011). "The stepwise two photon excited melanin fluorescence is a unique diagnostic tool for the detection of malignant transformation in melanocytes." Pigment Cell & Melanoma Research **24**: 438-445.
Levitt, J. M., M. E. McLaughlin-Drubin, et al. (2011). "Automated biochemical, morphological, and organizational assessment of precancerous changes from endogenous two-photon fluorescence images." PLoS ONE **6**(9): e24765.
Lin, S. J., S. H. Jee, et al. (2006). "Discrimination of basal cell carcinoma from normal dermal stroma by quantitative multiphoton imaging." Optics Letters **31**(18): 2756-2758.
Lin, S. J., R. Wu, Jr., et al. (2005). "Evaluating cutaneous photoaging by use of multiphoton fluorescence and second-harmonic generation microscopy." Optics Letters **30**(17): 2275-2277.
Lohmann, W., M. Nilles, et al. (1991). "In situ differentiation between naevi and malignant melanomas by fluorescence measurements." Naturwissenschaften **78**(10): 456-457.
Lohmann, W. and E. Paul (1988). "In situ detection of melanomas by fluorescence measurements." Naturwissenschaften **75**(4): 201-202.
Lovell, C. R., K. A. Smolenski, et al. (1987). "Type I and III collagen content and fibre distribution in normal human skin during ageing." British Journal of Dermatology **117**(4): 419-428.
Lu, K., J. Chen, et al. (2009). "Multiphoton laser scanning microscopy of localized scleroderma." Skin Research and Technology **15**(4): 489-495.
Lupton, R. (1993). Statistics in theory and practice, Princeton University Press.
Lutz, V., M. Sattler, et al. (2012). "Characterisation of fibrillar collagen types using multi-dimensional multiphoton laser scanning microscopy." International Journal of Cosmetic Science **34**(2): 209-215.
Lutz, V., M. Sattler, et al. (2012). "Impact of collagen crosslinking on the second harmonic generation signal and the fluorescence lifetime of collagen autofluorescence." Skin Research and Technology **18**(2): 168-179.

Maarek, J.-M. I., L. Marcu, et al. (2000). "Time-resolved Fluorescence Spectra of Arterial Fluorescent Compounds: Reconstruction with the Laguerre Expansion Technique." Photochemistry and Photobiology **71**(2): 178-187.

Machet, L., V. Belot, et al. (2009). "Preoperative Measurement of Thickness of Cutaneous Melanoma Using High-Resolution 20 MHz Ultrasound Imaging: A Monocenter Prospective Study and Systematic Review of the Literature." Ultrasound in Medicine & Biology **35**(9): 1411-1420.

Manfredini, M., F. Arginelli, et al. (2013). "High-resolution imaging of basal cell carcinoma: a comparison between multiphoton microscopy with fluorescence lifetime imaging and reflectance confocal microscopy." Skin Research and Technology **19**(1): e433-443.

Marchesini, R., A. Bono, et al. (2009). "In vivo characterization of melanin in melanocytic lesions: spectroscopic study on 1671 pigmented skin lesions." Journal of Biomedical Optics **14**(1): 014027.

Marcil, I. and R. S. Stern (2000). "Risk of developing a subsequent nonmelanoma skin cancer in patients with a history of nonmelanoma skin cancer: A critical review of the literature and meta-analysis." Archives of Dermatology **136**(12): 1524-1530.

Marcu, L., D. Cohen, et al. (2000). Characterization of type I, II, III, IV, and V collagens by time-resolved laser-induced fluorescence spectroscopy. Proceedings of SPIE, SPIE.

Marghoob, A. A., L. D. Swindle, et al. (2003). "Instruments and new technologies for the in vivo diagnosis of melanoma." Journal of the American Academy of Dermatology **49**(5): 777-797; quiz 798-779.

Masters, B. R., P. T. So, et al. (1997). "Multiphoton excitation fluorescence microscopy and spectroscopy of in vivo human skin." Biophysical Journal **72**(6): 2405-2412.

Mathews (2010). Sample Size Calculations: Practical Methods for Engineers and Scientists, Mathews Malnar and Bailey Inc.

Matthews, T. E., I. R. Piletic, et al. (2011). "Pump-Probe Imaging Differentiates Melanoma from Melanocytic Nevi." Science Translational Medicine **3**(71): 71ra15.

Mayevsky, A. and G. G. Rogatsky (2007). "Mitochondrial function in vivo evaluated by NADH fluorescence: from animal models to human studies." American Journal of Physiology - Cell Physiology **292**(2): C615-C640.

Menzies, S. W., C. Ingvar, et al. (1996). "A sensitivity and specificity analysis of the surface microscopy features of invasive melanoma." Melanoma Research **6**(1): 55-62.

Miller, A. J. and M. C. Mihm, Jr. (2006). "Melanoma." New England Journal of Medicine **355**(1): 51-65.

Mogensen, M., T. M. Joergensen, et al. (2009). "Assessment of Optical Coherence Tomography Imaging in the Diagnosis of Non-Melanoma Skin Cancer and Benign Lesions Versus Normal Skin: Observer-Blinded Evaluation by Dermatologists and Pathologists." Dermatologic Surgery **35**(6): 965-972.

Mogensen, M., B. M. Nurnberg, et al. (2009). "In vivo thickness measurement of basal cell carcinoma and actinic keratosis with optical coherence tomography and 20-MHz ultrasound." British Journal of Dermatology **160**(5): 1026-1033.

Mogensen, M., B. M. Nürnberg, et al. (2011). "How histological features of basal cell carcinomas influence image quality in optical coherence tomography." Journal of Biophotonics **4**(7-8): 544-551.

Mogensen, M., L. Thrane, et al. (2009). "OCT imaging of skin cancer and other dermatological diseases." Journal of Biophotonics **2**(6-7): 442-451.

Motley, R., P. Kersey, et al. (2002). "Multiprofessional guidelines for the management of the patient with primary cutaneous squamous cell carcinoma." British Journal of Dermatology **146**(1): 18-25.

Na, R., I. M. Stender, et al. (2001). "Can autofluorescence demarcate basal cell carcinoma from normal skin? A comparison with protoporphyrin IX fluorescence." Acta Dermato-Venereologica **81**(4): 246-249.

Nachbar, F., W. Stolz, et al. (1994). "The ABCD rule of dermatoscopy. High prospective value in the diagnosis of doubtful melanocytic skin lesions." Journal of American Academy of Dermatology **30**(4): 551-559.
Nakashima, N., K. Yoshihara, et al. (1980). "Picosecond fluorescence lifetime of the coenzyme of D-amino acid oxidase." Journal of Biological Chemistry **255**(11): 5261-5263.
Nofsinger, J. B. and J. D. Simon (2001). "Radiative relaxation of Sepia eumelanin is affected by aggregation." Photochemistry and Photobiology **74**(1): 31-37.
Nori, S., F. Rius-Diaz, et al. (2004). "Sensitivity and specificity of reflectance-mode confocal microscopy for in vivo diagnosis of basal cell carcinoma: a multicenter study." Journal of the American Academy of Dermatology **51**(6): 923-930.
Palero, J. A., A. N. Bader, et al. (2011). "In vivo monitoring of protein-bound and free NADH during ischemia by nonlinear spectral imaging microscopy." Biomedical Optics Express **2**(5): 1030-1039.
Palero, J. A., H. S. de Bruijn, et al. (2006). "In vivo nonlinear spectral imaging in mouse skin." Optics Express **14**(10): 4395-4402.
Palero, J. A., H. S. de Bruijn, et al. (2007). "Spectrally resolved multiphoton imaging of in vivo and excised mouse skin tissues." Biophysical Journal **93**(3): 992-1007.
Palero, J. A., G. Latouche, et al. (2008). "Design and implementation of a sensitive high-resolution nonlinear spectral imaging microscope." Journal of Biomedical Optics **13**(4): 044019.
Pan, Z. Y., J. R. Lin, et al. (2012). "In vivo reflectance confocal microscopy of Basal cell carcinoma: feasibility of preoperative mapping of cancer margins." Dermatology Surgery **38**(12): 1945-1950.
Panjehpour, M., C. E. Julius, et al. (2002). "Laser-induced fluorescence spectroscopy for in vivo diagnosis of non-melanoma skin cancers." Lasers Surg Med **31**(5): 367-373.
Paoli, J., M. Smedh, et al. (2008). "Multiphoton laser scanning microscopy on non-melanoma skin cancer: morphologic features for future non-invasive diagnostics." Journal of Investigative Dermatology **128**(5): 1248-1255.
Patalay, R., C. Talbot, et al. (2012). "Multiphoton Multispectral Fluorescence Lifetime Tomography for the Evaluation of Basal Cell Carcinomas." PLoS ONE **7**(9): e43460.
Patalay, R., C. Talbot, et al. (2011). "Quantification of cellular autofluorescence of human skin using multiphoton tomography and fluorescence lifetime imaging in two spectral detection channels." Biomedical Optics Express **2**(12): 3295-3308.
Pellacani, G., A. M. Cesinaro, et al. (2005). "Reflectance-mode confocal microscopy of pigmented skin lesions--improvement in melanoma diagnostic specificity." Journal of American Academy of Dermatology **53**(6): 979-985.
Pellacani, G., P. Guitera, et al. (2007). "The impact of in vivo reflectance confocal microscopy for the diagnostic accuracy of melanoma and equivocal melanocytic lesions." Journal of Investigative Dermatology **127**(12): 2759-2765.
Pena, A., M. Strupler, et al. (2005). "Spectroscopic analysis of keratin endogenous signal for skin multiphoton microscopy." Optics Express **13**(16): 6268-6274.
Pitts, J. D. and M.-A. Mycek (2001). "Design and development of a rapid acquisition laser-based fluorometer with simultaneous spectral and temporal resolution." Review of Scientific Instruments **72**(7): 3061-3072.
Pleitez, M. A., T. Lieblein, et al. (2012). "In Vivo Noninvasive Monitoring of Glucose Concentration in Human Epidermis by Mid-Infrared Pulsed Photoacoustic Spectroscopy." Analytical Chemistry **85**(2): 1013-1020.
Policard, A. (1924). "Etudes sur les aspects offerts par des tumeurs experimentales examinee a la lumiere de Woods. ." Comptes rendus des séances de la Société de biologie et de ses filiales. **91**: 1423-1424.
Psaty, E. L. and A. C. Halpern (2009). "Current and emerging technologies in melanoma diagnosis: the state of the art." Clinics in Dermatology **27**(1): 35-45.

Puschmann, S., C.-D. Rahn, et al. (2012). "Approach to quantify human dermal skin aging using multiphoton laser scanning microscopy." Journal of Biomedical Optics **17**(3): 036005.
Rajadhyaksha, M., M. Grossman, et al. (1995). "In Vivo Confocal Scanning Laser Microscopy of Human Skin: Melanin Provides Strong Contrast." Journal of Investigative Dermatology **104**(6): 946-952.
Rajaram, N., T. J. Aramil, et al. (2010). "Design and validation of a clinical instrument for spectral diagnosis of cutaneous malignancy." Applied Optics **49**(2): 142-152.
Rajaram, N., J. S. Reichenberg, et al. (2010). "Pilot clinical study for quantitative spectral diagnosis of non-melanoma skin cancer." Lasers in Surgery and Medicine **42**(10): 716-727.
Rajpara, S. M., A. P. Botello, et al. (2009). "Systematic review of dermoscopy and digital dermoscopy/ artificial intelligence for the diagnosis of melanoma." British Journal of Dermatology **161**(3): 591-604.
Ramanujam, N. (2000). "Fluorescence spectroscopy of neoplastic and non-neoplastic tissues." Neoplasia **2**(1-2): 89-117.
Redmond, R. W. (2003). Introduction to Fluorescence and Photophysics. Handbook of Biomedical Fluorescence. M. A. Mycek and B. W. Pogue, Marcel Dekker Inc.
Richards-Kortum, R. and E. SevickMuraca (1996). "Quantitative optical spectroscopy for tissue diagnosis." Annual Review of Physical Chemistry **47**: 555-606.
Roberts, D. L., A. V. Anstey, et al. (2002). "U.K. guidelines for the management of cutaneous melanoma." British Journal of Dermatology **146**(1): 7-17.
Roberts, M. S., Y. Dancik, et al. (2011). "Non-invasive imaging of skin physiology and percutaneous penetration using fluorescence spectral and lifetime imaging with multiphoton and confocal microscopy." European Journal of Pharmaceutics and Biopharmaceutics **77**(3): 469-488.
Roberts, M. S., M. J. Roberts, et al. (2008). "In vitro and in vivo imaging of xenobiotic transport in human skin and in the rat liver." Journal of Biophotonics **1**(6): 478-493.
Ross, J. A. and D. M. Jameson (2008). "Time-resolved methods in biophysics. 8. Frequency domain fluorometry: applications to intrinsic protein fluorescence." Photochemical & Photobiological Sciences **7**(11): 1301-1312.
Rubegni, P., M. Burroni, et al. (2002). "Digital dermoscopy analysis for automated diagnosis of pigmented skin lesions." Clinics in Dermatology **20**(3): 309-312.
Sanchez, W. Y., T. W. Prow, et al. (2010). "Analysis of the metabolic deterioration of ex vivo skin from ischemic necrosis through the imaging of intracellular NAD(P)H by multiphoton tomography and fluorescence lifetime imaging microscopy." Journal of Biomedical Optics **15**(4): 046008-046011.
Sandberg, C., J. Paoli, et al. (2011). "Fluorescence Diagnostics of Basal Cell Carcinomas Comparing Methyl-aminolaevulinate and Aminolaevulinic Acid and Correlation with Visual Clinical Tumour Size." Acta Dermato-Venereologica.
Sandby-Moller, J., T. Poulsen, et al. (2003). "Epidermal thickness at different body sites: relationship to age, gender, pigmentation, blood content, skin type and smoking habits." Acta Dermato-Venereologica **83**(6): 410-413.
Santos, A. F., A. B. Zaltsman, et al. (2008). "Angiogenesis: An Improved In Vitro Biological System and Automated Image-Based Workflow to Aid Identification and Characterization of Angiogenesis and Angiogenic Modulators." Assay and Drug Development Technologies **6**(5): 693-710.
Say, E. A., S. U. Shah, et al. (2011). "Optical coherence tomography of retinal and choroidal tumors." Journal of Ophthalmology **2011**: 385058.
Schneckenburger, H., K. König, et al. (1993). "Time-resolved in-vivo fluorescence of photosensitizing porphyrins." Journal of Photochemistry and Photobiology B: Biology **21**(2–3): 143-147.
Schweitzer, D., S. Schenke, et al. (2007). "Towards metabolic mapping of the human retina." Microscopy Research and Technique **70**(5): 410-419.

Scope, A., C. Benvenuto-Andrade, et al. (2007). "In vivo reflectance confocal microscopy imaging of melanocytic skin lesions: consensus terminology glossary and illustrative images." Journal of the American Academy of Dermatology **57**(4): 644-658.
Seidenari, S., F. Arginelli, et al. (2012). "Diagnosis of BCC by multiphoton laser tomography." Skin Research and Technology: doi: 10.1111/j.1600-0846.2012.00643.x. [Epub ahead of print].
Seidenari, S., F. Arginelli, et al. (2013). "Diagnosis of BCC by multiphoton laser tomography." Skin Research and Technology **19**(1): e297-304.
Seidenari, S., F. Arginelli, et al. (2012). "Multiphoton laser microscopy and fluorescence lifetime imaging for the evaluation of the skin." Dermatology Research and Practice **2012**: 810749.
Seidenari, S., F. Arginelli, et al. (2012). "Multiphoton laser tomography and fluorescence lifetime imaging of basal cell carcinoma: morphologic features for non-invasive diagnostics." Experimental Dermatology **21**(11): 831-836.
Skala, M. C., K. M. Riching, et al. (2007). "In vivo multiphoton fluorescence lifetime imaging of protein-bound and free nicotinamide adenine dinucleotide in normal and precancerous epithelia." Journal of Biomedical Optics **12**(2): 024014.
Skala, M. C., K. M. Riching, et al. (2007). "In vivo multiphoton microscopy of NADH and FAD redox states, fluorescence lifetimes, and cellular morphology in precancerous epithelia." Proceedings of the National Academy of Sciences of the United States of America **104**(49): 19494-19499.
Staples, M. P., M. Elwood, et al. (2006). "Non-melanoma skin cancer in Australia: the 2002 national survey and trends since 1985." Medical Journal of Australia **184**(1): 6-10.
Sterenborg, H., M. Motamedi, et al. (1994). "In vivo flourescence spectroscopy and imaging of human skin tumours." Lasers in Medical Science **9**(3): 191-201.
Sterenborg, H. J. C. M., M. Motamedi, et al. (1994). "In vivo fluorescence spectroscopy and imaging of human skin tumours." Lasers in Medical Science **9**: 191-201.
Sugata, K., S. Sakai, et al. (2010). "Imaging of melanin distribution using multiphoton autofluorescence decay curves." Skin Research and Technology **16**(1): 55-59.
Talbot, C. B., R. Patalay, et al. (2011). A multispectral FLIM tomograph for in-vivo imaging of skin cancer, San Francisco, California, USA, Proc. SPIE.
Talbot, C. B., R. Patalay, et al. (2011). "Application of ultrafast gold luminescence to measuring the instrument response function for multispectral multiphoton fluorescence lifetime imaging." Optics Express **19**(15): 13848-13861.
Tan, E. M., A. S. Cohen, et al. (1982). "The 1982 revised criteria for the classification of systemic lupus erythematosus." Arthritis & Rheumatism **25**(11): 1271-1277.
Telfer, N. R., G. B. Colver, et al. (2008). "Guidelines for the management of basal cell carcinoma." British Journal of Dermatology **159**(1): 35-48.
Teuchner, K., J. Ehlert, et al. (2000). "Fluorescence Studies of Melanin by Stepwise Two-Photon Femtosecond Laser Excitation." Journal of Fluorescence **10**(3): 275-275.
Teuchner, K., W. Freyer, et al. (1999). "Femtosecond two-photon excited fluorescence of melanin." Photochemistry and Photobiology **70**(2): 146-151.
Thompson, A. J., S. Coda, et al. (2012). "In vivo measurements of diffuse reflectance and time-resolved autofluorescence emission spectra of basal cell carcinomas." Journal of Biophotonics **5**(3): 240-254.
Ulrich, M., M. Klemp, et al. (2013). "In vivo detection of basal cell carcinoma: comparison of a reflectance confocal microscope and a multiphoton tomograph." Journal of Biomedical Optics **18**(6): 061229-061229.
van der Beek, N., J. de Leeuw, et al. (2012). "PpIX fluorescence combined with auto-fluorescence is more accurate than PpIX fluorescence alone in fluorescence detection of non-melanoma skin cancer: an intra-patient direct comparison study." Lasers in Surgery and Medicine **44**(4): 271-276.

Vander Heiden, M. G., L. C. Cantley, et al. (2009). "Understanding the Warburg effect: the metabolic requirements of cell proliferation." Science **324**(5930): 1029-1033.
Vishwasrao, H. D., A. A. Heikal, et al. (2005). "Conformational dependence of intracellular NADH on metabolic state revealed by associated fluorescence anisotropy." Journal of Biological Chemistry **280**(26): 25119-25126.
Wagnieres, G. A., W. M. Star, et al. (1998). "In vivo fluorescence spectroscopy and imaging for oncological applications." Photochemistry and Photobiology **68**(5): 603-632.
Wagnieres, G. A., W. M. Star, et al. (1998). "In vivo fluorescence spectroscopy and imaging for oncological applications." Photochem Photobiol **68**(5): 603-632.
Wang, H. W., V. Gukassyan, et al. (2008). "Differentiation of apoptosis from necrosis by dynamic changes of reduced nicotinamide adenine dinucleotide fluorescence lifetime in live cells." Journal of Biomedical Optics **13**(5): 054011.
Wang, H. W., Y. H. Wei, et al. (2009). "Reduced Nicotinamide Adenine Dinucleotide (NADH) Fluorescence for the Detection of Cell Death." Anti-Cancer Agents in Medicinal Chemistry **9**(9): 1012-1017.
Wang, Y., K. Maslov, et al. (2010). "Integrated photoacoustic and fluorescence confocal microscopy." IEEE Transanctions on Biomedical Engineering **57**(10): 2576-2578.
Warburg, O. (1956). "On the origin of cancer cells." Science **123**(3191): 309-314.
Warburg, O., F. Wind, et al. (1927). "The Metabolism of Tumors in the Body." The Journal of General Physiology **8**(6): 519-530.
Weedon, D. (2002). Skin Pathology, Elsevier.
Wetzig, T., M. Kendler, et al. (2010). "No clinical benefit of preoperative fluorescence diagnosis of basal cell carcinoma localized in the H-zone of the face." British Journal of Dermatology **162**(6): 1370-1376.
Wolf, D. J. and J. A. Zitelli (1987). "Surgical margins for basal cell carcinoma." Archives in Dermatology **123**(3): 340-344.
www.heine.com. Retrieved 26.4.2010.
www.lucid-tech.com. Retrieved 26/4/2010.
Yang, H., G. Luo, et al. (2003). "Protein conformational dynamics probed by single-molecule electron transfer." Science **302**(5643): 262-266.
Yu, Y., A. M. Lee, et al. (2012). "Imaging-guided two-photon excitation-emission-matrix measurements of human skin tissues." Journal of Biomedical Optics **17**(7): 077004.
Zeng, H. and C. MacAulay (2003). Fluorescence spectroscopy and imaging for skin cancer detection and evaluation. Handbook of Biomedical Fluorescence. M.-A. Mycek and B. Pogue. New York, Marcel Dekker**:** 315-360.
Zhang, E. Z., B. Povazay, et al. (2011). "Multimodal photoacoustic and optical coherence tomography scanner using an all optical detection scheme for 3D morphological skin imaging." Biomedical Optics Express **2**(8): 2202-2215.
Zhu, X., S. Zhuo, et al. (2011). "Characteristics of scar margin dynamic with time based on multiphoton microscopy." Lasers in Medical Science **26**(2): 239-245.
Zhuo, S., J. Chen, et al. (2006). "Multimode nonlinear optical imaging of the dermis in ex vivo human skin based on the combination of multichannel mode and Lambda mode." Optics Express **14**(17): 7810-7820.

Appendix - Permissions to Reproduce Material

This appendix list the requested permissions for copyright to reproduce figures or images from the following sources

I. Source Material

Arginelli, F., M. Manfredini, et al. (2012). "High resolution diagnosis of common nevi by multiphoton laser tomography and fluorescence lifetime imaging." Skin Research and Technology: n/a-n/a.

Dimitrow, E., M. Ziemer, et al. (2009). "Sensitivity and specificity of multiphoton laser tomography for in vivo and ex vivo diagnosis of malignant melanoma." Journal of Investigative Dermatology 129(7): 1752-1758.

Gambichler, T., A. Orlikov, et al. (2007). "In vivo optical coherence tomography of basal cell carcinoma." Journal of Dermatological Science 45(3): 167-173.

JenLab (2009). User Manual DermaInspect® Version 2.2.1e.

Karen, J. K., D. S. Gareau, et al. (2009). "Detection of basal cell carcinomas in Mohs excisions with fluorescence confocal mosaicing microscopy." Br J Dermatol 160(6): 1242-1250.

Koehler, M. J., S. Zimmermann, et al. (2011). "Keratinocyte morphology of human skin evaluated by in vivo multiphoton laser tomography." Skin Research and Technology 17(4): 479-486.

Krasieva, T. B., C. Stringari, et al. (2013). "Two-photon excited fluorescence lifetime imaging and spectroscopy of melanins in vitro and in vivo." Journal of Biomedical Optics 18(3): 31107.

Lutz, V., M. Sattler, et al. (2012). "Characterisation of fibrillar collagen types using multi-dimensional multiphoton laser scanning microscopy." International Journal of Cosmetic Science 34(2): 209-215.

Marghoob, A. A., L. D. Swindle, et al. (2003). "Instruments and new technologies for the in vivo diagnosis of melanoma." Journal of the American Academy of Dermatology 49(5): 777-797; quiz 798-779.

Nofsinger, J. B. and J. D. Simon (2001). "Radiative relaxation of Sepia eumelanin is affected by aggregation." Photochemistry and Photobiology 74(1): 31-37.

Palero, J. A., A. N. Bader, et al. (2011). "In vivo monitoring of protein-bound and free NADH during ischemia by nonlinear spectral imaging microscopy." Biomedical Optics Express 2(5): 1030-1039.

Palero, J. A., H. S. de Bruijn, et al. (2007). "Spectrally resolved multiphoton imaging of in vivo and excised mouse skin tissues." Biophysical Journal 93(3): 992-1007.

Pena, A., M. Strupler, et al. (2005). "Spectroscopic analysis of keratin endogenous signal for skin multiphoton microscopy." Optics Express 13(16): 6268-6274.

Ratto, Fulvio. Inst. di Fisica Applicata, Italy. EM photograph of gold nanorods.

Sanchez, W. Y., T. W. Prow, et al. (2010). "Analysis of the metabolic deterioration of ex vivo skin from ischemic necrosis through the imaging of intracellular NAD(P)H by multiphoton tomography and fluorescence lifetime imaging microscopy." Journal of Biomedical Optics 15(4): 046008-046011.

Seidenari, S., F. Arginelli, et al. (2013). "Diagnosis of BCC by multiphoton laser tomography." Skin Research and Technology 19(1): e297-304.

Teuchner, K., W. Freyer, et al. (1999). "Femtosecond two-photon excited fluorescence of melanin." Photochemistry and Photobiology 70(2): 146-151.

Wagnieres, G. A., W. M. Star, et al. (1998). "In vivo fluorescence spectroscopy and imaging for oncological applications." Photochemistry and Photobiology 68(5): 603-632.

II. Elsevier License Terms and Conditions

A. Introduction

1. The publisher for this copyrighted material is Elsevier. By clicking "accept" in connection with completing this licensing transaction, you agree that the following terms and conditions apply to this transaction (along with the Billing and Payment terms and conditions established by Copyright Clearance Center, Inc. ("CCC"), at the time that you opened your Rightslink account and that are available at any time at http://myaccount.copyright.com).

B. General Terms

2. Elsevier hereby grants you permission to reproduce the aforementioned material subject to the terms and conditions indicated.

3. Acknowledgement: If any part of the material to be used (for example, figures) has appeared in our publication with credit or acknowledgement to another source, permission must also be sought from that source. If such permission is not obtained then that material may not be included in your publication/copies. Suitable acknowledgement to the source must be made, either as a footnote or in a reference list at the end of your publication, as follows: “Reprinted from Publication title, Vol /edition number, Author(s), Title of article / title of chapter, Pages No., Copyright (Year), with permission from Elsevier [OR APPLICABLE SOCIETY COPYRIGHT OWNER].” Also Lancet special credit - “Reprinted from The Lancet, Vol. number, Author(s), Title of article, Pages No., Copyright (Year), with permission from Elsevier.”

4. Reproduction of this material is confined to the purpose and/or media for which permission is hereby given.

5. Altering/Modifying Material: Not Permitted. However figures and illustrations may be altered/adapted minimally to serve your work. Any other abbreviations, additions, deletions and/or any other alterations shall be made only with prior written authorization of Elsevier Ltd. (Please contact Elsevier at permissions@elsevier.com)

6. If the permission fee for the requested use of our material is waived in this instance, please be advised that your future requests for Elsevier materials may attract a fee.

7. Reservation of Rights: Publisher reserves all rights not specifically granted in the combination of (i) the license details provided by you and accepted in the course of this licensing transaction, (ii) these terms and conditions and (iii) CCC's Billing and Payment terms and conditions.

8. License Contingent Upon Payment: While you may exercise the rights licensed immediately upon issuance of the license at the end of the licensing process for the transaction, provided that you have disclosed complete and accurate details of your proposed use, no license is finally effective unless and until full payment is received from you (either by publisher or by CCC) as provided in CCC's Billing and Payment terms and conditions. If full payment is not received on a timely basis, then any license preliminarily granted shall be deemed automatically revoked and shall be void as if never granted. Further, in the event that you breach any of these terms and conditions or any of CCC's Billing and Payment terms and conditions, the license is automatically revoked and shall be void as if never granted. Use of materials as described in a revoked license, as well as any use of the materials beyond the scope of an unrevoked license, may constitute copyright infringement and publisher reserves the right to take any and all action to protect its copyright in the materials.

9. Warranties: Publisher makes no representations or warranties with respect to the licensed material.

10. Indemnity: You hereby indemnify and agree to hold harmless publisher and CCC, and their respective officers, directors, employees and agents, from and against any and all claims arising out of your use of the licensed material other than as specifically authorized pursuant to this license.

11. No Transfer of License: This license is personal to you and may not be sublicensed, assigned, or transferred by you to any other person without publisher's written permission.

12. No Amendment Except in Writing: This license may not be amended except in a writing signed by both parties (or, in the case of publisher, by CCC on publisher's behalf).

13. Objection to Contrary Terms: Publisher hereby objects to any terms contained in any purchase order, acknowledgment, check endorsement or other writing prepared by you, which terms are inconsistent with these terms and conditions or CCC's Billing and Payment terms and conditions. These terms and conditions, together with CCC's Billing and Payment terms and conditions (which are incorporated herein), comprise the entire agreement between you and publisher (and CCC) concerning this licensing transaction. In the event of any conflict between your obligations established by these terms and conditions and those established by CCC's Billing and Payment terms and conditions, these terms and conditions shall control.

14. Revocation: Elsevier or Copyright Clearance Center may deny the permissions described in this License at their sole discretion, for any reason or no reason, with a full refund payable to you. Notice of such denial will be made using the contact information provided by you. Failure to receive such notice will not alter or invalidate the denial. In no event will Elsevier or Copyright Clearance Center be responsible or liable for any costs, expenses or damage incurred by you as a result of a denial of your permission request, other than a refund of the amount(s) paid by you to Elsevier and/or Copyright Clearance Center for denied permissions.

C. Limited License

The following terms and conditions apply only to specific license types:

15. Translation: This permission is granted for non-exclusive world English rights only unless your license was granted for translation rights. If you licensed translation rights you may only translate this content into the languages you requested. A professional translator must perform all translations and reproduce the content word for word preserving the integrity of the article. If this license is to re-use 1 or 2 figures then permission is granted for non-exclusive world rights in all languages.

16. Website: The following terms and conditions apply to electronic reserve and author websites: Electronic reserve: If licensed material is to be posted to website, the web site is to be password-protected and made available only to bona fide students registered on a relevant course if: This license was made in connection with a course, This permission is granted for 1 year only. You may obtain a license for future website posting, All content posted to the web site must maintain the copyright information line on the bottom of each image, A hyper-text must be included to the Homepage of the journal from which you are licensing at http://www.sciencedirect.com/science/journal/xxxxx or the Elsevier homepage for books at http://www.elsevier.com , and Central Storage: This license does not include permission for a scanned version of the material to be stored in a central repository such as that provided by Heron/XanEdu.

17. Author website for journals with the following additional clauses:
All content posted to the web site must maintain the copyright information line on the bottom of each image, and the permission granted is limited to the personal version of your paper. You are not allowed to download and post the published electronic version of your article (whether PDF or HTML, proof or final version), nor may you scan the printed edition to create an electronic version. A hyper-text must be included to the Homepage of the journal from which you are licensing at http://www.sciencedirect.com/science/journal/xxxxx . As part of our normal production process, you will receive an e-mail notice when your article appears on Elsevier's online service ScienceDirect (www.sciencedirect.com). That e-mail will include the article's Digital Object Identifier (DOI). This number provides the electronic link to the published article and should be included in the posting of your personal version. We ask that you wait until you receive this e-mail and have the DOI to do any posting. Central Storage: This license does not include permission for a scanned version of the material to be stored in a central repository such as that provided by Heron/XanEdu.

18. Author website for books with the following additional clauses: Authors are permitted to place a brief summary of their work online only. A hyper-text must be included to the Elsevier homepage at http://www.elsevier.com . All content posted to the web site must maintain the copyright information line on the bottom of each image. You are not allowed to download and post the published electronic version of your chapter, nor may you scan the printed edition to create an electronic version. Central Storage: This license does not include permission for a scanned version of the material to be stored in a central repository such as that provided by Heron/XanEdu.

19. Website (regular and for author): A hyper-text must be included to the Homepage of the journal from which you are licensing at http://www.sciencedirect.com/science /journal/xxxxx. or for books to the Elsevier homepage at http://www.elsevier.com

20. Thesis/Dissertation: If your license is for use in a thesis/dissertation your thesis may be submitted to your institution in either print or electronic form. Should your thesis be published commercially, please reapply for permission. These requirements include permission for the Library and Archives of Canada to supply single copies, on demand, of the complete thesis and include permission for UMI to supply single copies, on demand, of the complete thesis. Should your thesis be published commercially, please reapply for permission.

21. Other Conditions:

v1.6

If you would like to pay for this license now, please remit this license along with your payment made payable to "COPYRIGHT CLEARANCE CENTER" otherwise you will be invoiced within 48 hours of the license date. Payment should be in the form of a check or money order referencing your account number and this invoice number RLNK500985425. Once you receive your invoice for this order, you may pay your invoice by credit card. Please follow instructions provided at that time.

Make Payment To:
Copyright Clearance Center
Dept 001
P.O. Box 843006
Boston, MA 02284-3006

For suggestions or comments regarding this order, contact RightsLink Customer Support: customercare@copyright.com or +1-877-622-5543 (toll free in the US) or +1-978 646- 2777.

Gratis licenses (referencing $0 in the Total field) are free. Please retain this printable license for your reference. No payment is required.

III. Nature Publishing Group License Terms and Conditions.

Nature Publishing Group hereby grants you a non-exclusive license to reproduce this material for this purpose, and for no other use, subject to the conditions below:

1. NPG warrants that it has, to the best of its knowledge, the rights to license reuse of this material. However, you should ensure that the material you are requesting is original to Nature Publishing Group and does not carry the copyright of another entity (as credited in the published version). If the credit line on any part of the material you have requested indicates that it was reprinted or adapted by NPG with permission from another source, then you should also seek permission from that source to reuse the material.

2. Permission granted free of charge for material in print is also usually granted for any electronic version of that work, provided that the material is incidental to the work as a whole and that the electronic version is essentially equivalent to, or substitutes for, the print version. Where print permission has been granted for a fee, separate permission must be obtained for any additional, electronic re-use (unless, as in the case of a full paper, this has already been accounted for during your initial request in the calculation of a print run). NB: In all cases, web-based use of full-text articles must be authorized separately through the 'Use on a Web Site' option when requesting permission.

3. Permission granted for a first edition does not apply to second and subsequent editions and for editions in other languages (except for signatories to the STM Permissions Guidelines, or where the first edition permission was granted for free).

4. Nature Publishing Group's permission must be acknowledged next to the figure, table or abstract in print. In electronic form, this acknowledgement must be visible at the same time as the figure/table/abstract, and must be hyperlinked to the journal's homepage.

5. The credit line should read:
Reprinted by permission from Macmillan Publishers Ltd: [JOURNAL NAME] (reference citation), copyright (year of publication)
For AOP papers, the credit line should read:
Reprinted by permission from Macmillan Publishers Ltd: [JOURNAL NAME], advance online publication, day month year (doi: 10.1038/sj.[JOURNAL ACRONYM].XXXXX)
Note: For republication from the British Jou rnal of Can cer, the following credit lines apply.
Reprinted by permission from Macmillan Publishers Ltd on behalf of Cancer Research UK: [JOURNAL NAME] (reference citation), copyright (year of publication) For AOP papers, the credit line should read:
Reprinted by permission from Macmillan Publishers Ltd on behalf of Cancer Research UK: [JOURNAL NAME], advance online publication, day month year (doi: 10.1038/sj. [JOURNAL ACRONYM].XXXXX)

6. Adaptations of single figures do not require NPG approval. However, the adaptation should be credited as follows:
Adapted by permission from Macmillan Publishers Ltd: [JOURNAL NAME] (reference citation), copyright (year of publication)
Note: For adaptation from the British J ournal of Cancer, the following credit line applies.
Adapted by permission from Macmillan Publishers Ltd on behalf of Cancer Research UK: [JOURNAL NAME] (reference citation), copyright (year of publication)

7. Translations of 401 words up to a whole article require NPG approval. Please visit http://www.macmillanmedicalcommunications.com for more information. Translations of up to a 400 words do not require NPG approval. The translation should be credited as follows:
Translated by permission from Macmillan Publishers Ltd: [JOURNAL NAME] (reference citation), copyright (year of publication).
Note: For translation from the British J ournal of Cancer, the following credit line applies.
Translated by permission from Macmillan Publishers Ltd on behalf of Cancer Research UK: [JOURNAL NAME] (reference citation), copyright (year of publication)

We are certain that all parties will benefit from this agreement and wish you the best in the use of this material. Thank you.

Special Terms:

v1.1

If you would like to pay for this license now, please remit this license along with your payment made payable to "COPYRIGHT CLEARANCE CENTER" otherwise you will be invoiced within 48 hours of the

license date. Payment should be in the form of a check or money order referencing your account number and this invoice number RLNK500985421. Once you receive your invoice for this order, you may pay your invoice by credit card. Please follow instructions provided at that time.

Make Payment To:
Copyright Clearance Center
Dept 001
P.O. Box 843006
Boston, MA 02284-3006

For suggestions or comments regarding this order, contact RightsLink Customer Support: customercare@copyright.com or +1-877-622-5543 (toll free in the US) or +1-978-646-2777. Gratis licenses (referencing $0 in the Total field) are free. Please retain this printable license for your reference. No payment is required.

IV. John Wiley and Sons license terms and conditions

1. The materials you have requested permission to reproduce (the "Materials") are protected by copyright.

2.You are hereby granted a personal, non-exclusive, non-sublicensable, non-transferable, worldwide, limited license to reproduce the Materials for the purpose specified in the licensing process. This license is for a one-time use only with a maximum distribution equal to the number that you identified in the licensing process. Any form of republication granted by this license must be completed within two years of the date of the grant of this license (although copies prepared before may be distributed thereafter). The Materials shall not be used in any other manner or for any other purpose. Permission is granted subject to an appropriate acknowledgement given to the author, title of the material/book/journal and the publisher. You shall also duplicate the copyright notice that appears in the Wiley publication in your use of the Material. Permission is also granted on the understanding that nowhere in the text is a previously published source acknowledged for all or part of this Material. Any third party material is expressly excluded from this permission.

3. With respect to the Materials, all rights are reserved. Except as expressly granted by the terms of the license, no part of the Materials may be copied, modified, adapted (except for minor reformatting required by the new Publication), translated, reproduced, transferred or distributed, in any form or by any means, and no derivative works may be made based on the Materials without the prior permission of the respective copyright owner. You may not alter, remove or suppress in any manner any copyright, trademark or other notices displayed by the Materials. You may not license, rent, sell, loan, lease, pledge, offer as security, transfer or assign the Materials, or any of the rights granted to you hereunder to any other person.

4. The Materials and all of the intellectual property rights therein shall at all times remain the exclusive property of John Wiley & Sons Inc or one of its related companies (WILEY) or their respective licensors, and your interest therein is only that of having possession of and the right to reproduce the Materials pursuant to Section 2 herein during the continuance of this Agreement. You agree that you own no right, title or interest in or to the Materials or any of the intellectual property

rights therein. You shall have no rights hereunder other than the license as provided for above in Section 2. No right, license or interest to any trademark, trade name, service mark or other branding ("Marks") of WILEY or its licensors is granted hereunder, and you agree that you shall not assert any such right, license or interest with respect thereto.

5. NEITHER WILEY NOR ITS LICENSORS MAKES ANY WARRANTY OR REPRESENTATION OF ANY KIND TO YOU OR ANY THIRD PARTY, EXPRESS, IMPLIED OR STATUTORY, WITH RESPECT TO THE MATERIALS OR THE ACCURACY OF ANY INFORMATION CONTAINED IN THE MATERIALS, INCLUDING, WITHOUT LIMITATION, ANY IMPLIED WARRANTY OF MERCHANTABILITY, ACCURACY, SATISFACTORY QUALITY, FITNESS FOR A PARTICULAR PURPOSE, USABILITY, INTEGRATION OR NON-INFRINGEMENT AND ALL SUCH WARRANTIES ARE HEREBY EXCLUDED BY WILEY AND ITS LICENSORS AND WAIVED BY YOU.

6. WILEY shall have the right to terminate this Agreement immediately upon breach of this Agreement by you.

7. You shall indemnify, defend and hold harmless WILEY, its Licensors and their respective directors, officers, agents and employees, from and against any actual or threatened claims, demands, causes of action or proceedings arising from any breach of this Agreement by you.

8. IN NO EVENT SHALL WILEY OR ITS LICENSORS BE LIABLE TO YOU OR ANY OTHER PARTY OR ANY OTHER PERSON OR ENTITY FOR ANY SPECIAL, CONSEQUENTIAL, INCIDENTAL, INDIRECT, EXEMPLARY OR PUNITIVE DAMAGES, HOWEVER CAUSED, ARISING OUT OF OR IN CONNECTION WITH THE DOWNLOADING, PROVISIONING, VIEWING OR USE OF THE MATERIALS REGARDLESS OF THE FORM OF ACTION, WHETHER FOR BREACH OF CONTRACT, BREACH OF WARRANTY, TORT, NEGLIGENCE, INFRINGEMENT OR OTHERWISE (INCLUDING, WITHOUT LIMITATION, DAMAGES BASED ON LOSS OF PROFITS, DATA, FILES, USE, BUSINESS OPPORTUNITY OR CLAIMS OF THIRD PARTIES), AND WHETHER OR NOT THE PARTY HAS BEEN ADVISED OF THE POSSIBILITY OF SUCH DAMAGES. THIS LIMITATION SHALL APPLY NOTWITHSTANDING ANY FAILURE OF ESSENTIAL PURPOSE OF ANY LIMITED REMEDY PROVIDED HEREIN.

9. Should any provision of this Agreement be held by a court of competent jurisdiction to be illegal, invalid, or unenforceable, that provision shall be deemed amended to achieve as nearly as possible the same economic effect as the original provision, and the legality, validity and enforceability of the remaining provisions of this Agreement shall not be affected or impaired thereby.

10. The failure of either party to enforce any term or condition of this Agreement shall not constitute a waiver of either party's right to enforce each and every term and condition of this Agreement. No breach under this agreement shall be deemed waived or excused by either party unless such waiver or consent is in writing signed by the party granting such waiver or consent. The waiver by or consent of a party to a breach of any provision of this Agreement shall not operate or be construed as a waiver of or consent to any other or subsequent breach by such other party.

11. This Agreement may not be assigned (including by operation of law or otherwise) by you without WILEY's prior written consent.

12. Any fee required for this permission shall be non-refundable after thirty (30) days from receipt

13. These terms and conditions together with CCCs Billing and Payment terms and conditions (which are incorporated herein) form the entire agreement between you and WILEY concerning this licensing transaction and (in the absence of fraud) supersedes all prior agreements and representations of the parties, oral or written. This Agreement may not be amended except in writing signed by both parties. This Agreement shall be binding upon and inure to the benefit of the parties' successors, legal representatives, and authorized assigns.

14. In the event of any conflict between your obligations established by these terms and conditions and those established by CCCs Billing and Payment terms and conditions, these terms and conditions shall prevail.

15. WILEY expressly reserves all rights not specifically granted in the combination of (i) the license details provided by you and accepted in the course of this licensing transaction, (ii) these terms and conditions and (iii) CCCs Billing and Payment terms and conditions.

16. This Agreement will be void if the Type of Use, Format, Circulation, or Requestor Type was misrepresented during the licensing process.

17. This Agreement shall be governed by and construed in accordance with the laws of the State of New York, USA, without regards to such states conflict of law rules. Any legal action, suit or proceeding arising out of or relating to these Terms and Conditions or the breach thereof shall be instituted in a court of competent jurisdiction in New York County in the State of New York in the United States of America and each party hereby consents and submits to the personal jurisdiction of such court, waives any objection to venue in such court and consents to service of process by registered or certified mail, return receipt requested, at the last known address of such party.

A. Wiley Open Access Terms and Conditions

Wiley publishes Open Access articles in both its Wiley Open Access Journals program [http://www.wileyopenaccess.com/view/index.html] and as Online Open articles in its subscription journals. The majority of Wiley Open Access Journals have adopted the Creative Commons Attribution License (CC BY) which permits the unrestricted use, distribution, reproduction, adaptation and commercial exploitation of the article in any medium. No permission is required to use the article in this way provided that the article is properly cited and other license terms are observed. A small number of Wiley Open Access journals have retained the Creative Commons Attribution Non Commercial License (CC BY-NC), which permits use, distribution and reproduction in any medium, provided the original work is properly cited and is not used for commercial purposes.

Online Open articles Authors selecting Online Open are, unless particular exceptions apply, offered a choice of Creative Commons licenses. They may therefore select from the CC BY, the CC BY-NC and the Attribution-NoDerivatives (CC BY-NC-ND). The CC BY-NC-ND is more restrictive than the CC BY-NC as it does not permit adaptations or modifications without rights holder consent.

Wiley Open Access articles are protected by copyright and are posted to repositories and websites in accordance with the terms of the applicable Creative Commons license referenced on the article. At the time of deposit, Wiley Open Access articles include all changes made during peer review, copyediting, and publishing. Repositories and websites that host the article are responsible for incorporating any publisher-supplied amendments or retractions issued subsequently. Wiley Open

Access articles are also available without charge on Wiley's publishing platform, Wiley Online Library or any successor sites.

Conditions applicable to all Wiley Open Access articles:

- The authors' moral rights must not be compromised. These rights include the right of "paternity" (also known as "attribution" - the right for the author to be identified as such) and "integrity" (the right for the author not to have the work altered in such a way that the author's reputation or integrity may be damaged).
- Where content in the article is identified as belonging to a third party, it is the obligation of the user to ensure that any reuse complies with the copyright policies of the owner of that content.
- If article content is copied, downloaded or otherwise reused for research and other purposes as permitted, a link to the appropriate bibliographic citation (authors, journal, article title, volume, issue, page numbers, DOI and the link to the definitive published version on Wiley Online Library) should be maintained. Copyright notices and disclaimers must not be deleted.
  Creative Commons licenses are copyright licenses and do not confer any other rights, including but not limited to trademark or patent rights.
- Any translations, for which a prior translation agreement with Wiley has not been agreed, must prominently display the statement: "This is an unofficial translation of an article that appeared in a Wiley publication. The publisher has not endorsed this translation."

B. Conditions applicable to non-commercial licenses (CC BY-NC and CC BY-NC-ND)

For non-commercial and non-promotional purposes individual non-commercial users may access, download, copy, display and redistribute to colleagues Wiley Open Access articles. In addition, articles adopting the CC BY-NC may be adapted, translated, and text- and data-mined subject to the conditions above.

C. Use by commercial "for-profit" organizations

Use of non-commercial Wiley Open Access articles for commercial, promotional, or marketing purposes requires further explicit permission from Wiley and will be subject to a fee. Commercial purposes include:

- Copying or downloading of articles, or linking to such articles for further redistribution, sale or licensing;
- Copying, downloading or posting by a site or service that incorporates advertising with such content;
- The inclusion or incorporation of article content in other works or services (other than normal quotations with an appropriate citation) that is then available for sale or licensing, for a fee (for example, a compilation produced for marketing purposes, inclusion in a sales pack)
- Use of article content (other than normal quotations with appropriate citation) by forprofit organizations for promotional purposes
- Linking to article content in e-mails redistributed for promotional, marketing or educational purposes;

- Use for the purposes of monetary reward by means of sale, resale, license, loan, transfer or other form of commercial exploitation such as marketing products
- Print reprints of Wiley Open Access articles can be purchased from: corporatesales@wiley.com

The modification or adaptation for any purpose of an article referencing the CC BYNC- ND License requires consent which can be requested from RightsLink@wiley.com

D. Other Terms and Conditions:

BY CLICKING ON THE "I AGREE..." BOX, YOU ACKNOWLEDGE THAT YOU HAVE READ AND FULLY UNDERSTAND EACH OF THE SECTIONS OF AND PROVISIONS SET FORTH IN THIS AGREEMENT AND THAT YOU ARE IN AGREEMENT WITH AND ARE WILLING TO ACCEPT ALL OF YOUR OBLIGATIONS AS SET FORTH IN THIS AGREEMENT.

v1.8

If you would like to pay for this license now, please remit this license along with your payment made payable to "COPYRIGHT CLEARANCE CENTER" otherwise you will be invoiced within 48 hours of the license date. Payment should be in the form of a check or money order referencing your account number and this invoice number RLNK500985419. Once you receive your invoice for this order, you may pay your invoice by credit card. Please follow instructions provided at that time.

Make Payment To:
Copyright Clearance Center
Dept 001
P.O. Box 843006
Boston, MA 02284-3006

For suggestions or comments regarding this order, contact RightsLink Customer Support: customercare@copyright.com or +1-877-622-5543 (toll free in the US) or +1-978-646-2777.

Gratis licenses (referencing $0 in the Total field) are free. Please retain this printable license for your reference. No payment is required.

V. Permissions

A. Arginelli 2012

This is a License Agreement between Rakesh Patalay ("You") and John Wiley and Sons ("John Wiley and Sons") provided by Copyright Clearance Center ("CCC"). The license consists of your order details, the terms and conditions provided by John Wiley and Sons, and the payment terms and conditions.

All payments must be made in full to CCC. For payment instructions, please see information listed at the bottom of this form.
License Number 3116170404706
License date Mar 25, 2013
Licensed content publisher John Wiley and Sons
Licensed content publication Skin Research and Technology
Licensed content title High resolution diagnosis of common nevi by multiphoton laser tomography and fluorescence lifetime imaging
Licensed copyright line © 2012 John Wiley & Sons A/S. Published by Blackwell Publishing Ltd
Licensed content author Federica Arginelli,Marco Manfredini,Sara Bassoli,Christopher Dunsby,Paul French,Karsten König,Cristina Magnoni,Giovanni Ponti,Clifford Talbot,Stefania Seidenari
Licensed content date Dec 29, 2012
Start page n/a
End page n/a
Type of use Dissertation/Thesis
Requestor type University/Academic
Format Print and electronic
Portion Figure/table
Number of figures/tables 1
Original Wiley figure/table number(s) figure 1 - 5 panels only
Will you be translating? No
Total 0.00 USD

B. Dimitrow 2009

This is a License Agreement between Rakesh Patalay ("You") and Nature Publishing Group ("Nature Publishing Group") provided by Copyright Clearance Center ("CCC"). The license consists of your order details, the terms and conditions provided by Nature Publishing Group, and the payment terms and conditions.

All payments must be made in full to CCC. For payment instructions, please see information listed at the bottom of this form.
License Number 3116170719911
License date Mar 25, 2013
Licensed content publisher Nature Publishing Group
Licensed content Publication Journal of Investigative Dermatology
Licensed content title Sensitivity and Specificity of Multiphoton Laser Tomography for In Vivo and Ex Vivo Diagnosis of Malignant Melanoma
Licensed content author Enrico Dimitrow, Mirjana Ziemer, Martin Johannes Koehler, Johannes Norgauer, Karsten Konig et al.
Licensed content date Jan 29, 2009
Volume number 129
Issue number 7
Type of Use reuse in a thesis/dissertation
Requestor type academic/educational
Format print and electronic
Portion figures/tables/illustrations
Number of figures/tables/illustrations 1

High-res required no
Figures Figure 5
Author of this NPG article no
Your reference number
Title of your thesis / dissertation The clinical application of multispectral fluorescence lifetime imaging of human skin using multiphoton microscopy
Expected completion date Apr 2013
Estimated size (number of pages) 200
Total 0.00 USD

C. Gambichler 2007

This is a License Agreement between Rakesh Patalay ("You") and Elsevier ("Elsevier") provided by Copyright Clearance Center ("CCC"). The license consists of your order details, the terms and conditions provided by Elsevier, and the payment terms and conditions.

All payments must be made in full to CCC. For payment instructions, please see information listed at the bottom of this form.
Supplier Elsevier Limited The Boulevard,Langford Lane Kidlington,Oxford,OX5 1GB,UK
Registered Company Number 1982084
Customer name Rakesh Patalay
Customer address Optics, Dept of Physics, Blackett Lab London, SW7 2AZ
License number 3116170978998
License date Mar 25, 2013
Licensed content publisher Elsevier
Licensed content Publication Journal of Dermatological Science
Licensed content title In vivo optical coherence tomography of basal cell carcinoma
Licensed content author Thilo Gambichler,Alexej Orlikov,Remus Vasa,Georg Moussa,Klaus Hoffmann,Markus Stücker,Peter Altmeyer,Falk G. Bechara
Licensed content date March 2007
Licensed content volume Number 45
Licensed content issue Number 3
Number of pages 7 Start Page 167 End Page 173
Type of Use reuse in a thesis/dissertation
Intended publisher of new Work other
Portion figures/tables/illustrations
Number of figures/tables/illustrations 1
Format both print and electronic
Are you the author of this Elsevier article? No
Will you be translating? No
Order reference number
Title of your thesis/dissertation The clinical application of multispectral fluorescence lifetime imaging of human skin using multiphoton microscopy
Expected completion date Apr 2013
Estimated size (number of pages) 200
Elsevier VAT number GB 494 6272 12
Permissions price 0.00 USD
VAT/Local Sales Tax 0.0 USD / 0.0 GBP
Total 0.00 USD

D. GmbH 2009

NO CONFIRMATION OF USAGE RECEIVED BEFORE PUBLICATION

Patalay, Rakesh
Subject: FW: permission to reproduce

From: Patalay, Rakesh
Sent: 26 March 2013 00:52
To: 'karsten koenig'
Subject: permission to reproduce

Dear Karsten,
I hope that you are well. At Imperial College, Chris and I are just finalising the details to submit my PhD thesis. In the thesis I have cited the DermaInspect® Manual and would like to reproduce this image. Can I formally ask for your permission to reproduce this adapted figure in my thesis?
Yours
Dr Rakesh Patalay

_____

E. Karen 2009

This is a License Agreement between Rakesh Patalay ("You") and John Wiley and Sons ("John Wiley and Sons") provided by Copyright Clearance Center ("CCC"). The license consists of your order details, the terms and conditions provided by John Wiley and Sons, and the payment terms and conditions.

All payments must be made in full to CCC. For payment instructions, please see information listed at the bottom of this form.
License Number 3116191089458
License date Mar 25, 2013
Licensed content publisher John Wiley and Sons
Licensed content Publication British Journal of Dermatology
Licensed content title Detection of basal cell carcinomas in Mohs excisions with fluorescence confocal mosaicing microscopy
Licensed copyright line © 2009 The Authors. Journal Compilation © 2009 British Association of Dermatologists
Licensed content author J.K. Karen,D.S. Gareau,S.W. Dusza,M. Tudisco,M. Rajadhyaksha,K.S. Nehal
Licensed content date Mar 30, 2009
Start page 1242 End page 1250
Type of use Dissertation/Thesis
Requestor type University/Academic
Format Print and electronic
Portion Figure/table
Number of figures/tables 1
Original Wiley figure/table number(s) Figure 1
Will you be translating? No
Total 0.00 USD

F. Koehler 2011

This is a License Agreement between Rakesh Patalay ("You") and John Wiley and Sons ("John Wiley and Sons") provided by Copyright Clearance Center ("CCC"). The license consists of your order details, the terms and conditions provided by John Wiley and Sons, and the payment terms and conditions.

All payments must be made in full to CCC. For payment instructions, please see information listed at the bottom of this form.
License Number 3116171271346
License date Mar 25, 2013
Licensed content publisher John Wiley and Sons
Licensed content Publication Skin Research and Technology
Licensed content title Keratinocyte morphology of human skin evaluated by in vivo multiphoton laser tomography

Licensed copyright line © 2011 John Wiley & Sons A/S
Licensed content author M. J. Koehler,S. Zimmermann,S. Springer,P. Elsner,K. König,M. Kaatz
Licensed content date Mar 31, 2011
Start page 479 End page 486
Type of use Dissertation/Thesis
Requestor type University/Academic
Format Print and electronic
Portion Figure/table
Number of figures/tables 1
Original Wiley figure/table number(s) Figure 2 - 3 panels
Will you be translating? No
Total 0.00 USD

G. Krasieva 2013

From: Tromberg, Bruce <bjtrombe@uci.edu>
Sent: 02 April 2013 19:57
To: Patalay, Rakesh
Subject: Re: Permission to reproduce figure
Follow Up Flag: Follow up
Flag Status: Flagged

Hi Rakesh,
Great to hear from you, I do remember meeting you and talking to you about your work (and other topics!). Of course, I am very glad for you to use figure 1 from our JBO paper. If you have a chance, send me a pdf of your thesis, we have a skin cancer group here that will be very interested in reading it and following your work. How have your patient measurements been going? Have you managed to get FLIM from patients in the clinic? Best, Bruce

Bruce J. Tromberg, Ph.D.
Director, Beckman Laser Institute and Medical Clinic
Professor, Departments of Biomedical Engineering and Surgery
Principal Investigator, Laser Microbeam and Medical Program (LAMMP)
An NIH National Biomedical Technology Research Center
University of California, Irvine
949-824-4713, 949-824-8705
bjtrombe@hs.uci.edu, www.bli.uci.edu

Patalay, Rakesh
From: Patalay, Rakesh
Sent: 29 March 2013 00:16
To: 'bjtrombe@uci.edu'
Subject: Permission to reproduce figure
Dear Professor Tromberg,
My name is Dr Patalay and I am currently a PhD student and doctor working in the optics group of Professor Paul French at Imperial College London. I have been researching FLIM applied to skin and skin cancer during my thesis and would like to use figure 1 from your recent JBO 2013 paper in my thesis. The publishes have granted permission to reproduce the figure but have suggested that I seek your permission also – see below
Yours
Dr Rakesh Patalay

From: Karen Thomas [mailto:karent@spie.org]

Sent: 27 March 2013 18:18
To: Patalay, Rakesh
Subject: RE: Reprint
Dear Dr. Patalay,
Thank you for seeking permission from SPIE to reprint material from our publications. Publisher's permission is hereby granted under the following conditions:
(1) you obtain permission of one of the authors;
(2) the material to be used has appeared in our publication without credit or acknowledgment to another source; and
(3) you credit the original SPIE publication. Include the authors' names, title of paper, volume title, SPIE volume number, and year of publication in your credit statement.

Sincerely,
Karen Thomas for
Eric Pepper, Director of Publications
SPIE
P.O. Box 10, Bellingham WA 98227-0010 USA
360/676-3290 (Pacific Time) eric@spie.org

_____

From: Patalay, Rakesh [mailto:r.patalay@imperial.ac.uk]
Sent: Monday, March 25, 2013 4:36 PM
To: reprint_permission
Subject: Reprint
2
I would like permission to reproduce the following figure in my PhD thesis
Krasieva, T. B., C. Stringari, et al. (2013). "Two-photon excited fluorescence lifetime imaging and spectroscopy of melanins in vitro and in vivo." Journal of Biomedical Optics **18**(3): 31107.
Reproduce – Figure 1 – graphs a,b For PhD thesis. Print and electronic copy
Yours
Dr Patalay

_____

H. Lutz 2012

This is a License Agreement between Rakesh Patalay ("You") and John Wiley and Sons ("John Wiley and Sons") provided by Copyright Clearance Center ("CCC"). The license consists of your order details, the terms and conditions provided by John Wiley and Sons, and the payment terms and conditions.

All payments must be made in full to CCC. For payment instructions, please see information listed at the bottom of this form.
License Number 3116180354597
License date Mar 25, 2013
Licensed content publisher John Wiley and Sons
Licensed content
Publication International Journal of Cosmetic Science
Licensed content title Characterization of fibrillar collagen types using multi-dimensional multiphoton laser scanning microscopy
Licensed copyright line © 2012 The Authors. ICS © 2012 Society of Cosmetic Scientists and the Société Française de Cosmétologie
Licensed content author V. Lutz,M. Sattler,S. Gallinat,H. Wenck,R. Poertner,F. Fischer
Licensed content date Jan 27, 2012
Start page 209 End page 215

Type of use Dissertation/Thesis
Requestor type University/Academic
Format Print and electronic
Portion Figure/table
Number of figures/tables 2
Original Wiley figure/table number(s) Figure 4b, Figure 5
Will you be translating? No
Total 0.00 USD

I. Marghoob 2003

This is a License Agreement between Rakesh Patalay ("You") and Elsevier ("Elsevier") provided by Copyright Clearance Center ("CCC"). The license consists of your order details, the terms and conditions provided by Elsevier, and the payment terms and conditions.

All payments must be made in full to CCC. For payment instructions, please see information listed at the bottom of this form.
Supplier Elsevier Limited The Boulevard,Langford Lane Kidlington,Oxford,OX5 1GB,UK
Registered Company Number 1982084
Customer name Rakesh Patalay
Customer address Optics, Dept of Physics, Blackett Lab London, SW7 2AZ
License number 3116180772524
License date Mar 25, 2013
Licensed content publisher Elsevier
Licensed content Publication Journal of the American Academy of Dermatology
Licensed content title Instruments and new technologies for the in vivo diagnosis of melanoma
Licensed content author Ashfaq A Marghoob,Lucinda D Swindle,Claudia Z.M Moricz,Fitzgeraldo A Sanchez Negron,Bill Slue,Allan C Halpern,Alfred W Kopf
Licensed content date November 2003
Licensed content volume Number 49
Licensed content issue
Number 5
Number of pages 21
Start Page 777 End Page 797
Type of Use reuse in a thesis/dissertation
Intended publisher of new Work other
Portion figures/tables/illustrations
Number of figures/tables/illustrations 1
Format both print and electronic
Are you the author of this Elsevier article? No
Will you be translating? No
Order reference number
Title of your thesis/dissertation The clinical application of multispectral fluorescence lifetime imaging of human skin using multiphoton microscopy
Expected completion date Apr 2013
Estimated size (number of pages) 200
Elsevier VAT number GB 494 6272 12
Permissions price 0.00 GBP
VAT/Local Sales Tax 0.0 USD / 0.0 GBP
Total 0.00 GBP

J. Nosfinger 2001

This is a License Agreement between Rakesh Patalay ("You") and John Wiley and Sons ("John Wiley and Sons") provided by Copyright Clearance Center ("CCC"). The license consists of your order details, the terms and conditions provided by John Wiley and Sons, and the payment terms and conditions.

All payments must be made in full to CCC. For payment instructions, please see information listed at the bottom of this form.
License Number 3116180970978
License date Mar 25, 2013
Licensed content publisher John Wiley and Sons
Licensed content Publication Photochemistry and Photobiology
Licensed content title Radiative Relaxation of Sepia Eumelanin is Affected by Aggregation
Licensed copyright line Copyright © 2007, John Wiley and Sons
Licensed content author J. Brian Nofsinger,John D. Simon
Licensed content date May 1, 2007
Start page 31 End page 37
Type of use Dissertation/Thesis
Requestor type University/Academic
Format Print and electronic
Portion Figure/table
Number of figures/tables 2
Original Wiley figure/table number(s) Figure 1, Figure 3d
Will you be translating? No
Total 0.00 USD

K. Palero 2007

This is a License Agreement between Rakesh Patalay ("You") and Elsevier ("Elsevier") provided by Copyright Clearance Center ("CCC"). The license consists of your order details, the terms and conditions provided by Elsevier, and the payment terms and conditions.

All payments must be made in full to CCC. For payment instructions, please see information listed at the bottom of this form.
Supplier Elsevier Limited The Boulevard,Langford Lane Kidlington,Oxford,OX5 1GB,UK
Registered Company Number 1982084
Customer name Rakesh Patalay
Customer address Optics, Dept of Physics, Blackett Lab London, SW7 2AZ
License number 3116201124618
License date Mar 25, 2013
Licensed content publisher Elsevier
Licensed content Publication Biophysical Journal
Licensed content title Spectrally Resolved Multiphoton Imaging of In Vivo and Excised Mouse Skin Tissues
Licensed content author Jonathan A. Palero,Henriëtte S. de Bruijn,Angélique van der Ploeg van den Heuvel,Henricus J.C.M. Sterenborg,Hans C. Gerritsen
Licensed content date 1 August 2007
Licensed content volume Number 93
Licensed content issue Number 3
Number of pages 16
Start Page 992 End Page 1007
Type of Use reuse in a thesis/dissertation
Intended publisher of new Work other
Portion figures/tables/illustrations
Number of figures/tables/illustrations 1
Format both print and electronic
Are you the author of this
Elsevier article? No
Will you be translating? No
Order reference number
Title of your thesis/dissertation The clinical application of multispectral fluorescence lifetime imaging of human skin using multiphoton microscopy
Expected completion date Apr 2013
Estimated size (number of pages) 200

Elsevier VAT number GB 494 6272 12
Permissions price 0.00 GBP
VAT/Local Sales Tax 0.0 USD / 0.0 GBP
Total 0.00 GBP

L. Palero 2011

From: prvs=796bea49e=copyright@osa.org on behalf of pubscopyright <copyright@osa.org>
Sent: 01 April 2013 21:19
To: Patalay, Rakesh
Subject: RE: permission to reproduce
Follow Up Flag: Follow up
Flag Status: Flagged

Dear Dr. Patalay,
Thank you for contacting The Optical Society.
OSA considers your requested use of its copyrighted material to be Fair Use under United States Copyright Law. It is requested that a complete citation of the original material be included in any publication. Let me know if you have any questions.

Kind Regards,
Susannah Lehman
Susannah Lehman
April 1, 2013 Authorized Agent, The Optical Society

Patalay, Rakesh
From: Patalay, Rakesh
Sent: 26 March 2013 00:04
To: 'copyright@osa.org'
Subject: permission to reproduce

Dear sir,

RE:

Palero, J. A., A. N. Bader, et al. (2011). "In vivo monitoring of protein-bound and free NADH during ischemia by nonlinear spectral imaging microscopy." Biomedical Optics Express **2**(5): 1030-1039. Figure 5A

I would like to reproduce this graph in my PhD thesis. This will be completed in print and available electronically.

Dr Rakesh Patalay
Division of Optics, Dept Physics
Blackett Lab
Imperial College London
South Kensington Campus
London
SW7 2AZ
Phone +442075947755
Fax +44 20 75947714

M. Pena 2005

From: prvs=796bea49e=copyright@osa.org on behalf of pubscopyright <copyright@osa.org>
Sent: 01 April 2013 21:19
To: Patalay, Rakesh
Subject: RE: permission to reproduce
Follow Up Flag: Follow up
Flag Status: Flagged

Dear Dr. Patalay,

Thank you for contacting The Optical Society.
OSA considers your requested use of its copyrighted material to be Fair Use under United States Copyright Law. It is requested that a complete citation of the original material be included in any publication. Let me know if you have any questions.
Kind Regards,
Susannah Lehman

Susannah Lehman
April 1, 2013
Authorized Agent, The Optical Society

Patalay, Rakesh
From: Patalay, Rakesh
Sent: 26 March 2013 00:20
To: 'copyright@osa.org'
Subject: RE: permission to reproduce

Dear sir,

RE: Pena, A., M. Strupler, et al. (2005). "Spectroscopic analysis of keratin endogenous signal for skin multiphoton microscopy." Optics Express **13**(16): 6268-6274. Figure 2c

I would like to reproduce this graph in my PhD thesis. This will be completed in print and available electronically.

Dr Rakesh Patalay
Division of Optics, Dept Physics
Blackett Lab
Imperial College London
South Kensington Campus
London
SW7 2AZ
Phone +442075947755
Fax +44 20 75947714

N. Ratto

Patalay, Rakesh
From: rattof@ifac.cnr.it
Sent: 27 March 2013 07:06
To: Patalay, Rakesh

Subject: Re: Gold nanorods
Follow Up Flag: Follow up
Flag Status: Flagged
Sure you can, it is my honor.
Yours,
Fulvio

Quoting "Patalay, Rakesh" <r.patalay@imperial.ac.uk>:
Dear Fulvio,

My name is Dr Rakesh Patalay and I work with Paul French, Christopher Dunsby and Clifford Talbot at Imperial College London in the Optics department. We have been working on a project studyin fluorescence lifetime imaging microscopy (FLIM) of human tissue over the last few years. We have also been using samples of gold nanorods, that your lab has provided us to acquire an IRF for our data analysis and Dr Talbot has written a paper about the subject.

I am currently writing up my PhD thesis of this work and would like to formally ask for permission to use the following EM picture of the gold nanorods that you provided our group a few years ago.

The image would be used in the thesis , which would be available in both print form and electronically.

I look forward to hearing from you

Yours
Dr Rakesh Patala

O. Sanchez 2010

Patalay, Rakesh

From: Michael Roberts <m.roberts@uq.edu.au>
Sent: 29 March 2013 02:57
To: Patalay, Rakesh
Subject: Re: Permission to use figure
Hi Rakesh
I am delighted to also give you permission as you have requested
Happy Easter
Mike Roberts
Sent from my iPhone

Patalay, Rakesh

From: Patalay, Rakesh
Sent: 29 March 2013 00:11
To: 'm.roberts@uq.edu.au'
Subject: Permission to use figure
Dear Dr Roberts,
My name is Dr Patalay and I am currently a PhD student and doctor working in the optics group of Professor Paul French at Imperial College London. I have been researching FLIM applied to skin and skin cancer during my thesis. I would like to use part of figure 3 from your JBO 2010 paper in my thesis.

The publishes have granted permission to reproduce the figure but have suggested that I seek your permission also – see below
Yours
Dr Rakesh Patalay

From: Karen Thomas [mailto:karent@spie.org]
Sent: 27 March 2013 18:21
To: Patalay, Rakesh
Subject: RE: Reprint
Dear Dr. Patalay,
Thank you for seeking permission from SPIE to reprint material from our publications. Publisher's permission is hereby granted under the following conditions:
(1) you obtain permission of one of the authors;
(2) the material to be used has appeared in our publication without credit or acknowledgment to another source; and
(3) you credit the original SPIE publication. Include the authors' names, title of paper, volume title, SPIE volume number, and year of publication in your credit statement.
Sincerely,
Karen Thomas for Eric Pepper, Director of Publications
SPIE
P.O. Box 10, Bellingham WA 98227-0010 USA
360/676-3290 (Pacific Time) eric@spie.org

From: Patalay, Rakesh [mailto:r.patalay@imperial.ac.uk]
Sent: Monday, March 25, 2013 5:24 PM
To: reprint_permission
Subject: RE: Reprint
Dear spie,
I would like permission to reproduce the following figure in my PhD thesis

Re : Sanchez, W. Y., T. W. Prow, et al. (2010). "Analysis of the metabolic deterioration of ex vivo skin from ischemic necrosis through the imaging of intracellular NAD(P)H by multiphoton tomography and fluorescence lifetime imaging microscopy." Journal of Biomedical Optics **15**(4): 046008-046011.
Reproduce – Figure 3 - 4 graphs
For PhD thesis. Print and electronic copy
Yours
Dr Rakesh Patalay
Division of Optics, Dept Physics
Blackett Lab
Imperial College London
South Kensington Campus
London
SW7 2AZ
Phone +442075947755
Fax +44 20 75947714

P. Seidenari 2013

This is a License Agreement between Rakesh Patalay ("You") and John Wiley and Sons ("John Wiley and Sons") provided by Copyright Clearance Center ("CCC"). The

license consists of your order details, the terms and conditions provided by John Wiley and Sons, and the payment terms and conditions.

All payments must be made in full to CCC. For payment instructions, please see information listed at the bottom of this form.
License Number 3116200048219
License date Mar 25, 2013
Licensed content publisher John Wiley and Sons
Licensed content Publication Skin Research and Technology
Licensed content title Diagnosis of BCC by multiphoton laser tomography
Licensed copyright line © 2012 John Wiley & Sons A/S
Licensed content author Stefania Seidenari,Federica Arginelli,Sara Bassoli,Jennifer Cautela,Anna Maria Cesinaro,Mario Guanti,Davide Guardoli,Cristina Magnoni,Marco Manfredini,Giovanni Ponti,Karsten König
Licensed content date Jul 8, 2012
Start page e297 End page e304
Type of use Dissertation/Thesis
Requestor type University/Academic
Format Print and electronic
Portion Figure/table
Number of figures/tables 1
Original Wiley figure/table number(s) Figure 3
Will you be translating? No
Total 0.00 USD

Q. Teuchner 1999

This is a License Agreement between Rakesh Patalay ("You") and John Wiley and Sons ("John Wiley and Sons") provided by Copyright Clearance Center ("CCC"). The license consists of your order details, the terms and conditions provided by John Wiley and Sons, and the payment terms and conditions.

All payments must be made in full to CCC. For payment instructions, please see information listed at the bottom of this form.
License Number 3116200231074
License date Mar 25, 2013
Licensed content publisher John Wiley and Sons
Licensed content Publication Photochemistry and Photobiology
Licensed content title Femtosecond Two-photon Excited Fluorescence of Melanin*
Licensed copyright line Copyright © 2008, John Wiley and Sons
Licensed content author Klaus Teuchner,Wolfgang Freyer,Dieter Leupold,Andreas Volkmer,David J. S. Birch,Peter Altmeyer,Markus Stucker,Klaus Hoffmann
Licensed content date Jan 2, 2008
Start page 146 End page 151
Type of use Dissertation/Thesis
Requestor type University/Academic
Format Print and electronic
Portion Figure/table
Number of figures/tables 1
Original Wiley figure/table number(s) Figure 4
Will you be translating? No
Total 0.00 USD

R. Wagnieres 1998

This is a License Agreement between Rakesh Patalay ("You") and John Wiley and Sons ("John Wiley and Sons") provided by Copyright Clearance Center ("CCC"). The

license consists of your order details, the terms and conditions provided by John Wiley and Sons, and the payment terms and conditions.

All payments must be made in full to CCC. For payment instructions, please see information listed at the bottom of this form.
License Number 3116200464210
License date Mar 25, 2013
Licensed content publisher John Wiley and Sons
Licensed content Publication Photochemistry and Photobiology
Licensed content title In Vivo Fluorescence Spectroscopy and Imaging for Oncological Applications
Licensed copyright line Copyright © 2008, John Wiley and Sons
Licensed content author Georges A. Wagnieres,Willem M. Star,Brian C. Wilson
Licensed content date Jan 2, 2008
Start page 603 End page 632
Type of use Dissertation/Thesis
Requestor type University/Academic
Format Print and electronic
Portion Figure/table
Number of figures/tables 1
Original Wiley figure/table number(s) An adaptation of Figure 1A
Will you be translating? No
Total 0.00 USD

S. Wagnieres 1998

This is a License Agreement between Rakesh Patalay ("You") and John Wiley and Sons ("John Wiley and Sons") provided by Copyright Clearance Center ("CCC"). The license consists of your order details, the terms and conditions provided by John Wiley and Sons, and the payment terms and conditions.

All payments must be made in full to CCC. For payment instructions, please see information listed at the bottom of this form.
License Number 3116200614223
License date Mar 25, 2013
Licensed content publisher John Wiley and Sons
Licensed content Publication Photochemistry and Photobiology
Licensed content title In Vivo Fluorescence Spectroscopy and Imaging for Oncological Applications
Licensed copyright line Copyright © 2008, John Wiley and Sons
Licensed content author Georges A. Wagnieres,Willem M. Star,Brian C. Wilson
Licensed content date Jan 2, 2008
Start page 603 End page 632
Type of use Dissertation/Thesis
Requestor type University/Academic
Format Print and electronic
Portion Figure/table
Number of figures/tables 1
Original Wiley figure/table number(s) Adaptation of Figure 1B
Will you be translating? No
Total 0.00 USD